The Interaction of Silver Nanoparticles with Triosephosphate Isomerase from Human and Malarial Parasite (*Plasmodium falciparum*): a Comparative Study

A thesis submitted in partial fulfilment of the requirements for the degree of

Master of Science

in Biochemistry

By

Warren Ralph Josephus de Moor
G04D3097

June 2013

Supervisor: Professor Chris Whiteley
Co-supervisor: Dr Jacqui van Marwijk

In the Department of Biochemistry, Microbiology and Biotechnology
Faculty of Science, Rhodes University, Grahamstown, 6139, South Africa

Abstract

The advent of advanced modern nanotechnology techniques offers new and exciting opportunities to develop novel nanotech-derived antimalarial nanodrugs with enhanced selective and targeting abilities that allow for lower effective drug dosages, longer drug persistence and reduced drug degradation within the body. Using a nanodrug approach also has the advantage of avoiding drug resistance problems that plague reconfigured versions of already-existing antimalarial drugs. In this study recombinant triosephosphate isomerase enzymes from *Plasmodium falciparum* (*Pf*TIM) and *Humans* (*h*TIM) were recombinantly expressed, purified and characterised. *Pf*TIM was shown to have optimal pH stability at pH 5.0-5.5 and thermal stability at 25°C with K_m 4.34 mM and V_{max} 0.876 µmol.ml^{-1}min^{-1}. For *h*TIM, these parameters were as follows: pH optima of 6.5-7.0; temperature optima of 30°C, with K_m 2.27 mM and V_{max} 0.714 µmol.ml^{-1}min^{-1}. Recombinant TIM enzymes were subjected to inhibition studies using polyvinylpyrrolidone (PVP) stabilised silver nanoparticles (AgNPs) of 4-12 nm in diameter. These studies showed that the AgNPs were able to selectively inhibit *Pf*TIM over *h*TIM with an 8-fold greater decrease in enzymatic efficiency (K_{cat}/K_m) observed for *Pf*TIM, as compared to *h*TIM, for kinetics tests done using 0.06 µM of AgNPs. Complete inhibition of *Pf*TIM under optimal conditions was achieved using 0.25 µM AgNPs after 45 minutes while *h*TIM maintained approximately 31% of its activity at this AgNP concentration.

The above results indicate that selective enzymatic targeting of the important, key metabolic enzyme TIM, can be achieved using nanotechnology-derived nanodrugs. It was demonstrated that the key structural differences, between the two enzyme variants, were significant enough to create unique characteristics for each TIM variant, thereby allowing for selective enzyme targeting using AgNPs. If these AgNPs could be coupled with a nanotechnology-derived, targeted localization mechanism – possibly using apoferritin to deliver the AgNPs to infected erythrocytes (Burns and Pollock, 2008) – then such an approach could offer new opportunities for the development of viable antimalarial nanodrugs. For this to be achieved further research into several key areas will be required, including nanoparticle toxicity, drug localization and testing the lethality of the system on live parasite cultures.

Acknowledgements

Firstly, I would first like to thank my supervisor Professor Chris Whiteley, who has guided me through this project, obtained funding from the NRF for me and helped me enormously with editing and advice throughout the project. My co-supervisor, Dr Jacqui van Marwijk, is thanked for her patience, excellent guidance and training on the use of various types of equipment, and for teaching me many new scientific methods and techniques. I would also like to thank Dr Brendan Wilhelmi who often acted as a supervisor even though he was not registered as one, and for the advice and motivational support which he gave during our weekly meetings and presentations. I would like to give a special thanks to all my lab mates whom helped me on numerous occasions and were an absolute joy to work with during the course of my masters. Finally I would like to thank all the people in the department, especially Mrs Margot Brooks who lent me undergraduate equipment and reagents when needed and Mr Sagran Abboo for helping to resolve equipment problems and also for fixing the ventilation to our laboratory. I also wish to thank everyone in the Department of Biochemistry Microbiology and Biotechnology at Rhodes for always being friendly offering assistance and being generally helpful.

I also want to thank my parents Ferdy and Irene de Moor for their continuous help, support and patience throughout the course of my MSc. Irene de Moor is also thanked for her help with language editing of this thesis.

The National Research Foundation is also acknowledged for providing funding to this project and to Rhodes for their excellent facilities and laboratories.

The Malaria Research and Reference Reagents Resource Center, known as MR4 is also thanked for donating the MRA898 *Plasmodium falciparum* 3D7 cDNA used as the PCR template to obtain the *P. falciparum* triosephosphate isomerase studied in this thesis.

Table of Contents

List of Abbreviations

%	- percentage
°C	- degrees celcius
αG3PDH	- alpha glycerol-3-phosphate dehydrogenase
µl	- microliter
µM	- micromolar
Å	- angstrongs
ACT	- artemisinin based combination therapy
Ag	- silver
aka	- also known as
AMT	- artemisinin based monotherapies
APS	- ammonium persulphate
ATCC	- American Type Culture Collection
ATP	- adenosine-5'-triphosphate
Au	- gold
bp	- basepair
BSA	- bovine serum albumen
C	- carbon
Ca^{2+}	- calcium 2^{+} ion
CDC	- Centres for Disease Control
cDNA	- complementary deoxyribonucleic acid
cm	- centimeters
Cys	- cysteine
$dddH_2O$	- triple distilled water
DDT	- dichlorodiphenyltrichloroethane
df	- dilution factor
D-GAP	- D-glyceraldehyde-3-phosphate
DHAP	- dihydroxyacetone phosphate
DL-GAP	- DL-glyceraldehyde-3-phosphate
DNA	- deoxyribonucleic acid
dsDNA	- double stranded deoxyribonucleic acid
DTDA	- 2,2´-dithiodianiline
E. coli	- *Escherichia coli*
EDTA	- ethylenediaminetetraacetic acid
EtOH	- ethanol
FAD	- flavin adenine dinucleotide
FADH	- flavin adenine dinucleotide hydroquinone form
Fe	- iron
FPLC	- fast protein liquid chromatography
g	- grams
G3P	- glycerol-3-phosphate
GAP	- glyceraldehyde-3-phosphate
Glu	- glutamic acid
gp	- glycoprotein
h	- hours
HEPES	- 4-(2-hydroxyethyl)-1-piperazineethanesulfonic acid
His	- histidine
HIV	- human immunodeficiency virus

HPLC	- high performance liquid chromatography
*h*TIM	- *human* triosephosphate isomerase *(Homo sapiens)*
IC_{50}	- concentration level for 50% inhibition.
IDT	- Integrated DNA Technologies
IPTG	- isopropyl-β-D-thiogalactoside
IRS	- indoor residual sprays
Kbp	- kilobasepair
K_{cat}	- enzymatic turnover number
K_m	- Michaelis constant, concentration of substrate at half V_{max}
K_m/K_{cat}	- enzyme catalytic efficiency number
L	- litre
LB	- Luria Bertani
LDH	- lactate dehydrogenase
m	- metre
mAU	- mass absorbance unit
MES	- 2-(N-morpholino)ethanesulfonic acid
Met	- methionine
min	- minutes
ml	- millilitre
mM	- milimolar
mol	- molar
MOPS	- 3-(N-morpholino)propanesulfonic acid
MR4	- The Malaria Research and Reference Reagents Resource Center
MRI	- magnetic resonance imaging
mRNA	- messenger ribonucleic acid
MW	- molecular weight
NaC*l*	- sodium chloride
NAD^+	- Nicotinamide adenine dinucleotide
NADH	- Nicotinamide adenine dinucleotide reduced
NADPH	- Nicotinamide adenine dinucleotide phosphate reduced
NCBI	- National Centre for Biotechnology Information
ng	- nanogram
NH	- amide group
nm	- nanometer
nmol	- nanomolar
NP	- nanoparticle
OD_{600}	- optical density at 600 nm
P. falciparum	- *Plasmodium falciparum*
P. malariae	- *Plasmodium malariae*
P. ovale	- *Plasmodium ovale*
P. vivax	- *Plasmodium vivax*
PCBS	- polychlorinated biphenyls
PCR	- polymerase chain reaction
*Pf*TIM	- *Plasmodium falciparum* triosephosphate isomerase
pmol	- picomolar
ppt'd	- precipitated
PVP	- Polyvinylpyrrolidone
R^2	- coefficient of determination
RNA	- ribonucleic acid
rpm	- revolutions per minute

*r*TIM	- rabbit triosephosphate isomerase
SDS-PAGE	- sodium dodecyl sulphate polyacrylamide gel electrophoresis
sec	- seconds
SOB	- super optimal broth
SOC	- super optimal broth with catabolite repression (i.e. SOB with glucose)
ssDNA	- single stranded deoxyribonucleic acid
T. Act	- total activity
T. brucei	- *Trypanosoma brucei*
T. cruzi	- *Trypanosoma cruzi*
TAE	- Tris-acetate EDTA buffer
TAPS	- N-[Tris(hydroxymethyl)methyl]- 3-aminopropanesulfonic acid
*Tb*TIM	- *Trypanosoma brucei* triosephosphate isomerase
TCA	- tricarboxylic acid
*Tc*TIM	- *Trypanosoma cruzi* triosephosphate isomerase
TEA	- triethanolamine buffer
TEMED	- N,N,N’,N' tetramethylethylenediamine
TIM	- triosephosphate isomerase
Tris	- tris-2-amino-2-hydroxymethyl-1,3-propanol
tRNA	- transfer ribonucleic acid
Trp	- tryptophan
Try	- tyrosine
UV	- ultra-violet
V	- volts
V_{max}	- maximum initial velocity of the enzyme catalysed reaction
WHO	- World Health Organisation
x g	- times gravity
x	- times

List of Figures

List of Tables

1. Literature review

1.1 Malaria

Malaria is a potentially fatal, yet treatable infectious disease, which kills hundreds of thousands of people every year, most of whom are children in Africa (Aregawi *et al.,* 2011; Miller *et al.,* 2002). It is caused by protozoan parasites of the genus *Plasmodium*. The disease is transmitted through female *Anopheles* mosquitoes. There are approximately 60 known species of *Anopheles* that act as hosts, with about 30 species being considered as highly important, of which only four can infect humans under natural conditions: *P. falciparum, P. vivax, P. ovale* and *P. malariae.* Of these it is only *Plasmodium falciparum* which results in severe and potentially fatal malaria (Tuteja, 2007; Miller *et al.,* 2002). According to the World Health Organisation (WHO) 2011 report on malaria, an estimated 3.3 billion people are at risk of being exposed to malaria, with 1.2 billion deemed to live in high risk locations. In 2010 there were approximately 216 million cases of infection and between 537000 and 907000 deaths, of which approximately 91% occurred in Africa with 86% being children below the age of 5 (Aregawi *et al.,* 2011). While it is true that the fight against malaria is showing signs of succeeding with a reduction in observed cases by approximately 17% since the year 2000 and a decrease in mortality by 26%, these figures are significantly lower than the targeted values of 50% fewer cases by 2010 (Aregawi *et al.,* 2011).

1.2 Fighting malaria

The WHO currently recommends a wide variety of approaches for malaria control and treatment. These methods target two main aspects of the disease (a) the vector of the disease, mosquitoes and (b) the parasite itself. To limit vectors for the disease, the use of insecticide-treated mosquito nets and indoor residual sprays (IRS) to treat walls and ceilings is currently recommended. Targeting insecticides to areas where mosquitoes typically land before and after feeding, limits vector spreading and overall pesticide usage. Pyrethroids, organophosphates and organochlorines, including Dichlorodiphenyltrichloroethane (DDT), are typically used as chemical insecticidal agents (Aregawi *et al.,* 2011). While the pyrethroids are the most widely used insecticides - due to their low toxicity, cost and long-levity - increasingly more toxic alternatives, such as DDT, are seeing a comeback.

The use of DDT is still controversial, but the potential benefits of its use, are often seen as a good enough reason to disregard scientific findings linking it to ill health effects. DDT exposure has shown links to various serious medical conditions such as; pancreatic cancer, breast cancer, non-hodgkins lymphoma and other cancers. Other concerning medical issues include; reproductive related problems, impaired lactation, androgen receptor antagonism linked to testicular cancers and low sperm counts, neurological poisoning effects such as; hypersensitivity, dizziness, irritability, tremors and convulsions (Longnecker *et al.,* 1997; Snedeker, 2001). Yet other research and statistical analysis has called many of these findings into question (Longnecker *et al.,* 1997). Nevertheless, DDT was initially banned in the 1970's, and is currently banned in many countries (Rogan and Chen, 2001).

Strategic monitoring for the spread of insecticide resistance is part of the WHO antimalaria program and 78 countries currently monitor for resistance. In sub-Saharan Africa, 27 countries have reported pyrethroid resistance (Aregawi *et al.,* 2011).

Monitoring includes a promotion of research into the mechanisms of insecticide resistance within the mosquitoes and, so far, two main mechanistic methods of resistance development in mosquitoes have being identified. These are target site resistance and metabolic resistance. Target site resistance typically involves modifications that prevent insecticide binding at target sites of the mosquitos' central nervous system. Such mutations have been shown to occur in acetylcholinesterase (the target of organophosphates and carbamates) and voltage-gated sodium channels (the target of pyrethroids and DDT). On the other hand, metabolic resistance mechanisms observed usually involve an increase in expression and regulation of detoxifying enzymes that prevent insecticides reaching their target sites (Aregawi *et al.,* 2011).

For treatment and prevention the WHO recommends that suspected malaria cases should undergo parasitological confirmation tests either via microscopy or with the use of rapid diagnosis tests that have been developed. For confirmed cases the recommended treatment is Artemisinin based combination therapy (ACT). In addition to this, a complete withdrawal of Artemisinin based monotherapies (AMT) is recommended. These AMT treatments are suspected of creating and harbouring the spread of Artemisinin-resistant parasites, which decrease the effectiveness of ACT's (Dondorp *et al.,* 2009; Aregawi *et al.,* 2011). As of November 2011, 28 pharmaceutical companies were still manufacturing the monotherapies, 39 fewer than in 2010. Limiting the production and sale of the monotherapies AMT has been

difficult due to weak regulation of the pharmaceutical industry. A greater collaboration in this regard is thus required (Aregawi *et al.,* 2011).

Since ACT currently represents the frontline in the fight against malaria and is often the drug of choice, the spread of resistance by using AMT's is a significant problem. ACT generally has the greatest success when compared with other commercially available drugs. In Cambodia however resistance to ACT is present and spreading (Dondorp *et al.,* 2009; Aregawi *et al.,* 2011). Seeing as ACT's are recommended as the replacement to older treatments, of quinine, chloroquine and sulfadoxine-pyrimethamine, to which there is a relatively widespread resistance, and since no better alternatives are currently available, resistance to ACT is likely to become more widespread in the future.

The rapid spread of resistance to relatively new drugs is possible, and has been seen in the past with other anti-parasitic drugs. Programs are in place to monitor and test for resistance and, where possible, intervene with more drastic measures like insecticide spraying when detected. These efforts to limit the spread of resistance will likely maximise the lifetime of the currently-available drugs but resistance to new drugs also threatens to unravel much of the successes achieved so far (Aregawi *et al.*, 2011). The WHO therefore actively encourages malaria research so as to ensure that new drugs, and methods for tackling this disease, will be available in the future. For this goal to be achieved malaria research needs to be an on-going field of research. Novel drugs, with new mechanisms of action, are required to ensure that new drugs have a useful life-span and are unaffected by currently-spreading resistance mechanisms.

1.3 The malarial life cycle and targeting it

Of all the malaria causing parasites, *P. falciparum* poses the greatest risk of death and severe morbidity. The life cycle of this interesting parasite is extremely complex and a detailed understanding of this life-cycle is required if new anti-parasitic drug targets are to be identified. The parasite expresses a variety of different, often specialised proteins, which are critical to its survival in the different cell lines and environments in which it lives (Tuteja, 2007). To survive the parasite progresses through several distinct life cycle stages (Figure 1.1) that are outlined in detail in the following pages.

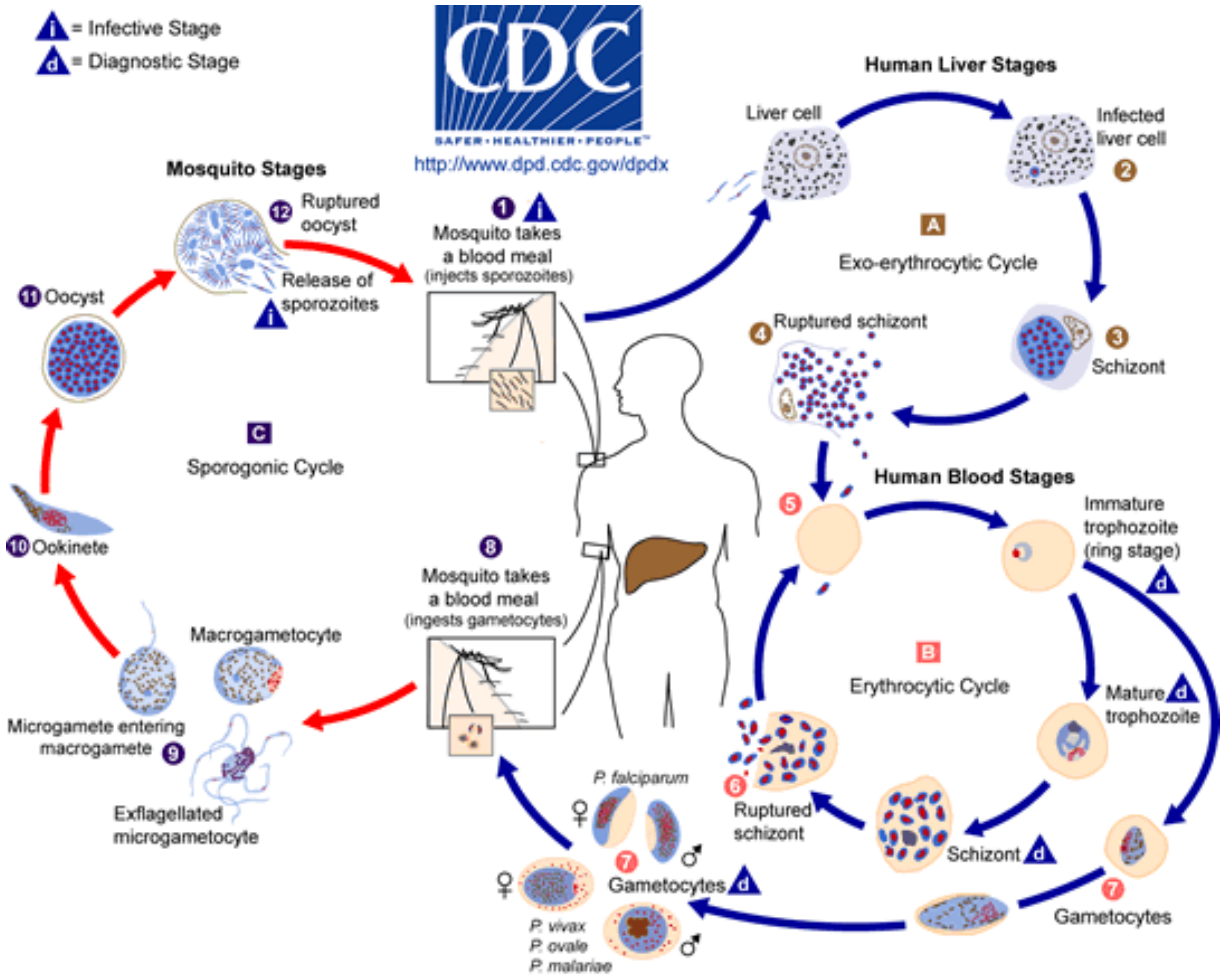

Figure 1.1: The life cycle of malaria parasites *P. falciparum* and *P. malariae*. Taken from the Centres for Disease Control website (CDC, 2010).

Infection starts with a mosquito taking a blood meal, during which sporozoites are injected from the mosquitos' salivary glands into subcutaneous tissues and, less frequently, into the blood system of the human host (Miller *et al.*, 2002). The sporozoites travel directly to the liver for *P. falciparum* and *P. malariae* where they infect liver hepatocytes. Studies (Mota *et al.*, 2001), have shown that the sporozoites are capable of traversing through different cell types in a process that involves piercing the cells plasma membrane of the cell, using special proteins to achieve entry. Unlike bacteria and most other parasites, which enter cells without disrupting the plasma membrane, malarial sporozoites make use of a parasitophorous vacuole to enter the cell (Mota *et al.*, 2001). Utilizing this process enables the parasite to reside freely within the cytosol and to exit the cell at a later stage, again by piercing its way out. The process results in leakage from effected cells due to entry and exit 'wounds' that can spill cytoplasmic fluids until they are able to close. This ability of the parasite to bore in and out of cells, allows it to traverse cellular barriers and penetrate through tough layers of skin cells,

which is necessary for it to reach its target, the liver hepatocytes (Mota *et al.,* 2001). It has been shown that the sporozoites tend to migrate through several hepatocytes within the liver before settling inside one of these cells, to start the next phase of the life cycle. This process has been shown to be essential in the parasites life cycle. The factor that triggers the decision to switch between entry mechanisms is unknown (Miller *et al.,* 2002; Tuteja, 2007). Once it has been triggered, the parasite alters its cell entry technique, to one using a parasitophorous vacuole for hepatocyte invasion. This is achieved using conventional receptor mediated endocytosis (Entzeroth *et al.,* 1998; Mota *et al.,* 2001; Kaiser *et al.,* 2003). The receptors involved in this process have been studied in detail. On the surface of the parasite, thrombospodin domains of the circumsporozite protein, along with the thrombospodin-related adhesive protein, interact with heparan sulphate proteo-glycans of the host hepatic cells to achieve cellular invasion via endocytosis (Frevert *et al.,* 1993).

Once this occurs, the sporozoites undergo several phases of asexual reproduction in the liver hepatocytes for between 9-16 days. This phase is known as exo-erythrocite schizogony (Figure 1.1A) and it results in the production of schizonts. In the case of *P.ovale* and *P.vivax,* a delayed schizogony phase may also occur. This is achieved by the production of dormant liver hypnozoites, which can remain dormant in the liver for several weeks or longer and will result in relapsing malaria in the patient, if untreated. Once inside the hepatocyte, sporozoites produce tens of thousands of merozoites, each capable of infecting a red blood cell (Miller *et al.,* 2002; Tuteja, 2007). Studies have shown that the parasite then induces cell death and detachment of the host hepatocyte. This is followed by budding of parasite-filled vesicles called merosomes which travel through pores into the lumen of sinusoidal blood vessels in the liver. During merosome budding from the hepatocyte, the parasite also simultaneously suppresses the expression of phosphatidylserine by the host. Suppression is achieved active accumulation, in the merozoite, of intracellular Ca^{2+} ions, which are normally released by the dying hepatocyte. This prevents the production of phosphatidylserine, an enzyme on the outer plasmid membrane merosomes, which functions as a cellular recognition signal for destruction to phagocytes. However, since the merosome membranes are derived from the host cell, and the production of phosphatidylserine by infected host cells is being suppressed by the parasite. Merosomes are therefore able to effectively avoid detection by host phagocytes and to safely enter into the blood stream (Miller *et al.,* 2002; Sturm *et al.,* 2006).

Once in the blood stream, the merosomes release merozoites directly into circulation (Sturm *et al.,* 2006). This represents the beginning of the erythrocytic cycle (Figure 1.1B), which is

primarily responsible for the symptoms of the disease (Frevert *et al.,* 1993; Tuteja, 2007). As such, and due to its complexity, this part of the life cycle has been identified as a good target for the development of drug interactions that may inhibit it (Frevert *et al.,* 1993). Merozoites enter the erythrocytes in a four-stage process. First, there is a reversible recognition and attachment to the outer membrane of the erythrocytes. Second, this is followed by a reorientation which then leads to irreversible binding and reorganisation of the parasite, forming a parasitophorous vacuole and allowing entry into the erythrocyte. Third, invagination of the merozoite occurs, in a process that simultaneously removes the merozoites surface coating - which protected it in the blood stream. Fourth, the invasion process is finalised by the resealing of the erythrocyte and the parasitophorous vacuole membranes (Tuteja, 2007). Within this process a series of cellular signalling reactions occur. These prepare the parasite and host cell for further development. The process is extremely complicated and not fully understood. It is known that it involves a set of protein interactions between host and parasite enzymes that allow for the parasitic takeover of the host's biochemical machinery (Miller *et al.,* 2002; Tuteja, 2007).

Asexual replication of the parasite within host erythrocytes then begins, starting with the characteristic 'ring form' of the trophozoite, which can be easily identified for diagnosis, using a microscope (Figure 1.1B). The reproduction process continues with trophozoite enlargement, which is accompanied by a highly active metabolism, using glycolysis. During this process the parasite uses its own glycolytic enzymes and actively imports glucose from the blood to satisfy its energy needs (Sherman, 1979). The parasite lacks a functional tricarboxcylic acid (Krebs) cycle and is thus entirely dependent on glycolysis for energy production (Parthasarathy *et al.,* 2002). This means that the glycolysis enzymes of the parasite are potentially good targets for drug development (Miller *et al.,* 2002; Ravindra and Balaram, 2005; Tuteja, 2007; Shekinah and Rajadurai, 2008; Gerdes and Overbeek, 2012). As the trophozoite enlarges and the replication continues, the parasite ingests host cell cytoplasm and uses proteolysis to break down haemoglobin in the red blood cells, forming free amino acids needed to feed the massive level of replication. A by-product of this digestion is the production of free heme, which is potentially toxic to the parasite. This toxic waste is dealt with by polymerizing it into hemozoin which then crystalizes and is stored within the parasite's food vacuole to form what is known as malaria pigment (Miller *et al.,* 2002; Tuteja, 2007). Inhibition of this process is considered as the mechanism of action of most of the currently-used antimalarial drugs, including Chloroquine and Artemisinin (Robert

et al., 2001). Resistance to this mechanism of action has also been described in detail (Sidhu *et al.,* 2002). Replication ends with multiple rounds of nuclear division and the construction of schizonts. In *P. falciparum* the whole erythrocytic cycle takes approximately 48 hour and the subsequent release of the merozoites occurs simultaneously throughout the body. This simultaneous rupture and release of red blood cell contents into the blood stream, results in the production of cytokines such as the tumour necrosis factor among others. Together, these cause the clinical manifestations (fever, and shakes) of malaria. The repetition of this process causes massive accumulation of toxins and destruction of red blood cells that ultimately results in malaria-associated death (Miller *et al.,* 2002; Sturm *et al.,* 2006; Tuteja, 2007).

A small percentage of the merozoites in red blood cells go on to form micro- and macro-gametocytes which later become male and female forms of the parasite, for the sexual reproduction phase, which occurs in the mosquito (Figure 1.1C). After these gametocytes are ingested by a mosquito they have no further function in the human host. After a mosquito has taken a blood meal from an infected individual, the gametocytes move into the mosquito's mid-gut, where they form into sexual micro- and macro- gametes. These gametes fuse together, creating a fertilized zygote, which transforms into an ookinete and then infects a mid-gut cell of the mosquito before developing into an oocyst (Tuteja, 2007). The malaria gamete surface antigen Pfs230 has been identified during this process. This is critical for the recognition and binding to exflagellating human red blood cells that contain the male parasite and form into exflagellation clusters, which release individual microgametes. The process has been shown to be a critical step in oocyst formation (Eksi *et al.,* 2006). Sporogony then occurs within the oocyst, producing many sporozoites that migrate to the mosquitos' salivary glands when the oocyts ruptures. The cycle is completed by the mosquito taking a blood meal from a new host (Figure 1.1A), (Tuteja, 2007; Miller *et al.,* 2002). Gaining a detailed understanding of this lifecycle is a critical step that will aid in finding drug targets for the development of the new drugs, required for the on-going efforts to fight malaria.

1.4 Triosephosphate isomerase (TIM)

Triosephosphate isomerase (TIM) is a well-studied homodimeric enzyme which was first discovered by Otto Meyerhof (considered one of the fathers of modern biochemistry) in 1935 (Meyerhof, 1935). TIM is a critical enzyme of glycolysis that catalyses the inter-conversion of dihydroxyacetone phosphate (DHAP) and D-glyceraldehyde-3-phosphate (D-G3P). Glycolysis is one of two basic energy-producing enzymatic cycles, along with the

tricarboxylic acid cycle or 'Krebs cycle'. These cycles produce cellular energy, by oxidative phosphorylation, in the form of ATP and NADH/NADPH, which are energetic biochemical agents required in the metabolism of all living organisms (Voet and Voet, 2003).

The enzyme TIM is therefore very old and has become highly evolved over time. It has been described as an enzyme honed to perfection, by the selective pressures of evolution (Knowles and Albery, 1977). The *human* TIM (*h*TIM) is a good example of this enzyme, shown in its loop-open and loop-closed forms in Figure 1.2 below.

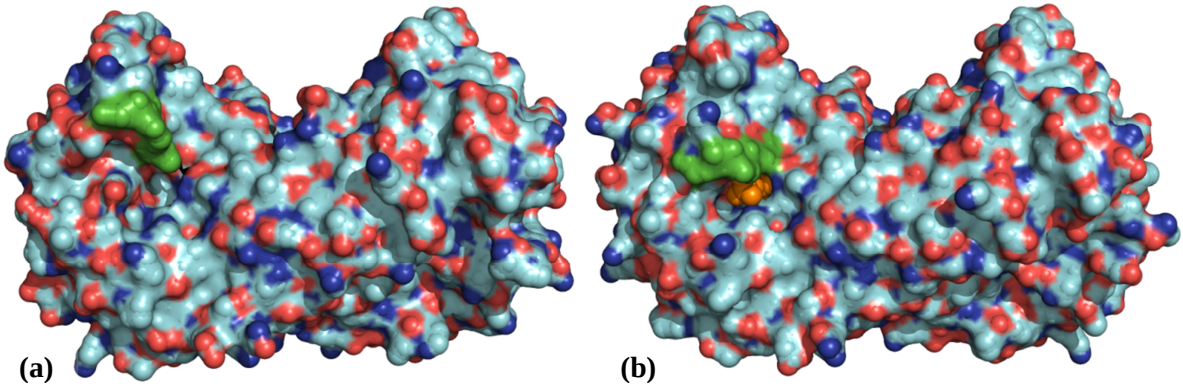

Figure 1.2: PDB images showing *h*TIM in loop-open (a) and loop-closed (b) forms, with bound substrate. The mobile loop is coloured in green (diagrams constructed with PyMol®).

1.4.1 Mechanism of action

The enzyme reaction occurs through the creation of a cis-enediol (intermediate), by the mediation of the protonation and deprotonation for two enol structures (Figure 1.3), (Knowles, 1991).

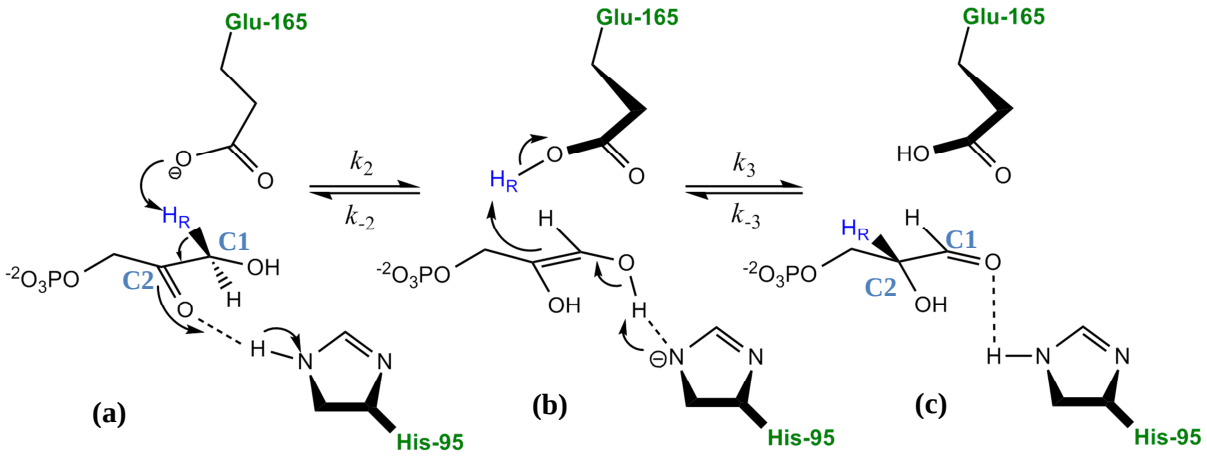

Figure 1.3: Diagram of the inter-conversion of DHAP (a) to the enediol intermediate (b) to D-G3P (c) via a catalytic acid/base proton abstraction involving Glu-165 and His-95 of TIM. Image from (Knowles, 1991).

How TIM achieves this mode of action has been extensively studied (Knowles, 1991; Joseph *et al.*, 1990; Pompliano *et al.*, 1990; Knowles *et al.*, 1972; Banner *et al.*, 1975; Lolis and Petsko, 1990). Three main functional components are in operation in TIM and will be discussed in detail. The first of these is a protein loop (residues 166-177), in which the subset residues (of 168-173) are highly conserved and form a rigid lid that moves ~7 Å in a hinge-like action from its open state (with no ligand present) to its closed position (with a substrate or inhibitor present), see (Figures 1.2 and 1.4), (Knowles *et al.*, 1972; Banner *et al.*, 1975; Joseph *et al.*, 1990; Lolis and Petsko, 1990; Pompliano *et al.*, 1990). While many enzymes have similar structures, the mechanisms of how such enzymes work are not always fully understood. It has been suggested that these structures move in an 'induced fit' mechanism upon substrate binding. A similar well-studied example of such a mechanism is that of lactate dehydrogenase (LDH). In LDH it has been shown that, upon binding of its substrate, loop movement is induced. LDH has a similar peptide loop, which contains a highly conserved catalytic Arg109 residue that is responsible for polarizing a carbonyl group on the substrate and stabilizing its transition state (Clarke *et al.*, 1986).

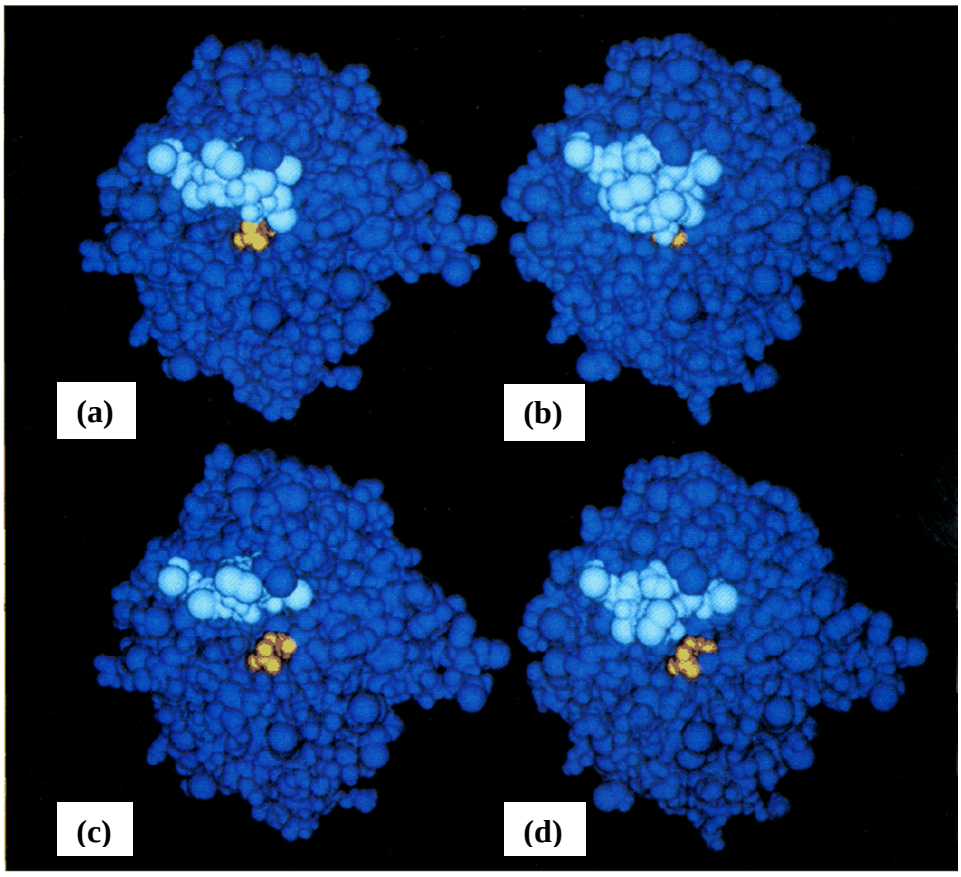

Figure 1.4: Models of wild-type and mutant TIM, with residues of the mobile loop 168-177 in (light blue) and the rest of the protein in (dark blue). The bound inhibitor phosphoglycolohydroxamate is in orange. **(a)** Wild-type TIM in open loop conformation, (inhibitor shown for visual reference only). **(b)** Wild-type in closed/liganded conformation with inhibitor bound. **(c)** Mutant TIM (lid 170-173 deletion) in open loop conformation (again inhibitor shown for visual reference only). **(d)** Mutant (lid 170-173 deletion) in closed/liganded conformation with inhibitor bound. Image from (Pompliano *et al.*, 1990).

As with LDH, in TIM the mobile loop appears to clamp down on the bound substrate/inhibitor complex. In TIM, unlike LDH, no new catalytic residues are brought into action. Instead it appears to effectively sequester the substrate from the solvent (Figure 1.5) and is thought to help stabilize the substrate through transition intermediary states. Crystallographic work has also shown these highly conserved lid residues 170-173, the main chain NH group of Gly171, creates at least one, and possibly two, hydrogen bonds with oxygen atoms on the substrate or inhibitor's phosphate group (Pompliano *et al.*, 1990). An example of this in *Plasmodium falciparum* (*Pf*TIM) is shown in Figure 1.5. This stabilises the substrate for TIM ensuring a tight fit as the enolization reaction transitions through its different states (Figures 1.2 and 1.3) (Pompliano *et al.*, 1990).

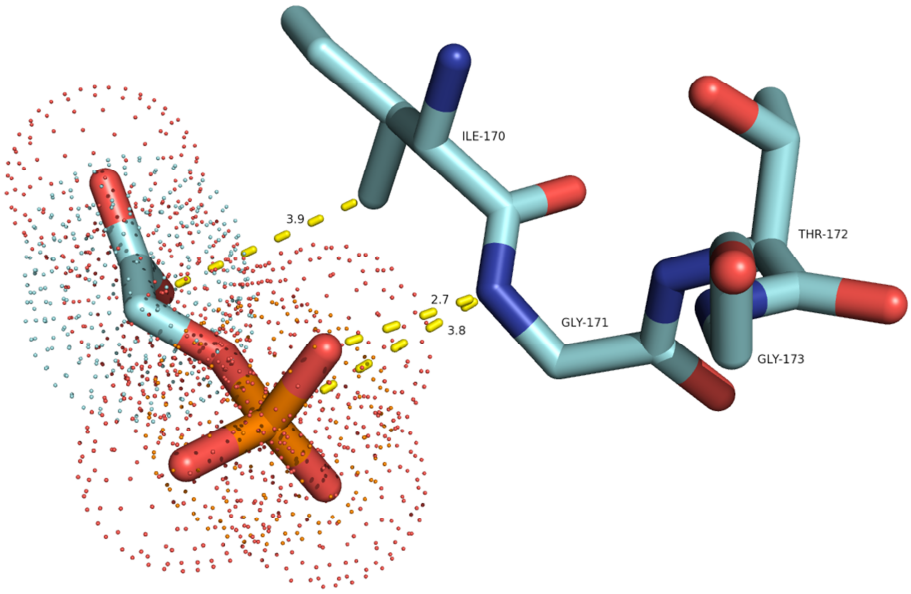

Figure 1.5: The hinged loop of *Pf*TIM, (pdb code: 1LZO), in closed conformation, forming a hydrogen bond of 2.7 Å, with its backbone Gly171 -NH group and an oxygen atom of the inhibitor complex 2-phosphoglycolate. Bond lengths shown are in angstroms. Image made using PyMol version 1.3.

The 'induced fit' hypothesis is acceptable for TIM as shown by crystallography data and computer simulation studies done by Joseph *et al.*, 1990, which indicates that residues 166-168 and 174-176, which are not conserved, act as the 'hinges' for the loop movement. The study points out that during the interaction between the substrate and the catalytic Glu165 residue, the residue shifts towards the substrate, in a relatively substantial positional change of ~3 Å from open to closed loop forms. This shift in turn induces further pseudo-dihedral angle changes between residues 166-168, which in turn weaken a hydrogen bond between Trp168 and Tyr164, causing a shift in the indole functional group of Trp168. The indole group then interacts with Glu129 and causes a cascade of dihedral angle changes that culminate in the bond angle changes of residues 174-175, ‘the other hinge’, which closes the loop. The study also notes that the loop is rigid throughout its movement. This is due to intra-loop hydrogen bonds and stacked ‘van der Waals’ forces between conserved loop residues. As the loop closes residues 173 and 176 form additional hydrogen bonds with the rest of the 3D protein structure as the loop clamps down (Figure 1.3), while residue 171 forms hydrogen bonds with the substrate (Figure 1.5). These help to lock the mobile-loop or ‘lid’ down, ensuring a tight fit and limiting substrate movement within the active site (Joseph *et al.*, 1990). Due to the complexity of this process, it is theorised that any conformational changes in overall TIM protein structure may have drastic effects on activity.

The next two components used by TIM for its reaction are, a catalytic base and a catalytic acid, which mediate the two enolization steps in each direction, (Figures 1.6a and 1.6b) respectively (Knowles, 1991). The catalytic base, responsible for the removal of the pro-R proton of C1 in DHAP (Figure 1.3), is the carboxylate group from Glu165 (Figures 1.3 and 1.6a). Isotope and crystallographic studies have shown this mechanism to be bi-dentate, meaning it is also capable of removing the proton from C2 in D-G3P (Figure 1.3). This is catalytically required for the reverse reaction (Knowles *et al.,* 1972; Banner *et al.,* 1975; Lolis and Petsko, 1990; Bash *et al.,* 1991; Knowles, 1991).

For the above to occur, strategic and extremely precise placing of the Glu165 residue relative to the substrate is required. Indeed it's been theorised that the reason proteins are often so much larger than their substrates, is simply to supply the necessary scaffolding required for such precision-placing of the catalytically active groups (Knowles, 1991). The removal of Glu165, or its substitution with alanine or glycine, has been shown to reduce catalytic activity by over a million fold (Knowles, 1991). The final active chemical component of this enzyme is a catalytic acid, which acts as an electrophile and aids in the enolization steps. Again it is the strategic placing of His95 that places its imidazole rings, NH group, precisely in-between and approximately 2.9 Å from each of the two possible substrate, C1 and C2 oxygen groups (Figures 1.3 and 1.6b). This allows for the creation of a hydrogen bond which aids in the chemical destabilisation of both substrate conformations DHAP and D-G3P, and aids in their catalytic inter-conversion. Mutations of His95 are known to decrease catalytic activity by a factor of nearly 400 fold, when compared to the wild type enzyme (Bash *et al.,* 1991; Nickbarg *et al.,* 1988). Essentially, it is the strategic and precise positioning of catalytic base and acid groups by the two α-helixes that hold these residues (Figures 1.6c, d) respectively, as well as the snug fit within the active site — which is further aided by the stabilisation of the substrate molecule by mobile lid closure — that makes this enzyme so efficient. The isomerisation reaction can therefore be said to function in a catalytic pull-push acid/base mechanism which relies on the precise positioning of active residues and a snug substrate fit.

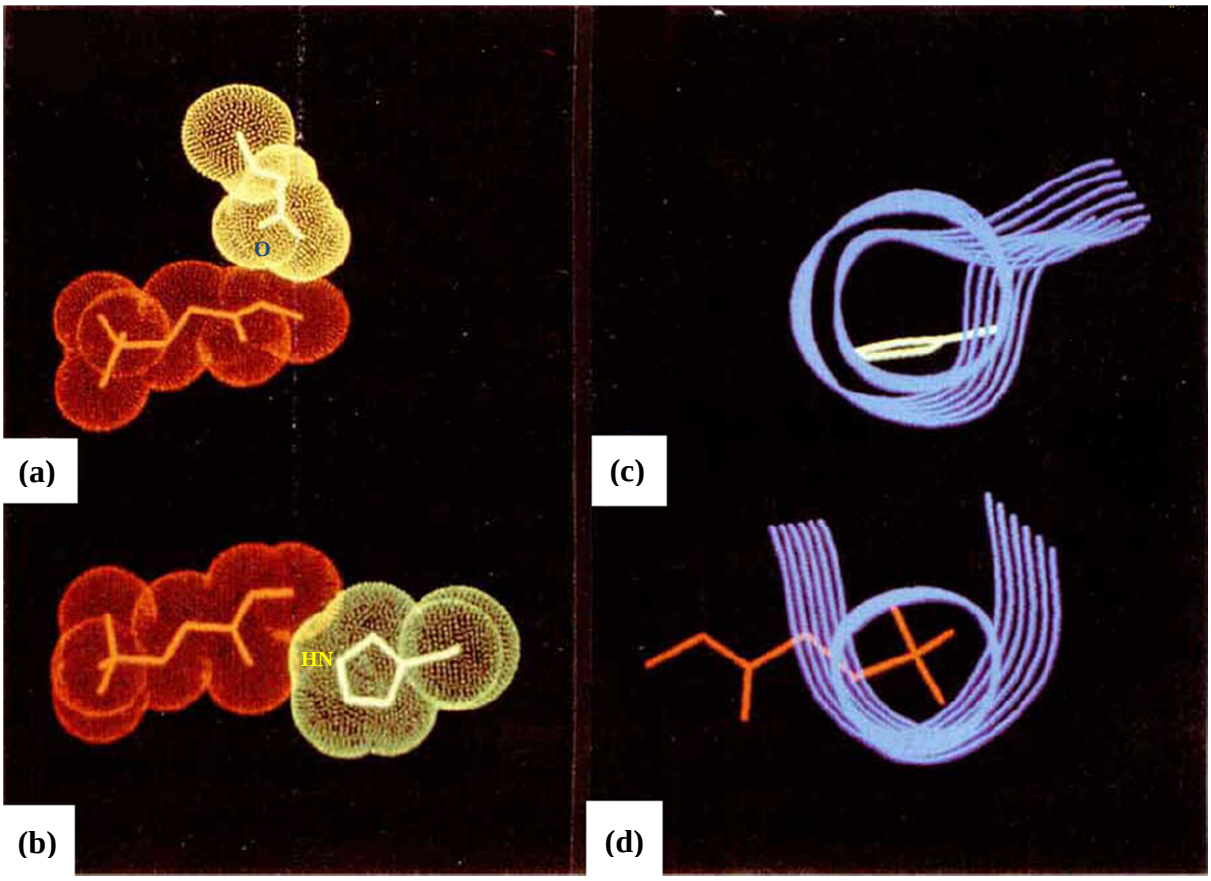

Figure 1.6: The catalytic residues of the active site in TIM. **(a)** The catalytic base of Glu165 (yellow) acts as a proton acceptor with the tightly-fit substrate (red). **(b)** The catalytic acid from the NH group of His95 acts as the electrophile. **(c)** The α-helix that stabilises the imidazole ring of His95. **(d)** The α-helix stabilising the lid over the phosphate group of the phosphoglycolohydroxamate (inhibitor). Note: the dots surfaces are at the van der Waals' radii. Image from (Knowles, 1991).

Understanding the remarkable chemical mechanisms involved in these catalytic events, which occur within angstrom distances allows one to form a deeper understanding of the enzyme TIM and how it functions. This information can then be used to aid in the design of new enzyme inhibiting drugs. The ability to selectively target a specific variant of such an important enzyme could be used to design antimetabolite drugs capable of disrupting this mechanism of action. To further investigate this possibility for the design and development of *P. falciparum* TIM targeted therapeutic agents, the genetic variation and unique structural features of this enzyme should be studied.

*Pf*TIM is one of the better-studied variants of TIM and is known to have several significant important differences, compared to its human host counterpart, version *h*TIM. These differences are discussed in detail in the following section. In this research it is assumed that nanoparticle interactions that could induce conformational changes in target *Pf*TIM would likely inhibit activity, because even a relatively small shift in residue positioning would

probably have strong effects on activity, due to the precise redox chemistry and nature of how TIM operates.

1.4.2 TIM from *Plasmodium falciparum* (*Pf*TIM) as a drug target

Critical evaluation of the specific genetic variations in *Pf*TIM reveals several key differences with the *h*TIM variant. Exploitation of these differences could make *Pf*TIM an excellent target for selective enzyme inhibition.

As previously mentioned, *P. falciparum* lacks a functional energy-producing Krebs cycle, making it entirely dependent on glycolysis for energy production (Velanker *et al.*, 1997; Ravindra and Balaram, 2005; Tuteja, 2007; Gerdes and Overbeek, 2012). This, coupled with the parasite's massive energy demands during asexual, blood-stage, reproduction (Sherman, 1979), means that the parasites glycolytic enzymes are potentially good drug targets. Disrupting this cycle will starve the parasite of the cellular energy it needs to survive and reproduce. The sheer scale of the parasites reproduction process puts a huge strain on the host's system and the ability to slow this process down, could make the difference between life and death.

The parasite's use of its own glycolysis enzymes offers an opportunity to identify genetic differences between it and its *human* host. DNA sequencing and X-Ray crystallographic studies have helped identify *Pf*TIM as having several notable genetic and structural differences that may be useful for targeted drug development (Velanker *et al.*, 1997; Parthasarathy *et al.*, 2003; Ravindra and Balaram, 2005).

The search for therapeutic agents against pathogens, targeting key enzymes that only exist within the pathogens themselves, is usually the best option. If this is not possible, selectively targeting analogous parasite enzymes is also a possibility (Maithal *et al.*, 2002; Ravindra and Balaram, 2005). Two methodological approaches have been used for this purpose. The first approach is to design benign inhibitors that compete for the active site. Ideally, these inhibitors will remain in the active site or, in some cases, may even modify the active site chemically. This method is only useful, however, when there aren't any important host analogues to the target enzyme. The approach involves designing inhibitor peptides that specifically target the active site of the enzyme. If analogous enzymes are present, similarities with the homologous host enzyme's active site usually limit the use of this approach, because the residues within active sites of analogues are usually highly conserved. In such cases a better strategy is to target dimer interfaces, if present, which are typically less conserved and

often exhibiting clear genetic and structural differences. In this case the approach is to target non-conserved, but functional, interface residues for disruption. This can also be done using synthetic peptides, or by covalently modifying reactive surface residues that could disrupt the oligomeric state of the protein (Smith *et al.*, 1975; Gómez-Puyou *et al.*, 1995; Maithal *et al.*, 2002). As demonstrated (Gómez-Puyou *et al.*, 1995), this approach worked well when targeting the blood parasite *Trypanosoma brucei* TIM (*Tb*TIM), which shares many similarities in enzymatic structure with *Plasmodium* (Greenbaum *et al.*, 2004; Velanker *et al.*, 1997). *Tb*TIM features a subunit interface cysteine residue, in position 14 (Cys14), which was shown to be influential in subunit binding. Gómez-Puyou *et al.* (1995) were able to selectively inhibit *Tb*TIM using a methyl methanethiosulfonate to derivatize its Cys14 into a methyl sulphide. The treatment showed dramatic inhibition on other TIMs that featured interface Cys14 residues. TIMs without this variation showed only low levels of inhibition. For rabbit TIM a 20% decrease in activity was observed and in yeast TIM the inhibition was negligible (Gómez-Puyou *et al.*, 1995).

In the case of *Pf*TIM, the enzyme is known to only be fully active in its dimeric form (Maithal *et al.*, 2002). In addition it also features dimer-interface cysteine residues, in this case at position 13 (Cys13), while in *h*TIM this residue is methionine. Methionine is similar to cysteine, as it also has a sulphur atom within its side chain, but its sulphur atom is shielded by a terminal CH_3 group, which makes it less reactive. The presence of this mutation makes selective enzyme inhibition of *Pf*TIM an attractive option, as targeting of TIM dimer cysteines has already been successfully demonstrated for selective inhibition (Gómez-Puyou *et al.*, 1995). *Pf*TIM contains four cysteine residues per subunit at positions 13, 126, 196 and 217 (Figure 1.7b). Disruption of the interface Cys13 of *Pf*TIM or its removal (C13D mutant) results in a significant, 7-fold, decrease in catalytic activity and reduces dimer stability. In addition to this, Cys196, of *Pf*TIM, is also located on the enzyme surface and opposite to the active site (Figures 1.7b, c). Maithal *et al.*, 2002 demonstrated that this residue is the most accessible and reactive of the cysteine residues, presenting its sulphur atom in the surface structure (Figure 1.7c). This provides an external site for chemical targeting of cysteine sulphur atoms with nanoparticle-based nanodrugs (Maithal *et al.*, 2002; Malabadi *et al.*, 2012).

The presence of the reactive sulphur atoms in the cysteines side chain is what makes these mutations of such interest. Sulphur is a known reactive element in this amino acid, and is responsible for the creation of disulphide bonds and strong ‘van der Waals’ forces, which are

highly influential in enzymatic folding and structure conformation. Sulphur atoms are also known to form bonds with gold and silver atoms and are used to interface gold and silver surfaces, or nanoparticles, in various biotech applications, such as biosensor design, peptide metallic interfacing and nanoparticle stabilisation (Willner *et al.*, 2007; Malabadi *et al.*, 2012).

Of the four cysteine residues, X-ray crystallography has shown that both Cys196 and Cys217 are surface-accessible for *Pf*TIM. Additionally, the sulphur atom of Met248 is also exposed on the surface (Figures 1.7a and 1.7c).

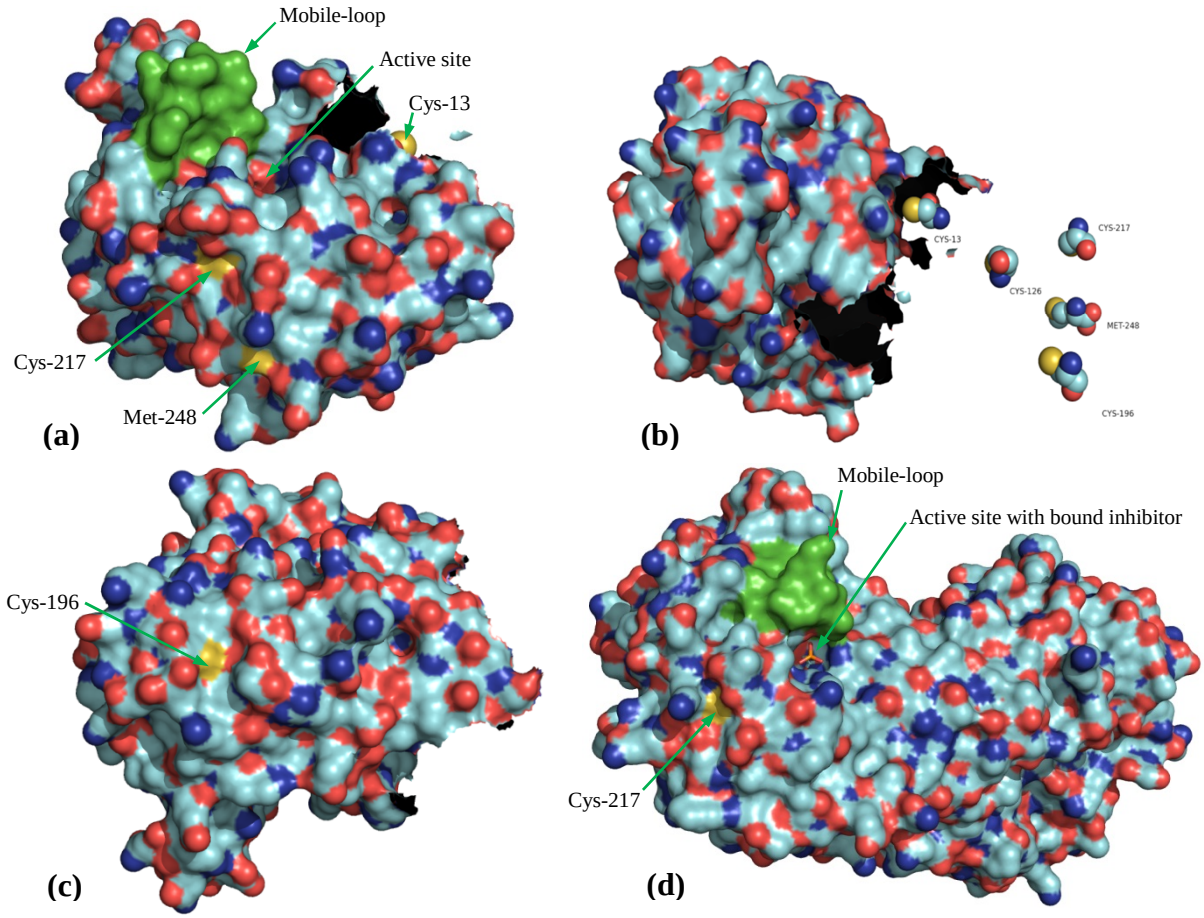

Figure 1.7: PyMol (v1.3) representations of *Pf*TIM (a,b,c) and *h*TIM (d) with sulphur atoms in yellow. (PDB codes: 1YDV and 1HTI respectively). **(a)** *Pf*TIM monomer, showing Mobile-loop above the active site, the sulphur atom of the dimer interface Cys13 and surface accessible sulphur atoms of Cys217 and Met248. **(b)** *Pf*TIM dimer showing surface of chain A, with sphere representations for the 4 cysteines and the one methionine 248, (note Cys13 at dimer interface). **(c)** Reverse side of *Pf*TIM showing surface accessible Cys196 sulphur atom. **(d)** Surface structure of *h*TIM showing mobile-loop, active site with bound inhibitor (2-phosphoglycolic acid - $C_2H_5PO_6$) and the only surface accessible sulphur atom on Cys217.

Maithal *et al.,* 2002 performed a sophisticated evaluation of *Pf*TIM cysteine residues by differentially labelling the residues using iodoacetic acid and iodoacetamide. This was followed by electron spray ionization, mass spectroscopy and tryptic fragment digestion analysis, to determine the positioning of the labels. These data indicated that the accessibility of the cysteine residues is as follows: Cys196>Cys13>>Cys217 and Cys126. This correlated well with crystallography data which shows Cys126 buried inside the enzyme and while Cys217 was largely covered; only partly exposing its sulphur atom (Figures 1.7a, b). Likewise Cys196 is highly available on the reverse side of the structure (Figure 1.7c). Interestingly, while the crystallography data indicates Cys13 has a generally-limited accessibility, due to dimer formation, labelling experiments indicated otherwise, with Cys13 undergoing relatively rapid modification, indicating access by the labelling residues is possible and therefore possibly by other interfering agents. Due to the proximity of Cys13 to the active site, labelling of this residue was also accompanied by loss in enzyme activity (Maithal *et al.,* 2002).

1.5 Medical Nanotechnology

The field of nano-medicine using nanoparticles is relatively new and, to date, few nanodrugs have been tested in humans (Chen *et al.,* 2008; De Jong and Borm, 2008; Lévy *et al.,* 2010; Sperling *et al.,* 2008). Recent research has however shown progress in this field with developments involving transition metal complexes as therapeutic agents, used to treat carcinomas, lymphomas, control infections, as anti-inflammatory agents, neurological disorders, and diabetes (Rafique *et al.,* 2010). Many challenges that face conventional therapeutic agents, such as poor bioavailability and intrinsic toxicity, often compromise or seriously limit the abilities of otherwise beneficial drugs. Nanotechnology has allowed the creation of nanoscopic systems which can be altered through the addition of various functional surface molecules thereby altering pharmacological and therapeutic properties. These designed systems are capable of overcoming many of the limitations associated with conventional treatments (Chen *et al.,* 2008; De Jong and Borm; 2008, Lévy *et al.,* 2010). Drug delivery with nanotechnology is designed to exploit pathophysiological conditions and anatomical changes that often exist within diseased tissues. This allows for the creation of site-specific targeted therapeutics (Sahoo *et al.,* 2007).

Nanosystem selective targeting allows for the accumulation of higher concentrations of therapeutics at targeted sites, and lower concentrations elsewhere in the body. This enhances

bioavailability and reduces systemic toxicity. Incorporation of the drugs into nanosystems also overcomes solubility issues that are often associated with otherwise-effective functioning drugs. Nanosystems also allow therapeutic drugs to bypass immune detection, during circulatory transportation to target locations. This enables targeting sites that are hard to reach, such as the brain, which offers an additional challenge due to the blood brain barrier (Sahoo *et al.,* 2007). Chen *et al* (2008), outline several nanosystems and their targets, which have been developed and are currently in use. It is important to note that nanotechnology-derived drugs are usually custom designed yet often make use of the same base nanoparticle system, such as gold or silver nanoparticles. It is the various modifications and functionalising of these systems that creates modern, highly specific and capable nanodrugs/nanosystems (Chen *et al.,* 2008). The nanosystems are typically less than 100 nm in size, thus allowing delivery through capillaries and uptake by cells. Drugs coupled to nanosystems also generally benefit from longer circulation times and less loss of therapeutic potential during circulation (Sahoo *et al.,* 2007). For drug delivery, nanosystems can employ encapsulation, entrapment, adsorption, and attachment, and are even able to dissolve active agents into or onto the nanoparticle matrix. This can be used to allow for the creation of targeted release mechanisms, or triggers, which greatly aid in limiting toxicity and increased concentrating at target sites (Sahoo *et al.,* 2007; Chen *et al.,* 2008; Lévy *et al.,* 2010).

Regulation of protein activity has important biomedical applications and can be used to influence the processes of signal transduction, DNA replication and other key metabolic systems (Toogood, 2002; Gadek and Nicholas, 2003). Nanoparticles can be made in the same size range as enzymes and have several key advantages when considering therapeutic agents. They have large relative surface areas for interactions and attachments, they easily enter into cells, and their synthesis can now be performed relatively easily to make various sizes and shapes with alterable surface properties (Conte *et al.,* 1999; Wu *et al.,* 2009). These abilities allow for more than just cellular targeting and make selective enzymatic targeting both a viable and attractive option in modern therapeutic development.

Due to these multi-capabilities that can be attributed through such modifications, the modern nanodrug development trend is to create multifunctional nanoparticle systems to fulfil virtually all the drug requirements of selective delivery, biocompatibility, solubility, and limited toxicity. An example of such a system is the use of polymeric micelles, developed by Nasongkla *et al.* (2006), which target cancer cells, deliver drugs, and allow magnetic resonance imaging (MRI) for tracking.

1.5.1 Medical applications for transition metals using nano-technology

Many nanomedical applications involve the use of transition metals, which have several unique properties that make them useful. Transition metals all have unfilled d-orbitals and occupy groups 3-12 on the periodic table. This allows them to have various reactive oxidative states, giving them both oxidation and reduction capabilities. They are capable of forming many different types of bonds of varying strength, usually with negatively charged molecular groups. This confers transition metal complexes with promising pharmacological properties and has spurred a great deal of interest and research into investigating the development of compounds that use the transition metals (Rafique *et al.,* 2010). Transition metal medical applications come in many forms, from modified single atom/ion enhanced ligand structures, which can be new or may just improve older therapeutics, to complex functionalised nanoparticles.

An example of the use of transition metals in medical antimalarial research is the modification of chloroquine using Fe ions to create ferroquine, which was synthesised and tested *in-vitro* on live parasites resistant to chloroquine. The new synthetic organometallic analogue was shown to be 5.3 times more active against the chloroquine resistant parasite than chloroquine (Atteke *et al.,* 2003).

1.5.2 Gold and silver nanoparticles

Gold nanoparticles (AuNPs) are one of the more studied nanoparticle variants for use in nanomedical and nanosensing applications. Properties of AuNPs include biocompatiblity, bioavailability, photo-optical activity, and easy functionalization. Applications such as diagnostic imaging, biosensing, and various cancer therapeutic techniques have greatly benefited from these unique properties. In addition to this there are various delivery methods for gold nanoparticles that can target diseased tissues (Chen *et al.,* 2008). Silver is in the same group (Group 11) on the periodic table as gold. Indeed gold and silver share the same outer electron orbital valences' and consequently this means that silver (Ag) and gold (Au) nanoparticles tend to have similar chemical reactive properties when reacted with the same elements or compounds (Kholoud *et al.,* 2010). This effect is noted with special reference to bond length properties when reacting with sulphur containing compounds as indicated by Sellers *et al.,* (1993).

Gold nanoparticles have been used in photothermal therapies by exiting AuNPs at 650-900 nm which then transform absorbed energy into heat in a photothermal ablation technique

used to kill targeted cancer cells (Chen *et al.,* 2008). The technique demonstrated effective destruction of the cancer cells, although the cell targeting techniques that were used lacked selectivity (Huang *et al.,* 2006; Chen *et al.,* 2007).

Silver nanoparticles (AgNPs) have also shown a wide variety of uses and can be synthesised in many ways. They have commonly been used as disinfectant and antibacterial agents (Kholoud *et al.,* 2010; Guzmán *et al.,* 2008). One area of silver nanoparticle research that has been widely explored is nanoparticle-virus interactions. Elechiguerra *et al.* (2005), showed that silver nanoparticles, of sizes ranging from 1-10 nm, are able to interact with the HIV-1 virus, through exposed sulphur atoms that were present on HIV glycoprotein (gp) knobs of gp120. The AgNP-gp120 binding also demonstrated viral inhibition by preventing host cell entry.

Applications of silver have a long history of therapeutic uses and silver has being extensively studied for its antimicrobial and antiviral properties. Silver has seen applications as nanoparticles for water treatment and sterilization, as nanoparticles or nano-crystalline silver in dressings, gels and creams have being used to treat burn wounds and reduce bacterial infections in chronic wounds among other treatments and have generally being found to be non-toxic to humans in minute concentrations but have shown cytotoxicity to some cell lines depending on nanoparticle size (Rai *et al.,* 2009). The manner in which silver nanoparticles obtain such desired properties is being investigated and is not yet fully understood. It has being shown that size and shape of the silver nanoparticles is important however with generally the smaller range of approximately <20 nm generally exhibiting higher efficacy and greater biocompatibility (Kim *et al.,* 2007; Rai *et al.,* 2009). Studies have shown that AgNPs interact with the lipopolysaccharides in the exterior cellular membranes of bacteria, causing structural changes and degradation that leads to increased cell membrane permeability and ultimately cell death (Sondi and Salopek-Sondi, 2004; Kim *et al.,* 2007; Rai *et al.,* 2009). A study investigating by Hao and Schatz (2004) indicates that as the size (particularly below 100 nm) and shape of silver nanoparticles change, corresponding changes in the electromagnetic field and surface Plasmon resonance of AgNPs are observed. These changes allow for differences in electrostatic interactions resulting in dipole and tripole moments between nanoparticles that are notably different. The effect these altered field states and strengths may have on interactions with complex molecules, such as proteins, is unknown but it is fair to assume that if they appear to notably affect characteristics of simpler NP-NP interactions, the effect on more complex molecules - such as proteins – will be presumably

more notable and definitely far more complex. This may potentially explain the variability in toxicity effects observed in various studies (Sondi and Salopek-Sondi, 2004; Kim *et al.*, 2007; Rai *et al.*, 2009).

A demonstrated application of AuNPs is in biosensor design, where redox enzymes typically lack the direct electrical conductivity required to 'wire' them into amperometric sensors with high sensitivities able to detect the binding of microscopic levels of target compounds that require detection. By using enzyme-nanoparticle hybrid systems, gold nanoparticles can be tethered to gold nano-electrodes using cross-linkages to form dithiol bridges with ligand-linked detector enzymes. The AuNPs mediate electron charge transport, thereby increasing the amperometric detector efficiency (You *et al.*, 2005; Willner *et al.*, 2007).

1.5.3 Biomolecular nanoparticle engineering

Biomolecules, like proteins, antibodies, antigens and small DNA segments, offer the reactive potential to design unique nanoparticle-biomolecule hybrid systems. In terms of scale, these building blocks are of a size which allows for them to be attached to nanoparticles and travel with them, allowing them to complement the nanoparticles by conferring the unique properties they possess and thereby creating novel nanoscale substances with diverse capabilities. The engineering of nanosystems capable of molecular recognition and selective binding to target cells and enzymes, is a relatively new field of research with exciting prospects in biomedical applications (You *et al.*, 2005). Fischer *et al.* (2002), demonstrated an engineered NP-enzyme interaction capable of recognizing and inhibiting α-chymotrypsin. This system used monolayer-protected nanoparticles with functionalized anionic termini for recognition and inhibition, similar to the generic sample shown in Figure 1.8b.

Being able to engineer the nanoparticle protein interactions is a critical step in the methodology of designing multi-capable nanomedical systems. Typically, two fundamentally-different approaches are used to conjugate proteins to nanoparticles. These are direct covalent linkage of the protein to the nanoparticle surface, which can be done in several different ways, or the use of non-covalent interactions between the protein and nanoparticle to generate supra-molecular assemblies (Rana *et al.*, 2010).

In the direct conjugation approach, multiple protein side chains may potentially be involved in interactions. In such cases conditions that limit non-specific binding are often sought, as it has been shown that direct conjugation interactions may often result in the loss of enzyme activity, usually due to conformational changes in protein structure. A commonly-used

method for direct conjugation is the use of a single cysteine residue for monovalent attachment. This approach is also plagued by protein denaturation but it may be useful for protein targeting, where enzyme denaturation and loss of activity may be desired. The ability of cysteine to directly conjugate to metallic nanoparticles makes it a useful bio-nanotechnology tool, which can be used as a functionalizing nanoparticle linkage or for direct protein-nanoparticle interactions, if present on a target enzyme surfaces (Rana *et al.*, 2010; Majzik *et al.*, 2009).

Another direct conjugation method relies on the engineering of custom ligands for nanoparticle conjugation and functionalization. This method generally has had greater success, due to its wide range of modification possibilities and easy development methods available. Some common attachment methods are outlined in Figure 1.8 (Rana *et al.*, 2010).

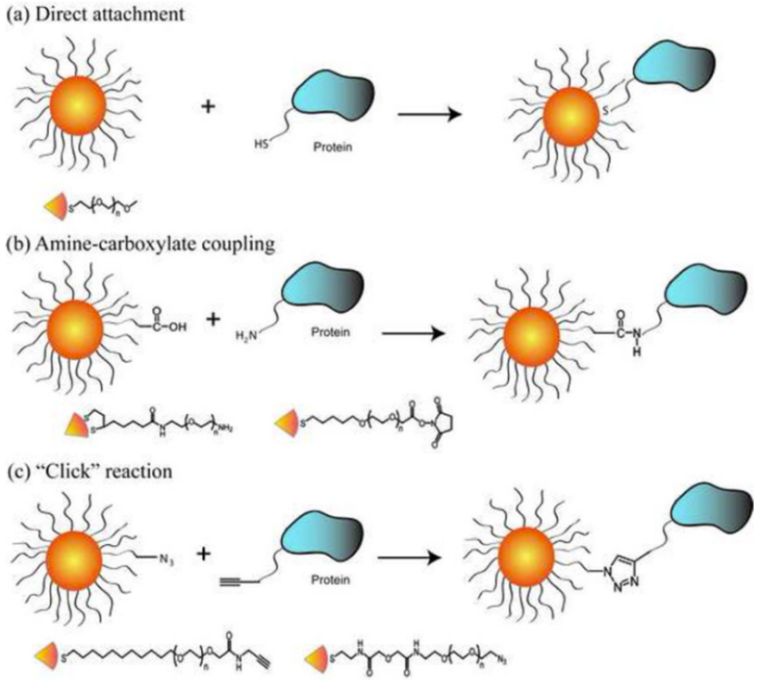

Figure 1.8: Three examples from Rana *et al.* (2010), for direct protein-nanoparticle attachment. **(a)** Direct attachment using a thiol groups on the proteins surface. **(b)** Amine-carboxylate coupling linking NP carboxylate and protein amine groups. **(c)** An alkyne-azide Huisgen 'click' reaction, which uses a catalyst to aid linking the azide tagged NP and the alkyne tagged protein to achieve high yields.

An example of the application and possibilities of modern nanoparticle drugs has been demonstrated recently, as highlighted by (Sheridan 2012; Hrkach *et al.*, 2012). This passed Phase 1 human drug trials for a clinical cancer nanodrug and the nanodrug is currently

undergoing further testing. The study done by BIND Biosciences of Cambridge, Massachusetts (Hrkach *et al.*, 2012) provided positive evidence for the progressive development and clinical application of new nanomedicines. The nanodrug system that was used consisted of a hydrophobic nanoparticle core, with polylactide polymers encapsulating the cytotoxic drug docetaxel. This was surrounded by a hydrophilic corona of polyethylene glycol bound to a small designed molecule, (S-2-[3-35-amino-1-carboypentyl]-ureido]-pentanedioic acid), which targets the prostate-specific membrane antigen that is known to be overexpressed in most solid cancer tumours (Hrkach *et al.*, 2012). A computer-generated image of this molecule is shown in Figure 1.9a (Sheridan, 2012).

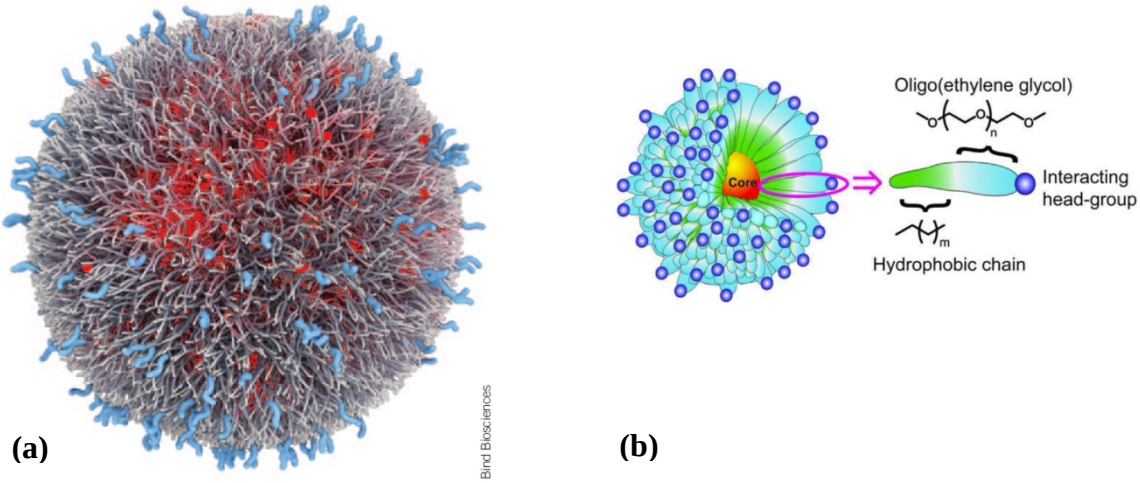

Figure 1.9: (a) Theoretical image of the anti-cancer nanoparticle drug under human clinical trials developed by BIND Biosciences. The nanoparticle drug functions as a targeting and safe drug delivery vessel by utilising layers of peptides to confer different functionality to the overall nanodrug system (Sheridan, 2012; Hrkach *et al.*, 2012). **(b)** A general schematic of a common ligand system used as a linker to help maintain structure and function of linked proteins (Rana *et al.*, 2010).

The second, non-covalent method, using supramolecular interactions is also commonly used for the creation of bioconjugates (Shang *et al.*, 2007). With this approach it has been shown that either 'naked' or fully functionalised NPs, generally interact in a similar manner as normal protein-protein interactions. This occurs through the evolution of a loosely attached protein 'corona' around the nanoparticles, which varies depending on the environment it is in, as well as the concentration and type of proteins present (Rana *et al.*, 2010). The 'naked' nanoparticles tend to irreversibly bind and deform an initial layer of biomolecules which form the first 'corona' layer, while functionalized NPs, which already have an irreversible bound initial layer, act similarly by also loosely binding available biomolecules (Rana *et al.*,

2010; Lynch and Dawson, 2008). This is further discussed in section 1.5.5, Non-functionalized protein-nanoparticle interactions.

1.5.4 Nanoparticle toxicity

Nanoparticle toxicity has been investigated under various conditions and have being found to be both benign and toxic depending of circumstances (Hao and Schatz 2004; Kim *et al.*, 2007; Chen *et al.*, 2008; Rai *et al.*, 2009; Lasagna-Reeves *et al.*, 2010). Size similarities of nanoparticles with other biological components, such as enzymes, have raised concerns about the ability of nanoparticles to be disguised and pass through natural cellular barriers. This can lead to undesired cellular entry into otherwise healthy cells, with unknown effects. Yet this ability is also a potential benefit, allowing for drug delivery in hard-to-reach places, like the brain and cell nuclei (Connor *et al.*, 2005; De Jong and Borm, 2008). To investigate cellular toxicity, Pan *et al.* (2007), studied the size-dependent nature of NP cytotoxicity, using triphenylphosphine-stabilised, AuNPs. Four different mammalian cell lines were tested, including human *Hela* cells. They found that AuNPs of 1-2 nm in size showed cytotoxic effects, with IC_{50} values in the high micro-molar range, while AgNPs of 15 nm in size were determined to be generally nontoxic, even at 60 fold higher concentrations than the small NPs.

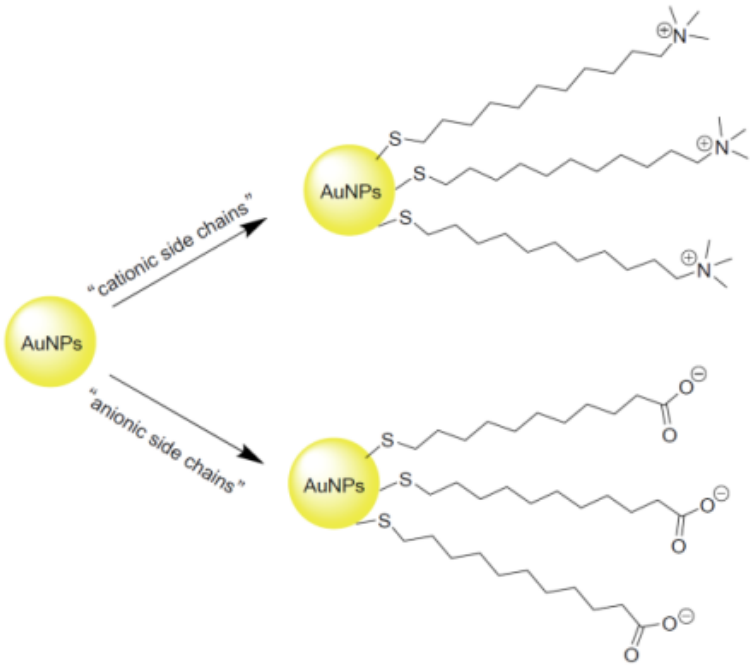

Figure 1.10: Gold nanoparticles functionalized with cationic and anionic side chains used in toxicity studies. Image from Chen *et al.* (2008), original study done by Goodman *et al.* (2004).

Other investigations by Goodman *et al.* (2004), have shown that toxicity is influenced by the nature of the functionalizing and stabilising side chains. Cationic side chains tended to have low cytotoxic levels, while anionic side chains were shown to be generally nontoxic (Figure 1.10).

Current literature generally supports the notion that nanoparticles are generally nontoxic. However, size, composition and the way in which they are functionalized can strongly influence their toxicity. Additional research in this field is required to further understand and define nanoparticle toxicology (Chen *et al.*, 2008; De Jong and Borm, 2008).

1.5.5 Non-functionalized protein-nanoparticle interactions

Nanoparticles and the study of their interactions with various enzymes, *in-vitro* and *in-vivo*, has created a new field of nanomedicinal studies in which these interactions are being characterised and potential medical applications are being investigated (Lynch and Dawson, 2008).

Early studies on protein-nanoparticle interactions revealed that proteins often become distorted upon adsorption with various surfaces. Protein adsorption onto various materials is generally well studied, with interactions being generally defined by electrostatic and hydrophobic forces. Understanding this process and how it relates to protein nanoparticle interactions is somewhat more difficult, due to the complexity of size-to-surface ratios. Yet this is critical in understanding how adsorbed protein layers function and even mediate other enzymatic interactions around them (Lynch and Dawson, 2008). Protein-nanoparticle interactions typically involve highly curved surfaces, with NPs often on the scale of the enzymes themselves. This curvature adds a complex new dynamic that is often overlooked, when trying to understand nanoparticle-protein interactions (Lynch and Dawson, 2008).

In material biology any material that comes in contact with a physiological environment is generally considered to become almost immediately saturated in biological matter, consisting mostly of proteins (Lynch and Dawson, 2008). This phenomenon requires careful consideration in the case of non-functionalized protein-nanoparticle interactions. Physiological environments, like blood plasma, typically contain over 3000 proteins (Omenn, 2007). Such a variety of proteins represents a wide range of association and dissociation constants, each with different affinities and exchange times. One way of studying this phenomenon can be to consider the nanoparticle as surrounded by a protein corona. This

‘corona’ is in a constant state of change, dependent on its environment and the proteins present in it (Lynch and Dawson, 2008).

Protein adsorption studies, using AuNPs with self-adsorbed monolayers of mercaptoundecanoic acid, have focused on adsorption with bovine serum albumin (BSA), myoglobin, and cytochrome c. All three of these proteins were shown to form adsorption layers with both irreversibly- and reversibly- bound fractions (Kaufman *et al.,* 2007), highlighting the observation that protein adsorption onto solid surfaces is a complex process, involving structural changes of protein surfaces, dehydration of sections of the protein, and new direct electrostatic interactions, including hydrogen bonding and van der Waal interactions (Kaufman *et al.,* 2007).

Protein 3D structure is tightly controlled through the composition and conformation of α-helixes and β-sheets. The positioning of hydrophobic residues is also influential and they are usually localized to the protein core. The overall tertiary protein structure is more than just a scaffold for the active site as it helps determine solubility, stability and longevity of the molecules in various sensitive cellular environments (Word *et al.,* 1999). Due to the sensitivity and a relatively low number of stabilising bonding reactions, such as disulphide bonds, proteins are often considered as only marginally stable entities that tend to get replaced relatively regularly, due to their inherent instabilities. As such, a strong interaction – even with the surface of a protein – has the potential to easily disrupt their fragile conformational state. Such disruption will usually result in some form of deformation and the likely loss of enzyme activity/function (Word *et al.,* 1999; Lynch and Dawson, 2008). In addition to active disruption, it has been shown that once a protein’s conformational state is altered, it may often remain deformed, even after the removal or desorption of the disrupting agent. This depends on the particular protein and some proteins are able to refold better than others. Still other proteins are aided in folding by chaperones that encourage a desired protein conformation. For example, Sabatino *et al.* (2007) demonstrated that BSA undergoes irreversible conformation changes upon adsorption and desorption with an asbestos surface. Similar effects were also shown on BSA using polystyrene nanoparticles. This indicated that BSA is susceptible to irreversible adsorption and desorption changes (Sweryda-Krawiec *et al.,* 2004). It can thus be assumed that adsorption and desorption of nanoparticles in a selective manner, that targets one particular variant of otherwise identically-functioning enzymes, may result in a selective inhibition effect on the target protein that underwent

stronger nanoparticle adsorption. This requires the identification of a target interaction site for adsorption.

The influence of protein cysteine residues on non-functionalized nanoparticles has been shown to be very important. In one study by Shen *et al.*, (2007), Raman spectra results indicated that the sulphur atoms on cysteine residues in haemoglobin were able to form direct chemical bonds with cadmium sulphide nanoparticles under a normal physiological pH of 7.43. The functionalization of gold nanoparticles using cysteine residues is well established, as previously discussed (Majzik *et al.*, 2009). It should also be noted that gold, silver and copper are all known to form bonds with sulphur atoms due to their grouping on the periodic table, which makes them attractive nanoparticle choices for protein-nanoparticle interactions of this type. The malarial TIM (*Pf*TIM), shown (Figures 1.7a, b, c, d), has several exposed surface sulphur residues that are not present on the *h*TIM variant. This offers an opportunity for such selective nanoparticle targeting.

1.6 Conclusions

The malarial triosephosphate isomerise enzyme has a potential as a nanoparticle enzyme target. First, it has been identified as a biomedical target due to its importance in energy production for *Plasmodium falciparum*. Second, it has key amino acid, and structural, differences from its human host counterpart. These offer potential targets for gold and silver nanoparticle interactions due to their ability to associate with sulphur atoms of accessible cysteine and methionine residues (Figures 1.7 a, b, c, d). Finally, the selective inhibition of the *Trypanosoma brucei* TIM variant, which is known to be similar in structure to *Pf*TIM, has been demonstrated by targeting cysteine residues that are also present in *Pf*TIM and has being shown to be fatal for *T. brucei*. This indicates that, if successful, this methodology has the potential to be fatal to *P. falciparum,* as it was to *T. brucei* (Gómez-Puyou *et al.*, 1995; Velanker *et al.*, 1997; Parthasarathy *et al.*, 2002; Parthasarathy *et al.*, 2003).

1.7 Hypothesis

Due to amino acid sequence and structural differences between *human* and *Plasmodium falciparum* triosephosphate isomerases, silver nanoparticles, of less than 20 nm in size, will selectively inhibit the parasite enzyme over its *human* counterpart.

1.8 Research objectives

1. Obtain cDNA for recombinant expression of *human* and *Plasmodium falciparum* triosephosphate isomerases.
2. PCR amplify and sub-clone these genes into the pET28(b+) expression plasmid.
3. Transform this plasmid into *E. coli* BL21(DE3) cells for protein over-expression.
4. Purify large quantities of highly pure recombinant enzymes using Ni-Affinity chromatography and test enzyme activity, using a suitable assay.
5. Assess and characterise the recombinant enzyme kinetics and activity and establish enzyme stability under different temperature and pH conditions.
6. Synthesize and characterise silver nanoparticles, assessing their stability, size and shape using transmission electron microscopy and spectrophotometry.
7. Interact the recombinant enzymes with the silver nanoparticles and monitor for changes in catalytic activity.
8. Suggest a theorised mechanism for differences in activity that may be observed in data.

2. Gene cloning and verification

2.1 Introduction

The aims of this chapter was to sub-clone the gene sequences for *h*TIM and *Pf*TIM into the pET28(b+) expression vector and transform the plasmids into the appropriate cell lines for recombinant protein overexpression. These were *E. coli* BL21(DE3) cells for *h*TIM and *E. coli* BL21(DE3), with the pRARE2 plasmid for *Pf*TIM, since *P. falciparum* is AT-rich and uses rare codons (Su *et al.,* 1996; Baca and Hol, 2000). To achieve this goal several molecular techniques were used. For molecular DNA cloning, plasmid vectors were used as they have several natural advantages. First, typically they are small in size making them easy to purify and manipulate. Second, they can replicate independently of host cells as they have their own origin of replication. Third, they can have a multiple copy number, meaning several copies can reside within a single cell, which is advantageous when plasmid propagation is required. Fourth, selectable agents such as antibiotics can be incorporated, which simplifies screening and isolation. Fifth, commercial plasmids incorporate many easy-to-use restriction endonuclease sites, allowing for easy cutting and ligating of genes (Madigan and Martinko, 2006).

To obtain the *Pf*TIM gene from the malarial parasite, complementary DNA (cDNA) was obtained from the 'Malaria Research and Reference Reagents Resource Center', (MR4), a part of the American Type Culture Collection (ATCC), and the *Pf*TIM gene was amplified using polymerase chain reaction (PCR). This technique makes use of two PCR primers that flank, or are a part of, the target sequence. Therefore, some knowledge of the gene sequence being acquired is necessary. Primers can then be designed and tested, using several modern bioinformatics tools, and then ordered pre-synthesised from a company such as Integrated DNA Technologies. The design of primers typically also incorporates the restriction endonuclease sites, which are used to manipulate the amplified DNA during sub-cloning procedures and for cutting and ligating the gene sequence into an expression vector. PCR works through repetitive heating and cooling cycles. First, the double stranded DNA is denatured by heating, at high temperatures such as 95°C or 98°C, separating the dsDNA into two ssDNA sequences. Second, the sample is cooled to allow the primer sequences to 'anneal' to the ssDNA at their specific target sites. At this stage DNA replication is also initiated, when a thermally stable DNA polymerase enzyme, such as *Taq* or *Pfu*, binds the

double stranded primer and template sequence segment. The polymerase then replicates the template DNA, downstream of the primer binding site, over a period of time known as the extension time. This process typically involves a slight increase in temperature and an increase in the replication speed of the DNA polymerase. However, this may not always be necessary or advisable for AT-rich genes, as it could result in DNA separation. These processes are typically optimised for use, with the sequence being amplified. Once extension is complete the sample is heated again to separate the now-double-stranded DNA and the process repeated 35 to 40 times, each time theoretically doubling the amount of target DNA isolated by the two primers (Wilson and Walker, 2005).

Once DNA is obtained through PCR, and sub-cloned into a vector for further propagation, it can be sequenced. DNA sequencing is now fully automated but essentially works in the same manner as the original un-automated systems. Two methods have been developed. The first was the Maxam and Gilbert method that made use of chemical reactants to achieve base-specific cleavage of DNA strands, although this method has now been replaced by the chain-terminator method, which makes use of modified dNTP's. The second sequencing method is known as the Sanger procedure, which exploits the use of a DNA polymerase from *E. coli* to synthesise complementary DNA from ssDNA without the need of primers. In both sequencing methods the chain-terminator sub-method may be used. This works by incorporating natural deoxynucleotides and 2',3'-dideoxynucleotide analogues (at a lower concentration); these lack a hydroxyl group, which causes the termination of DNA strand elongation after they are inserted. A radiolabelled dNTP analogue (e.g. α^{35}S-dATP) is also included, and the reactions are run four times, once for each base. If done correctly, the DNA elongation is terminated at all possible bases and can be imaged using autoradiography after running denaturing (SDS-PAGE). The banding patterns of the four sequences are read together and the sequence can be directly deduced from this method. Similarly, fluorescent-dye-labelled substrates can also be used for more rapid (real-time) DNA sequence detection, using capillary polyacrylamide gels. This illustrates how modifications to essential basic techniques (i.e. PCR and gel electrophoresis) can result in entirely new powerful applications of such procedures. Indeed the many different forms of gel electrophoresis and chromatography techniques, that all essentially work on basic principles, have allowed for the development of an astounding number of unique and extremely powerful molecular and biochemical methods (Karp, 2005; Ratledge and Kristiansen, 2006).

In this chapter the experimental work, used to obtain both the *h*TIM and *Pf*TIM genes in an expression-ready form, is outlined. This involved DNA amplification techniques, using PCR and plasmid sub-cloning in *E. coli* JM109 cell lines for gene propagation. For *h*TIM the optimised gene was sub-cloned from the pMK-T plasmid into the pET28(b+) vector. While for *Pf*TIM samples, the PCR product was ligated into the pJET1.2 vector for propagation and then sub-cloned into the pET28(b+) vector. Once both genes had being sub-cloned into the pET28(b+) cvector making pET28(b+) expression ready plasmids, the plasmids were transformed into the *E. coli* BL21(DE3) expression ready cells for protein overexpression.

2.2 Materials and methods

A full list of reagents is also supplied (Appendix A) as well as a list of buffer preparation procedures of common buffers used (Appendix B). When kits were used they all included the necessary reagents. An Eppendorf bench-top micro-centrifuge was used for the centrifugation steps, unless otherwise stated.

For double digestion reactions the Thermo scientific Fermentas double digest tool, available on their website, was used (http://www.fermentas.com/en/tools/doubledigest). Plasmid DNA extraction was done using the Bioflux, Biospin plasmid DNA extraction kit, Cat#BSC01S1, available from (www.bioer.com.cn). DNA extractions made use of the Bioflux, Biospin gel extraction kit from Bioer Cat#BSC02S1, available at (www.bioer.com.cn). The CloneJET™ PCR Cloning Kit Ref #K1231, sold by Inqaba Biotechnology (part of ThermoScientific), was used. The kit is available on their website at http://www.fermentas.com/. Extracted plasmid DNA was sent into Inqaba biotechnology (http://www.inqababiotec.co.za/) for DNA sequencing with the pJet1.2 sequencing primers provided in the plasmid kit.

2.2.1 DNA ligations

Three DNA ligation reactions were required in this project: One to ligate the *Pf*TIM PCR product into the pJET 1.2 vector, and two more to ligate both *h*TIM and *Pf*TIM into the pET28(b+) vector. All reactions were designed (using Equations 2.2.1 and 2.2.2) to calculate the optimal concentrations of vector DNA, to insert DNA for efficient ligation reactions using 50 ng of vector DNA (Table 2.1).

Equation 2.2.1

$$\text{Insert concentration} = \frac{50\ \text{ng(vector DNA)} \times \text{insert DNA size}}{\text{Size of vector used}}$$

Equation 2.2.2

$$\text{Volume of vector required} = \frac{\text{concentration of vector after restriction analysis}}{\text{50 ng of vector needed}}$$

For ligation reactions, the unknown concentrations of the pET28(b+) and/or pJET1.2 vectors, as well as for the *h*TIM and *Pf*TIM genes, were determined using a Nanodrop 2000c spectrophotometer (ThermoScientific), after the double-digest restriction analysis (Section 2.2.5) using EcoRI, NdeI and XhoI and gel purification. The determined DNA concentration data, was used to calculate reaction reagent concentrations (Equations 2.2.1 and 2.2.2) for the ligation reactions. The calculated values are indicated in Table 2.1.

Table 2.1: Ligation reactions for *h*TIM and *Pf*TIM ligation into the pET28(b+) vector and the *Pf*TIM PCR product into the pJET1.2 vector.

Reagents	***h*TIM in pET28(b+)**	***Pf*TIM in pET28(b+)**	***Pf*TIM in pJET 1.2**
Linearized pET28(b+)	1.8 µl	3 µl	-
pJET 1.2 (50 ng/µl)	-	-	1 µl
DNA insert	0.5 µl	3.2 µl	3.8 µl
Ligase buffer	1 µl	1 µl	-
T4 DNA Ligase	1 µl	1 µl	1 µl
Nuclease free H_2O	5.7 µl	1.8 µl	4.2 µl
pJET1.2 (ligase buffer)	-	-	10 µl
Total Volume	**10 µl**	**10 µl**	**20 µl**

Ligation reactions were performed overnight (approximately 12-16 hours) at 4°C, except for the pJET1.2 ligation, which was incubated at room temperature for 5 min before being immediately transformed into *E. coli* JM109 cells.

2.2.2 Preparation of competent cells

A procedure outlined by Inoue *et al.* (1990) was used for the preparation of competent cells and transformation with prepared plasmids. The preparation of competent cells was performed three times to make competent *E. coli* JM109 cells and *E. coli* BL21(DE3) cells for propagation/expression, and again on a selection of *E. coli* BL21(DE3) transformed with the pRARE2 plasmid, to allow for expression of *Pf*TIM, which contained rare codons.

For growth media, super optimal broth (SOB), super optimal broth with catabolite suppression (SOC) and luria broth (LB), were prepared as described by Hanahan (1983) (Appendix B). For selection and screening of transformed *E. coli* JM109 cells, LB agar plates were prepared with relevant antibiotics, when necessary. These included, ampicillin 100 µg/ml (pJET1.2), kanamycin 30 µg/ml [pMK-T or pET28(b+)] and chloramphenicol 34

μg/ml (pRARE2 plasmid), where the concentrations here represent the final concentration present in the prepared agar, or broth, solution.

Frozen cell stocks were thawed, streaked on LB agar plates, and cultured overnight at 37°C. A swipe of large colonies was isolated using a platinum loop and inoculated in 250 ml of SOB medium in a 1 litre flask. This was grown overnight (~8-10 hours) at 18-20°C, with shaking at ~150-200 rpm, until an OD_{600} of ~0.55 was obtained. This broth was then removed from the incubator and immediately placed on an ice/water slurry for 10 min. The culture was transferred into a 500 ml centrifuge bottle and centrifuged (2500 x g; 10 min; 4°C). The pellet was resuspended using 80 ml of ice-cold TB buffer and incubated on ice for a further 10 min. After incubation it was centrifuged again, as described above. The cell pellet was gently resuspended in 20 ml of TB buffer, and 1.5 ml DMSO was added and gently swirled to facilitate mixing. The sample was placed on ice for a final 10 min, distributed as 100 μl aliquots in 1.5 ml sterile tubes, and then rapidly frozen in liquid nitrogen. Samples were then stored at -80°C until use.

2.2.3 Transformation procedure

Previously prepared competent cells of *E. coli* JM109 or Bl21(DE3) were thawed at on ice and 10 μl of extracted ligation mixture/plasmid was added. Tubes were gently tapped to mix, and incubated on ice for 20 min. Samples were then heat-shocked by putting them in a heat block at 42°C for 40-60 sec, then immediately placing them in an ice water slurry for 2 min. Thereafter, 250 μl of SOC media was added and samples were incubated at 37°C for 1 hour. Cells were centrifuged (2500 x g; 5 min). The supernatant was decanted until 100 μl was left and the pellet was resuspended by gently pipetting the volume up and down several times. The resuspended sample was then spread-plated onto selective LB-Agar plates with appropriate relevant antibiotics: kanamycin (30 μg/ml) for transformations using pET28(b+) and pMK-T plasmids, and ampicillin (100 μg/ml) for transformations using the pJet1.2 plasmid. Chloramphenicol (34 μg/ml) was also used when transformations were done using cell cultures that contained the pRARE2 plasmid. Samples were then grown overnight (for 12-16 hours) and individual colonies picked and grown in LB with relevant antibiotics (for 12-16 hours) before restriction analysis screening (Inoue *et al.*, 1990).

2.2.4 Plasmid DNA extraction

The standard protocol provided with the Bioflux, Biospin plasmid DNA extraction kit, is described as follows. Broth cultures continuing plasmid were grown for 16 hours. From this 2

ml was centrifuged (10000 rpm; 30 sec), the supernatant discarded and the process repeated once more. The pellet was resuspended, using 250 µl resuspension buffer, and vortexed. To this 250 µl of lysis buffer was added and sample inverted 4-6 times, followed by the addition of 350 µl of neutralization buffer, followed by inversion (for mixing). This was centrifuged at 13000 rpm for 10 min, the supernatant added to a spin column, and then centrifuged for 1 min at 6000 rpm. Flow-through was discarded and 650 µl of wash buffer was added, and the solution centrifuged at 12000 rpm for 1 min, discarding the flow-through. This process was then repeated once. Sample columns were then transferred to sterile 1.5 ml tubes, 50 µl of elution buffer was added, and the tubes incubated at 37°C for 15 min. Finally, plasmid DNA was collected by centrifuging the elution buffer through the column at 12000 rpm for 1 min and collecting the flow-through in 1.5 ml tubes.

2.2.5 DNA double digestion reactions

Double digestion reactions were performed on plasmid DNA samples extracted as described in Section 2.2.4. By performing double digestion reactions, target genes could be screened for on agarose gels (Section 2.2.6) and cleaned from the gel for downstream cloning (Section 2.2.7). In total, three double digestion reactions were performed, as outlined in Table 2.2, using 'Fermentas' reagents. The double digestion reactions for the pMK-T and pJET1.2 plasmids resulted in sticky-end gene sequences for ligation into the pET28(b+) expression plasmid. Generally, 10 µl double digestion reaction repeats of these reactions were done for screening purposes.

Table 2.2: Double digestion reactions performed on the pMK-T, pET28(b+) and pJET1.2 plasmids.

Reagent	**pMK-T & *h*TIM**	**pET28(b+) & *h*TIM**	**pJET1.2 & *Pf*TIM**	**pET28(b+) & *Pf*TIM**
Buffer R	5 µl	1 µl	-	-
Buffer O	-	-	1 µl	2.5 µl
XhoI	2.5 µl	0.2 µl	-	-
NdeI	5 µl	0.4 µl	0.5 µl	1 µl
EcoRI	-	-	0.5 µl	1 µl
Plasmid DNA	30 µl	8.4 µl	4 µl	20.5 µl
Sterile H_2O	7.5 µl	-	4 µl	-
Total volume	**50 µl**	**10 µl**	**10 µl**	**25 µl**

Double digestion reactions were incubated at 37°C for 1-3 hours though in some cases the reaction was run overnight. The overall volumes of reactions did vary between individual

experiments, but the relative concentration ratios of reagents always remained as indicated (Table 2.2).

2.2.6 Agarose gels

All agarose gels were made as 0.8% by mixing 0.8 g agarose with 100 ml of 1 x TAE buffer (Appendix B). This was microwaved for approximately 1-2 min until all agarose was dissolved and the liquid appeared clear. This was allowed to cool to approximately 55°C and 4 µl of ethidium bromide (10 mg/ml) was added. The sample was swirled several times to mix, then poured into a Bio-Rad® gel system and electrophoresed (90 V, 60 min). Samples loaded in the gel wells were mixed with 1 µl, 6 x loading dye (ThermoScientific), per 4 µl of sample, and loaded into the gel wells (typically 10 µl).

2.2.7 Agarose gel DNA extraction

Agarose gels were visualised on a gel doc (Vilber Lourmat) under 365 nm UV light to limit DNA denaturation. Samples were loaded with GeneRuler DNA Ladder marker, supplied by Inqaba biotechnology, but a product of ThermoScientific, which were used to help identify the relevant bands to be excised from the gel, using a sterile scalpel. Gel slices were placed in 2 ml tubes and weighed, then 3 x their weight of extraction buffer was added and samples were incubated at 50°C for 10 min and periodically vortexed until the gel had melted. For pET28(b+) samples 1 x gel weight of isopropanol was also added. The sample was transferred to the supplied spin columns and centrifuged at 6000 rpm for 1 min and the flow-through discarded. This was repeated until all samples had been loaded onto the columns. An additional 500 µl of extraction buffer was added and centrifuged at 12000 rpm for 30 sec, discarding the flow-through. Wash buffer was added (750 µl) and allowed to stand for 5 min. It was then centrifuged for 1 min at 12000 rpm and the column transferred to a 1.5 ml tube. To this, 50 µl of elution buffer was added and the sample was incubated for 15 min at 37°C. Finally, the DNA was eluted by centrifugation at 12000 rpm for 1 min.

Extracted DNA (plasmid or gene) was quantified using a Nanodrop 2000c spectrophotometer (ThermoScientific), (Section 2.2.1).

2.2.8 Preparation of glycerol stocks

To prepare glycerol stocks a swipe of transformed colonies was taken and grown for 12-16 hours in LB broth containing relevant antibiotics (kanamycin 30 µg/ml, and/or chloramphenicol 34 µg/ml). Aliquots were then taken from this broth and stored in 1.5 ml

tubes containing 1 ml of cultured cells and 0.5 ml of a sterile 50% glycerol solution. Stocks were then frozen at -80°C, for later use.

2.2.9 PCR primer design

Plasmodium falciparum 3D7, blood-stage, cDNA obtained from the Malaria Reference Reagents and Resource Center (MR4), a part of the American Type Culture Collection (ATCC), was used as a template for PCR to amplify the *Pf*TIM gene sequence. To do this the *Pf*TIM gene sequence in the cDNA needed to be known so that a suitable pair of PCR primers could be designed. The entire genome and mRNA of *P. falciparum* has being sequenced and, as such, the cDNA sequence, which is in fact a complementary strand of mRNA made using reverse transcriptase, could be downloaded from the National Centre for Biotechnology Information (NCBI). Website: (http://www.ncbi.nlm.nih.gov/genbank/), Sequence #XM_001348516.2. Using the mRNA sequence also has the benefit of not having to remove the introns, as this has already been done by the parasite's biochemical machinery during mRNA expression. The sequence listed here was 1486 bp in length, of which positions 318-1064 (inclusive) were identified by the NCBI website as being the coding sequence. This meant that the target sequence for PCR was 747 bp in length (Appendix C). To target this sequence, the following forward and reverse primers were designed, tested, and analysed using the pDraw32 program as well as the Integrated DNA Technologies (IDT), website-based, primer design tool at: (http://eu.idtdna.com/analyzer/Applications/OligoAnalyzer/). For further details of these designed primers, the target sequence, and analysis of primers - including melting temperatures (Tm), and BLAST primer analysis - see Appendix C**.**

Primer sequences designed to bind to *Pf*TIM cDNA for PCR

Forward primer (binding sequence)
5'-ATGGCTAGAAAATATTTTGTCGCAGC-3' (26 bp)

Reverse primer (binding sequence)
5'-TTACATAGCACTTTTTATTATATCAACAAAAGATTC-3' (36 bp)

After designing the binding primer sequence (above), they were redesigned to incorporate restriction endonuclease sites for NdeI (forward) and EcoRI (reverse). This allowed for easy sub-cloning of the gene into the pET28(b+) expression vector via restriction analysis: i.e. the 'double digest' reactions (Section 2.2.5). The redesigned primers, with restriction sites, also function to forcefully introduce the restriction sites during PCR at the right points and in the

right reading frame for problem-free DNA manipulations. The redesigned primers are indicated below, with restriction sequences highlighted: NdeI (CATATG) and EcoRI (GAATTC). These redesigned sequences (below) were synthesised, by IDT whom also provided analysis of the ordered primer sequences – see Appendix C.

Final primer sequences designed for PCR amplification of *Pf*TIM from *P. falciparum* cDNA

Forward primer (ordered sequence)
5'-CATATGGCTAGAAAATATTTTGTCGCAGC-3' (29 bp)
-NdeI

Reverse primer (ordered sequence)
5'-GAATTCTTACATAGCACTTTTTATTATATCAACAAAAGATTC-3' (42 bp)
-EcoRI

2.2.10 Optimized PCR Protocol

The PCR procedure underwent many optimisations (Appendix D) before a functioning procedure was developed. One paper in particular, by Su *et al.*, (1996), was used extensively as an aid for customising and optimising the PCR protocol, as it focuses extensively on dealing with highly AT-rich genes. Troubleshooting guidelines from the manual for *Pfu* high fidelity DNA polymerase were also extensively used to develop optimisations that allowed this PCR to work. The highly AT-rich nature of the *Plasmodium falciparum* genome rendered several common PCR protocols and DNA polymerase enzymes completely ineffective (for *P. falciparum* cDNA). Eventually, a completely redesigned optimized PCR protocol was developed (see Table 2.3, with cycling parameters indicated in the following paragraph). This optimized protocol, using *Pfu* high fidelity DNA polymerase, was successfully used to amplify the *Pf*TIM gene in large amounts.

Table 2.3: Optimised PCR protocol used to amplify AT-rich *Pf*TIM from *P. falciparum* cDNA.

Reagents	**Volume**
P. falciparum cDNA (2 ng/µl)	1 µl
HF Buffer (5 x concentration)	10 µl
Forward Primer (10 pmol)	2.5 µl
Reverse Primer (10 pmol)	2.5 µl
dNTPs (10 mM)	1 µl
Sterile DNA free H_2O	32.5 µl
Phusion Hot Start II *Pfu* Taq	0.5 µl
Total	50 µl

Samples, prepared as in Table 2.3, were run on a rapid thermal cycler, starting with 2 min incubation at 98°C to activate the Phusion Hot Start II Taq (ThermoScientific). Cycling parameters then started with 20 sec at 98°C to separate DNA, followed by a custom two-step annealing process of 10 sec at 62°C, then 10 sec at 57°C, and finally DNA extension for 40 sec at 60°C. This process was cycled through for 35 to 40 times before a final extension step, of 10 min at 60°C. The program ended with cooling to 4°C for a maximum time of 16 hours, or until the sample could be removed.

This procedure produced blunt ended unphosphorylated DNA, ready for blunt end ligation, using the CloneJET™ PCR cloning kit described below (Section 2.2.11).

2.2.11 CloneJET PCR cloning kit aka: (pJET1.2 vector)

The blunt end cloning procedure, as detailed in the kit manual, was performed using DNA extracted from an agarose gel (Section 2.2.6) of the PCR product (Section 2.2.10) using the gel purification kit (Section 2.2.7). The gel-extracted DNA was quantified using a Nanodrop 2000c spectrophotometer, which indicated 9.9 $ng^{-1}.\mu l^{-1}$ of *Pf*TIM DNA had been extracted from gel of the PCR product. Using the manual guidelines, a 20 µl ligation reaction - to ligate the *Pf*TIM gene into the blunt end pJET1.2 cloning vector - was setup (Table 2.4).

Table 2.4: Blunt end ligation into CloneJET - pJET1.2 vector.

Reagents	**Volume**
2x Buffer	10 µl
PCR Product (37.5 ng)	3.8 µl
pJET1.2 (50 ng/µl)	1 µl
Nuclease free H_20	4.2 µl
T_4 DNA Ligase	1 µl
Total	**20 µl**

Reagents were mixed by vortexing (3-4 sec) and then incubated (22°C, 5 min). Ligated plasmid mixture was used for transformations, with *E. coli* JM109 cells - see Section 2.2.3.

This kit is a positive identification kit for high-efficiency cloning of PCR products and it includes the use of a lethal restriction enzyme gene, which is disrupted by the ligation of a DNA insert into the cloning site. This means that only cells with a DNA insert ligated into the plasmid cloning site are able to grow, thus allowing for positive selection screening. In addition to this, the kit included sequencing primers, for DNA sequencing. These were used to sequence the successful ligations to confirm the presence of the *Pf*TIM gene (Appendix F).

2.3 Results and discussion

The following sub-sections present the experimental work done to obtain expression ready forms of the *h*TIM and *Pf*TIM genes.

2.3.1 Obtaining the *h*TIM gene and sub-cloning

The *human* TIM gene was purchased already-synthesised by Invitrogens' Life Technologies division using their GeneArt® Gene Synthesis service. This included codon optimization for expression in *E. coli* cultures. The gene was supplied in the pMK-T vector (5 µg), with a plasmid map (Figure 2.1) and DNA sequencing results indicating the sent DNA sequence aligned with the codon-optimized sequence for *h*TIM gene. A translated amino acid sequence, for comparison with the known *h*TIM amino acid sequence, was included because the codon optimization process for *E. coli* meant the DNA coding sequence had being changed, due to silent mutations, and therefore would not be identical (in terms of DNA) to the known *h*TIM sequence, but the amino acid sequence it produced would be. These data and the supplied chromatogram are included in Appendix E.

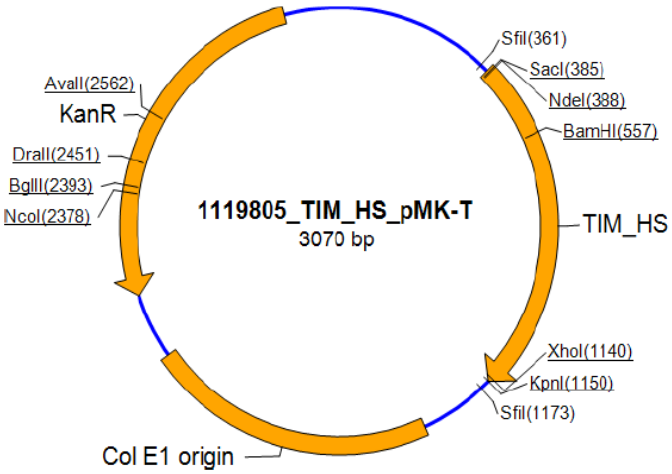

Figure 2.1: Map of the pMK-T plasmid, containing the *h*TIM and kanomycin-resistance genes, an origin of replication, for cloning in *E. coli* cell cultures. All relevant restriction sites are also shown.

As shown in Figure 2.1 the gene has an NdeI site at its start and an XhoI site at its end. A double digestion reaction of pMK-T, using these restriction endonucleases, would therefore produce two bands on an agarose gel, ~2.3 Kbp in size (vector backbone) and the other ~750 bp in size (*h*TIM gene). Using these restriction endonucleases would eloquently remove the target *h*TIM gene sequence, with sticky ends ready for sub-cloning into the pET28(b+) expression system, which also contains these restriction endonuclease sites.

The *h*TIM gene was cloned into the pET28(b+) expression vector for protein overexpression in *E. coli* BL21(DE3) cells. To achieve this, the supplied pMK-T plasmid was transformed into *E. coli* JM109 competent cells (Sections 2.2.2 and 2.2.3). A swipe of transformed colonies was selected from the plate and transferred into Luria broth, containing kanamycin, and incubated overnight (12-16 hours) at 37°C. After plasmid DNA extraction (Section 2.2.4) the sample was quantified using nanodrop, which indicated approximately 122 ng/µl of pMK-T plasmid DNA containing the *h*TIM gene had being obtained and was relatively pure, as indicated by the A_{260}/A_{280} readings.

Similarly, a culture of *E. coli* JM109 cells containing unmodified pET28(b+) plasmid, was grown in in Luria broth containing kanamycin for 12-16 hours at 37°C, and plasmid DNA extraction performed (Section 2.2.4), and the DNA concentration quantified indicating approximately 143 ng/µl of the pure pET28(b+) plasmid DNA had being obtained.

A virtual DNA cloning, to evaluate the sticky end ligation of *h*TIM into pET28(b+) after both plasmids had undergone double digestion reactions using NdeI and XhoI restriction endonucleases, was computed using the freely-available pDraw32 application from (http://www.acaclone.com/). The result of this gave the following plasmid map (Figure 2.2).

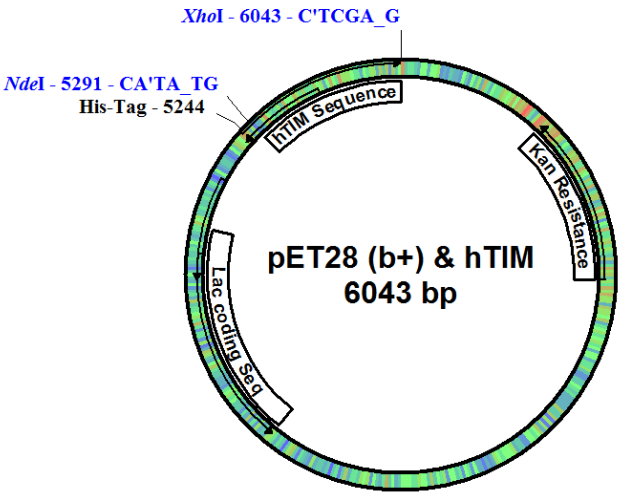

Figure 2.2: Plasmid map of the virtual cloning of *h*TIM into the pET28(b+) expression plasmid using NdeI and XhoI restriction endonucleases (designed using the open source program pDRAW32).

Similarly the the virtual cloning procedure also indicated that a double digest reaction of empty pET28(b+) vector backbone, using NdeI and XhoI restriction endonucleases –

(plasmid map not shown), will produce only one visible band, of ~5.32 Kbp in size, on an agarose gel.

After performing the virtual cloning and calculating the band sizes that should be observed from a successful double digestion procedure, the pMK-T and pET28(b+) plasmids were digested overnight using NdeI and XhoI. A 0.8% agarose gel (Section 2.2.6) of these samples was run to determine if the digested band sizes were correct (Appendix A). This gel was visualised under 365 nm light and bands corresponding to the calculated sizes for *h*TIM and pET28(b+) were excised from the gel, for DNA extraction (Section 2.2.7) see Appendix E4 for this gel image.

Extracted *h*TIM and pET28(b+) sticky end DNA was then ligated as per the DNA ligation procedure (Section 2.2.1). Ligated DNA was transformed into *E. coli* JM109 cells and screened on kanamycin plates (Section 2.2.3). Individual colonies were then picked and grown in LB overnight (12-16 hours). To screen for transformed colonies, a 'dirty prep' Lysis by boiling procedure (Appendix B) was used to screen ten colonies. Double digestion reactions were done and samples were electrophoresed for screening on a 0.8% agarose gel (Appendix E5). Clean plasmid DNA was then extracted (Section 2.2.4) from the two sample cultures identified from the 'dirty prep' procedure (Appendix E5). Extracted pure DNA from these transformed colonies was then screened using the double digest reaction (Section 2.2.5) to confirm if bands for *h*TIM were present at the expected size range, of ~750 bp, that would indicate a successful ligation of the correct DNA sequence into the pET28(b+) plasmid. This result is presented in Figure 2.3.

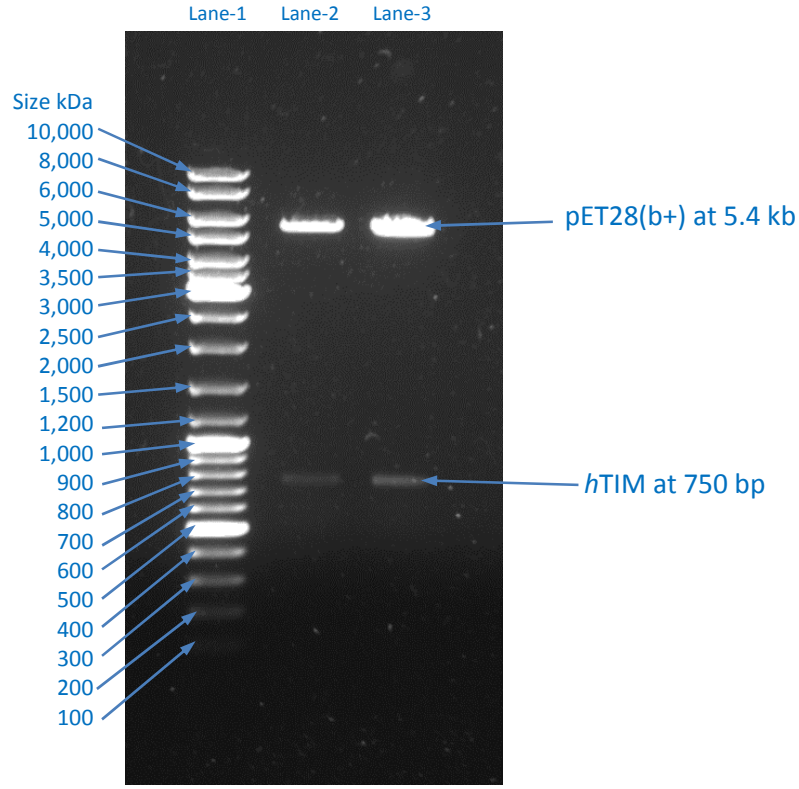

Figure 2.3: Agarose gel showing, Lane 1: GeneRuler DNA ladder and Lanes 2 and 3: Double digestion reactions (Section 2.2.5) on plasmid DNA extracted from select picked colonies that had been transformed using the pET28(b+) and *h*TIM DNA ligation mixture.

Figure 2.3 confirms that *h*TIM was successfully ligated into the pET28(b+) expression system. Remaining extracted plasmid, used to produce Figure 2.3, was used to transform competent *E. coli* Bl21(DE3) expression-ready cells, (Sections 2.2.2 and 2.2.3). A swipe of transformed colonies was picked and grown in LB broth with kanamycin to make glycerol stocks (Section 2.2.8) that could be used later for recombinant protein expression of *h*TIM.

2.3.2 Obtaining *Pf*TIM from cDNA by PCR and sub-cloning

Initially complementary DNA (cDNA) of *Plasmodium falciparum* 3D7 parasites blood-stage messenger RNA was obtained from the American Type Culture Collection (ATCC). To extract and amplify the *Pf*TIM gene from this sample, a highly modified and optimised polymerase chain reaction (PCR) protocol had to be designed (Section 2.2.10) along with suitable PCR primers that introduced the restriction endonuclease sites of NdeI (forward) and EcoRI (reverse) on the primers, for easy DNA manipulation.

After PCR amplification reactions (Sections 2.2.9 and 2.2.10) the PCR product was concentrated under a vacuum (Vacutec Centrivap cold trap and DNA concentrator). The dry PCR product DNA was then resuspended in MilliQ H_2O and electrophoresed on a 0.8% agarose gel (Section 2.2.6). Some of this sample was photographed at 320 nm (Figure 2.4)

while the remainder was visualised under 365 nm light, excised from the agarose gel, and a DNA extraction performed (Section 2.2.7). Extracted DNA was then used as a template for a subsequent PCR reaction (Sections 2.2.9 and 2.2.10) which produced the necessary quantities of blunt end *Pf*TIM DNA required for ligation into the blunt end pJet1.2 cloning vector.

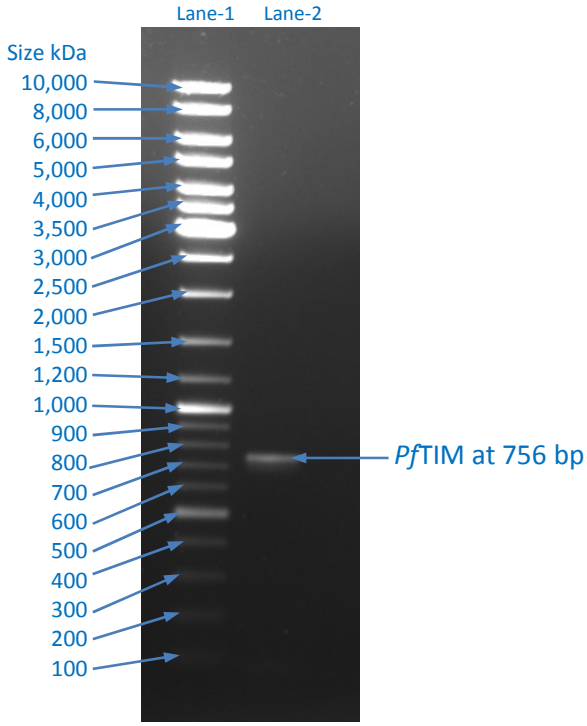

Figure 2.4: Agarose gel showing; Lane 1: GeneRuler DNA ladder, and Lane 2: The product of a PCR reaction detailed in Sections 2.2.9 and 2.2.10 using *Plasmodium falciparum* cDNA as template.

As with *h*TIM, virtual cloning was done to assess the viability of the cloning procedure and to identify any potential problems. For *Pf*TIM, however, the process was done twice: once for cloning into the pJet1.2 cloning vector and then again for cloning into pET28(b+) expression vector. Virtual cloning maps generated in this process are presented as Figure 2.5.

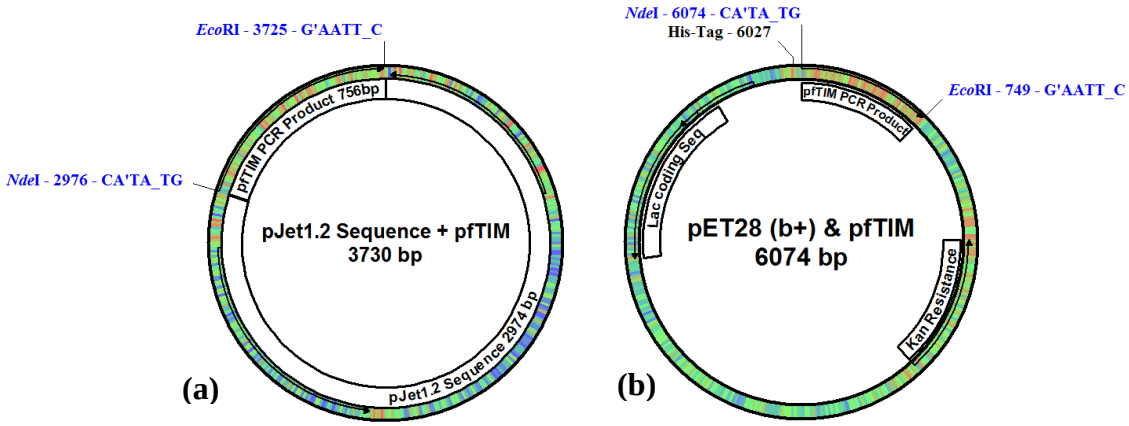

Figure 2.5: Virtual cloning using the pDRAW application of the *Pf*TIM PCR product into, **(a)** the blunt end pJet1.2 PCR cloning vector, and **(b)** the virtual cloning into the pET28(b+) expression vector using NdeI and EcoRI restriction endonucleases to cut the *Pf*TIM gene and pET28(b+) plasmid for sub-cloning and sticky end ligation reactions.

Virtual cloning confirmed the viability of the cloning procedures being used and also indicated what band sizes to expect in agarose gels done on double digest reactions using NdeI and EcoRI restriction endonucleases.

Cloning began with the ligation of the extracted PCR product into the blunt end pJet1.2 cloning vector (Section 2.2.11). No phosphorylation process was required as this vector came pre-phosphorylated. After ligation (Section 2.2.1) the pJet1.2 and *Pf*TIM ligation mixture was transformed into *E. coli* JM109 competent cells (Section 2.2.2) and grown on selective LB agar media containing ampicillin. Five colonies were picked from these plates and LB cultures grown with ampicillin (Section 2.2.3). Plasmid DNA was then extracted (Section 2.2.4), followed by a double digestion reaction using NdeI and EcoRI (Section 2.2.5). The five samples were then electrophoresed on a 0.8% agarose gel to screen for successfully transformed colonies (Section 2.2.6). The result of this sub-cloning of the PCR product into pJet1.2 vector (Figure 2.5a) produced Figure 2.6, which indicates three of the five colonies selected appear to have the *Pf*TIM gene insert.

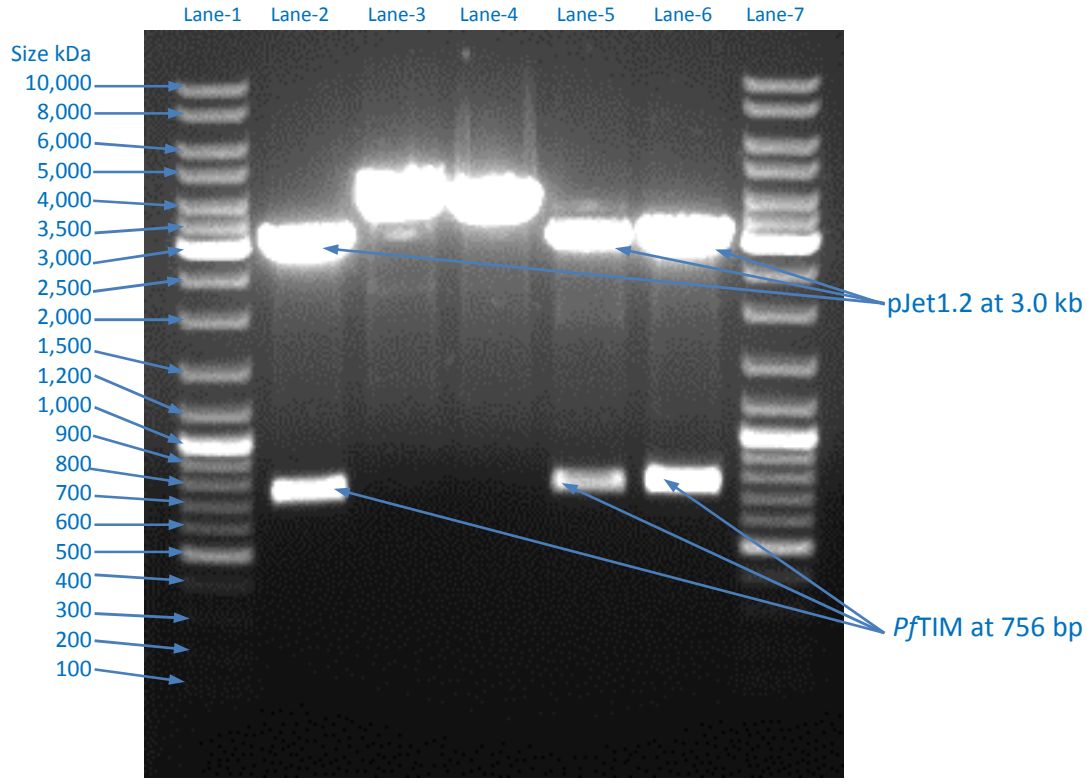

Figure 2.6: Agarose gel of plasmid extracted from JM109 cells and digested using NdeI and EcoRI. Lanes 1 and 7 are GeneRuler DNA ladder. Bands in lanes 2, 5 and 6 correspond with the known sizes of pJet1.2 vector (3 kb) and *Pf*TIM (756 bp), as indicated on the right of the Figure. Lanes 3 and 4 have only 1 band that roughly corresponds to a plasmid that had only been cut once (~3.7 kb).

As calculated in the virtual cloning process (Figure 2.5a), bands for *Pf*TIM and the pJet1.2 vector are clearly visible in their correct positions, of 756 bp for *Pf*TIM and ~3 kbp, for pJet1.2 vector from the double digestion reaction using NdeI and EcoRI. After having obtained this result, additional plasmid DNA from the broth cultures of lanes 2 and 6 (Figure 2.6) was extracted (Section 2.2.4). Samples of each (10 µl) were sent to Inqaba Biotech (South Africa) for DNA sequencing in both forward and reverse directions using the sequencing primers provided with the pJet1.2 cloning kit. The sequencing results from both samples were an exact match with the known *Pf*TIM DNA sequence, indicating that no mutations had occurred during PCR or sub-cloning into pJet1.2 and the correct sequence had been obtained. The chromatogram and blast search using the DNA sequence returned from sequencing can be seen in Appendix F.

After sequencing confirmed that the correct *Pf*TIM gene sequence had been inserted into the pJet1.2 vector, it was digested using NdeI and EcoRI (Section 2.2.5). Similarly, a double digest reaction on empty pET28(b+) vector was also done using these restriction endonucleases. A 0.8% agarose gel (Section 2.2.6) was then prepared and electrophoresed for the sub-cloning and the digestion products visualised under UV light at 365 nm. Bands

corresponding to *Pf*TIM and empty pET28(b+) vector were excised from the gel and the DNA extracted (Section 2.2.7). The image of this gel can be seen in Appendix D4. Extracted DNA was quantified and DNA ligation reactions set up and run (Section 2.2.1). The ligation mixture was then transformed into *E. coli* JM109 cells (Section 2.2.3) and cultured on selective LB agar plates containing kanamycin. Seven colonies were picked from the selective media and then grown in selective LB broth cultures (Section 2.2.3). Cells were harvested from the seven broth cultures and plasmid DNA extractions were performed (Section 2.2.4) on each sample, followed by double digest reactions using NdeI and EcoRI (Section 2.2.5) and then electrophoresed on a 0.8% agarose gel (Section 2.2.6). The image of this gel is shown in Figure 2.7 below.

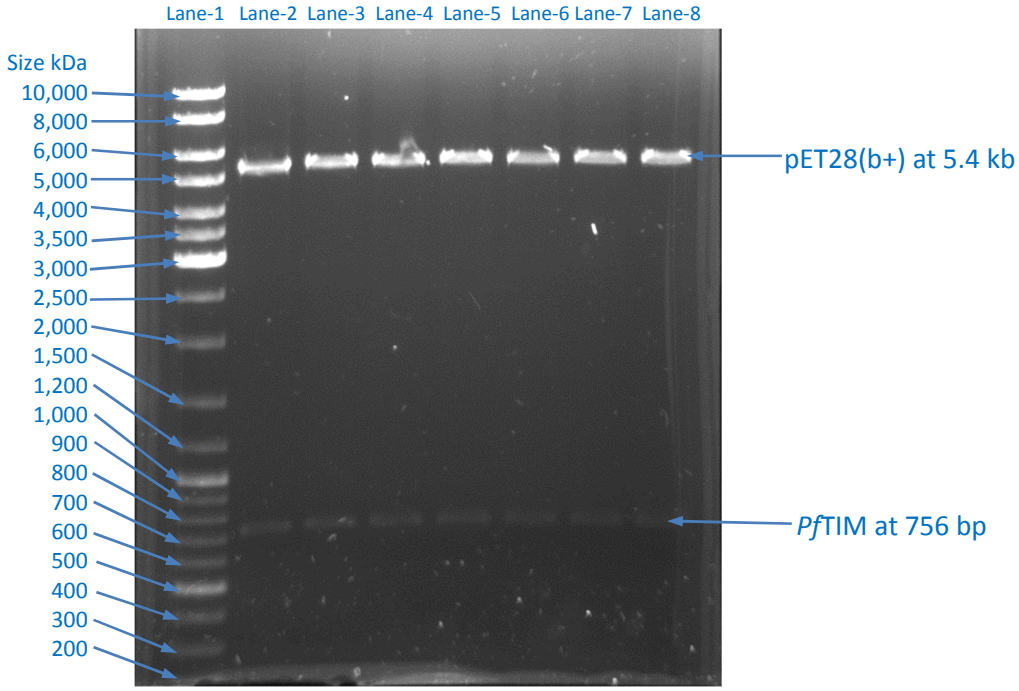

Figure 2.7: Agarose gel of, Lane1: GeneRuler DNA ladder, and Lanes 2-8: Double digest reactions using NdeI and EcoRI (Section 2.2.5) on plasmid DNA extracted from broth cultures of individually picked colonies that had being transformed with pET28(b+) plasmid ligated with *Pf*TIM DNA.

As shown in Figure 2.7 above, all picked colonies had successful ligations of the *Pf*TIM gene into the pET28(b+) expression vector. The extracted plasmid sample that gave lane 2 (Figure 2.7) was chosen to transform (Section 2.2.3) previously-prepared *E. coli* BL21(DE3) cells containing the pRARE2 plasmid. For this transformation, selective LB agar plates containing chloramphenicol and kanamycin were used (Section 2.2.3). A swipe of transformed colonies was picked from the selective media plates and grown for 12-16 hours in LB containing these

two antibiotics. This broth culture was then used to create glycerol stocks (Section 2.2.8). These *E. coli* BL21(DE3) expression ready cells contained the pRARE2 plasmid and the pET28(b+) expression vector with the *Pf*TIM gene insert, as indicated by Figure 2.7, and were ready to be used for recombinant protein overexpression of *Pf*TIM.

2.4 Conclusions

Thus the goal of this chapter, which was to obtain cell cultures of both *h*TIM and *Pf*TIM that were ready for overexpression of these two recombinant enzymes, had been achieved. The glycerol stock aliquots were stored at -80°C so that when desired a 1.5 ml sample could be thawed, new broths grown, and the recombinant protein overexpression procedure initiated, as detailed in the next chapter.

3. Recombinant protein expression, purification and characterisation.

3.1 Introduction

The aims of this chapter are to outline the experimental procedures and results done to obtain pure recombinant *h*TIM and *Pf*TIM enzymes, to confirm enzyme activity, and characterise these two enzyme variants.

Recombinant protein overexpression was performed using the prepared glycerol stocks which contained the pET28(b+) expression vector with the relevant genes ligated into the vectors expression site, using *E. coli* BL21(DE3) expression ready cultures. The *Pf*TIM cultures also contained the pRARE2 plasmid due to the AT-rich nature of the *Pf*TIM gene and its use of rare codons (Su *et al.*, 1996; Baca and Hol, 2000). The pET28(b+) expression vector introduces a 6x histidine tag (His-Tag) to the N-terminal end of any expressed recombinant protein. This allowed for efficient and easy purification using Ni-affinity chromatography, which strongly binds these his-tagged proteins, resulting in a highly effective purification step. The recombinant proteins were then eluted from the Ni-Affinity column using increasing concentrations of imidazole in a 'linear gradient' achieved by the FPLC system, which gradually altered the ratio of (running:elution buffers) increasing the amount of elution buffer - which contains much higher concentrations of imidazole - from 0% to 100%. The imidazole then competes with the bound his-tagged recombinant protein displacing it and allowing it to elute out of the column. Further purification steps were also performed including, gel filtration - on Sephadex 200HR column - to remove the imidazole, and dialysis to eliminate NaC*l* used in the gel filtration buffer.

An auto-induction medium was chosen because it has several advantages, such as creating a better-folded and more soluble target protein, which is typically several folds higher in concentration, compared to that produced by isopropyl-β-D-thiogalactoside (IPTG), induction methods (Studier, 2005). A typical induction system, such as that found in *E. coli* BL21(DE3) cells, uses the T7 RNA polymerase under the control of the inducible *lacUV*5 promoter. Upon the introduction of any inducer (typically IPTG), T7 RNA polymerase is made and any DNA controlled by the T7 promoter is transcribed. T7 is so active that the amount of target RNA produced can be comparable to the total amount of RNA produced in a

cell (Studier, 2005). Target RNA, produced during this process, will typically contain a coding sequence with an appropriate translation initiation sequence upstream of the start codon. In pET28(b+) this sequence is of the T7 major capsid protein, which promotes gene translation and transcription. Consequently, the majority of protein synthesis is directed to the target gene, which usually becomes a large component of the total protein content in the cell, provided no further complications occur, such as gene toxicity in the *E. coli* cells (Studier, 2005; Sørensen and Mortensen, 2005).

One of the problems with the T7 expression system is that it is so active that even small basal levels of expression can result in substantial amounts of protein being expressed in cells, even in the absence of an inducer. This can cause toxicity problems and also result in lower yields. This problem can be circumvented by inserting the *lac* operator sequence downstream of the T7 start site, creating a T7*lac* promoter site (Sørensen and Mortensen, 2005). This allows for gene suppression, by interfering with the binding of the *lac* repressor to the *lac* operator site. This *lac* repressor prevents the establishment of an elongation complex by T7 RNA polymerase, resulting in substantial reduction in background mRNA expression (Sørensen and Mortensen, 2005). During induction, both the T7*lac* and *lacUV*5 sites are unblocked by the release of the *lacI* tetramer (Figure 3.1), allowing for maximal translation and expression levels to be obtained. The *lacI* tetramer release is triggered by the binding of IPTG to it or binding of a similar *lac* inducer to IPTG such as α-lactose used in auto-induction. The pET vectors utilise this *lacI* gene to control the repression of the *lacUV* promoter and the T7/lac hybrid promoter (Sørensen and Mortensen, 2005). This repression function of the *lacI* gene may also be further enhanced 10 fold, with the use of a mutant $lacI^{q}$ gene - which is overexpressed by the *E. coli* host. This whole system is represented graphically in Figure 3.1, obtained from Sørensen and Mortensen (2005).

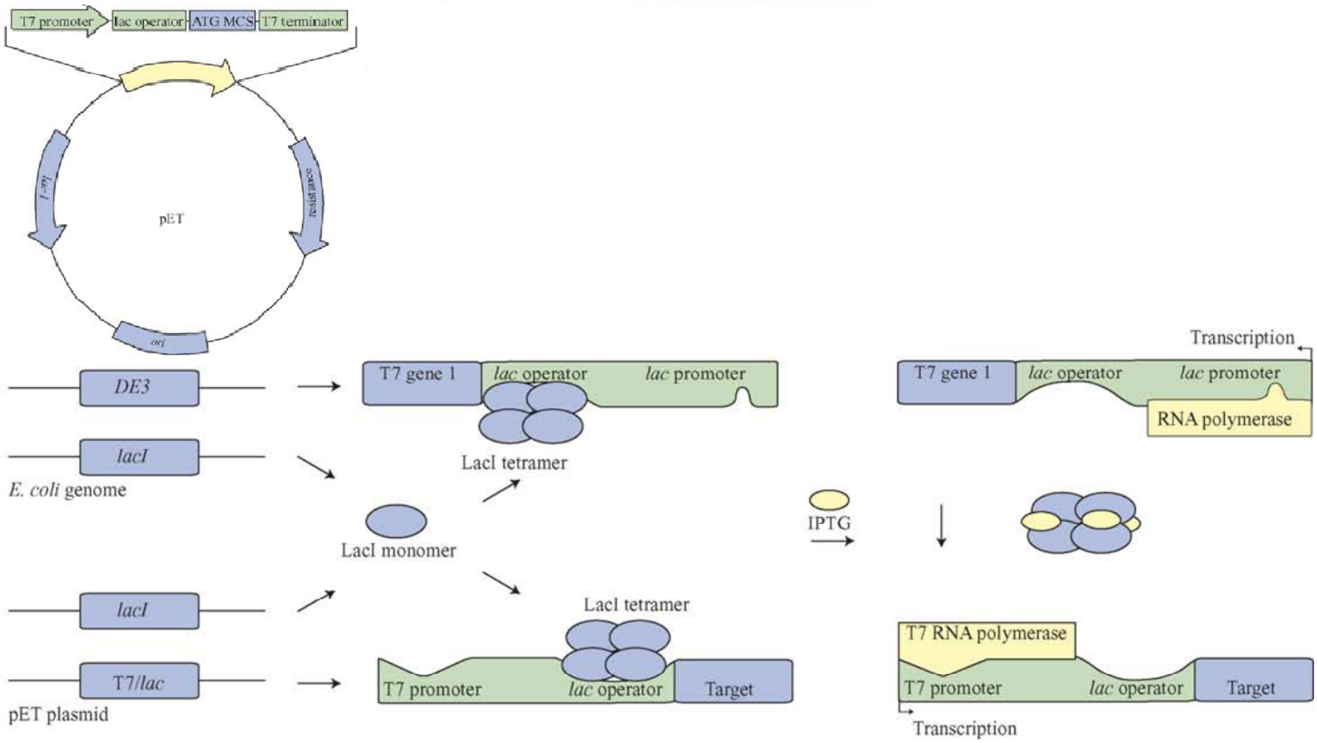

Figure 3.1: The general overview of the pET expression system is shown on the left, and on the right the biochemical molecular interactions before and after induction are represented, Sørensen and Mortensen, (2005).

The average half-life of mRNA in *E. coli* at 37°C can range from seconds to a maximum of 20 min (Sørensen and Mortensen, 2005). This is worth noting because, while the expression system and conditions were the same for both *h*TIM and *Pf*TIM, the AT-rich *Pf*TIM gene which was not codon optimised for *E. coli* expression unlike the *h*TIM DNA sequence which was. As a result it is likely that destruction of the *Pf*TIM mRNA would have been more rapid resulting in lower expression.

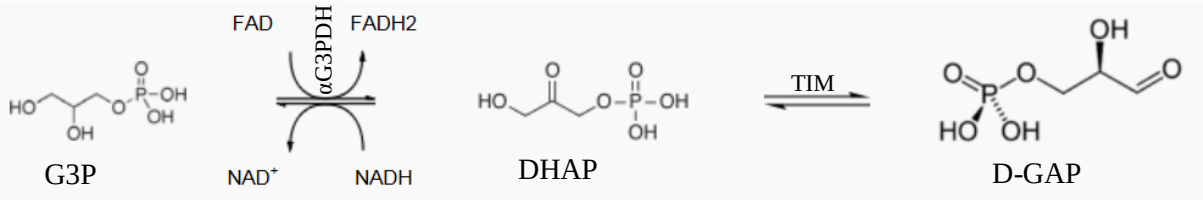

Figure 3.2: The direction of the assay runs from right to left for the TIM reaction that will be monitored. On the far right is D-glyceraldehyde-3-phosphate (D-GAP) which is converted by TIM to dihydroxyacetone phosphate (DHAP) (centre). This is then converted to glycerol-3-phosphate (G3P) by α-glycerol-3-phosphate dehydrogenase (αG3PDH) with the concomitant oxidation of NADH, which is observed at 340 nm, to track the reaction.

The assay used for determining TIM activity is a coupled enzyme assay that monitors the oxidation of β-Nicotinamide Adenine Dinucleotide (NADH to NAD^+) at 340 nm (Figure 3.2). This assay is relatively well studied and understood (Albertyn *et al.,* 1992; De la Roche *et al.,* 2012; Warkentin and Fondi, 1973; Von Kalm *et al.,* 1989). Adjustments of standard assay parameters of concentration, volume and mixing procedures were modified for use in 96 well plates. Results of some of the test experiments, performed in order to obtain good reproducibility, are included in Appendix G.

Understanding the mechanisms of the TIM assay used in this project provides useful insight into assessing the results presented in this chapter. The two-stage TIM assay (depicted in Figure 3.2) works on the principal of the TIM product (DHAP) being immediately used by αG3PDH and producing a steady state reaction. The biomechanics of this process have being investigated (Knowles *et al.,* 1972; Plaut and Knowles, 1972; Blacklow *et al.,* 1988). The validity of such a system depends on the rapid removal of product from the first reaction by the second reaction, to ensure that product inhibition does not hinder the speed of the first reaction. Bergmeyer (1974) considered this mathematically and concluded that, to observe true activity with a 99% level of accuracy, the coupling enzyme would have to be 1000 times more concentrated. This observation by Bergmeyer (1974), while true, is 'not so bleak' as pointed out by Plaut and Knowles (1972), who note that coupled enzyme systems, such as the TIM and αG3PDH assay, go through a brief acceleration phase before reaching steady state kinetics. These produce consistent and accurate results from far lower coupling enzyme concentrations than suggested by Bergmeyer (1974) - provided that the product is removed at a sufficient rate, and that the ratio of substrate to product remains high, in favour of substrate to the first enzyme. Observed kinetic data are consistent, reliable, and accurately reflects the true kinetics parameters. This can be confirmed by assessing the linearity of the observed data after steady state kinetics is reached. As any shift in the substrate-to-product-saturation ratios would result in slowing the reaction rate and, subsequently, an observed decrease in linearity, indicating a deviation of the data from steady state kinetics (Putman *et al.*,1972; Plaut and Knowles, 1972). Understanding and checking for this provided an additional control and quality assessment when conducting TIM assays.

Subsequently, good reproducibility was achieved using the micro-titre plate system and the final protocol described in Section 3.2.8 (Plaut and Knowles, 1972; Albertyn *et al.,* 1992; De la Roche *et al.,* 2012).

3.2 Materials and methods

This section outlines protocols and reagents used in the experiments described in this chapter. A full list of reagents is also supplied (Appendix A) and a list of buffer preparation procedures of common buffers used, is provided (Appendix B).

3.2.1 Recombinant protein expression using auto-induction

The auto-induction protocol that was used is an adaptation of the protocol developed by Studier (2005). To start auto-induction, 100 ml aliquots of ZYP505/5052 (Appendix B) were distributed into autoclaved 500 ml Erlenmeyer flasks sealed with cotton wool. To this, suitable concentrations of sterile antibiotics were added: 30 µg/ml kanamycin (to retain pET28(b+) plasmid) and 34 µg/ml chloramphenicol (only in *Pf*TIM samples, to retain pRARE2 plasmid).

Prior to auto-induction, pre-cultures of the *E. coli* BL21(DE3) expression-ready cells, which included pET28(b+) plasmids containing the *h*TIM or *Pf*TIM genes, were grown from frozen glycerol stocks (Chapter 2). For pre-cultures, 1 ml of relevant glycerol stock (*h*TIM or *Pf*TIM) was grown in 100 ml LB broth with antibiotics (as mentioned) in 500 ml sterile Erlenmeyer flasks sealed with cotton wool (12-16 h, 30°C, 150 rpm). Pre-culturing ensured that cellular recovery from freeze thaw was complete, and that cells were ready for log phase growth when the auto-induction process was initiated.

One ml of the pre-cultures were inoculated into the prepared ZYP505/5052 auto-induction media and grown (24-36 h, 20°C, 150 rpm). Cells were harvested by centrifugation (5000 x g, 10 min, 4°C).

For the purpose of constructing a purification table, samples were taken every 2 h, from the auto-induction cultures, during the induction study. These samples were micro-centrifuged, (5000 x g, 45 sec) and frozen at -20°C, so that enzyme expression levels during auto-induction could be analysed by SDS-PAGE. To assess the overall purification, samples were set aside at the following stages: pre lysis, post lysis, post 2700 x g centrifugation, post 100000 x g centrifugation, post Ni-affinity chromatography, post gel filtration and post dialysis.

3.2.2 Cell lysis and preparation for Ni-affinity chromatography

Pelleted cells from auto-induction were washed with potassium phosphate ($KHPO_4$) working buffer (3 washes, 100 ml, 100 mM, pH 7.4) and centrifuged after each wash step (5000 x g, 10 min, 4°C).

Cells were re-suspended in working buffer (20 ml/g wet weight) with lysozyme (1 mg/ml) and an EDTA-free protease inhibitor cocktail tablet (Roche) was added to the mixture and incubated (37°C, 1 h, 120 rpm). The mixture was then frozen at -80°C overnight, for cell rupture.

Samples were thawed on ice (also overnight) and centrifuged (2700 x g, 30 min, 4°C), after which the supernatant was collected and the sample was ultra-centrifuged (100000 x g, 90 min, 4°C). Ni-affinity chromatography was then performed using a fast protein liquid chromatography (FPLC) system from GE Healthcare (Section 3.2.3).

3.2.3 Ni-affinity chromatography using FPLC

In preparation for Ni-affinity chromatography using the FLPC system, several FPLC buffers were prepared (Appendix B).

Ni-affinity chromatography was run, using a 150 ml superloop injection system with a 5 ml His-trap FF column on a GE, Amersham FPLC system. Sample preparation for the superloop injection system involved mixing 1 part (4x loading buffer) to 3 parts supernatant from ultracentrifugation (Section 3.2.2). The volume of samples varied, due to different wet weights obtained during cell collection (Section 3.2.2).

The superloop system and the column were connected to the FPLC system and the His-Trap FF column was equilibrated by washing successively with dddH_2O (50 ml) and running buffer (Appendix B) until the UV absorbance of eluate remained at base level. The sample (in the superloop) was then injected onto the column by injecting 90-150 ml running buffer (i.e. the volume in the superloop) through the superloop injection system at a flow rate of 5 ml/min. This was followed with a wash step of 50 ml running buffer, to wash out unbound protein from the column. An elution buffer gradient (0 - 100%) set to occur over 100 ml, was set up, starting with 100% running buffer and ending with 100% elution buffer (Appendix B). After the elution gradient finished an additional 25 ml of 100% elution buffer was passed through the column. Fractions (5.0 ml) were collected from the start of the elution buffer gradient. UV absorbance was monitored over the entire process so that fractions containing protein could be identified. From each fraction a 20 µl sample was set aside for SDS-PAGE. The 5 ml fractions corresponding to a spike in UV absorbance from the detector and containing the target protein were pooled.

3.2.4 Gel filtration chromatography using FPLC

Active fractions from the Ni-affinity chromatography steps - 60 ml for (*h*TIM) and 45 ml for (*Pf*TIM) were centrifuged (4000 x g; 5 min; 4 °C) in a spin column (Sartorius Stedim Vivaspin2, 10K MW columns) to a final volume (400 µl). To this, glycerol (200 µl) was added, and the sample mixed by inversion, before being subjected to further purification by gel filtration chromatography. A Sephadex G-200 HR gel column (1 m x 1.6 cm) was used on the FPLC system (GE Amersham) with an injection loop (5.0 ml) loading system. The column was equilibrated using 2 column volumes of FPLC gel filtration running buffer (Appendix B). The sample was then injected into a 5 ml injection loop on the FPLC system. The system then loaded the sample - in the loop - onto the column by emptying the loop with 10 ml of running buffer. Afterwards the system equilibrated with 0.1 column volumes before eluting the sample with 1.5 column volumes of running buffer (Appendix B). During the elution phase 5 ml fractions were collected. Flow rate throughout was 1 ml/min always using FPLC gel running buffer (Appendix B).

3.2.5 Dialysis

Dialysis was performed (Snake-skin 10 kDa MWCO; Thermo Scientific, South Africa) with four buffer changes in 24 h using ($KHPO_4$,100 mM; 2 *l*, 4°C) with vigorous stirring, using a magnetic stirrer. The volume of the samples, post–dialysis, were measured as *h*TIM (35 ml) and *Pf*TIM (25 ml), and approximately 8-12 drops of glycerol were added. Samples mixed by inversion and 500 µl aliquots made in sterile tubes and frozen at -20°C.

3.2.6 SDS-PAGE and staining/de-staining

Sodium dodecyl sulphate – polyacrylamide gel electrophoresis (SDS-PAGE) was performed on each stage of the purification, according to the manufacturer's published procedures BioRad® (http://www.bio-rad.com/). SDS-PAGE buffers and gel preparations for a 12.5% resolving gel and a 4% stacking gel are included in Appendix B.

Each gel was loaded with 10 µl of pre-stained PageRuler™ protein ladder (ThermoScientific). Wells not containing samples were loaded with 25 µl TS+TD solution (Appendix B). Gels were then electrophoresed (100 V, 75 min).

A staining/de-staining protocol developed by Fairbanks *et al.* (1971) was used. In this protocol four solutions (Fairbanks A, B, C, D) are prepared (Appendix B). To stain/de-stain, gels are microwaved in Fairbanks A (100 ml, 2 min), mixed on a rocker (5 min), and then

rinsed with dddH_2O. This process is repeated using Fairbanks B, C and D solutions until a clear de-stained gel is obtained in ~1 h, on which 25 ng or more of protein can be visualised.

3.2.7 Protein determination (Bradfords Assay)

Protein concentration was determined by Bradfords method (Bradford, 1976). An adaptation of this protocol, for use in 96-well micro-titre plates using pre-made Bradfords reagent (Sigma-Aldrich, 2012), was used. Active sample (5 µl) was mixed with Bradfords reagent (250 µl), left at room temperature (15 min) to allow complete colour development, followed by absorbance, read at 595 nm. A standard curve using bovine serum albumen (BSA) as protein standard in concentrations of 0.1 - 1.2 mg/ml, was constructed (Appendix G, Figure G1). From this, an equation to determine protein concentration from absorbance readings at 595 nm was determined (Appendix G, Equation G1).

It is noted that the protocol provided by Sigma-Aldrich, (2012) listed many incompatible reagents and the concentration levels at which they may start to interfere with the assay. Several reagents used during purification were listed, including imidazole, glycerol, EDTA, and Tris, among others. Of all of these, only imidazole was in a concentration range that may interfere with the Bradfords assay method but only in post-Ni-affinity samples.

3.2.8 Triosephosphate isomerase assay

This assay procedure (Figure 3.2) was adapted from published protocols (Bergmeyer, 1974; Knowles *et al.*, 1972). All buffer, reagent and enzyme preparations are explained in Appendix B. A positive enzyme control was also conducted using commercial rabbit TIM (*r*TIM), (Appendix H, Figure H2).

The assay was performed in a 96-well micro-titre plate, as follows: in a 1st well, NADH (10 µl, 8 mM), αG3PDH (10 µl, 20 U/ml), DL-GAP (50 µl, 20 mM) were mixed with TEA buffer (230 µl, 300 mM, pH 7.6). In a 2nd well, a suitably diluted TIM sample was added (10 µl). Dilutions determined by optimization experiments (Appendix H) were for *h*TIM (1/2000) and *Pf*TIM (1/300) from their purified stocks. The micro-titre plate was equilibrated at 25 °C in a BioTek Synergy MX spectrophotometer. The plate was then shaken (variably, for 30 sec) and change in absorbance at 340 nm of the 1st well measured (2 min, 15 sec intervals). This provided a baseline reading after equilibration and functioned as a negative enzyme control for each well. The micro-titre plate was then ejected from the spectrophotometer and the enzymatic reaction initiated by pipetting 290 µl from the 1st well and injected into the 2nd well

containing 10 µl of the relevant TIM (*h*TIM or *Pf*TIM). The micro-titre plate was then shaken (variably, 30 sec) and change in absorbance measured (340 nm, 15 sec intervals, 10 min).

Equation 3.1

$$\text{Units/ml} = \frac{(\Delta A_{340\ nm}.\text{min}^{-1}\ \text{sample}) \times (V_t = \text{volume of assay}) \times (\text{df} = \text{dilution factor})}{\varepsilon_{NADH} \times (V_e = \text{volume of enzyme})}$$

$\varepsilon_{NADH} = 6.22\ \mu\text{mol}^{-1}.\text{ml}^{-1}.\text{min}^{-1}$ /aka/: $6220\ \text{Mol}^{-1}.l^{-1}.\text{cm}^{-1}$

One unit will convert 1.0 µmol of dihydroxyacetone phosphate to α-glycerophosphate per minute at 25°C, pH 7.6.

The αG3PDH assays (Chapter 4; Section 4.2.1) also made use of Equation 3.1 because both the TIM and the αG3PDH assays monitor the depletion of NADH at 340 nm.

3.3 Results and discussion

3.3.1 Protein over-expression by auto-induction

Transformed and ready-to-express cells from both *h*TIM and *Pf*TIM (chapter 2) were over-expressed using an auto-induction technique (Section 3.2.1).

The processes described here for both *h*TIM and *Pf*TIM were run concurrently, where possible, to minimise differences in their preparations and ensure accuracy and consistency.

During auto-induction, 5 Erlenmeyer flasks were used for each sample (*h*TIM or *Pf*TIM), only 4 of these were harvested for enzyme purifications while the 5th was used exclusively for the induction study over 36 hours. This eliminated the possibility of contamination being introduced when samples were taken every 2 hours for the induction study. For purification purposes the 4 *h*TIM Erlenmeyer flasks were harvested at 24 hours while the *Pf*TIM ones were harvested at 36 hours. This was because it was known at this stage that the *Pf*TIM-expressing cells grew and expressed recombinant *Pf*TIM slower than was the case for the *h*TIM expressing cells.

3.3.1.1 SDS-PAGE of auto-induction

The SDS-PAGE of the induction study tracks the growth and protein expression levels during auto-induction. The recombinant proteins, both of which are approximately 27 kDa (Ray *et al.*, 1999; Orosz *et al.*, 2006) in size, emerge amongst the other protein bands.

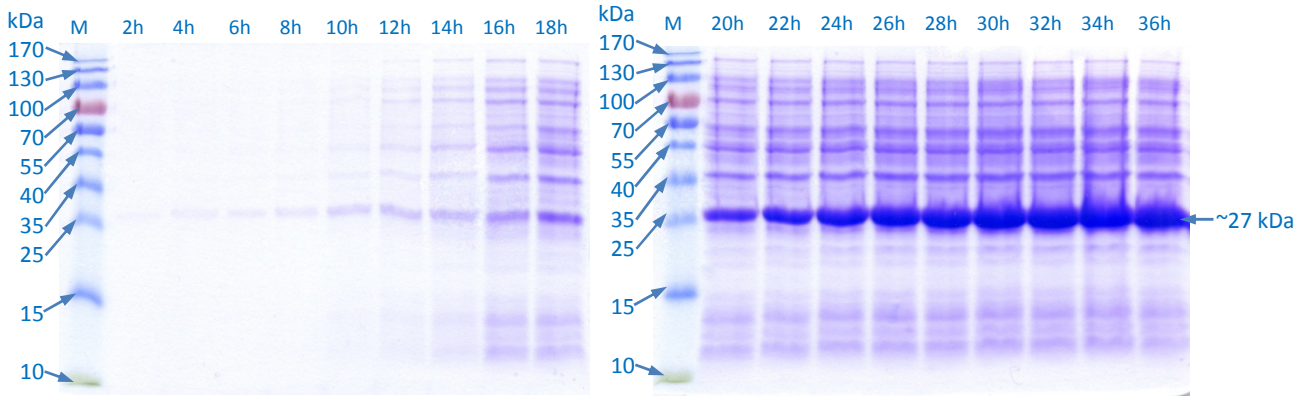

Figure 3.3: SDS-PAGE of the *h*TIM sample showing all protein expression during the 36 hour auto-induction. Note: *h*TIM monomer is 27 kDa in size (Orosz *et al.*, 2006). Lanes are labelled with the time they were harvested at and M represents lane loaded with PageRuler™ protein ladder (ThermoScientific).

From the SDS-PAGE of the *h*TIM induction study (Figure 3.3) the dense bands that develop at the 27 kDa size range are consistent with the known size of *h*TIM, reported as a 54 kDa homodimer made up of two 27 kDa monomers (Orosz *et al.*, 2006).

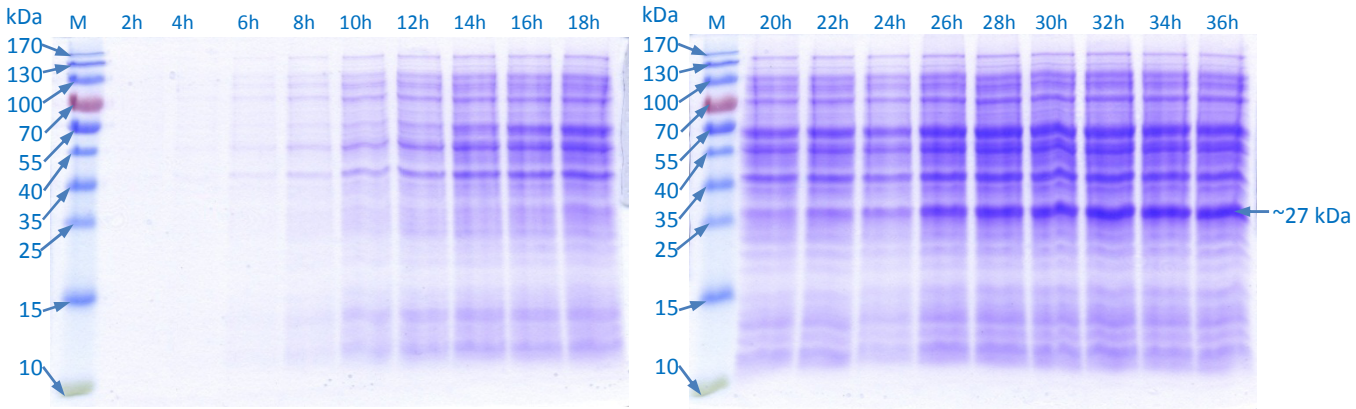

Figure 3.4: SDS-PAGE of the *Pf*TIM sample showing all protein expression over the 36 hour auto-induction study. Note: *Pf*TIM monomer is 27 kDa in size (Ray *et al.*, 1999). Lanes are labelled with the time they were harvested at and M represents lane loaded with PageRuler™ protein ladder (ThermoScientific).

The SDS-PAGE of the *Pf*TIM induction study (Figure 3.4) also shows a strong band developing at the 27 kDa size range, in accordance with *Pf*TIMs known size (Ray *et al.*, 1999). It is notable that this band is significantly weaker than that from *h*TIM (Figure 3.3), indicating a lower concentration of protein. The band also takes longer to appear, only noticeably showing up at approximately 18 hours for *Pf*TIM (Figure 3.4) as opposed to a clear presence in the *h*TIM sample as early as 4 hours into auto-induction (Figure 3.3). Both

the *h*TIM and *Pf*TIM SDS-PAGE gels were loaded with the exact same volume of sample per well and all preparation procedures were identical.

Data relating to the *h*TIM samples (Figure 3.3) are interesting because it appears that the *h*TIM gene is being expressed before induction should begin. A low level of background expression is known to occur in plasmids. However, in this case, expression also appears to be relatively strong, despite the fact that notable early expression should not occur during the auto-induction process (Studier, 2005). Considerable amounts of recombinant enzyme seem to have been produced, and concentrations continued to increase throughout the induction study (Figure 3.3). This indicates that the early expression observed did not have any negative effect on host cell growth and high concentrations of recombinant enzyme were well tolerated, without any apparent toxicity and recombinant *h*TIM retained its activity. It is also notable that *h*TIM-expressing cells were grown in the presence of kanamycin only (to retain the pET28(b+) expression vector), while *Pf*TIM samples had both kanamycin and chloramphenicol (to retain pRARE2 plasmid). This helps explain the more rapid growth and earlier expression seen for *h*TIM-expressing cultures, as compared with *Pf*TIM-expressing cultures. The *h*TIM gene sequence was also 'codon optimised' for expression in *E. coli*, while the *Pf*TIM gene was not. The *Pf*TIM gene sequence is also highly AT-rich, meaning that translated *Pf*TIM mRNA would likely suffer more rapid degradation in the host *E. coli* BL21(DE3) cells. This is because *E. coli* is known to not tolerate AT-rich genes and their transcribed mRNA very well, with the *E. coli* identifying the foreign mRNA by its 'codon bias' and degrading it rapidly (Sørensen and Mortensen, 2005).

The strong early expression seen in *h*TIM samples (Figure 3.3), prior to full induction (Studier, 2005), is an indication that *h*TIM mRNA is probably well tolerated and able to exist for a long period of time in the *E. coli* BL21(DE3) cells. By codon optimizing the *h*TIM gene, its mRNA is able to appear as a native mRNA species to the host cells and avoid destruction by the host cells (Sørensen and Mortensen, 2005). In auto-induction, typically a low background level of mRNA is produced during cell growth by an expression plasmid (in this case, pET28(b+)). This background mRNA does not usually result in significant levels of recombinant enzyme expression, primarily due to natural mRNA degradation by the host cell and especially so if the sequence is recognised as foreign. All mRNA is not created equal, however, and depending on sequence, the life span of an mRNA stand can vary from seconds to up to 20 minutes. Regulation of mRNA longevity and DNA translation to mRNA are two main methods used in cellular biochemistry for controlling protein expression (Sørensen and

Mortensen, 2005). The early recombinant *h*TIM expression (Figure 3.3) indicates that the low level background *h*TIM mRNA produced was retained sufficiently long enough to result in noticeable and significant levels of recombinant *h*TIM production, indicating that *h*TIM mRNA is long-lived. For the 'unoptimised' *Pf*TIM, on the other hand, being AT-rich, its mRNA was likely identified by the host *E. coli* BL21(DE3) cells as foreign and more rapidly degraded, meaning the *Pf*TIM mRNA, was short-lived (Sørensen and Mortensen, 2005). This is indicated by the fact that no bands corresponding to recombinant *Pf*TIM are present in Figure 3.4 prior to induction and a lower overall concentration of recombinant *Pf*TIM is achieved. This was why it was decided to only harvest recombinant *Pf*TIM after 36 hours, while *h*TIM was harvested at 24 hours, as per standard auto-induction protocol.

Once full induction occurs in the auto-induction process, massive levels of *Pf*TIM mRNA are produced and this effectively minimises any mRNA destruction effects by host cells. This is why relatively high levels of recombinant *Pf*TIM could to be achieved. This massive induced mRNA production is part of how expression plasmids, such as pET28(b+), function and are able to achieve high expression levels of any gene used with them. The effectiveness of the expression plasmid to produce massive levels of mRNA does not entirely mitigate the effects of host cell mRNA destruction and, as a result different levels of recombinant enzyme, expression is often achieved, as was the case here (Figures 3.1 and 3.2). Another possible negative effect of *Pf*TIM not being 'codon optimised', is that it can result in pauses during protein translation and elongation, when a codon triplet sequence - that requires a rare tRNA - is encountered. This possible problem was anticipated, and compensated for by the inclusion of the pRARE2 plasmid, which produces these rare tRNA's. For this reason it is unlikely that rare tRNA codon use by the *Pf*TIM gene is responsible for the lower level of *Pf*TIM expression compared to that of *h*TIM (Figures 3.3 and 3.4).

In conclusion, it is most likely that the more rapid *Pf*TIM mRNA destruction by the host cells is due to the foreign, AT-rich nature, of this gene sequence (Su *et al.*, 1996; Baca and Hol, 2000; Sørensen and Mortensen, 2005). Additional environmental strain, on the *Pf*TIM cultures, due to the presence of a second antibiotic (chloramphenicol), which was required to maintain the pRARE2 plasmid – can also partially explain the lower recombinant enzyme expression observed in *Pf*TIM expressing cultures (Figure 3.4), under otherwise identical, auto-induction expression parameters to *h*TIM expressing cultures (Figure 3.3), (Sørensen and Mortensen, 2005).

3.3.2 Purification

3.3.2.1 Ni-affinity chromatography using His-Trap FF columns

Ni-affinity chromatography was performed (Section 3.2.3). The chromatogram profiles for both *h*TIM and *Pf*TIM are illustrated in Figures 3.5 and 3.6, respectively.

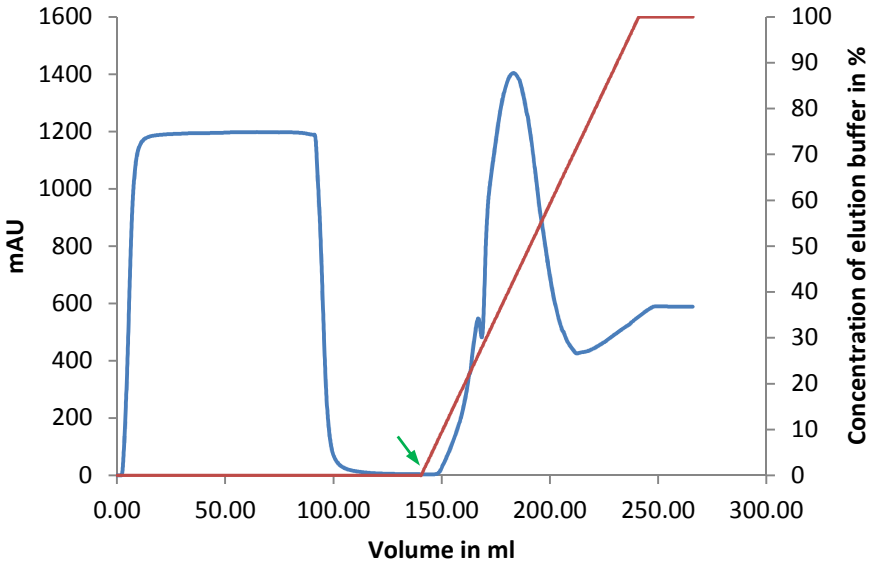

Figure 3.5: Ni-affinity chromatogram of the *h*TIM sample, showing mAU readings in blue (primary y-axis) and the concentration of the elution buffer in red (secondary y-axis) versus elution volume. Fraction collection (5.0 ml) began at the start of gradient elution (140 ml), marked with a green arrow.

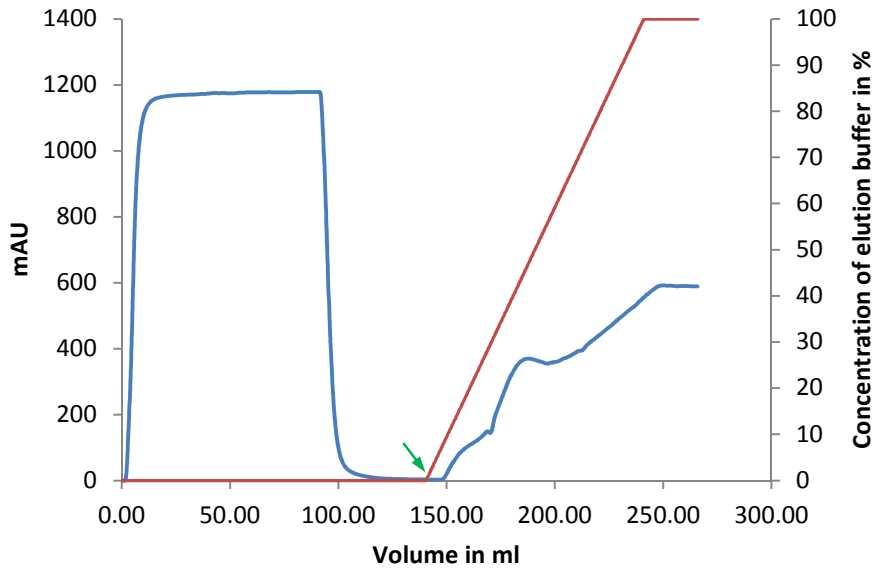

Figure 3.6: Ni-affinity chromatogram of the *Pf*TIM sample, showing mAU readings in blue (primary y-axis) and the concentration of the elution buffer in red (secondary y-axis) versus elution volume. Fraction collection (5.0 ml) began at the start of gradient elution (140 ml), marked with a green arrow.

As seen in Figures 3.5 and 3.6, it is clear from the mass Absorbance Unit (mAU) readings that substantially more *h*TIM (Figure 3.5) was obtained than *Pf*TIM (Figure 3.6). For *h*TIM the protein starts eluting when the elution buffer concentration reached ~20% and finished eluting at ~70% concentration. *Pf*TIM elution began at a slightly higher elution buffer concentration, of ~30%, and completed at ~55%. The different durations seen between the two elutions, and the differences in elution buffer starting percentage, can be attributed to the apparent large differences in concentration, indicated by the mAU response: 1403 mAU at the apex of the elution peak for *h*TIM, and only 369 mAU at the apex of the *Pf*TIM peak. Although this implies a 3.8 fold higher protein concentration for *h*TIM than *Pf*TIM, there are other factors, such as residue concentration and positioning, which influence this response. This is because UV absorbance is different for different amino acid residues and other organic compounds. Residues such as phenylalanine, tyrosine, tryptophan and histidine are therefore known to produce stronger UV absorbance readings (due to their imidazole and/or benzene rings) than other amino acid residues (Voet and Voet, 2004). Imidazole is also part of the elution buffer, further interfering with UV protein estimations. Nevertheless, the UV response gives a fairly accurate indication of protein concentration. In this case, two different variants of the same enzyme (TIM) are being compared and they therefore share a similar size and amino acid composition, meaning that UV protein estimations should be comparable. Bradford's protein assay method was used to determine protein concentrations quantitatively.

SDS-PAGE analysis for collected fractions from Ni-affinity chromatography for *h*TIM (Figure 3.7) and *Pf*TIM (Figure 3.8) are represented.

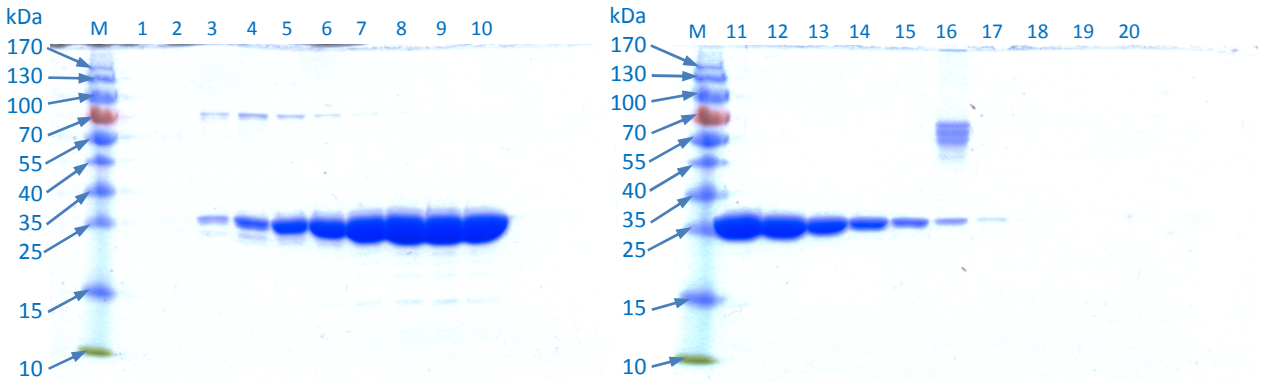

Figure 3.7: SDS-PAGE of 5.0 ml fractions (labelled 1-20) collected from the *h*TIM Ni-affinity chromatography purification.

The SDS-PAGE gels from the *h*TIM Ni-affinity chromatography (Figure 3.7) indicate strong protein bands present at ~27 kDa in size, as would be expected for *h*TIM (Orosz *et al.*, 2006). There also appears to be noticeable bands of contaminating proteins at ~70 kDa, visible in fractions 3-6, and from ~55-70 kDa in fraction 16. Fractions 4-15 (Figure 3.7) were pooled, concentrated in a spin column and subjected to gel filtration.

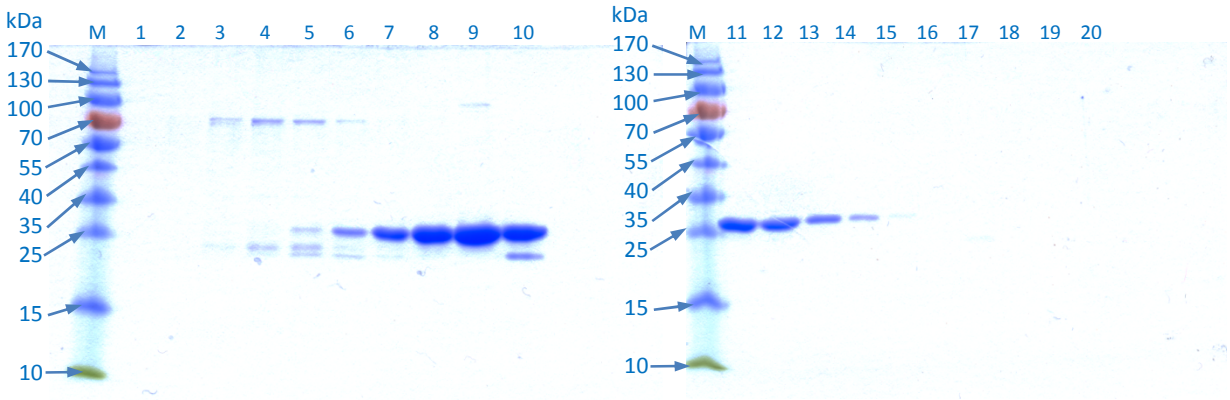

Figure 3.8: SDS-PAGE of 5.0 ml fractions (labelled 1-20) collected from the *Pf*TIM Ni-affinity chromatography purification.

For *Pf*TIM (Figure 3.8), bands at 27 kDa appear fainter than for *h*TIM (Figure 3.7), indicating that a lower concentration was obtained. Contaminating proteins appear to have eluted in fractions 3-6 (Figure 3.8). These contaminating bands in the SDS-PAGE analysis for both *h*TIM and *Pf*TIM can be explained. It is known that several *E. coli* proteins have a high affinity to divalent nickel or cobalt ions, due to the presence of clustered histidine residues and/or biological metal binding sites. These *E. coli* proteins are known to only elute at relatively high imidazole concentrations during Ni-affinity chromatography (Robichon *et al.*, 2011). Fractions 6-14 (Figure 3.8) were collected and pooled from *Pf*TIM Ni-affinity chromatography, concentrated and subjected to gel filtration.

3.3.2.2 Gel filtration chromatography on a Sephadex G-200 HR column

To further improve purification and to eliminate the imidazole introduced from Ni-affinity chromatography, samples were subjected to gel filtration chromatography using a Sephadex G-200 HR column (Section 3.2.4).

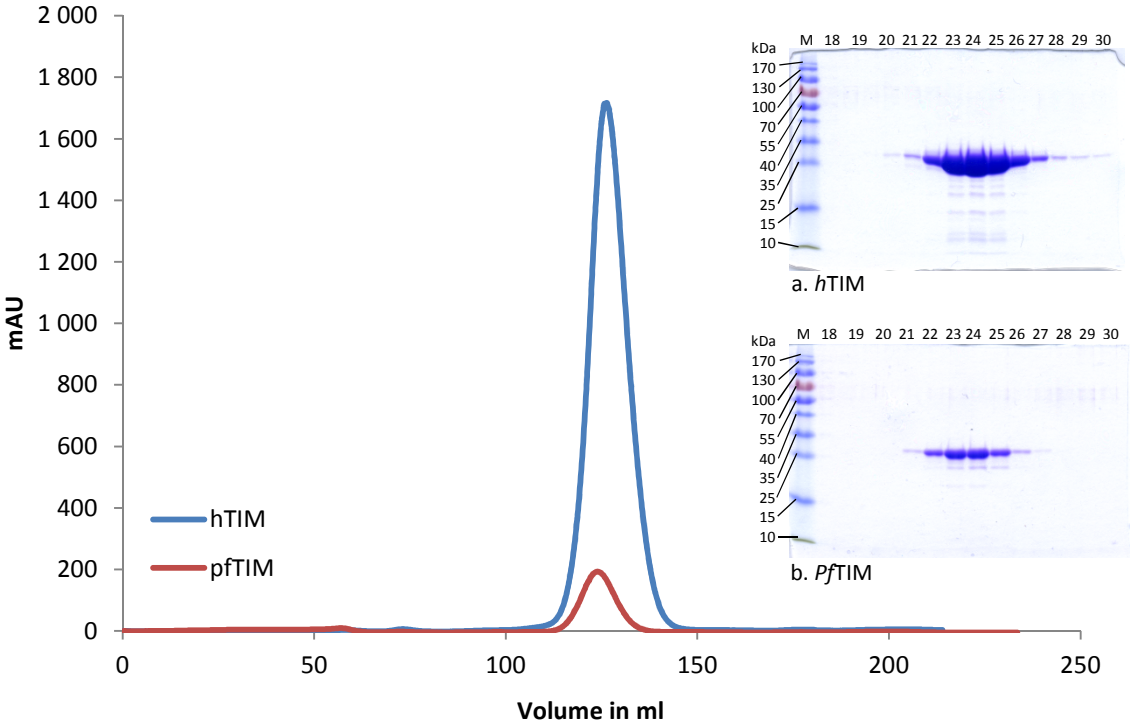

Figure 3.9: Gel filtration showing *h*TIM purification in blue and *Pf*TIM purification in red. **(a)** The SDS-PAGE of *h*TIM 5.0 ml fractions (18-30) of which (20-27) were collected for dialysis. **(b)** SDS-PAGE of *Pf*TIM fractions (18-30) of which (21-26) were collected for dialysis.

When compared to the Ni-affinity chromatography results, the gel filtration produced a very similar set of results, in terms of relative mAU readings obtained. Gel filtration was successful in eliminating some of the larger contaminating proteins, seen before (Figures 3.7 and 3.8), for both the *h*TIM and *Pf*TIM samples, respectively. Close inspection of the SDS-PAGE gels (Figure 3.9 a; b) reveals several smaller bands that co-eluted with the target protein during gel filtration. These amounted to an estimated < 1 % total protein and were only visible using enhanced SDS-PAGE de-staining procedures that are capable of visualizing as little as 25 ng of protein. It was thought that this low level of contamination would not cause any subsequent problems in terms of enzyme analysis and activity.

3.3.3 Characterisation

A final dialysis step, to remove excess salt, was performed (Section 3.2.5). Each step of the protein expression and purification procedures for *h*TIM and *Pf*TIM was then subjected to a Bradford protein determination assay (Section 3.2.7), enzymatic activity assays (Section 3.2.8) and SDS-PAGE analysis (Figures 3.10 and 3.11), which meant that enzyme concentration, activity, and the quality of the purification were assessed.

3.3.3.1 SDS-PAGE

SDS-PAGE analysis of each purification step for the *h*TIM and *Pf*TIM purifications.

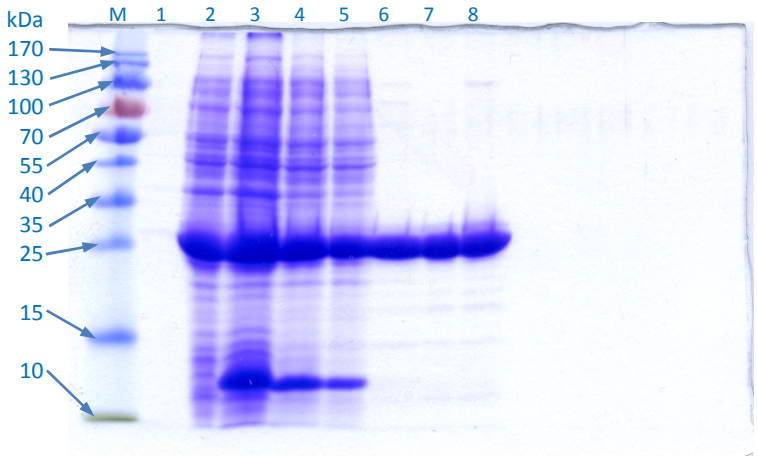

Figure 3.10: SDS-PAGE analysis of the purification steps for *h*TIM. (M) protein MW-marker, (1) extracellular fraction from auto-induction, (2) pelleted washed cells 3 x at 10000 x g centrifugations, (3) post lysis using lysozyme, (4) post 2700 x g 30 min centrifugation, (5) post ultra-centrifugation 100000 x g for 90 min, (6) post Ni-affinity chromatography pooled fraction, (7) post gel filtration pooled fraction, (8) post dialysis. NB: This fraction was stored for use in all subsequent experimentation.

As shown in Figure 3.10 the purification process proved to be successful overall, with a single dense band at 27 kDa indicating the presence of the *h*TIM in large quantities. It is clear from Figure 3.10 that the most effective step was the Ni-affinity chromatography, where most contaminating bands were eliminated. Gel filtration was also successful in eliminating some heavier proteins, which appear faintly at ~70 kDa (Figure 3.10, lane 6) and were also visible in (Figure 3.7, lane 16). It is apparent that by carefully selecting which fractions are pooled, greater purification is achieved (Figures 3.7 and 3.8). The gel filtration did not however separate some lower-weight contaminating proteins, which can be seen as faint bands at ~12-20 kDa in the post-gel-filtration products. Final confirmation about the success of the purification however, will only be proven once enzyme activity has been demonstrated.

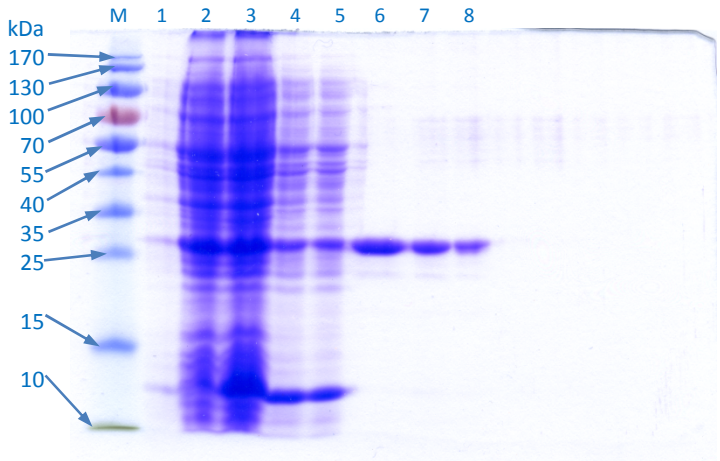

Figure 3.11: SDS-PAGE analysis of the purification steps for *Pf*TIM. (M) protein MW-marker, (1) extracellular fraction from auto-induction, (2) pelleted washed cells 3 x at 10000 x g centrifugations, (3) post lysis using lysozyme, (4) post 2700 x g 30 min centrifugation, (5) post ultra-centrifugation 100000 x g for 90 min, (6) post Ni-affinity chromatography pooled fraction, (7) post gel filtration pooled fraction, (8) post dialysis. NB: This fraction was stored for use in all subsequent experimentation.

The *Pf*TIM purification results (Figure 3.11) appear similar to that of the *h*TIM purification (Figure 3.10), however close inspection indicates the presence of a relatively thick band at 27 kDa, (target TIM size), after lysis with lysozyme, (Figure 3.11, lane 3), which becomes noticeably fainter after 2700 x g centrifugation (Figure 3.11, lane 4). It is interesting to note that at this point in the *h*TIM purification (Figure 3.10, lane 4) there is no noticeable decrease in target protein concentration and since the overall concentration *h*TIM is generally significantly higher throughout the purification process (Figure 3.10), this may indicate that *Pf*TIM is more likely to aggregate under the current purification conditions (buffer type, ionic strength and pH level). Interestingly, this is an indicator of differences in surface structure and charge at the used pH levels but, at this stage, all that can be deduced is that *h*TIM is more soluble under the given conditions than *Pf*TIM is. The 3D protein structures of these two TIM variants are already known to exhibit several key differences in amino acid sequence, protein surface structure, and residue exposure (Figure 1.7; pg. 16). These differences, interestingly, appear to have already resulted in differences during the purification of these two isozymes. Nevertheless, the two purifications produced similar results, with relatively excellent levels of purification being achieved after the Ni-affinity chromatography step.

During these purification steps it was also noted that *h*TIM samples appeared lighter (a whitish cream) in colour when compared to *Pf*TIM samples that were greyish yellow in colour. Another observation was that *h*TIM samples compacted better at 2700 x g

centrifugation (forming a denser pellet) than *Pf*TIM samples. It is not known what caused this, but it could be theorised that the additional proteins (for chloramphenicol resistance) and/or rare tRNA production, created by the pRARE2 plasmid, somehow caused the changes that resulted in these observations. Alternatively, the higher concentrations of *h*TIM protein produced in *h*TIM cultures could equally account for the observed differences and, logically, a combination of these factors should also be considered.

3.3.3.2 Protein concentration (Bradfords assay) and enzyme activity assay

Bradfords assays (Section 3.2.7) and TIM enzyme activity assays (Section 3.2.8) were performed at each step of protein purification, for both *h*TIM and *Pf*TIM samples (Bergmeyer, 1974; Bradford, 1976). Activity assay graphs are included in Appendix I.

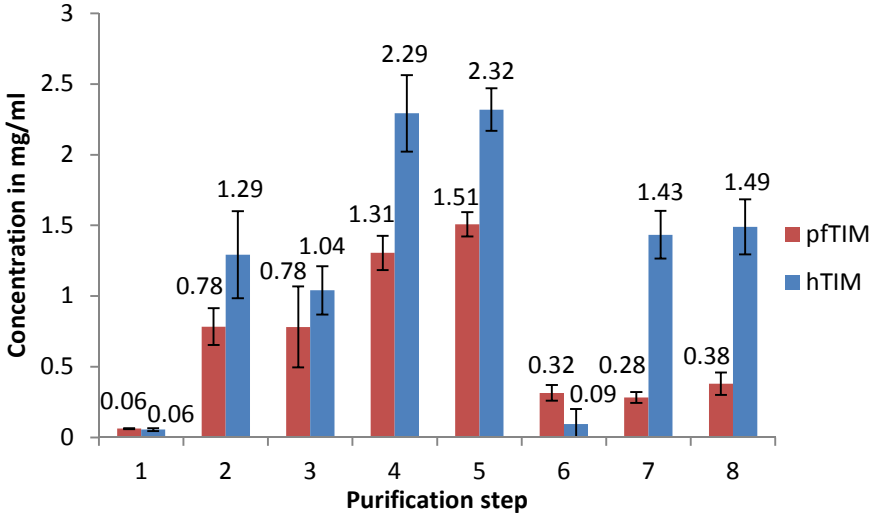

Figure 3.12: Protein concentrations for *Pf*TIM (red) and *h*TIM (blue) as determined by Bradfords assay for each purification step: (1) extracellular fraction from auto-induction, (2) pelleted washed cells 3 x at 10000 x g centrifugations, (3) post lysis using lysozyme, (4) post 2700 x g 30 min centrifugation, (5) post ultra-centrifugation: 100000 x g for 90 min, (6) post Ni-affinity chromatography pooled fraction, (7) post gel filtration pooled fraction, (8) post dialysis.

It is noted that approximately 3.9 fold more *h*TIM than *Pf*TIM was obtained, which correlates with the estimated values, based on UV mAU readings taken during purification using gel filtration (Figure 3.9). Calculated protein concentrations (Bradford, 1976) are indicated for all purification steps in Figure 3.12. Step 1 (extracellular fraction) is not technically part of the purification but was included to show that no significant amount of protein was present in this fraction, which was discarded. Concentration values determined for purification steps 2 (whole cells) and 3 (un-centrifuged lysed cells) are included (Figure 3.12) but are considered inaccurate, due to cellular debris interference with the Bradfords assay method (Bradford,

1976). These steps are not however included as part of the purification tables, because any subsequent calculated values determined using this method would be invalid and incorrect. Purification step 6 for *h*TIM (Figure 3.12) contained a noticeable precipitate, and very low protein concentration (0.09 mg/ml) was recorded. This was caused by the high concentrations of imidazole and protein present in the *h*TIM sample. This resulted in protein aggregation that could not be alleviated by sonication. The step 6 *Pf*TIM sample (Figure 3.12) had a significantly lower protein concentration and did not have any precipitate.

Separate samples were used for Bradfords assays and activity assays to eliminate any effects on activity that may have been caused by the freeze thaw process. Graphs to determine TIM activity and an example of Equation 3.1 are included in Appendix I.

The purification tables for *h*TIM and *Pf*TIM are represented as Tables 3.1 and 3.2, respectively. Note: Fold Purification = specific activity / specific activity 2700 x g centrifugation; Yield = total activity of sample / total activity 2700 x g centrifugation.

Table 3.1: Protein purification table of *h*TIM

Fraction	**Volume in ml**	**Protein ($mg.ml^{-1}$)**	**Total Protein (mg)**	**Activity ($\mu mol.ml^{-1}.min^{-1}$)**	**Total activity (U)**	**Specific Activity ($U.mg^{-1}$)**	**Fold Purificat-ion**	**Yield (T.Act/T. Act start (%)**
Crude 2700 x g centrifugation	71.5	2.29	163.7	1554.5	111147	679	1.0	100
Ultra (100000 x g) centrifugation	70.5	2.32	163.5	1531.8	107994	660	1.0	97
Ni-affinity chromatography	55 ppt'd	NA ppt'd	NA ppt'd	NA ppt'd	NA ppt'd	NA ppt'd	NA ppt'd	NA ppt'd
Gel Filtration	37	1.43	52.9	1436.8	53162	1005	1.5	48
Dialysis	35	1.49	52.1	1799.0	62966	1207	1.8	57

Important variables used to draw up purification tables are; protein concentration, enzyme activity and volume of sample, which are then used to calculate other values. Each assay used (i.e. Bradfords and enzymatic TIM assays) has an inherent margin of error, as do volume measurements. Error (standard deviation) was determined for each experiment and varied between purification steps. The determined margin of error range was around +/- 5% for both protein concentration and activity assays, and volume measurements were accurate to about 0.5 ml. The margin of error is compounded for calculations in which these three variables are used, meaning that a margin of error of +/- 10-15% is more accurate for values determined on the purification tables. Purification tables used single averaged values for practical reasons

when doing calculations and therefore do not show this margin of error. This should however be considered when inspecting purification tables. Samples taken at each purification step differed in concentration and therefore required different dilutions to obtain suitable assay ranges. Because different dilutions had to be performed, this also introduced an additional step, where error could be introduced. After completing the assays, the determined values were multiplied by their relative dilution factors. This has the disadvantage of also further multiplying any additional error that may have been introduced. Milligram levels of enzyme were obtained during both enzyme purifications (Figure 3.12). For this reason, high dilutions were needed (for example, 1/1000 and 1/2000 dilutions were used for *h*TIM enzymatic assays for gel filtration and dialysis, respectively).

In Table 3.1, the final calculated yield for *h*TIM was 57% (post dialysis) which was higher than the calculated yield of the previous step (gel filtration) at 48%. This appears to be incorrect, but this discrepancy can be accounted for if a 10% margin error for each step is assumed. Samples were all run in triplicate but it may have been better to run them in sextuplicate or even nonuplicate, so as to minimise the margin of error as much as possible.

The standard deviation margins of error for Bradfords assays are included as error bars (Figure 3.12). On inspecting these error bars across purification steps one can see that, where protein concentration seems to have changed in an unexpected manner on the purification tables, the calculated margin of error in the Bradfords assays (Figure 3.12) can account for the discrepancy. Keeping this in mind, as well as the changes in volume levels during purification, these aspects effectively account for all the discrepancies seen in the purification tables as each aspect has its own relatively small margin of error.

Table 3.2: Protein purification table of *Pf*TIM

Fraction	**Volume in ml**	**Protein ($mg.ml^{-1}$)**	**Total Protein (mg)**	**Activity ($\mu mol.ml^{-1}.min^{-1}$)**	**Total activity (U)**	**Specific Activity ($U.mg^{-1}$)**	**Fold Purificat-ion**	**Yield (T.Act/T. Act start (%)**
Crude 2700 x g centrifugation	71	1.31	93.0	268.2	19040	205	1.0	100
Ultra (100000 x g) centrifugation	70	1.51	105.7	307.7	21540	204	1.0	113
Ni-affinity chromatography	42	0.32	13.44	434.1	18232	1357	6.6	96
Gel Filtration	28	0.28	7.84	388.3	10871	1387	6.8	57
Dialysis	25	0.38	9.5	178.3	4458	469	2.3	23

Likewise, the results (in Table 3.2) for *Pf*TIM indicate that there is an increase in yield of 13% after ultracentrifugation. This is clearly not possible, but lies well within a 10% margin of error of each sample as is therefore deemed insignificant.

Analysis of the purification tables (Tables 3.1 and 3.2) indicates that a substantial amount of activity loss (more than 50%) occurred during dialysis for *Pf*TIM (Table 3.2). This level of loss was not seen for *h*TIM (Table 3.1) and is significantly greater than the 10% margin of error considered for these samples. This indicates that *Pf*TIM was not stable during dialysis under the conditions used (4°C, pH 7.4, 100 mM $KHPO_4$), while *h*TIM was. This instability was later shown to be due to a low pH tolerance of *Pf*TIM for levels above pH 6.5. The lower protein concentration of *Pf*TIM (~0.38 mg/ml) may also partially account for this instability, because proteins are generally more stable at higher protein concentrations (i.e. >1 mg/ml), (Ugwu and Apte, 2004; Link, 2008). Further details of this are revealed in Chapter 4, where each TIM variant is characterized for kinetics, pH and temperature optima, and stability.

In summarizing these results, it is clear that high concentrations of *h*TIM (1.4 +/- 0.1 mg/ml) and excellent retention of enzyme activity was achieved, with a fold purification of ~1.8 and a yield of around 50% +/- 10%. The high levels of *h*TIM obtained is the reason why a relatively low-fold purification level was achieved, because fold purification is relative to starting protein concentration and activity, which was already very high for *h*TIM, indicating that relatively excellent expression occurred for *h*TIM during auto-induction. On the other hand, *Pf*TIM samples had a fold purification level of ~6.8 and a yield of 57% +/- 10% after gel filtration. This then dropped to ~2.3 and 23% +/- 10% respectively after dialysis indicating that this purification step was unsuccessful and generally destructive, effectively reversing gains made during previous purification steps.

3.4 Conclusions

In conclusion, however, it can be said that both purifications were a success: active *h*TIM and *Pf*TIM enzymes were obtained in high concentrations that required large dilutions for enzymatic assays. In fact more than enough enzyme was obtained from a single purification to conduct all the subsequent enzymatic assay experiments a thousand times over. That said *Pf*TIM purification could have been improved if a different dialysis buffer - with a lower pH - was used for *Pf*TIM dialysis, as this would have suited its lower pH optimal stability of *Pf*TIM. This however, was only determined after these purifications and more than enough active enzyme had already been obtained at this stage.

4. Characterisation of purified enzymes

4.1 Introduction

One of the key aspects of understanding enzymatic interactions and reactions is to understand the conditions that the enzyme favours. This can be achieved by performing experiments that assess activity under variable pH, temperature and time conditions whilst maintaining other conditions in a steady state, using suitable buffers to maintain pH and ionic concentrations in a cell-like environment.

Glycolysis metabolism in *P. falciparum* is a critical energetic process to the survival of the parasite and triosephosphate isomerase is a key enzyme in this process (Parthasarathy *et al.*, 2002). The glycolysis pathway of the parasite essentially uses the same core enzymes found in almost all eukaryotes. The biochemical function of this pathway, as well as that of other essential biochemical pathways in *Plasmodium species,* however differs from the standard biochemical model. Something not commonly known about these biochemical pathways is that they have been repeatedly remodelled over the course of eukaryote evolution, to adapt to different environments (Vaidya and Mather, 2009; Ginger *et al.,* 2010). Remodelling, involving sub-compartmentalisation of parts of the ubiquitous intermediary metabolic pathways has been shown to have occurred extensively in many *Protists,* while being largely conserved in other groups, such as plants, animals and yeasts. The metabolic remodelling, or 'rewiring', seen in *Protists* can greatly influence the regulatory mechanisms that control carbon flux through the core metabolic processes (Ginger *et al.,* 2010). This metabolic compartmentalisation occurs through the acquisition of new organelles, photosynthetic plastids, or non-photosynthetic plastid-like relics such as apicoplasts, as seen in malarial parasites (Figure 4.1), (Vaidya and Mather, 2009; Ginger *et al.,* 2010; Olszewski and Llinás 2010). Through apicomplexan complex acquisitions, organisms are able to reorganise the functional nature of their metabolism on a large scale, allowing metabolic adaptations, which better suit new environments (Ginger *et al.,* 2010; Olszewski and Llinás 2010). In *Plasmodium* the glycolysis pathway is surrounded by several unexpected modes of compartmentalisation, which offer new insights and possible opportunities for drug developments (Lian *et al.,* 2009; Ginger *et al.,* 2010; Olszewski and Llinás, 2010).

Plasmodium species follow a very similar life cycle to that of *Trypanosoma* species, such as *T. brucei* and *T. cruzi,* which also depend heavily on glycolysis for energy production and

share a high genetic similarity with *Plasmodium species* (Michels, 1988; Mande *et al.*, 1994; Gómez-Puyou, 1995; Parthasarathy *et al.*, 2002). It has been suggested that the development of any selective inhibitors for one of these parasite species will likely work in a similar manner as for others, due to genetic and life cycle similarities. Thus, the targeting of key metabolic pathway enzymes has become a cornerstone for the development of new antimetabolite drugs, to target these parasites (Singh *et al.*, 2001; Parthasarathy *et al.*, 2002; Olivares-Illana *et al.*, 2007; Ginger *et al.*, 2010; Olszewski and Llinás 2010). Extensive work on tracking the carbon flux as it moves through the *P. falciparum* parasites biochemical pathways has allowed for the construction of an overall view of the parasite's unique metabolic processes. The development of such new metabolic pathways is more modular and streamlined than the metabolic pathways of free-living Protozoa (Olszewski and Llinás 2010). This new metabolic network map has recently being described, summarizing decades of work done to elucidate these processes, as illustrated in Figure 4.1 (Olszewski and Llinás 2010).

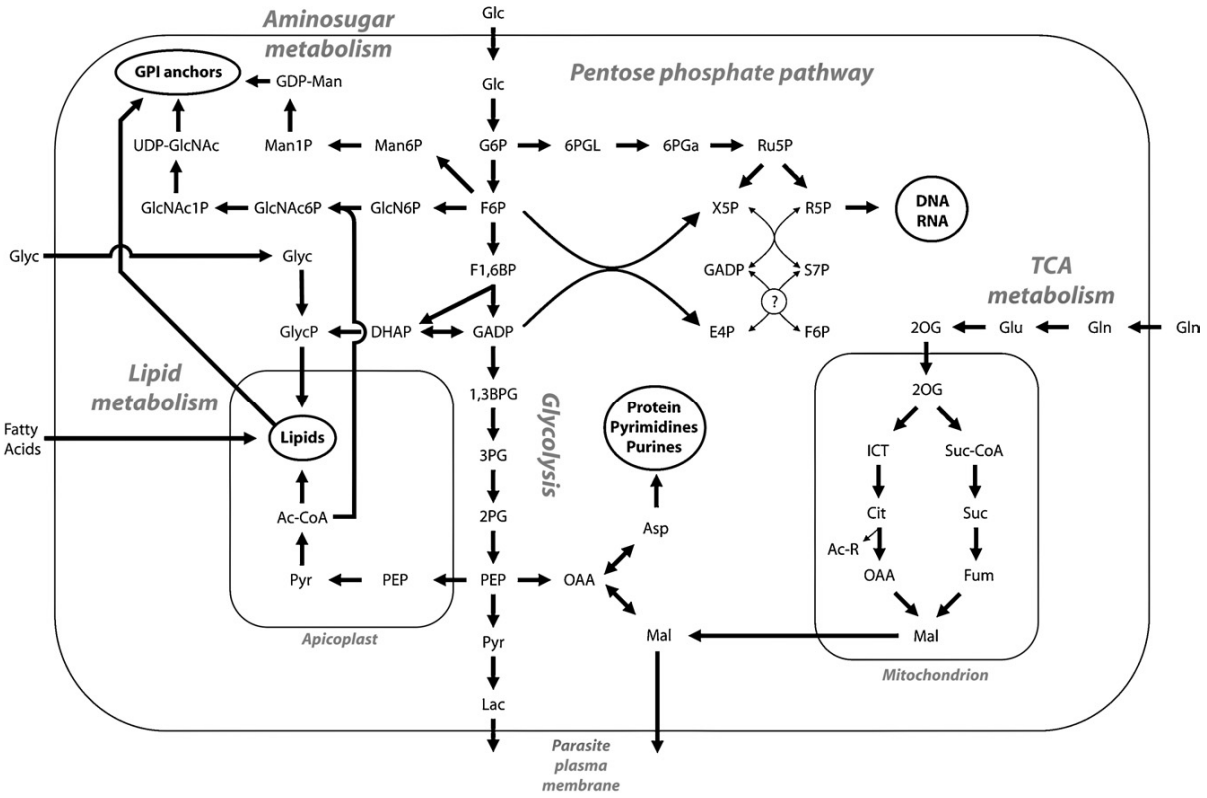

Figure 4.1: The metabolic network in *Plasmodium falciparum* in which the carbon flow and metabolism is tracked with arrows, indicating the proposed net flow of carbon during the blood-stage metabolism of the parasite. Text in circles represents major biomass components. Image taken directly from (Olszewski and Llinás, 2010).

The whole process of energy production in *P. falciparum* is unique and known to be crucial for survival. As mentioned earlier, (Section 1.3: pg. 3-6), it has long been known that the parasite does not have an active tricarboxylic acid (TCA) cycle (Velanker, *et al.,* 1997; Sherman, 1979; Miller *et al.,* 2002; Parthasarathy *et al.,* 2002; Ravindra and Balaram, 2005; Tuteja, 2007; Shekinah and Rajadurai, 2008). This, however, has been shown to be not entirely true and the situation is more complicated than was originally thought. Recent DNA evidence shows that the parasite does actually have all the necessary genes for a functioning TCA cycle. However, metabolic observation experiments have shown that something different is occurring in the *P. falciparum* TCA metabolic pathway. The early researchers showed, via electron-micrographs, that malarial mitochondria have minimal cristae and, therefore, are unable to function in a conventional sense (Trager *et al.,* 1966). The red blood cells of the host also do not possess mitochondria, eliminating the possibility of metabolic hijacking. This, along with very low observed levels of oxygen consumption, all confirms that the TCA cycle is not functional in a typical sense (Trager *et al.,* 1966; Olszewski and Llinás 2010) and implies that its absence, as stated by many researchers (Velanker *et al.,* 1997; Sherman, 1979; Miller *et al.,* 2002; Parthasarathy *et al.,* 2002; Ravindra and Balaram, 2005; Tuteja, 2007; Shekinah and Rajadurai, 2008).

More recent research into *Plasmodium spp* metabolism (Olszewski *et al.,* 2010), has shown that *Plasmodium spp* have a 'highly streamlined carbon metabolic network' (Figure 4.1) in which enzymes of the TCA cycle are present and do indeed play an important and novel 'alternative' metabolic role (Figure 4.2). The blood-stage parasite still relies almost entirely on glucose fermentation, via glycolysis, for energy production and the parasite only consumes very little oxygen, required for the TCA (Olszewski *et al.,* 2010). This is because the mitochondria of *P. falciparum* have undergone significant metabolic remodelling and a downscaling of functionality (Trager *et al.,* 1966). In fact *P. falciparum* was shown to have the smallest mitochondrial DNA sequence to date, when it was sequenced in 2009, encoding just three proteins, it has drastically reduced metabolic functionality compared to other eukaryotes (Vaidya and Mather, 2009). In spite of this *Plasmodium* mitochondrial enzymes are still considered attractive targets for antimalarial drug design (Vaidya and Mather, 2009). This reduced functioning is emphasised by the observable reduction in cristae, which are normally critical for mitochondrial functioning (Trager *et al.,* 1966; Vaidya and Mather, 2009; Olszewski *et al.,* 2010). *P. falciparum* mitochondria are thought to have originated

when dinoflagellates and apicomplexan parasites diverged from ciliates (Vaidya and Mather, 2009).

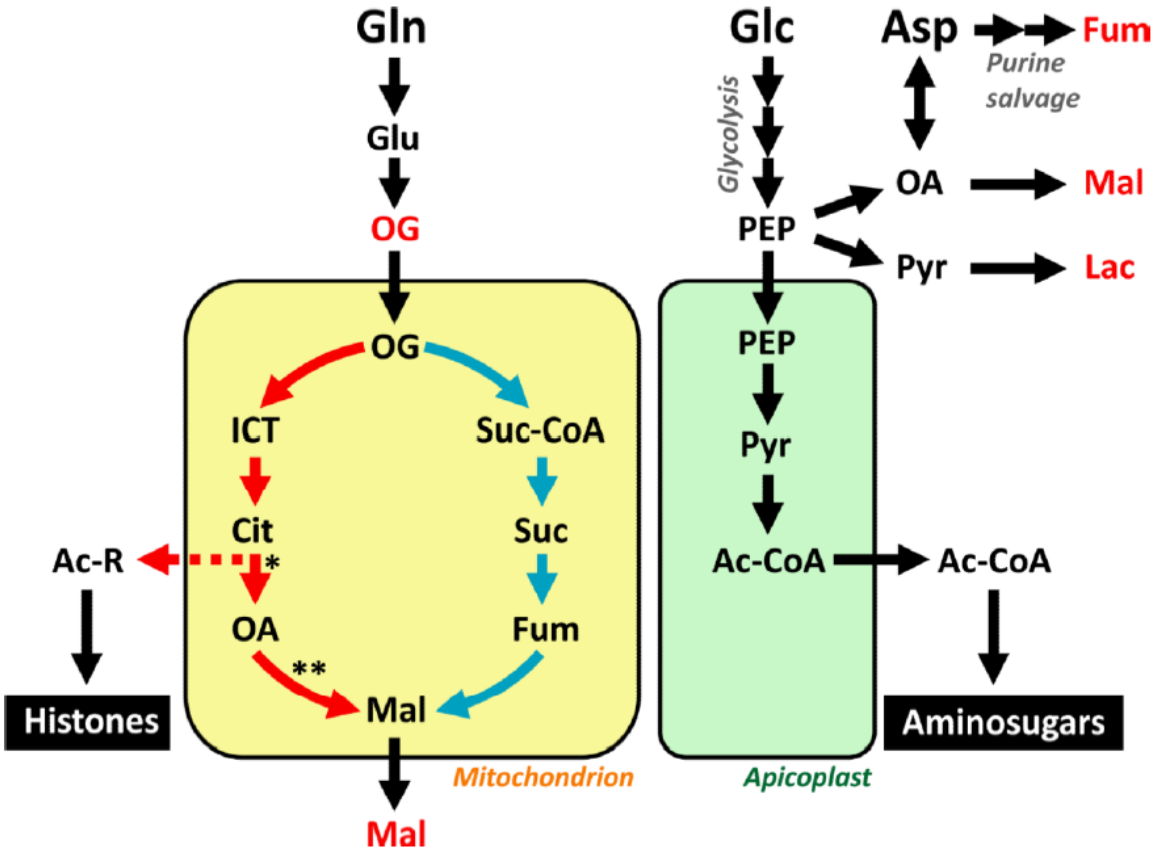

Figure 4.2: Schematic of the modified, (in red), TCA (half-cycle) of *Plasmodium falciparum*, with arrows indicating the direction of net metabolic flux. This indicates the reversal of several TCA cycle steps, to allow for the creation of Malate as a net waste product. Asterisk (*): the enzyme responsible for the citrate cleavage step and its localization are unclear; double asterisk (**): there are two predicted enzymes capable of catalysing this reaction: (1) cytosolic malate dehydrogenase (PFF0895w), and (2) putative mitochondrial malate quinone oxidoreductase (MAL6P1.258). Image taken directly from (Olszewski *et al.*, 2010).

Such metabolic rewiring and remodelling, via compartmentalisation and other changes, has also being discussed in evolutionary terms (Ginger *et al.*, 2010; Olszewski and Llinás, 2010). The parasite encodes orthologues of all the TCA cycle enzymes and they are also all transcribed during the parasites blood-stage of infection. Still other known mitochondrial TCA cycle-associated biochemical processes, such as *de novo* amino acid biosynthesis, have being disposed of and are entirely absent from the parasite, having been replaced by a new metabolic model (Olszewski *et al.*, 2010). It has also been shown that the critical metabolic function of the electron transport chain in blood-stage malaria mitochondria is not to regenerate chemical energy (its typical function) but instead to regenerate ubiquinone, to

supply the pyrimidine biosynthesis process (Painter *et al.,* 2007). Furthermore, radioactive labelling with C_{13} has shown that the TCA enzymes do not all perform as expected in blood-stage malaria, with several of the biochemical reactions optimised to run in reverse to the typical cycle, counter clockwise to the TCA cycle. This means the development of a new metabolic process for *P. falciparum* (Figure 4.2), which is different from any previously–described process (Olszewski *et al.,* 2010). This novel process, (Figure 4.2), is seen to link up with the other altered metabolic processes, (Figure 4.1), of blood-stage *P. falciparum*, note the link point is labelled 'TCA metabolism' in Figure 4.1.

The branched TCA cycle, depicted in Figure 4.2, is considered as an evolutionary trade off which has resulted in a loss of metabolic flexibility, but allows for enhanced growth in a specific environment. This trade off relies heavily on an abundant source of glucose, which is readily supplied through the host's blood stream (Olszewski *et al.,* 2010; Olszewski and Llinás, 2010). This allows for a modified mitochondrial metabolism, which uses C_5 carbon skeletons - provided from plasma glutamine - to biochemically produce ubiquinone, succinyl-CoA, and C_2 acetyl units. This has also been shown to link up with regulatory mechanisms that sense changes in the nutrient environment, for organisms that follow a diverse life style with changing nutrient availability (Olszewski *et al.,* 2010). There is also evidence that infected erythrocytes incorporate small extracellular macro-molecules for digestion too - something that does not normally occur in mature erythrocytes which are incapable of endocytosis (Burns and Pollack, 2008). It was demonstrated that *P. falciparum* parasitized erythrocytes incubated with ferritin internalised the macro-molecules, with the parasitized cells being shown to bind and incorporate ferritin and apoferritin while normal erythrocytes did not (Burns and Pollack, 2008).

The complexity and evolutionary history and specialization, described above, allows for targeted drug developments, to target the metabolic enzymes of *Plasmodium spp.* This is possible because of significant genetic changes in key, fundamentally important, biochemical pathway enzymes, such as TIM. The fundamental biochemical importance of these processes and the genetic loss of metabolic flexibility - associated with such evolutionary specializations - have created an inflexible, but optimised metabolism for the parasite (Ginger *et al.,* 2010; Olszewski and Llinás, 2010). It is this optimisation that allows for the extremely rapid growth and proliferation of the parasite during the blood stages of its life cycle. Indeed it is the rapidity of the process, which strains the host to such an extent, it is able to cause the heavy fever and anaemia that is ultimately the cause of the fatalities associated with malaria

(Miller *et al.,* 2002; Trampuz *et al.,* 2003; Tuteja, 2007). Targeting these modified metabolic pathways in the parasite is however complicated by evolutionary changes, most notably the compartmentalisations that have evolved in many *Protists* - including *Plasmodium spp* - as they adapted to their complex life cycles (Ginger *et al.,* 2010). One of the advantages that the nanotechnology approach has - is that nanoparticles, as drug delivery mechanisms - are highly mobile and known to freely travel between the various intracellular compartmentalisations, including the mitochondria, glycosomes, and even the nucleus (Jong and Borm, 2008). Nanoparticle-based drugs would therefore theoretically be able to target any metabolic enzyme, because they can move freely throughout the complex, compartmentalised, metabolic network, of malaria and other *Protist* parasites, something that conventional drugs cannot do (Jong and Borm, 2008; Ginger *et al.,* 2010). This, and the ability of nanoparticle base drugs to persist in the blood stream (Charoenphol *et al.,* 2010; Huang *et al.,* 2010; Charoenphol *et al.,* 2011) - increases the likelihood of nanodrug developments being able to target key parasite enzymes, such as TIM, in new and novel ways, giving scientists new tools to create advanced, selective and powerful antimetabolite drugs, that would also be difficult for the parasite to develop drug resistance to (Jong and Borm, 2008). This would have a strong and lasting impact on combating malaria (Jong and Borm, 2008; Ginger *et al.,* 2010; Tuteja, 2007; Vaidya and Mather, 2009).

Due to this compartmentalisation of metabolic enzymes and evolutionary re-ordering it is important to carefully characterise enzyme parameters, as these data might elucidate further understanding that aids in selective drug development aimed at targeting the *P. falciparum* variant TIM. In biochemical terms, the pH of different sub-cellular compartments and cell environments can vary noticeably. For *P. falciparum,* the life cycle of the parasite requires it to adapt to several different environments and conditions. The parasite conducts a highly catabolic biochemical digestive process in its sub-cellular compartments, even creating its own sub-cellular compartment within host red blood cells. Using digestive proteases extensively for its catabolism of host haemoglobin requires that it creates compartmentalisations for catabolic digestive metabolism (Figure 4.1), (Trager, 1966; Sherman, 1979; Entzeroth *et al.,* 1998; Wilkesman *et al.,* 2009; Olszewski and Llinás, 2010).

4.2 Materials and methods

To assess differences between the two purified TIM enzymes, parameters of pH, temperature and stability over time were tested. To establish a suitable test range for each parameter under

examination, preliminary tests were conducted by incubating the purified TIM enzymes (pH 7.0, temperature 30°C) for (3 h, 6 h and 18 h) to assess stability. Results were compared with published data of *h*TIM, *Pf*TIM and other studied TIMs (Mier and Cotton, 1970; Knowles *et al.,* 1972; Plaut and Knowles, 1972; Putman *et al.,* 1972; Sigma-Aldrich, 2012,). More tests, to analyse differences between freshly thawed and refrozen/rethawed TIMs, were also done, as to ascertain the effects of freeze-thaw cycles and to ensure that all aliquots used in characterisation tests had being subjected to the same number of freeze-thaw cycles.

4.2.1 α-Glycerol phosphate dehydrogenase assay (EC 1.1.1.8)

Alpha-glycerol phosphate dehydrogenase (αG3PDH) converts dihydroxyacetone phosphate (DHAP) into glycerol-3-phosphate (G3P), with the concomitant oxidation of NADH to NAD^+ (Figure 3.2; pg. 50). This oxidation process is used to monitor the reaction progress for both αG3PDH reactions and coupled triosephosphate isomerase reactions (Section 3.2.8; pg. 55).

The second step of the coupled assay (Figure 3.2; pg. 50) using only αG3PDH and DHAP as substrate was tested separately so as to independently determine the effects of the AgNPs on the coupling enzyme αG3PDH of the coupled TIM assay (Figure 3.2; pg. 50). The protocol used was adopted from the Sigma-Aldrich website and ultimately developed from published protocols (Beisenherz *et al.,* 1955; Bergmeyer, 1974). For reagent and buffer preparations, see Appendix B.

The αG3PDH assay, adapted from a Sigma-Aldrich assay (bulletin #: SPDHAP02), was performed in 96-well micro-titre plates as follows: DHAP (10µl, 76 mM) and NADH (10 µl, 8 mM) was mixed with TEA buffer (280 µl, 300 mM, pH 7.4) in a well (1^{st}). In a separate (2^{nd}) well, αG3PDH (10 µl, 1 U/ml) was added. The micro-titre plate was then equilibrated in a BioTek Synergy MX spectrophotometer (25°C, 5 min). Change in absorbance at 340 nm of the (1^{st}) well was measured for 2 min, at 15 sec intervals, after shaking (variably for 30 sec). This provided a baseline reading after equilibration as well as functioning as a negative enzyme control for each sample. The micro-titre plate was then ejected from the BioTek Synergy MX spectrophotometer and the enzymatic reaction initiated by pipetting 290 µl from the 1^{st} well and injecting it into the 2^{nd} well containing the 10 µl of αG3PDH. The micro-titre plate was then shaken (variably, for 30 sec) and the change in absorbance recorded (340 nm, 15 sec intervals, 10 min).

The progress of the reaction was monitored by the depletion of NADH, which is explained mathematically in Equation 3.1 (pg. 56) (Sigma-Aldrich, bulletin #: SPDHAP02). Further details about the optimisation of this assay are presented (Appendix B).

4.2.2 pH

For the pH study a buffer cocktail was prepared using zwitterionic 'Goods' buffers. These buffers exhibit highly similar characteristics and are homologous to each other, making them excellent for pH studies (Link, 2008). The buffer cocktail covered the pH range from pH 3.5 to 9.0 in 0.5 pH-level increments over 12 individually-prepared buffers. For details on buffer preparation, see Appendix B.

The pH study was conducted at 25°C using a BioRad® heat block, with readings taken at 0, 15, 45, 75, 105, 135 and 180 minutes, to evaluate stability at different pH levels. For this study, serial dilutions, to obtain *h*TIM and *Pf*TIM in suitable assay concentrations, were set up in a 2 ml tube, using the pH buffer being tested.

Once both TIM enzymes were diluted to effective assay concentrations in a 2 ml tube and mixed at a test pH level, an immediate (T0) sample was taken for assay in triplicate. All other necessary reagents for these assays were prepared in advance, so that assays could be recorded immediately. The remaining TIM sample (in 2 ml tubes at test pH levels) were incubated on a BioRad® heat block, (25°C) until the next set of samples were taken for assay. Pipetting out of micro-titre plates was done during the interim between assays. This ensured that the reagents in the plates were not left standing for more than 5-10 min. For assay details see Section 4.2.4.

4.2.3 Temperature optimum study

The temperature study was conducted at 20°C, 25°C, 30°C, 35°C, 45°C, 55°C and 65°C, at optimum pH 5.25 (0.1 M potassium acetate buffer) for *Pf*TIM and pH 6.75, (0.1 M potassium phosphate buffer) for *h*TIM. The assay procedure is detailed in (Section 4.2.4). BioRad® heat blocks (2.0 ml) were used pre-heated to the desired temperatures. To obtain a temperature of 20°C, (i.e. below room temperature), the heat block was placed in a 4°C walk in fridge and set to maintain its temperature at 20°C. Buffer aliquots in 2 ml tubes were prepared in advance and pre-incubated at the set temperatures for approximately 20 min before the TIM enzyme dilutions were made. This ensured that at T0 and T15 recording times the TIM enzymes had being subjected to the desired temperatures indicated for the full duration

intended, eliminating any heating 'lag' that may have occurred in the 2 ml volume in the tubes.

4.2.4 Assay protocol for pH and temperature stability studies

This assay was the same as the TIM assay (Section 3.2.8; pg. 55). However, some procedural differences had to be incorporated (see Appendix J), for pH and temperature tests to run systematically. Using these values, a relative % activity level was determined for each pH and temperature so that the optimums could be determined. These tests were run concurrently on the same day using the same dilutions and same perishable reagents, such as NADH preparations that were always prepared fresh. The pH and temperature study samples were only directly compared with negative control samples that were setup in an identical manner as test samples and run concurrently with these studies. This ensured that the relative percentage activity levels calculated for the studies were valid, comparable and as accurate as possible. The relative percentage activity levels could then be used to objectively compare the different TIM samples to observe the relative effects.

4.2.5 Kinetics study

The kinetic properties, namely the Michaelis-Menten constant (K_m) and the maximal enzyme velocity (V_{max}), were determined by varying the assay at the following substrate concentrations: 0.25, 0.5, 0.75, 1.25, 2.5, 5.0, 7.5 and 10.0 mM of DL-GA3P. Kinetic parameters were calculated using three methods, namely the Lineweaver-Burk and Hanes-Woolf plots and a non-linear regression - considered the most accurate (Greco and Hakala, 1979). All these plots employ variations of the Michaelis-Menten equation indicated below (Equation 4.1).

Equation 4.1: Michaelis-Menten equation

$$v = V_{max}.[S]/(K_m+[S])$$

Kinetics assays are different to the standard TIM assays done in (Section 3.2.8; pg. 55), because kinetics assays use varying substrate concentrations, so the following adjustments had to be made. In the 1st well the following is added: NADH (10 µl, 8 mM), αG3PDH (10 µl, 40 U/ml), DL-GA3P (50 µl, varying concentrations) and TEA buffer (230 µl, pH 7.6). In the 2nd well, TIM (10 µl) is added in a suitably diluted concentration described previously (Section 3.2.8). The micro-titre plate is then pre-incubated (5 min, 25°C) and change in absorbance (340 nm, 2 min) monitored.

After the 5 min pre-incubation, to equilibrate, the plate was placed in a BioTek Synergy MX micro-titre plate (25°C) and shaken for 45 sec. The kinetic readings of the 1st well were recorded (21 sec intervals, 2 min, 340 nm) - note recording intervals also had to change due to the fully used micro-titre plate. 290 µl from the 1st well was pipetted into the 2nd well containing the 10 µl of TIM (*Pf*TIM or *h*TIM). The tray was then pulled back into the system and shaken variably for 17 sec and kinetics recorded (340 nm, 21 sec intervals for 10 min).

The linearity of NADH was also tested which constituted another form of a control (Appendix H, Figure H3). Additional details and calculations are given in Appendix J.

4.3 Results and discussion

4.3.1 pH

The pH study readings from 45 min incubations were taken, to determine pH optima, as these samples showed the greatest level of contrast. The following graphs (Figure 4.3) show the relative percentage activity of *h*TIM and *Pf*TIM versus pH. Converting enzymatic activity levels to relative percentage activity allows for side-by-side comparison of *h*TIM and *Pf*TIM.

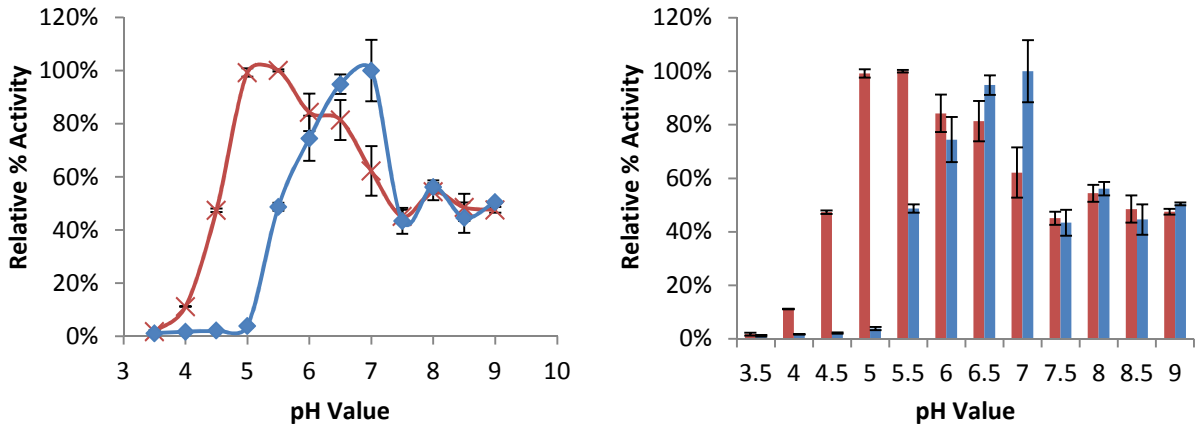

Figure 4.3: Comparative pH study data for the T45 min incubation period at varying pH levels for both *Pf*TIM (red) and *h*TIM (blue). All pH tests done in triplicate and error bars calculated using standard deviation. See Appendix K for, in assay, activity levels at each pH and time frame.

These data (Figure 4.3) indicate a clear preference of *Pf*TIM (red) for lower pH levels, with a pH optimum between pH 5.0 and 5.5. The *Pf*TIM also appears to have a wider range of an acceptable >50% level of activity, represented by a greater area under the curve. For *h*TIM, (blue) the pH optimum is between pH 6.5 and 7.0, with a sharp decline between pH 7.0 and

7.5. This corresponds with the homeostatic controlled environment that *h*TIM can operate in, while *Pf*TIM may often exist in a less stringently controlled environment throughout its life cycle (Olszewski and Llinás, 2010). These pH optima levels for *h*TIM correspond well with the literature regarding TIMs of yeast, rabbit (Sigma-Aldrich 2012) and others (Plaut and Knowles, 1972; Gracy, 1975; Orosz *et al.*, 2006) while the pH optimum for *Pf*TIM seems to diverge from most known TIM pH optimum levels.

Both enzymes still had almost 50% relative activity remaining at pH 9.0 and could therefore have been tested at even higher pH levels. Other information in the literature however indicates that this point (pH 9.0) is typically a drop-off point for TIM, where activity rapidly declines to zero (Veech *et al.*, 1969; Plaut and Knowles, 1972). Graphs for all pH tests with recorded activity levels, instead of relative % activity, are included in Appendix K.

After careful inspection the pH optimum for *Pf*TIM was selected as pH 5.25 and that for *h*TIM was pH 6.75. The next series of experiments, to find temperature optimums, made use of buffers configured for these pH values.

4.3.2 Temperature study

As was the case for the pH study, the temperature study readings from 45 min tests had the greatest contrast and were used to determine temperature optima. These data were used to determine relative percentage activity for each temperature (Figure 4.4). A full breakdown of all temperature tests and their recorded activity levels is available in Appendix L.

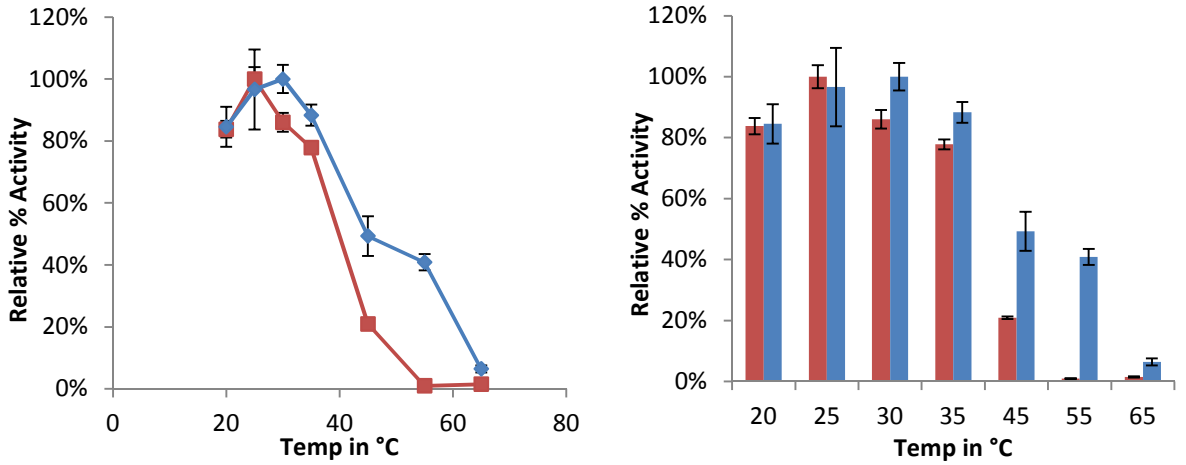

Figure 4.4: Temperature study data indicating relative percentage activity of *Pf*TIM (red) and *h*TIM (blue) over temperatures from 20°C to 65°C. For activity graphs of all test times, see Appendix L.

As was seen for the pH studies, these temperature data (Figure 4.4) indicate clear differences in the thermal stability of *Pf*TIM and *h*TIM. For *Pf*TIM, a temperature optimum at a relatively low 25°C, a rapid drop off in activity from 35°C to 45°C and complete enzyme inactivation at 55°C and above. This is interesting as one might speculate that the temperatures experienced by the *P. falciparum* parasite, within the mosquito environment, could vary greatly due to the relatively large surface area to volume ratio of the tiny insect, possibly requiring this low optimum at cooler times such as night time. Malaria mosquitoes and the parasite *P. falciparum* are only known to occur in warmer climates, mostly within the tropics where the mosquitoes come out in the evenings when it's somewhat cooler, around 20-30°C. Within the human host the parasite experiences a well regulated homeostatic temperature of 37°C (Kaiser *et al.*, 2003).

The *h*TIM seems to be more stable in higher temperature environments: incubation, even at temperatures of (55°C; 45 min), still had over 40% relative activity remaining (Figure 4.4). This ability to handle higher temperatures emphasises that *h*TIM is adapted to be stable within the human body at 37°C for significantly longer periods of time than tested, as would be expected. *Pf*TIM, on the other hand, appears to be operating at its upper thermal limit at 37°C within the human body. This implies that it is not fully optimised to operate at human body temperatures and tends to prefer a room temperature environment of around 25°C. The evolutionary requirement of the parasite's *Pf*TIM - to be able to conduct energy production via glycolysis within the human host - can however be said to be satisfied by these temperature data. These data indicate that *Pf*TIM is not well adapted to temperatures greater than human body temperature, with rapid activity loss occurring over 40°C. Considering these data, in conjunction with the complex life cycle of the parasite - which requires it to be able to function and survive in a small mosquito at low temperatures at night and in a warm host at a constant 37°C - these data support the notion that the parasite enzyme (*Pf*TIM) is adapted for flexibility and has not become optimised to any specific environment. This is in accordance with literature, which indicates that adaptations of life to suit a new-niche environment that is different to the standard one do not become fully optimised in such an environment (Miller *et al.*, 2002; Painter *et al.*, 2007; Tuteja, 2007; Ginger *et al.*, 2010; Olszewski and Llinás, 2010).

Stability at optimum pH and temperature was also tested for up to 3 hours and, under optimal conditions, there was no observed loss in activity between incubated samples and freshly thawed samples. These data are shown in Appendixes K and L.

4.3.3 Kinetics study

A kinetics study was prepared and performed as described (Section 4.2.5). To evaluate results Hanes-Woolf and Lineweaver-Burk plots were drawn and a non-linear regression performed, to determine the most accurate possible K_m and V_{max} values, using the Michaelis-Menten equation (Equation 4.1) and the solver in MS Excel, to find the minimum sum of the difference of squares between recorded data and Michaelis-Menten-modelled data by iteratively altering the values of K_m and V_{max} and checking against the sum of the difference of squares for the lowest value. This method, while computationally intense, is known to be considerably more accurate, for determining K_m and V_{max} values, than the Hanes-Woolf and Lineweaver-Burk plots (Greco and Hakala, 1979). Further details are included in Appendix M.

For *h*TIM, Lineweaver-Burk and Hanes-Woolf linear plots are shown (Figure 4.5) and a Michaelis-Menten curve, including the non-linear regression 'best fit' curve, is shown in Figure 4.6. The equations used to determine K_m and V_{max} values from these plots and the mathematical methodology for the non-linear regression, with examples, are included in Appendix M (Equations M1, M2 and M3).

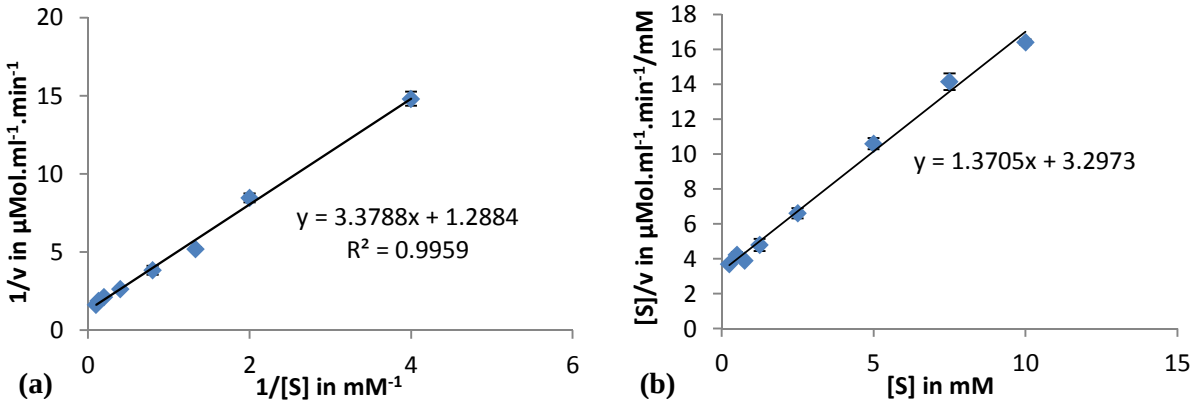

Figure 4.5: The Lineweaver-Burk plot (a), and Hanes-Woolf plot (b) for enzyme kinetics experiments done on *h*TIM samples (n=3) with error bars calculated using standard deviation. The linear equations of these plots were used to determine K_m and V_{max} values with the aid of Equations M1 and M2, see Appendix M for calculations.

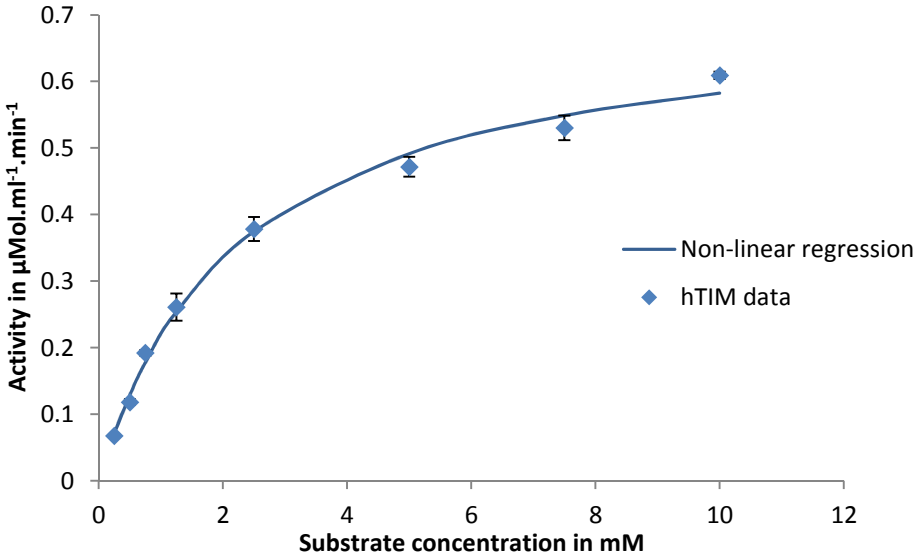

Figure 4.6: Michaelis-Menten curve showing the *h*TIM kinetic data points with error bars calculated using standard deviation, and the curve calculated from the K_m and V_{max} values, determined by non-linear regression computation and plotted using the using the Michaelis-Menten equation (see Equation 4.1).

As can be seen for *h*TIM (Figure 4.6) the non-linear regression line fits actual data on the Michaelis-Menten curve exceptionally well. Good correlation between the non-linear regression method results and the Hanes-Woolf data indicates strong and robust kinetics experiment data were obtained for *h*TIM samples.

Similarly K_m and V_{max} values were also calculated for *Pf*TIM, Lineweaver-Burk and Hanes-Woolf plots are shown in Figure 4.7 and the Michaelis-Menten plot with non-linear regression 'best fit' curve shown in Figure 4.8.

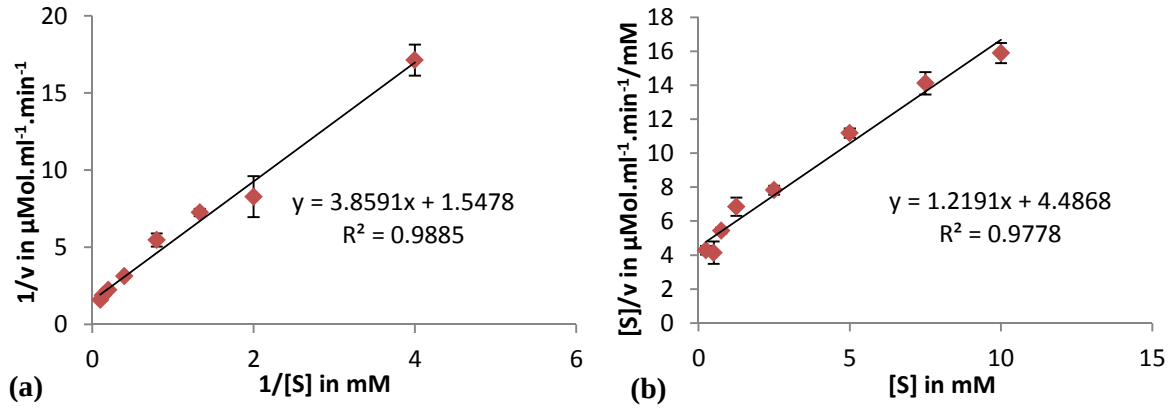

Figure 4.7: The Lineweaver-Burk plot (a), and Hanes-Woolf plot (b) for enzyme kinetics experiments done on *Pf*TIM samples (n=3) with error bars calculated using standard deviation. The linear equations of these plots were used to determine K_m and V_{max} values with the aid of Equations M1 and M2, see Appendix M for calculations.

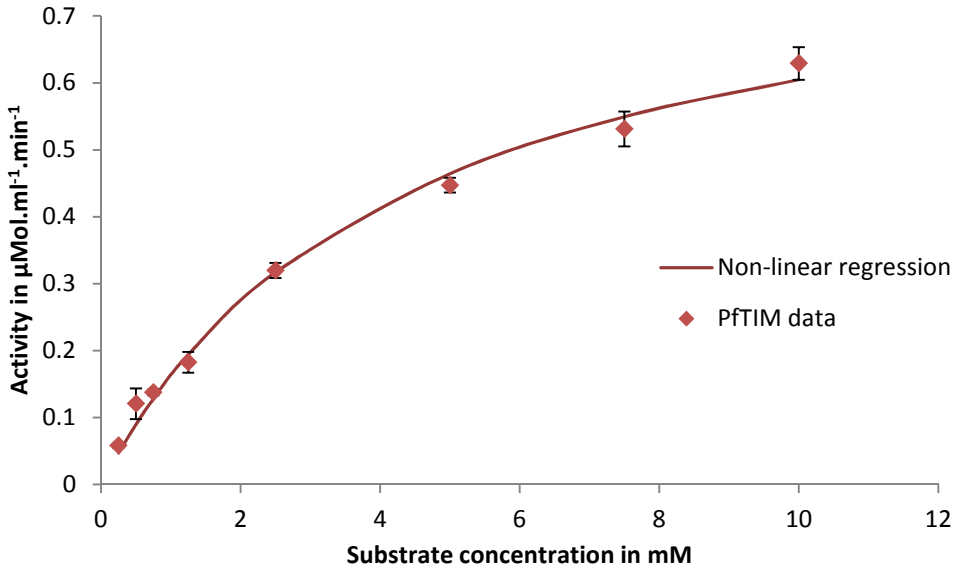

Figure 4.8: Michaelis-Menten curve showing the *Pf*TIM kinetic data points with error bars calculated using standard deviation (n=3), and the curve calculated from the K_m and V_{max} values determined by non-linear regression and plotted using the using the Michaelis-Menten equation (see Equation 4.1).

The equations used to determine the kinetics values were identical for both the *h*TIM (Figures 4.5 and 4.6) and the *Pf*TIM (Figures 4.7 and 4.8) samples. Results of these calculations and additional details including the calculations used to determine the K_{cat} and K_{cat}/K_m values (presented in Table 4.1) are provided with examples in Appendix M - see Equations M 1, 2, 3 and 4.

Table 4.1: Kinetic parameters calculated from the three graphical plots, Lineweaver-Burk, Hanes-Woolf and Non-linear regression using Michaelis-Menten (Figures 5.9 to 5.12). Analysis of *human* and *Plasmodium falciparum* TIM enzymes, units under each parameter.

Plot Type and Sample	***Homo sapiens* TIM**				***Plasmodium falciparum* TIM**			
Variables	K_m (mM)	V_{max} (µmol.ml^{-1}min^{-1})	K_{cat} (min^{-1})	K_{cat}/K_m (Mol^{-1}.min^{-1})	K_m (mM)	V_{max} (µmol.ml^{-1}min^{-1})	K_{cat} (min^{-1})	K_{cat}/K_m (Mol^{-1}.min^{-1})
Line-weaver Burk	2.62	0.7762	2.81×10^4	1.07×10^7	2.49	0.6461	1.38×10^4	5.54×10^6
Hanes-Woolf	2.41	0.7297	2.64×10^4	1.10×10^7	3.68	0.8203	1.75×10^4	4.76×10^6
Non-linear Regression	2.27	0.7148	2.59×10^4	1.14×10^7	4.34	0.8671	1.85×10^4	4.26×10^6

Values from the linear plots, Lineweaver-Burk and Hanes-Woolf plots correlate well for *h*TIM data (Figure 4.5a and b). Correlation between the different mathematical linearization

methods, which skew the results in different ways, indicates that accurate data was obtained for the *h*TIM assays (Greco and Hakala, 1979).

Of the linear plots, the Hanes-Woolf plot is considered the most accurate; however, the Lineweaver-Burk is useful for distinguishing different types of inhibition and is included for this reason. The Hanes-Woolf plot is also used as a comparison for values obtained from the non-linear regression method, which is not a linear plot but considered to be the most accurate of all methods for determining kinetics, due to is ability to exhaustively find the 'best fit' Michaelis-Menten curve. It also serves to act as a control to assess if calculations were done correctly as well as offering an alternative method (Greco and Hakala, 1979).

From Table 4.1 it can be seen that the K_m values obtained from the different methods for *Pf*TIM show significant variation, which is notably higher for *h*TIM data. This indicates that the *Pf*TIM data are not as consistent or as accurate as the *h*TIM data. This is also indicated by observing that the error bars for *Pf*TIM samples are noticeably larger (Figures 4.7 and 4.8). The V_{max} values for *Pf*TIM samples are more consistent, especially for values determined by Hanes-Woolf and non-linear regression. Lineweaver-Burk values should be excluded from consideration because, as stated, this plot was primarily included for its ability to aid in identifying different types of inhibition, and not for its accuracy.

The non-linear regression data were used to extrapolate the Michaelis-Menten curve to very high (80 mM) substrate concentrations that would be practically impossible to test. This was done so that the two TIM enzymes could be compared 'side-by-side' on a Michaelis-Menten plot that had suitably high substrate concentrations, to approach V_{max} (Figure 4.9). These data indicate that the kinetics of the two enzymes *h*TIM and *Pf*TIM have noticeably different profiles, with noticeably different K_m and V_{max} values. The kinetics experiments were sensitive, effective and capable of producing the quality of data necessary for identifying differences in the kinetics of these two TIM variants under identical running conditions.

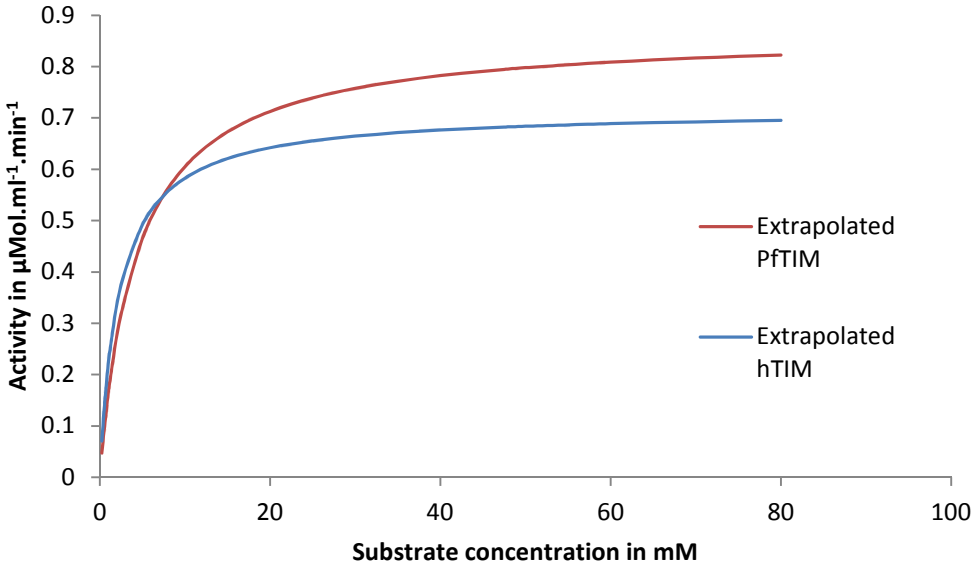

Figure 4.9: Michaelis-Menten curves showing the extrapolated data for both *Pf*TIM (red) and *h*TIM (blue) using non-linear regression determined values and the Michaelis-Menten (Equation 4.1) to determine the shape curves.

The extrapolation indicates that substrate concentrations of around 60 mM to 80 mM may have being required to show over 90% of the full Michaelis-Menten curve, while to show 100% of the curve is literally impossible. Given the constraints associated with purifying the substrate DL-GA3P – which is a structural isomer of DHAP – it can be concluded that these kinetic tests were well optimised because achieving a maximum substrate concentration of anything over 15 mM would be experimentally difficult and not necessary. For inhibition experiments with AgNPs (Chapter 5) all kinetics had to be repeated because the negative controls (with no nanoparticles) still had to have the nanoparticle stabilizing mixture (PVP and EtOH) included in the negative controls. For this reason the kinetics data shown here cannot be compared with the inhibition kinetics data of Chapter 5. The experiments were also conducted on different days using different preparations of buffer, NADH, substrate and enzyme dilutions. For maximum accuracy these were always prepared on the day of any particular comparative experiment and the experiments run concurrently, to ensure identical running conditions.

4.4 Conclusions

This chapter has outlined the methodologies and experiments used to characterise the two TIM enzymes (*h*TIM and *Pf*TIM) being investigated. Subsequently, it has been revealed that *h*TIM has a pH stability optimum ranging from pH 6.5 to pH 7.0, a thermal stability optimum of approximately 30°C, and enzymatic kinetic parameters of K_m 2.27 mM and V_{max} 0.7148

μMol.ml^{-1}.min^{-1} and K_{cat} 2.59 x 10^4 min^{-1}, as determined by a non-linear regression method. Similarly it was shown that *Pf*TIM has a pH stability optimum ranging between pH 5.0 and pH 5.5, a thermal stability optimum of approximately 25°C, and enzymatic kinetic parameters of K_m 4.34 mM and V_{max} 0.8671 μMol.ml^{-1}.min^{-1} and K_{cat} 1.85 x 10^4 min^{-1}. Due to enzyme inactivation, however, it is not known what portion of the measured TIM enzyme concentration (in mg) was active or inactive, although these data indicate that, after purification, more *Pf*TIM was inactive than was the case for *h*TIM. In conclusion, the characterisation experiments were successful, spotting a rapid thermal drop-off in activity of *Pf*TIM (above 45°C), as well as a clear inclination for *Pf*TIM to favour significantly lower pH values (pH 5.0-5.5). When this is considered in conjunction with our knowledge of the *P. falciparum* metabolic processes using subcellular compartmentalisation (Figure 4.1) along with the catabolic nature of the parasite's life cycle with regard to consuming red blood cell haemoglobin (Miller *et al.,* 2002; Trampuz *et al.,* 2003), it is not really surprising that a low pH environment is favoured, as such an environment is generally useful for digestive processes (Painter *et al.,* 2007; Ginger *et al.,* 2010; Olszewski and Llinás, 2010; Vaidya and Mather, 2009).

5. Nanoparticle synthesis, characterisation and TIM interactions

5.1 Introduction

Nanoparticle technology has advanced rapidly in recent years and the possibility of using nanoparticles as functionalized, nanotechnology-derived, integrated drug development systems is now a reality. This approach involves customising the functional and chemical properties of nanoparticles using modern nanotechnology techniques. The nanoscale systems that can be ultimately obtained through such customizations are seemingly limitless and have the ability to satisfy the highly specific and difficult set of biochemical properties demanded for use as modern nanodrugs. The recent release of such nanodrug systems (Hrkach *et al.,* 2012; Sheridan, 2012) demonstrates the importance and versatility of this methodology. Success is dependent on the ability of the nanodrug 'nanoparticle system' to achieve the desired biochemical properties of decreased host toxicity and increased specificity to target cell lines or locations. Advanced targeting methods, using nanoparticle functionalization, is a key aspect of this and is what allows for lower overall dosage levels to be achieved, by employing highly specific targeting, to localise the nanodrug to target areas. This limits body-wide drug damage while also preventing or limiting side effects associated with high drug dosage (Guzmán *et al.,* 2008; Rana *et al.,* 2010). Another important aspect of nanoparticle systems as drug delivery 'vessels' is that the key nanoparticle is able to persist in the body longer than is the case for conventional drugs, typically resulting in decreased catabolic destruction of active compounds (Kholoud *et al.,* 2010; Rana *et al.,* 2010). This is due to the alien nature of nanoparticle systems, which makes it difficult for host biochemical processes to handle and process. Long-term effects of using nanoparticle systems are however still widely unknown and a complete understanding of all possible nanoparticle system interactions are difficult to establish and are not currently fully understood.

Extensive research in this field is still required and already well underway, with some recent studies showing promise (Rana *et al.,* 2010; Sheridan, 2012). Several nanoparticle-based drugs have been developed and some are already being used to treat various cancers. Still more are currently in drug trials, with promising results (Sheridan, 2012). With an increasing number of NP-development and customisation techniques being discovered, nanosystems represent a new approach in drug development with ever-increasing advanced capabilities.

5.2 Materials and methods

Subsections here outline the protocols used to develop, characterise and interact silver nanoparticles with the two TIM enzymes being studied.

5.2.1 Silver nanoparticle preparation and characterisation

To obtain silver nanoparticles, a 0.1 M solution of $AgNO_3$ was prepared and 0.2 ml of this solution was then added to 9.8 ml of absolute (95%) ethanol (EtOH) with 0.1 g of polyvinylpyrrolidone (PVP). The solution was then mixed and placed into a 25 ml Erlenmeyer flask, covered with cotton wool, and microwaved (800 W, 5 sec) in a Sharp 800 W microwave. After removal from the microwave, the solution had a pale yellow tint, indicating the formation of silver (Ag) nanoparticles (Pal *et al.,* 2009). Samples were left overnight at room temperature to allow for AgNP seed growth. This process was monitored by performing wavelength scans (300-700 nm) in a Synergy MX spectrophotometer. Microwave heating rapidly creates high temperature zones or 'micro-pockets' throughout the solution, which aids in small- and nano- particle creation (Liu *et al.,* 2005) while PVP works as a stabilizing agent, functionalising the nanoparticles and ensuring that they are mono-dispersed and remain highly soluble.

Nanoparticles were also assessed by Transmission Electron Microscopy (TEM), using a Zeiss Libra 120 TEM, with imaging done at different times to assess particle growth, size, shape, distribution, stability, and whether aggregation was occurring over time. All NP samples were stored wrapped in tinfoil, to limit light exposure for at least 1 day, so that seed growth could occur prior to TEM imaging.

5.2.2 Evaluation of the effect of AgNPs on αG3PDH

To test AgNP effects on the αG3PDH coupling enzyme, the following assay experiment was conducted using dihydroxyacetone phosphate (DHAP) as substrate. This represents the second part of the coupled TIM assay (Chapter 3, Section 3.2.8; pg. 55).

An assay series, using final AgNP concentrations of 0, 20, 40, 60, 80, 100, and 150 µM, was performed in triplicate. AgNP negative controls, using only PVP and EtOH in equivalent dilutions to that of the 150 µM AgNP sample, were also performed, as well as a full negative control using the standard assay protocol. The full negative control was then used as the reference sample to calculate relative percentage activity. These data were then used to determine the effect of AgNPs on αG3PDH, covering an effective inhibition range from 0-100%.

The assay for this experiment was performed in a slightly different manner to that previously described, because in this case the assay is designed to replicate the TIM assay, where the AgNPs are part of the 5 min pre-incubation. To replicate this, the reaction was initiated by the addition of substrate (DHAP) instead of enzyme (αG3PDH).

Using a 96-well-plate: In a 1st set of wells the following solutions were added: NADH (8 mM, 10 µl), αG3PDH (1 U/ml, 10 µl), TEA buffer (280 µl, pH 7.4), with relevant AgNP concentrations to obtain final AgNP 'assay concentration levels' of 0, 20, 40, 60, 80, 100, or 150 µM. In the 2nd set of wells; DHAP (76 mM, 10 µl) was added. Pre-incubation was performed (25°C, 5 min) and then the pre-assay change in absorbance was monitored (2 min, 340 nm, 15 sec intervals). After which 290 µl from the 1st wells was pipetted into the 2nd wells – initiating the assay – and the decrease in absorbance for the assay was monitored (10 min, 340 nm, 15 sec intervals), (Beisenherz *et al.*, 1955; Bergmeyer, 1974).

5.2.3 TIM and AgNP incubations under optimum conditions

Using optimum pH and temperature parameters for the two enzymes *h*TIM and *Pf*TIM (Chapter 4, Section 4.4; pg. 86), the AgNPs interaction assays were performed in the presence of varying concentrations of AgNPs. The activity was monitored immediately (at 0 min) and again after 45 min.

The standard TIM assay protocol (Section 3.2.8; pg. 55) was used (Beisenherz *et al.*, 1955; Knowles *et al.*, 1972; Bergmeyer, 1974). AgNPs were diluted with buffer, after calculating the correct dilution ratios to obtain the desired AgNP concentrations, of 0 µM (-ve control), and 0.015, 0.03, 0.06, 0.12, 0.25, 0.5, 0.75, 1.0, 1.5 and 2.0 µM in the 2 ml incubation tube (Appendix N). As per the standard TIM assay, 10 µl of this solution was added to micro-titre plate for assay. This 'in assay' dilution of nanoparticles also further limits the nanoparticle effects on αG3PDH during assays.

5.2.4 TIM kinetics in the presence of AgNPs

To evaluate the inhibitory effects of AgNPs, a full set of kinetic experiments, using varying substrate concentrations, was performed with and without AgNPs. This allowed for a direct comparison to gauge the effects of AgNPs on TIM kinetics. This also helped to identify the mode of enzyme inhibition/activation occurring. Experiments were set up in a similar manner as that of previous kinetics experiments, (Section 4.2.5; pg. 78), but additional substrate concentrations were used.

In these kinetics experiments, substrate concentrations of 0.25, 0.75, 1.25, 2.5, 5, 7.5, 10 and 15 mM of DL-GA3P were prepared. For the inhibition kinetics study 0.06 µM AgNPs was chosen as this concentration was determined to be a concentration level where both *h*TIM and *Pf*TIM showed a noticeable level of inhibition (Figures 5.5 to 5.8), yet still maintained enough activity to produce reliable results. Assays were performed concurrently against negative controls, which contained PVP and ethanol at the exact same concentration level as that of the 0.06 µM AgNP samples. For calculations, see Appendices M and N.

In a 1st well the following was added: αG3PDH (10 µl, 40 U/ml), NADH (8 mM, 10 µl), DL-GA3P (50 µl, varying concentrations listed) and TEA buffer (230 µl, pH 7.6). In a 2nd well 10 µl of the respective diluted TIM (*h*TIM and *Pf*TIM) was added. Diluted TIM samples were incubated (45 min, 25°C) with AgNPs (0.06 µM) or PVP + EtOH (0.06 µM equivalent dilution) - negative controls. Kinetics data were then recorded (10 min, 20 sec intervals at 340 nm) – samples all run in triplicate.

5.2.5 Sample preparation for TEM

TEM samples were prepared at least one day in advance so that the NP samples could mature after sysnthesis so they could completely form before running TEM. Sample preparation involved depositing one drop of sample onto a copper TEM grid and allowing it to settle for 30 seconds. The drop was then reabsorbed by touching the corner of the grid sample with filter paper. The grid sample was then set aside to dry out completely – (at least 4 hours).

AgNPs were visualised using Transmission Electron Microscopy (TEM) on a Zeiss Libra 120 at operating at 120 KeV.

5.3 Results and discussion

5.3.1 AgNP preparation and characterisations

The sysntesised AgNPs were visualised by TEM (Zeiss) and characterised in terms of size and conformation see Figures 5.1 to 5.3.

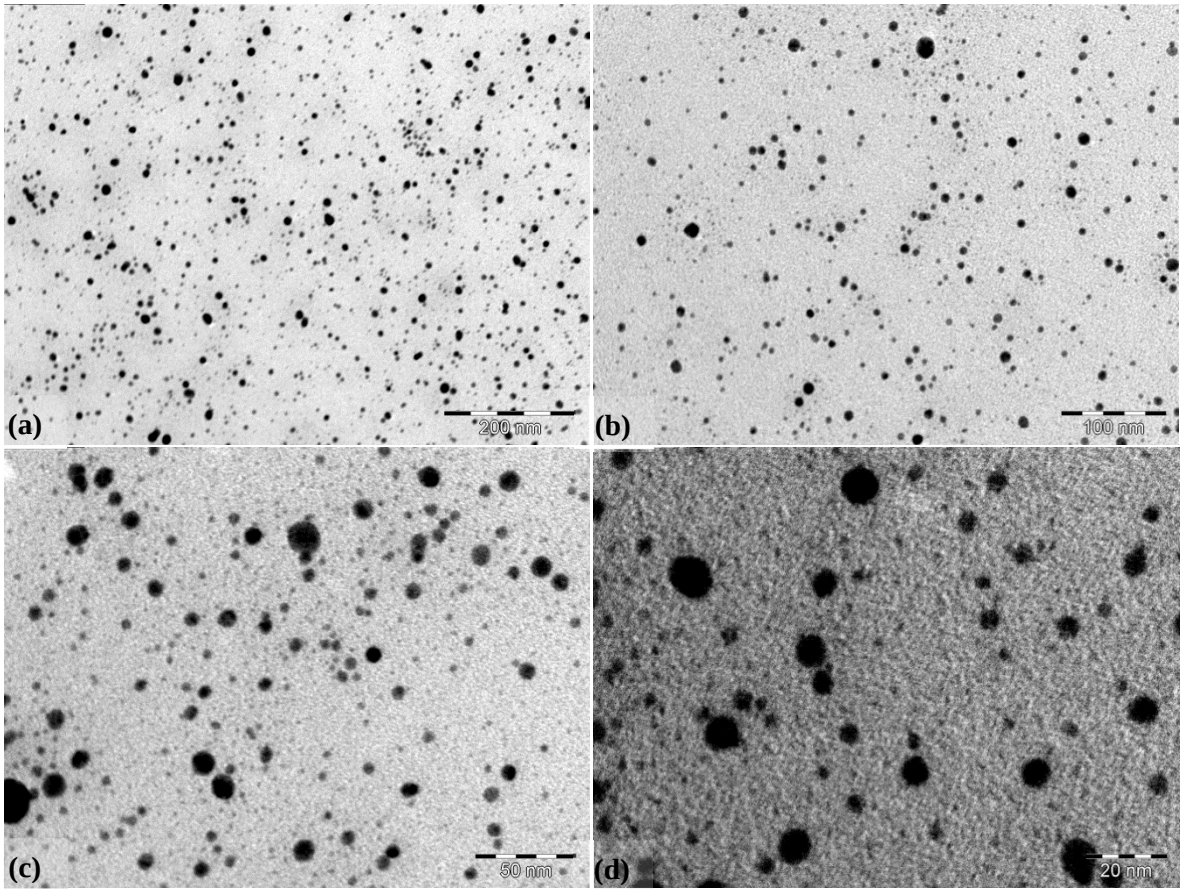

Figure 5.1: Four progressively zoomed-in (a to d), TEM images of AgNPs. Note: AgNPs appear to be mostly spherical in shape and of varying size. (Scale bars are in nm and differ for each image).

After removal from the microwave, a faint yellow colour was observed indicating the presence of AgNPs. After aging the samples, this colour darkened to a yellow-orange and spectral scans indicated a stronger peak at 400-408 nm, indicating more NPs (Appendix O).

A size distribution graph of AgNPs was made using the Zeiss Libra TEM software to measure NP size (Figure 5.2a) from TEM images of a 1-day-old AgNP sample. An additional spectral wave-scan (300-700 nm) was done by sampling different preparations of AgNPs after various storage times. This was to assess for NP aggregation, which is known to cause a detectable shift in peak absorbance on spectral scans (Figure 5.2b).

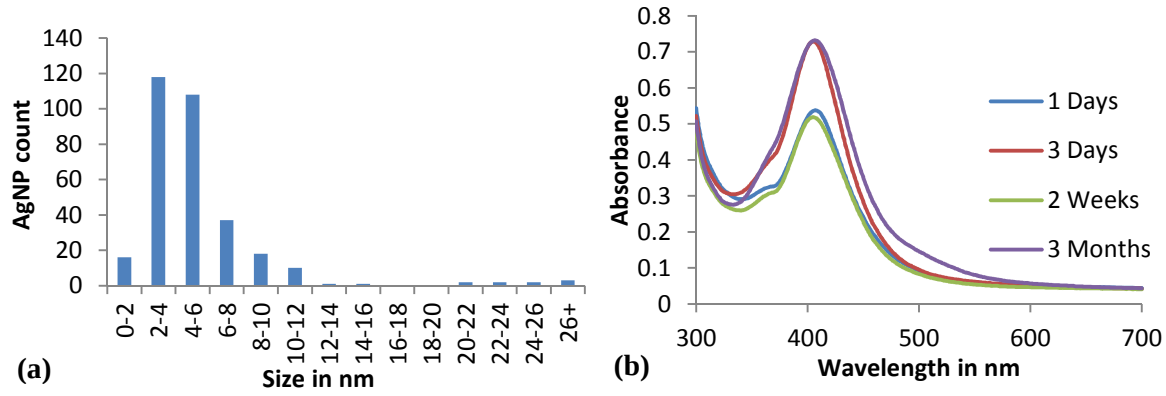

Figure 5.2: (a). Calculated size distribution graph of freshly prepared AgNPs where a majority of NPs were less than 10 nm in size. **(b).** Spectral wave scans of AgNP samples taken at different times, as indicated on the graphs.

Results illustrated in Figure 5.2a show that freshly prepared AgNPs have a slightly different size distribution profile (majority 2-8 nm) compared to those of the 1-week old samples stored at room temperature (majority 4-10 nm; Figure 5.3). This is consistent with a seeded growth process of AgNPs, where maturation results in the smallest NPs aggregating slowly over time, due to a larger surface area to volume ratio (Pal *et al.*, 2009). Maturation of AgNP seeds is important, to ensure that all of the $AgNO_3$ in solution is depleted. $AgNO_3$ is eliminated when Ag^+ ions link with the AgNP seeds, causing them to increase in size. The smallest AgNPs are the most mobile and interactive and pick up the most Ag+ ions. This ensures relatively consistent AgNP seed growth.

Absorbance peaks (400-408 nm) are consistent with the known AgNP absorbance peak range (Elechiguerra *et al.*, 2005; Sivaraman and Elango, 2009). Measurements from different AgNP preparations after different storage times (Figure 5.2b) indicate that the process slowly evolves, tending towards more aggregation and larger AgNPs a process known to occur during NP sample storage. These data (Figure 5.2b) indicate no significant shift in peak absorbance between 1 day and 3 months, meaning that the PVP-stabilized AgNPs that were synthesised were stable and could be kept for at least 3 months. TEM images also confirmed this, indicating only a slight (2-4 nm) increase in the overall average AgNP size distribution, which was considered insignificant for the purposes of this thesis. Furthermore, the overall size distribution range (~2-12 nm) was considered as an exceptionally narrow range for NP production, outperforming several other NP production methods tested (data not shown).

Nanoparticle stability was tested under different storage conditions. Freshly prepared samples were wrapped in tinfoil to limit light exposure and stored at 4°C or at room temperature for 1

week. Analysis**,** using TEM to inspect for nanoparticle size and level of aggregation**,** was then performed on the stored samples (Figure 5.3).

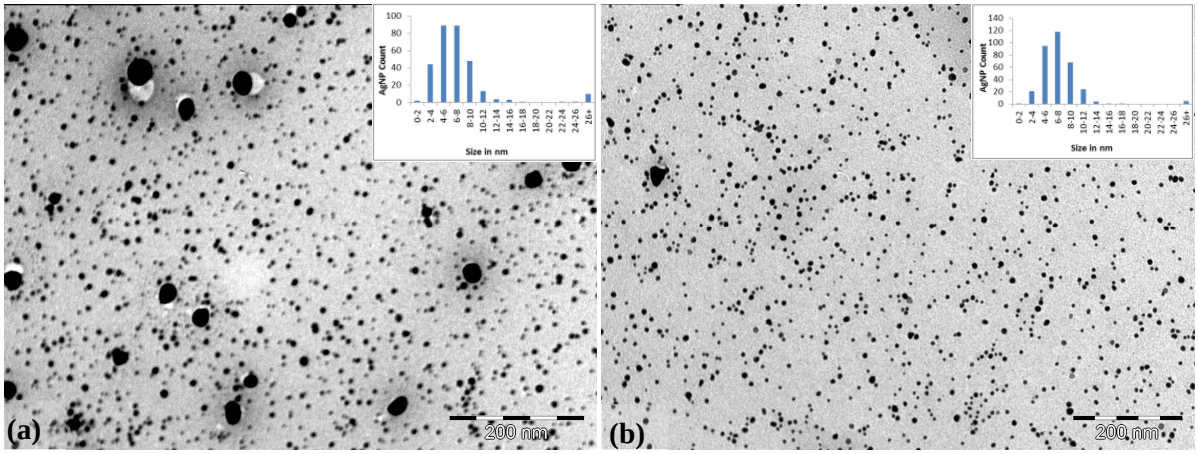

Figure 5.3: TEM images of AgNPs stored for 1 week at 4°C (a) and at room temperature (b). Less nanoparticle aggregation is observed for room temperature samples (b). This is consistent for all images taken using TEM at all different magnifications used. Size distribution graphs indicate more AgNPs > 26 nm in samples stored at 4°C.

Storage at room temperature appears to be less prone to aggregation after 1 week (Figure 5.3). Consequently, all AgNP samples used in enzymatic experiments were those stored at room temperature. This could possibly be due to lower solubility of PVP at lower storage temperatures thereby allowing for increased aggregation. A study investigating dipole and tripole formation from electrostatic energy fields around AgNPs and the effects of NP size on these energy fields may provide further insight into AgNP aggregation. This study goes on to explain the creation of rods, triangles or prisms in AgNP solutions by investigating the energy fields of AgNPs with reference to electromagnetic theory for spherical particles also known as Mie Theory (Hao and Schatz, 2004).

5.3.2 Effect of AgNPs on αG3PDH

A key aspect to ensure the validity of all the TIM assays that were carried out was to establish the concentrations of AgNPs that have an effect on the coupled αG3PDH, as this enzymatic reaction is critical for monitoring the TIM activity of the two TIMs being studied. The following results (Figure 5.4) indicate the range of AgNP concentrations tested, and their relative effect on αG3PDH activity.

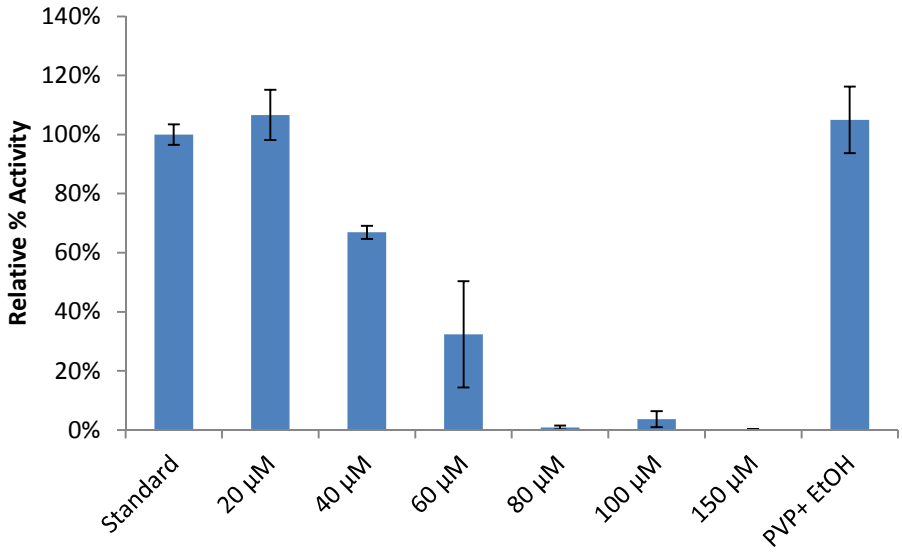

Figure 5.4: The interaction of AgNP, at different concentrations, with αG3PDH. The 'Standard' represents the full negative control (i.e. the standard assay). The sample labelled 'PVP + EtOH' is a negative AgNP control (i.e. it contains PVP + EtOH, but no Ag) in an equivalent dilution as that of the 150 µM AgNP sample. Samples run in triplicate.

Data presented in Figure 5.4 indicate that αG3PDH is not affected by 20 µM AgNPs. Furthermore, at two-times concentration (40 µM AgNPs), over 60% activity still remained. The activity of αG3PDH was more significantly affected by 60 µM AgNPs, albeit with a large margin of error, implying that active disruption of enzyme activity is occurring. At 80 µM AgNPs no activity remains. The PVP and EtOH control — tested using an equivalent dilution level to that of the 150 µM AgNP sample — indicates that, at this concentration, PVP and EtOH have no significant effect on αG3PDH activity (Figure 5.4). Therefore, the observed loss in activity is entirely due to the presence of the AgNPs and not due to PVP or EtOH.

This experiment — which specifically tested the effects of AgNPs on the coupled enzyme reaction, using αG3PDH — established the upper AgNP concentration limit that could be tolerated by αG3PDH under assay conditions without losing any noticeable level of activity (Section 5.2.2). Results illustrated in Figure 5.4 indicate that this limit is 20 µM AgNPs. While the TIM assay is different to the αG3PDH assay used here, the determined limits (Fig. 5.4) are still applicable to TIM assays because the αG3PDH assay is more sensitive to changes in αG3PDH activity than is the TIM assay. This is because the TIM assay uses significantly more αG3PDH: 20 x more under normal conditions or 40 x more for kinetics. This excess is critical, to ensure that αG3PDH activity is not rate-limiting and also serves to mitigate fluctuations in the activity of αG3PDH, making the coupled reaction in TIM assays very robust.

The timing, incubation temperature and buffers of the αG3PDH assay with AgNPs were all standardised to ensure that any observed effects in this test would translate objectively to tests done using the TIM assay. A final notable aspect of importance is that, in the TIM assay, samples containing TIM were prepared separately and only added to the rest of the assay mixture after the pre-assay incubations. This further minimises αG3PDH exposure to AgNPs and also results in an additional dilution. This test established that the coupling TIM assay enzyme αG3PDH is highly resilient to AgNPs at concentrations of up to 20 µM.

During TIM-AgNP interactions the highest AgNP concentration to achieve full TIM inhibition was only 2 µM for both TIM variants. This confirms the original suspicions about TIM that it would be susceptible to inhibition by AgNPs. At this concentration (2 µM) the αG3PDH, in the TIM assays, is well within this limit. After the necessary dilutions for the other TIM assay reagents, the AgNP concentration 'exposure level', to αG3PDH, drops to 0.065 µM. From these data and dilution factors it was therefore concluded that the AgNPs do not affect the coupling enzymatic reaction of αG3PDH in TIM assays (Figure 3.2; pg. 50).

These results indicate that any observed changes in TIM activity are entirely due to the AgNP effect on the relevant TIM enzyme (*h*TIM or *Pf*TIM) used for the TIM assays. These data thus confirm that it is acceptable and scientifically valid to test the effects of AgNPs on TIM enzymes, using the assay methodology described (Sections 5.2.2, 5.2.3 and 5.2.4).

5.3.3 AgNP interactions with TIM enzyme variants

After characterising the two different TIM variants being studied (*h*TIM and *Pf*TIM) and optimizing protocols, the inhibitory effects of AgNP on these two enzymes were investigated.

A set of comparative enzyme inhibition experiments was performed (Section 5.2.3). Data on the AgNP inhibition effects after immediate introduction of AgNPs (0 min) and after 45 min are shown in Figures 5.5 to 5.8. Samples immediately taken for assay (0 min samples) were technically exposed to AgNPs during pre-incubation (5 min), which was standardised across all assay experiments.

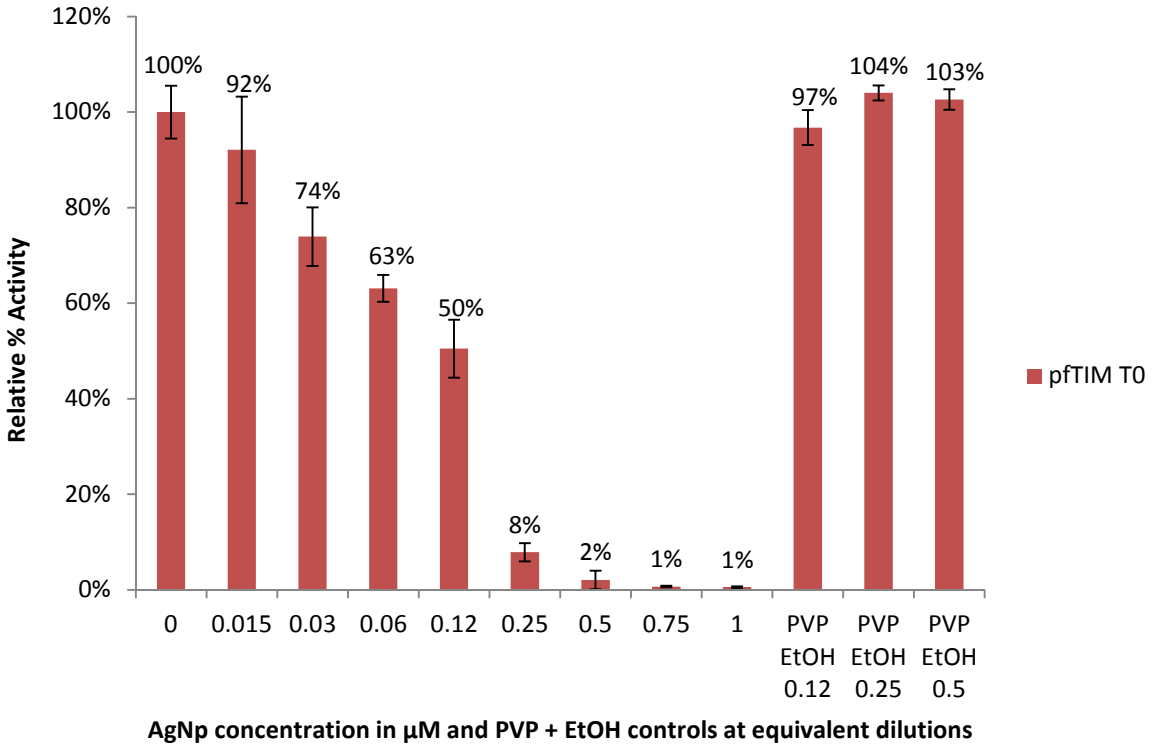

Figure 5.5: Bar graph showing relative percentage activity of *Pf*TIM when incubated with different concentrations of AgNPs for T0 min. The 0 sample represents the full –ve control and is also used as reference for 100% standard when calculating relative % activity. Samples run in triplicate and error bars indicate standard deviation.

An examination of Figure 5.5 indicates that the PVP and EtOH negative controls, run at dilutions equivalent to 0.12, 0.25 and 0.5 µM AgNP samples, did not affect *Pf*TIM activity in any statistically significant manner. Several PVP and EtOH control concentrations were assayed and it was shown that, at higher concentrations, PVP and EtOH can affect TIM enzyme activity. This phenomenon was investigated in a separate set of experiments (Section 5.3.5) which revealed some interesting observations regarding the PVP and EtOH controls. For the purposes of these experiments, under the AgNP concentrations used here, only the relevant PVP and EtOH controls are shown. Dilution calculation examples, to determine concentrations of PVP and EtOH in the AgNPs samples and in the 'equivalent' dilutions, are available in Appendix N.

Figure 5.5 indicates that 0.03 µM AgNPs reduced *Pf*TIM activity to 74% +/- 6%, as compared to the negative control (0 µM). This decrease in activity continues as AgNP concentrations increase. At 0.25 µM AgNPs the *Pf*TIM activity decreased to only 8% +/- 1.9% relative percentage activity and at 0.5 µM virtually no detectable activity remains. The PVP and ethanol controls at these equivalent dilutions (0.25 µM and 0.5 µM) are completely unaffected in any statistically significant manner, compared to the 0 µM negative control.

This indicates that the observed decrease in *Pf*TIM activity is entirely due to the presence of the AgNPs, which appear to have significant inhibitory effects on *Pf*TIM at final AgNP concentrations of 0.03 µM and higher. This inhibitory effect appears to occur relatively rapidly, considering the brief time (5 min) of exposure to AgNPs experienced by the T0 min *Pf*TIM samples.

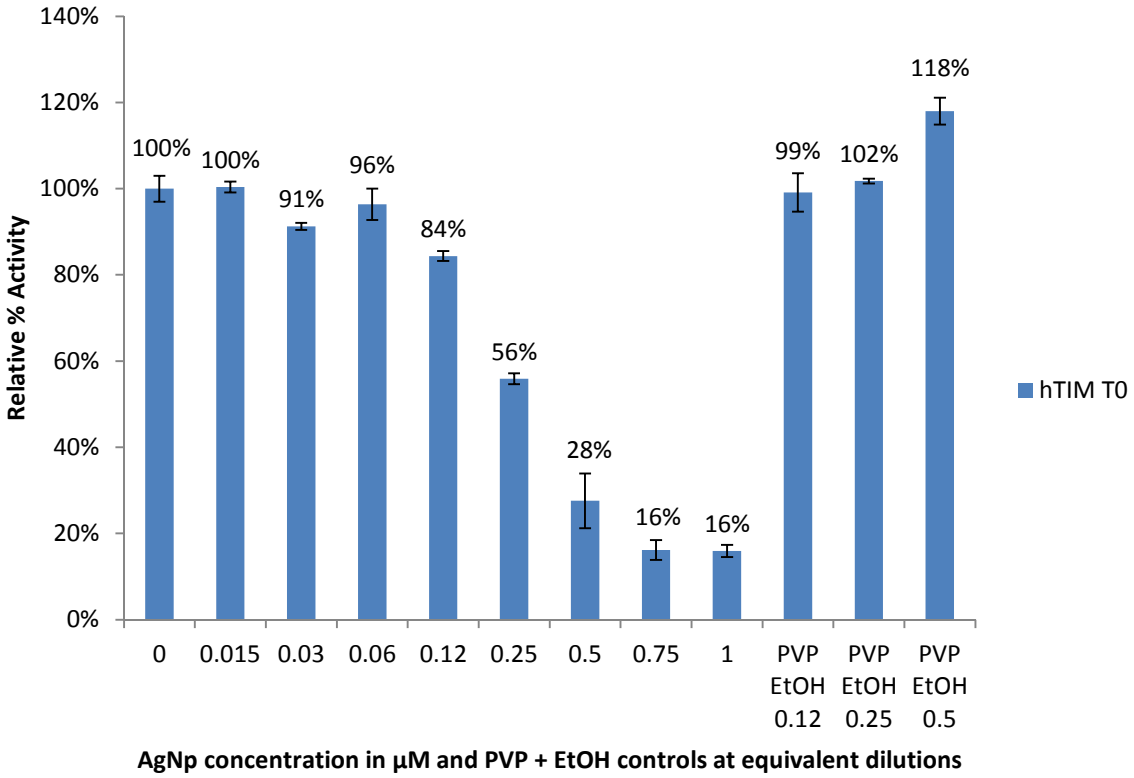

Figure 5.6: Bar graph showing relative percentage activity of *h*TIM when incubated with different concentrations of AgNPs for T0 min. The 0 sample represents the full –ve control and is also used as reference for 100% standard when calculating relative % activity. Samples run in triplicate and error bars indicate standard deviation.

A comparison of Figure 5.5 (*Pf*TIM) and Figure 5.6 (*h*TIM) indicates some key differences. Inhibition by AgNPs is notably less pronounced for *h*TIM than for *Pf*TIM, with *h*TIM showing only statistically-insignificant effects by AgNPs concentrations of up to 0.06 µM. At 0.25 µM AgNPs around 56% +/- 1.3% activity remains, which is significantly greater than the 8% +/- 1.9% observed for *Pf*TIM samples at the same AgNP concentration. This trend is similar at higher AgNP concentrations, from 0.5 µM to 1.0 µM AgNPs, where *h*TIM is still active in a statistically-significant way, while *Pf*TIM is not, with 0% being within its margin of error. This indicates that activity had been affected, even after the briefest possible exposure to AgNPs.

A detailed investigation into the PVP and EtOH controls was also done, because of the observed increase in activity, of approximately 18%, which was seen only in the *h*TIM control samples, using 0.5 µM equivalent PVP and EtOH dilutions (Figure 5.6 and 5.8). This increase in activity could not be accounted for by the error bars so it was investigated separately. This was done by setting up a range of PVP and EtOH controls, to investigate this observation. These control experiments are described in detail in Section 5.3.5.

Figures 5.7 and 5.8 show the relative percentage inhibition by AgNPs after a 45 min exposure at optimum conditions (Section 5.2.3). The two exposure times chosen (0 min and 45 min) are in accordance with the optimal stability determined in pH and temperature experiments outlined in Chapter 4 (Sections 4.3.1 and 4.3.2; pgs. 79 and 80).

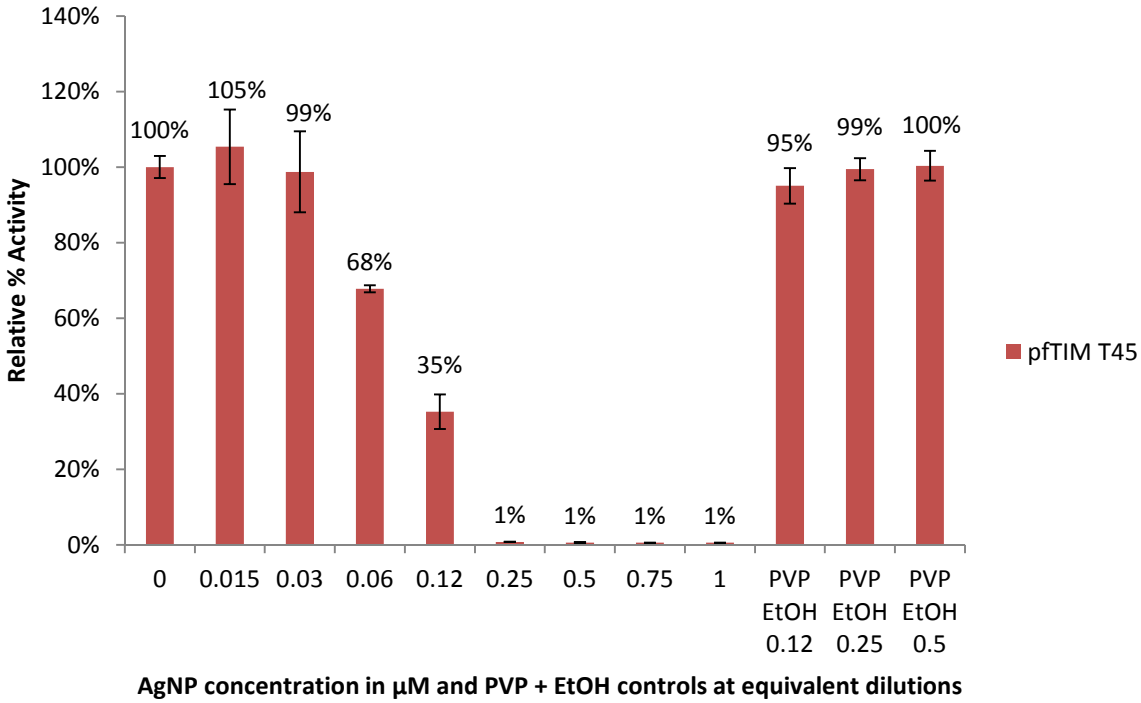

Figure 5.7: Bar graph showing relative percentage activity of *Pf*TIM when incubated with different concentrations of AgNPs for T45 min. The 0 sample represents the full –ve control and is also used as reference for 100% standard when calculating relative % activity. Samples run in triplicate and error bars indicate standard deviation.

As with the T0 min sample (Figure 5.5) the trend of inhibition is consistent for T45 min samples for *Pf*TIM (Figure 5.7). Complete loss of activity for *Pf*TIM samples (Figure 5.7), is observed for 0.25 µM AgNP concentrations, while the PVP and EtOH controls at this equivalent dilution (PVP EtOH 0.25) are unaffected, compared to the 0 µM negative controls.

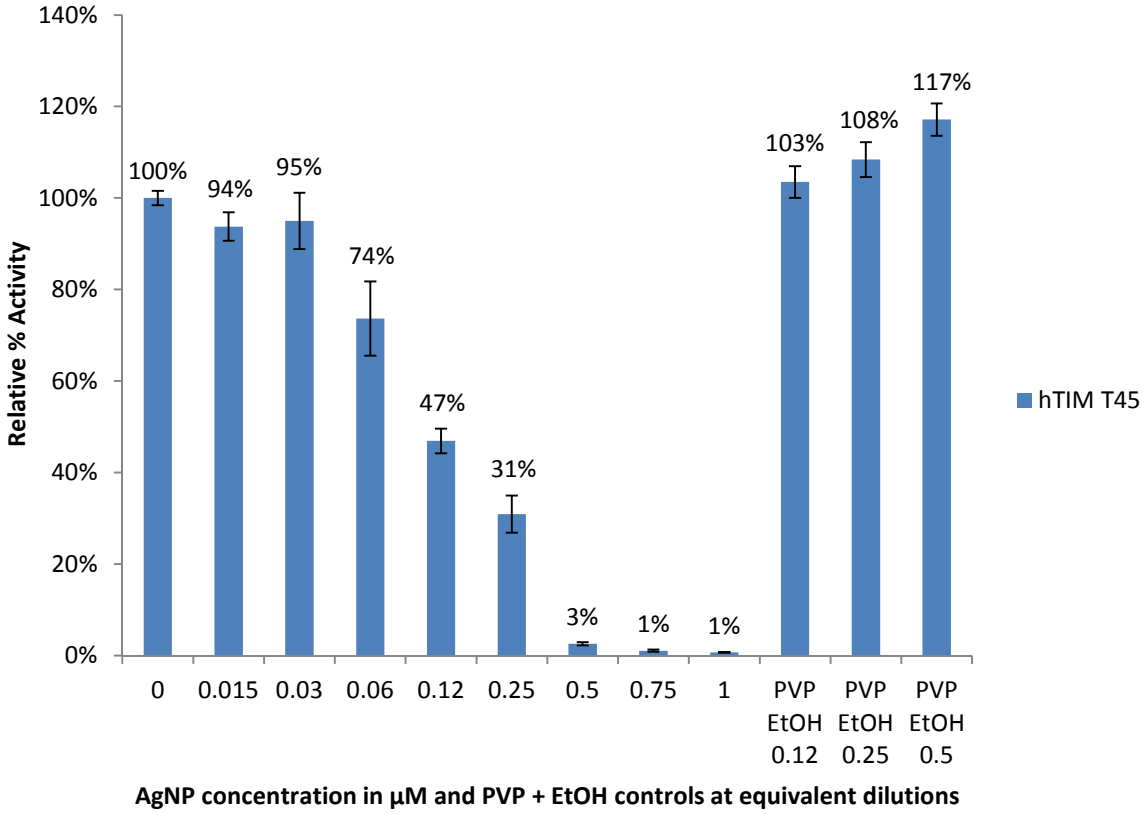

Figure 5.8: Bar graph showing relative percentage activity of *h*TIM when incubated with different concentrations of AgNPs for T45 min. The 0 sample represents the full –ve control and is also used as reference for 100% standard when calculating relative % activity. Samples run in triplicate and error bars indicate standard deviation.

Inhibition of *h*TIM samples at concentrations up to 0.03 µM is statistically insignificant (error bars overlap with 0 control) however, at concentrations of 0.06 µM, notable significant level of inhibition (error bars do not overlap with the 0 control) is observed after 45 min incubations with AgNPs for *h*TIM samples (Figure 5.8). Complete inhibition for *h*TIM is achieved with 0.75 µM AgNPs, while the closest equivalent control sample (PVP EtOH 0.5) shows an increased level of activity of approximately 117% which appears to be significant (error bars do not overlap with the 0 control). Across all AgNP concentrations a greater level of enzyme inhibition is observed after 45 minutes incubation with AgNPs (Figures 5.5 to 5.8). This indicates that the relative level of inhibition by AgNP increases with incubation

exposure time. This implies a destructive or 'inactivating' nature of the AgNPs to both of the TIM enzymes, something that would not likely occur with a standard competitive inhibitor and emphasises that protein-AgNP interactions are different to conventional (i.e. competitive, uncompetitive, non-competitive and mixed) inhibitors.

The results from the 45 minute AgNP incubations, *h*TIM (Figure 5.8) and *Pf*TIM (Figure 5.7), indicate that *h*TIM samples can maintain approximately 47% +/- 2.7% of activity after 45 minutes of exposure to 0.12 µM AgNP concentrations and 31% +/- 4% activity with 0.25 µM AgNP concentrations. *Pf*TIM samples for these AgNP concentrations, on the other hand, show activity levels 35% +/- 4.6% and 1% (considered inactive) respectively. This indicates that AgNPs appear to selectively inhibit *Pf*TIM over *h*TIM.

To assess this level of inhibition as an IC_{50} value a linear regression was performed on the 45 minute incubation data (Figures 5.7 and 5.8) only selecting the linear decrease range i.e. (0.03 to 0.025 µM AgNP) for *h*TIM samples and (0.03 to 0.12 µM AgNP) for *Pf*TIM samples. The regression line equation was then used to determine an IC_{50} concentration level for both *h*TIM and *Pf*TIM. These determined IC_{50} values were 0.158 µM AgNPs for *h*TIM and 0.095 µM AgNPs for *Pf*TIM – see Appendix N, Equations N1 and N2 for calculations. These IC_{50} levels were only determined with a limited set of data points and the inhibition curve may not actually be linear, even though it may appear so (Figures 5.7 and 5.8). These IC_{50} values therefore can only provide a rough estimate of the true IC_{50} values. That said, the IC_{50} data indicate that an almost 2-fold greater AgNP concentration is required to reach the IC_{50} for *h*TIM samples compared to *Pf*TIM samples.

These results indicate that the hypothesis, "Due to amino acid sequence and structural differences between *Human* and *Plasmodium falciparum* triosephosphate isomerases, silver nanoparticles, of less than 20 nm in size, will selectively inhibit the parasite enzyme over its *Human* counterpart.", must be true.

5.3.4 Kinetics studies with AgNPs on TIM variants

Kinetics experiments conducted on the two TIM variants were done after determining inhibition levels at different AgNP concentrations (Section 5.3.3). Initially AgNP concentration of 0.12 µM was chosen for kinetics as this was thought to represent the ~50% inhibition level desired for kinetics tests across both TIM samples. Tests using this concentration for *Pf*TIM samples however produced unreadable kinetic data at low substrate concentrations (data not shown). For this reason a lower AgNP concentration level, of 0.06

µM AgNPs, had to be used. Kinetics assays were performed as described in Section 5.2.4. To analyse kinetics data the Hanes-Woolf, Lineweaver-Burk, and non-linear regression analyses were performed with the use of the Michaelis-Menten equation (Equation 4.1; pg. 78) - see Appendix M.

To see the kinetic plots of Lineweaver-Burk, Hanes-Woolf and the Michaelis-Menten plot - with the Non-Linear regression curve incorporated - see Figures 5.9 and 5.10 for *h*TIM samples and Figures 5.11 and 5.12 for *Pf*TIM samples.

Calculated kinetic parameters from all the plots (Figures 5.9 to 5.12) are presented in Table 5.1. The negative kinetic controls used for comparative inhibition kinetics were run concurrently with the AgNP inhibition kinetics samples as detailed in Section 5.2.4.

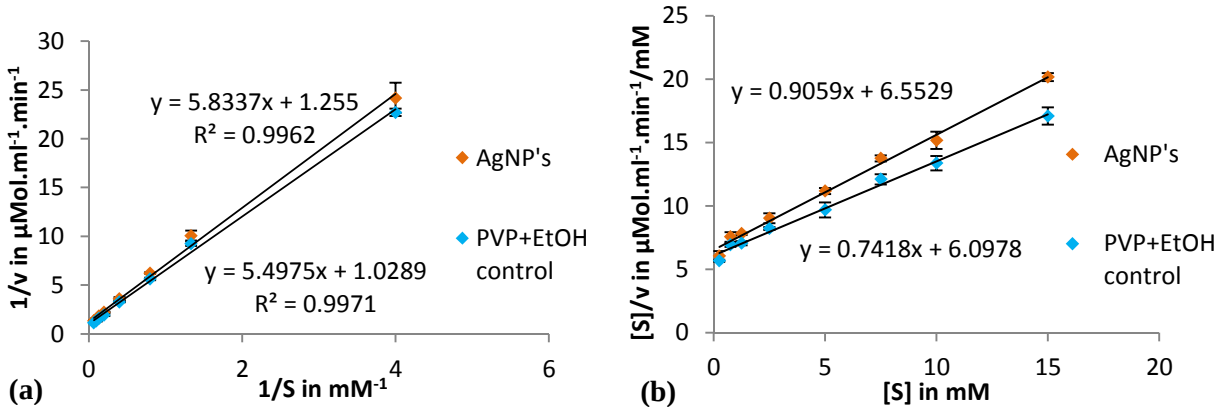

Figure 5.9: The Lineweaver-Burk plot (a), and Hanes-Woolf plot (b) for enzyme kinetic inhibition studies on *h*TIM using 0.06 µM AgNPs. Samples run in triplicate and error bars indicate standard deviation.

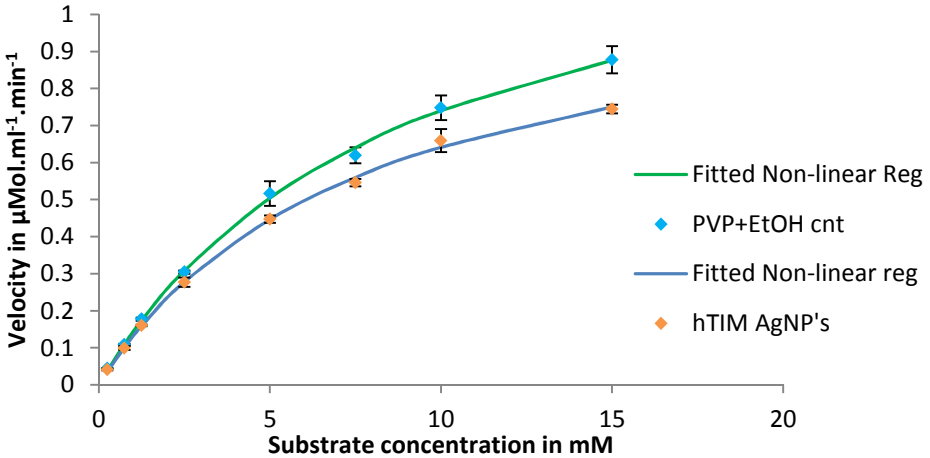

Figure 5.10: Kinetic activity of *h*TIM indicating velocity versus substrate concentration. K_m and V_{max} values, determined by non-linear regression computation, were used to plot the solid line graphs using the Michaelis-Menten equation (Equation 4.1) The *h*TIM samples used 0.06 µM AgNPs and controls had PVP and EtOH at an equivalent dilution level. Samples run in triplicate and error bars indicate standard deviation.

At the 0.06 µM AgNP concentrations used, kinetics data indicate the occurrence of only minimal inhibition for *h*TIM samples (Figures 5.9 and 5.10), while the *Pf*TIM samples (Figures 5.11 and 5.12) appear to be experiencing relatively strong inhibition in comparison. All calculated kinetic parameters; V_{max}, K_m, K_{cat}, and K_m/K_{cat} are reported in Table 5.1.

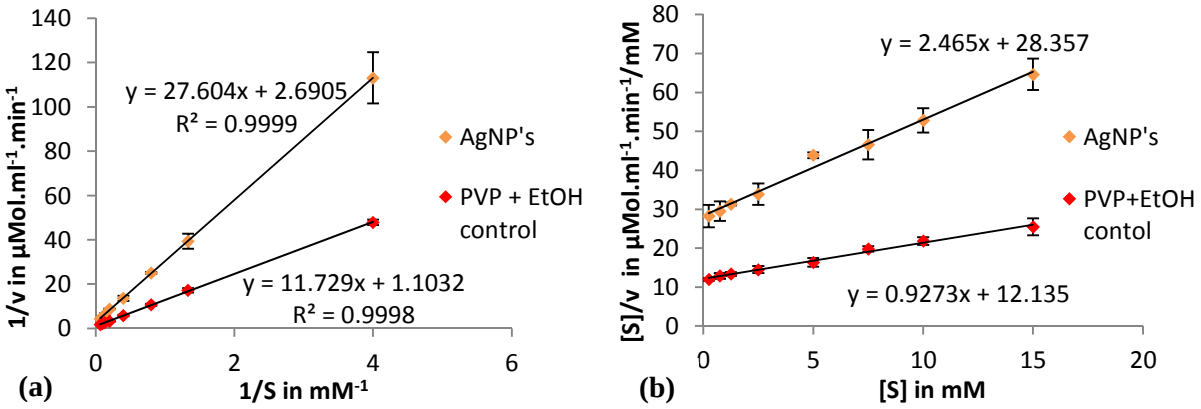

Figure 5.11: The Lineweaver-Burk plot (a), and Hanes-Woolf plot (b) for enzyme kinetic inhibition studies on *Pf*TIM using 0.06 µM AgNPs. Samples run in triplicate and error bars indicate standard deviation.

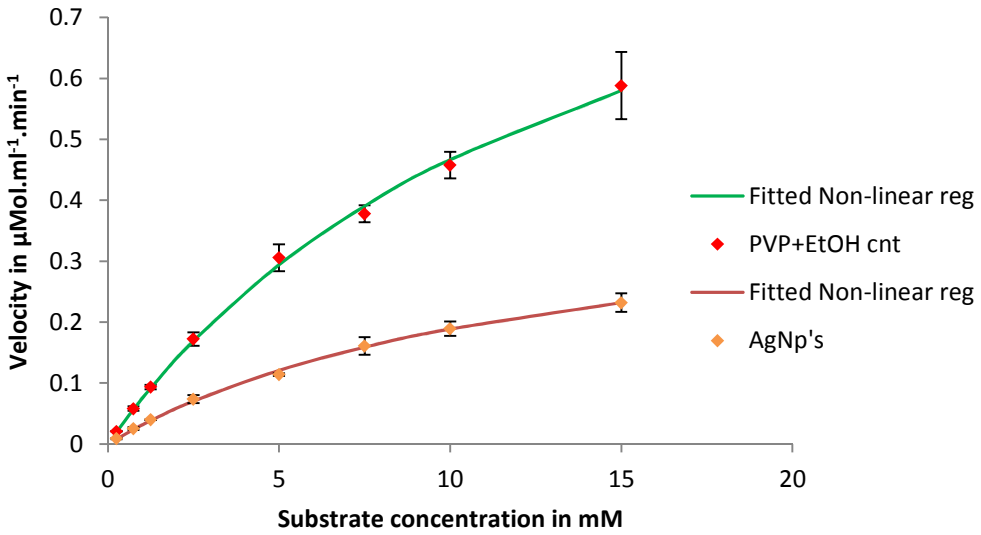

Figure 5.12: Kinetic activity of *Pf*TIM showing velocity versus substrate concentration. K_m and V_{max} values, determined by non-linear regression computation, were used to plot the solid line graphs using the Michaelis-Menten equation (Equation 4.1) *Pf*TIM samples used 0.06 µM AgNPs and controls had PVP and EtOH at an equivalent dilution level. Samples run in triplicate and error bars indicate standard deviation.

Kinetics data from *Pf*TIM samples (Figures 5.11 and 5.12) indicate that comparatively far more inhibition is occurring for *Pf*TIM samples than for *h*TIM samples when run under identical conditions relative to the negative controls containing PVP and EtOH. The Lineweaver-Burk plot (Figure 5.11a) indicates the type of inhibition which probably follows a mixed or non-competitive inhibition model. The Hanes-Woolf and the Michaelis-Menten graphs with non-linear regression analysis are considered to give the most accurate K_m and V_{max} values. The Lineweaver-Burk values, although included, are considered significantly less accurate. These data are presented for comparative purposes in Table 5.1.

Table 5.1: Kinetic parameters calculated from the three graphical plots: Lineweaver-Burk, Hanes-Woolf and Non-linear regression using Michaelis-Menten (Figures 5.9 to 5.12). Analysis of *human* (*h*TIM) and *Plasmodium falciparum* (*Pf*TIM) in the presence and absence (control) of silver nanoparticles (AgNPs), (Units presented under each parameter).

Plot Type and Sample	***human* TIM**				***Plasmodium falciparum* TIM**			
Lineweaver-Burk	K_m (mM)	V_{max} (μmol.ml^{-1}min^{-1})	K_{cat} (min^{-1})	K_{cat}/K_m (Mol^{-1}.min^{-1})	K_m (mM)	V_{max} (μmol.ml^{-1}min^{-1})	K_{cat} (min^{-1})	K_{cat}/K_m (Mol^{-1}.min^{-1})
AgNPs	4.65	0.7968	2.89×10^4	6.22×10^6	10.26	0.3717	7.92×10^3	7.72×10^5
Control	5.34	0.9719	3.52×10^4	6.59×10^6	10.63	0.9065	1.93×10^4	1.82×10^6
Hanes-Woolf	K_m (mM)	V_{max} (μmol.ml^{-1}min^{-1})	K_{cat} (min^{-1})	K_{cat}/K_m (Mol^{-1}.min^{-1})	K_m (mM)	V_{max} (μmol.ml^{-1}min^{-1})	K_{cat} (min^{-1})	K_{cat}/K_m (Mol^{-1}.min^{-1})
AgNPs	7.23	1.1039	4.00×10^4	5.53×10^6	11.5	0.4057	8.65×10^3	7.52×10^5
Control	8.22	1.3481	4.89×10^4	5.95×10^6	13.09	1.0784	2.30×10^4	1.76×10^6
Non-linear Regression	K_m (mM)	V_{max} (μmol.ml^{-1}min^{-1})	K_{cat} (min^{-1})	K_{cat}/K_m (Mol^{-1}.min^{-1})	K_m (mM)	V_{max} (μmol.ml^{-1}min^{-1})	K_{cat} (min^{-1})	K_{cat}/K_m (Mol^{-1}.min^{-1})
AgNPs	7.73	1.1362	4.12×10^4	5.33×10^6	12.8	0.4299	9.16×10^3	7.16×10^5
Control	8.78	1.3894	5.04×10^4	5.74×10^6	14.21	1.1299	2.41×10^4	1.70×10^6

Hanes-Woolf and Non-linear regression data correlate reasonably well, indicating that these data are reliable, since these two methods are considered to be the most accurate and were derived from completely different mathematical methods. Good correlation can be taken as an indication that a good data set was obtained. It is noted that a theoretically perfect data set should produce identical results. Thus, the production of similar results from two different methods (Table 5.1) indicates that the quality of these data can be considered good. The non-linear regression analysis of data is still regarded as the most powerful method, producing the most accurate results. For this reason, results from this method will be used when a single set of values needs to be quoted. The non-linear regression method data is considered more accurate than the Hanes-Woolf plot data - (which is considered the most accurate of the linear

plots). This is because the Hanes-Woolf plot is flawed, in that it uses substrate concentration in the abscissa (x-axis) and the ordinate (y-axis), meaning neither axis is independent as it should be. This in turn means that the R^2-value, typically used to determine the accuracy or 'goodness of fit' for linear regressions, is not applicable to Hanes-Woolf plots (Voet and Voet, 2004). The non-linear regression method does not suffer from this issue or any of the other issues that are associated with the linearization of the Michaelis-Menten equation. For this reason it is considered the most accurate (Greco and Hakala, 1979). Lineweaver-Burk plots are considered even less accurate because, by dividing by 1/S and 1/V, any inaccuracies in substrate concentration, particularly in velocity readings at low substrate concentrations, are amplified dramatically when using this methodology (Voet and Voet, 2004).

As indicated in Table 5.1 for all the plots, V_{max} clearly decreases in the presence of AgNPs, compared to negative controls. The effects of this are far more pronounced in *Pf*TIM samples than in *h*TIM samples. K_m values also appear to change, decreasing in all the plots when compared to negative controls, even though the decrease is not as significant as that seen for V_{max} values. This suggests that the inhibition that is occurring here is most similar to a mixed inhibition model rather than a non-competitive model. It should however be noted that, due to the different nature of inhibition occurring with AgNPs, these conventional models of inhibition are not necessarily even relevant when considering enzyme inhibition by AgNPs. Evidence, discussed above, suggesting that there is a mixed mode of inhibition emphasises this conclusion.

The Lineweaver-Burk plot (Figure 5.11a) provides a clearer indication that inhibition is occurring and it appears to be operating in a non-competitive, or possibly mixed, manner. Enzyme inhibition using nanoparticles is a relatively new technique that is not fully understood. What is known, however, is that this unconventional method can either enhance or decrease enzyme activity and that factors, such as of nanoparticle size, concentration, nanoparticle functionalization and the type of nanoparticle used, can greatly affect the outcome of nanoparticle enzyme interactions (Paciotti *et al.,* 2006; Wilner *et al.,* 2007; Lynch and Dawson, 2008; Rana *et al.,* 2010). It is clear from these data that the AgNPs do target and interact with the TIM enzymes, regardless of whether or not the substrate is bound. In this way they act in a similar manner as a non-competitive inhibitor. The binding mechanisms of nanoparticles however operate in a vastly different manner and it is likely that they induce 3D conformational changes when they bind. This makes it unlikely that enzyme activity may be restored after AgNP binding has occurred (You *et al.,* 2005; Willner *et al.,* 2007; Lynch and

Dawson, 2008; Wu *et al.*, 2009; Rana *et al.*, 2010). Any conformational changes induced during AgNP binding would need to be reversed if activity were to be restored. This is discussed in further detail in Chapter 6, with reference to 3D protein models of the two TIM enzymes being studied. These data further support the hypothesis (Section 1.7; pg. 27).

5.3.5 Unforeseen observations from control experiments

For the inhibition experiments (Section 5.3.2) a series of additional PVP and ethanol controls were prepared and assayed (Section 5.2.3). This was done because during testing it was shown that, depending on concentration, the presence of PVP and ethanol could have a statistically significant effect on *h*TIM activity, most notably at dilution levels equivalent to the (2 µM AgNP) concentrations (Figure 5.13).

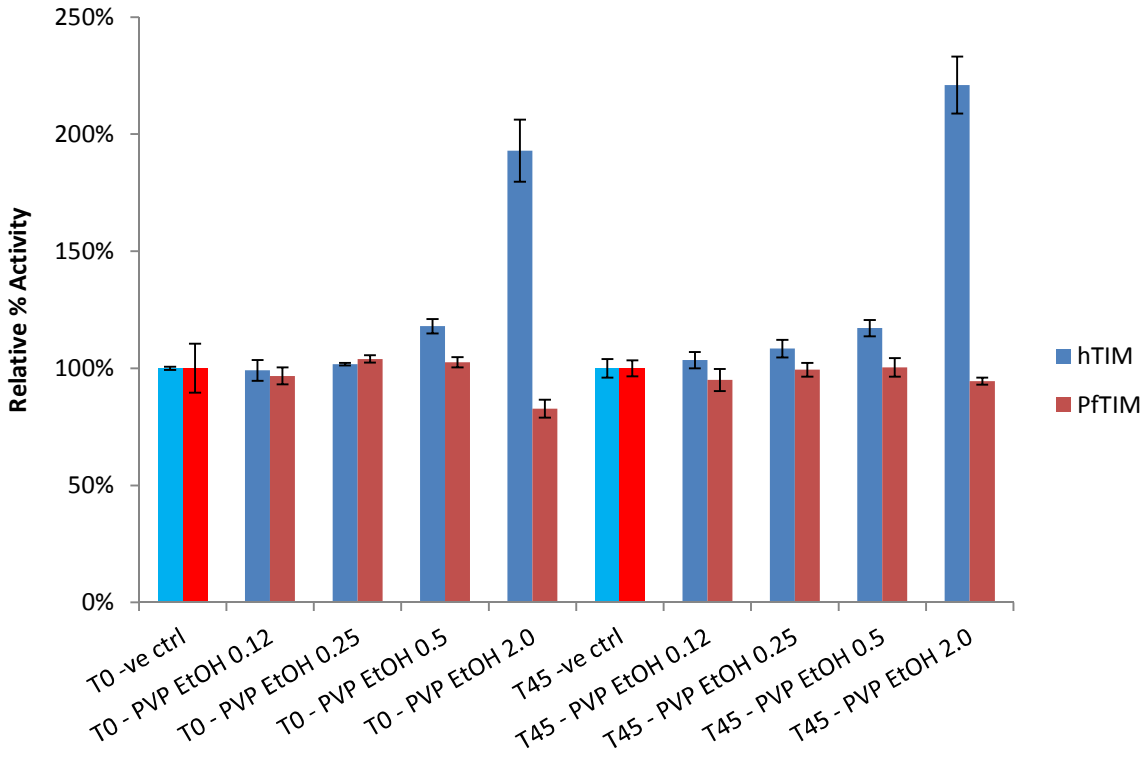

Figure 5.13: Analysis of all PVP and EtOH controls run for both *h*TIM (Blues) and *Pf*TIM (Reds) at T0- and T45- minute sample times versus the negative controls (Bright colours), used to determine relative percentage activity. Samples run in triplicate and error bars indicate standard deviation.

For *h*TIM samples (blue), higher concentrations — equivalent to 2.0 µM AgNP dilutions of PVP and EtOH (see Appendix N for actual PVP and EtOH concentrations) — resulted in an approximate doubling of *h*TIM activity (Figure 5.13). Additionally, at PVP and EtOH dilutions that were equivalent to the 0.5 µM AgNP samples (Section 5.3.3), a statistically

significant increase, of approximately 18% +/- 3%, was observed for both incubation times (Figures 5.6 and 5.8). This did not occur for *Pf*TIM samples (red), where PVP and EtOH controls at 2.0 µM-equivalent dilutions maintained approximately the same level of activity as the T0 negative control samples (Figure 5.13). For *Pf*TIM at T0 time (2.0 µM) a slight, but statistically significant (i.e. error bars don't overlap), decrease in activity was observed, while for 45 minute samples no statistically-significant change was observed (i.e. error bars overlap with those of the T0, negative control).

These control experiments were repeated several times and conducted under carefully controlled conditions, using fresh reagents, dilutions and new negative controls for each set of experiments. Results from all repeats of these PVP and EtOH control experiments were identical (Figure 5.13). This indicates that *h*TIM and *Pf*TIM are affected differently by the presence of PVP and EtOH at the concentrations investigated (Appendix N). This observation emphasises that the differences between the two TIM variants (*PF*TIM and *h*TIM) are indeed important with noticeable variations observed for pH optima, temperature optima, AgNP concentrations and now PVP and EtOH concentrations. This strongly supports the notion that a selective *Pf*TIM inhibitor could be designed. Ironically it appears that a selective enzyme activator/enhancer, (PVP and EtOH at the tested concentrations – see Appendix N), for *h*TIM appears to have also been found by serendipity. Fortunately, for the relevant AgNP concentrations required to achieve noticeable enzyme inactivation (0.25 µM AgNPs) – Figures 5.7 and 5.8, the equivalent controls, (0.25 PVP EtOH), showed no statistically significant (i.e. error bars overlap) differences compared to the 0 µM negative control (which contained no AgNPs, PVP or EtOH in it) – see Figure 5.13. This indicates that the two enzymes are affected differently by AgNPs and the PVP and EtOH solution used to create the AgNPs.

Therefore the controls that were prepared and assayed were able to rule out the possibility - that this observed enhancement in activity (Figure 5.13) may have resulted in interference with the AgNP inhibition experiments (Figures 5.5 to 5.8). Indeed complete enzyme inhibition by 1.0 µM AgNPs for both TIM samples was observed (Figures 5.7 and 5.8) irrespective of any possible PVP and EtOH enhancements. As such it appears that the ability of AgNPs to inhibit activity superseded and enhancement activity of PVP and EtOH (Figures 5.5-5.8).

5.4 Conclusions

Firstly, the TEM and spectral analyses (Figures 5.1 to 5.3) were able to confirm that the AgNPs obtained were well within the desired size range desired (of < 20 nm), with the majority of AgNPs being ~4-12 nm in size and stable during storage. At this size the range the AgNPs are of a size comparable to that of the TIM enzymes being studied, i.e. Approximately 7.8 nm x 5.2 nm x 5.0 nm as measured by PyMol: pdb files; {1HTI-(*h*TIM); 1YDV-(*Pf*TIM)}. The AgNPs therefore have sufficient 'curvature' to interact with the natural surface curvature of the TIM enzymes and probe the exposed sulphur atoms of the targeted residues (Figures 1.7a, b, c; pg. 16) (You *et al.,* 2005; Willner *et al.,* 2007; Lynch and Dawson, 2008; Wu *et al.,* 2009; Rana *et al.,* 2010).

On analysing the most accurate kinetic data, obtained from the non-linear regression (Table 5.1), it becomes apparent that both K_m and V_{max} values are affected by the presence of AgNPs, indicating that a complex type of inhibition is occurring. After further study of the kinetics 'turn over' values, (K_{cat} values), it becomes apparent that - at the 0.06 µM AgNP concentration tested - AgNPs had a noticeably greater effect on *Pf*TIM than on *h*TIM (Table 5.1). It is noted that for *Pf*TIM a ~62% decrease in 'enzymatic turnover' (K_{cat}), is observed while for *h*TIM the decrease in K_{cat} is only ~18% (Table 5.1), (Plaut and Knowles, 1972; Blacklow *et al.,* 1988; Mann *et al.,* 1990). If one further considers K_{cat}/K_m, also known as the enzyme 'catalytic efficiency' value, which incorporates any observed shifts in K_m as well, and is therefore more accurate, an even greater difference between *Pf*TIM and *h*TIM is observed (Plaut and Knowles, 1972; Blacklow *et al.,* 1988; Mann *et al.,* 1990). With 0.06 µM AgNPs there was a decrease of ~58% in 'catalytic efficiency' for the *Pf*TIM enzyme while only a ~7% decrease was observed for the *h*TIM enzyme – see Table 5.1. This clearly indicates that AgNPs inhibit *Pf*TIM selectively over *h*TIM by a significant margin of approximately 8 fold, as based on K_{cat}/K_m values determined from kinetics data of the non-linear regression analysis (Table 5.1) for both enzymes when inhibited with 0.06 µM AgNPs. This selective inhibition trend is consistent across the range of AgNPs tested, when incubated at both the time durations tested (Figures 5.5 to 5.8).

Data indicating that the PVP and ethanol controls at equivalent dilutions (to 2.0 µM AgNPs) resulted in selective activity enhancement for *h*TIM, but and not for *Pf*TIM, supports the idea that these two variants of the same enzyme (TIM) are sufficiently different for selective enzyme inhibition or activation to be induced by foreign substances, namely AgNPs (Figures 5.5 to 5.12) and the PVP and EtOH solution (Figure 5.13), discovered by serendipity.

6. Final discussion, conclusions and recommended future work

6.1 Final discussion and conclusions

From the experimental data presented it is clear that AgNPs selectively inhibit *Pf*TIM over *h*TIM and that this has the potential to be utilised in drug design and development. Considering the recently-discovered propensity for NPs and macro-molecules of the same size studied, (4-12 nm), to associate with red blood cells and persist in the blood stream due to the complicated fluid dynamics of the human vascular system (Charoenphol *et al.,* 2010; Huang *et al.*, 2010; Charoenphol *et al.*, 2011).

Given the discovery that erythrocytes infected with *Plasmodium falciparum* have been shown to uptake ferritin/apoferritin protein cages – which have also subsequentially been shown to have the capacity to encapsulate Au and Ag NPs (Fan *et al.,* 2010; Kasyutich *et al.,* 2010) – this offers a realistic and achievable means, of targeting, and deliving NPs to infected erythrocytes (Burns and Pollack, 1988). It is noted that the AgNPs used in these studies were functionalized or stabilized with the PVP during the AgNP preparation and synthesis procedure. PVP acts as a stabilizing agent to the AgNPs by loosely associating with the AgNPs and preventing aggregation (Pal *et al.,* 2009). Considereing that the PVP and EtOH solution also appeared to have an interesting enhancing effect on *h*TIM activity when incubated with the enzyme by itself, this indicates that the PVP and EtOH solution also has a notable level of interaction with the *h*TIM enzyme and this should not be overlooked.

PVP shells associated with stabilizing the AgNPs only weakly associate with the AgNP surface through van der Waals forces which are sufficiently strong enough to greatly limit and reduce AgNP aggregation but not strong enough to compete with the relatively stronger bonding associated with AgNP and atomic sulphur on the TIM surface which can more accurately be viewed as similar to a CH3-S—AgNP bond. PVP binds to the AgNP via its thiol group forming an Ag thiol bond while the CH3-S—Ag shows similar bond strength to CH3-S—Au/Ag bonds as reported by (Sellers *et al.,* 1993) who also made comparisons between hydrogen bonds and CH3-S—Ag/Au bonds as well as disulphide bonds indicating their relative strength. Another paper (Ramachandran *et al.,* 2003) indicates the bond dissociation energies for an Au-S under optical testing was 1.6 eV while that of the thiol-Au

bond was 0.1 eV (Ramachandran *et al.,* 2003; Jain *et al.,* 2006). Indicating that Sulphur binds are at least an order of magnitude greater than that of thiol type bonds (Ramachandran *et al.,* 2003). This would likely also be the case when tested with AgNPs as the data from Sellers *et al.,* (1993), indicates that Ag and Au CH3-S—Ag/Au bonds are comparable in terms of strength only differing by a relatively small percentage typically less than 10% (Sellers *et al.,* 1993). Thus it is assumed that in the presence of the surface sulphur atoms of *Pf*TIM in particular the predicted S-Ag bonds created with AgNPs will displace any thiol bonds present between the PVP stabilizing molecules and the AgNPs due to sulphurs greater affinity. This is further supported by the fact that the PVP only controls exhibited no detectable changes in either of the TIM activities when tested at equivalent concentrations to strongly inhibiting AgNP experiments. If PVP were playing a noticeable role in inhibition when in conjunction with AgNPs it would be logical to assume some trace of this effect might be detectable in the PVP controls, the experimental data however indicates this is not the case.

The targeting of *P. falciparum* infected erythrocytes using ferritin/apoferritin which become incorportated into the erythrocytes via endocytosis and ultimately digested (Burns and Pollack, 1988). Offer an intriguing possible drug delivery mechanism as anything captured inside the ferritin/apoferritin cage would presumably be released inside the infected erythrocyte upon digestion of the protein cage by the parasites biochemical digestive processes (Burns and Pollack, 1988).

In this study, AgNPs successfully inhibited both *h*TIM and *Pf*TIM enzymes. The inhibition observed was also significantly higher for *Pf*TIM samples as compared to *h*TIM samples, across all AgNP concentrations tested. For the inhibition kinetics experiments, performed using 0.06 µM AgNPs, an 8-fold higher level of inhibition was observed in the enzyme catalytic efficiency (K_{cat}/K_m) for *Pf*TIM samples, compared to *h*TIM samples, which were barely affected (i.e. ~8% decrease observed at this level) – see Table 5.1 (Blacklow *et al.,* 1988; Mann *et al.,* 1990).

AgNPs were hypothesised to exhibit this selective inhibition on *Pf*TIM, due to the exposed sulphur atoms, prevalent on the surface of *Pf*TIM and at its dimer interface – see (Figures 1.7a, b, c; pg. 16). Most of these exposed sulphur atoms are not present on *h*TIM, which only has one exposed sulphur atom on its surface (Figure 1.7d; pg. 16). It is known that silver interacts strongly with sulphur atoms, forming a relatively strong bond with sulphur chemisorption (SH and SCH3 sulphur) occurring at a bond length of 2.337 Å and 2.332 Å

respectively with a silver surface (Sellers *et al.*, 1993). This is smaller than the bond length of disulphide bonds lengths which are considered highly influential in protein tertiary structure formation (Sellers *et al.*, 1993; Rafique *et al.*, 2010). Furthermore, it is known that, when nanoparticles are able to interact strongly with enzymes, they tend to induce conformational changes in the 3D tertiary structures of those enzymes, which in turn can affect enzyme activity (Fischer *et al.*, 2002; You *et al.*, 2005; Lynch and Dawson, 2008; Rana *et al.*, 2010). When strong interactions occur, with short bond lengths, or when bonds occur at multiple sites, it is more likely that such proteins will join up with the nanoparticle and become a part of the 'hard corona' of proteins directly conjugated to the nanoparticle. When this happens, the affected proteins typically experience a large degree of protein deformation, resulting in a loss of enzymatic activity (Fischer *et al.*, 2002; You *et al.*, 2005; Lynch and Dawson, 2008; Rana *et al.*, 2010). This is because any significant conformational changes will likely change the tertiary conformation of the enzyme to such a degree that the key catalytic residues will shift in position, enough to render them ineffective. It is known from literature that, for TIM, the positioning of the key catalytic residues (His95 and Glu165) within the TIM active site is critical and finely tuned for efficient enzyme function (Knowles and Albery, 1977). As indicated by Knowles and Albery (1977) and Knowles (1991), any minor shift in TIM structure – an enzyme he describes as "honed to perfection" – could likely reposition these key residues and thereby alter catalytic efficiency. Considering Knowles's argument – about this enzyme being a "perfect enzyme" to start with – it is likely that such an alteration will destroy this "perfection".

The selectivity of the AgNPs to *Pf*TIM comes from both the exposure level of cysteine sulphur atoms on the surface of *Pf*TIM and the fact that there are more of them present on the surface of *Pf*TIM compared to *h*TIM. The Cys13, which resides in the dimer interface, is theoretically shielded from AgNP exposure but it is known that enzymes, particularly multimeric enzymes, are in a constant state of flux, essentially having a constant 'wobble' to them as they continually associate and disassociate and interact with their surrounding environment (Lynch and Dawson, 2008). This essentially means that protein dimer interfaces can be targeted because, while the dimer interface of each monomer is generally protected by the other monomer, the dynamic flux interactions with the exposed surface may cause a shift that weakens dimer stability allowing the dimer itself to be targeted. This has already been shown for TIM enzymes by the selective inhibition of *Trypanosoma cruzi* TIM by Olivares-Illana *et al.* (2007) where the dimer interface was targeted. This showed that the dimer

interface of TIM is not effectively as shielded in practice as one might expect when studying 3D protein structures. Hypothetically, if the AgNPs interact with the already exposed surface sulphur atoms on *Pf*TIM, it is likely that this initial interaction could cause conformational changes that would result in the exposure of the dimer interface. This would raise the possibility of further AgNP interactions and binding with the TIM dimer interface that, in the case of *Pf*TIM, will likely bind AgNPs with the dimer interface Cys13 via the highly-exposed sulphur atom present at the dimer interface (Figure 1.7d; pg. 16). Olivares-Illana *et al.* (2007), noted that this residue (Cys13) is also present on the *T. cruzi* TIM, which was selectively inhibited using 2,2´-dithiodianiline (DTDA) and also interacts with the sulphur atom of Cys13.

6.2 Recommended future works

The work done here has raised interesting possibilities with regards to the design of selective nanodrugs. A lot more work, however, would be required to advance this research to a point where such an objective could become a real possibility. To start with, the kinetics studies could be extended, to study the forward and reverse reactions of TIM and also to study the kinetic effects of AgNPs under a wider range of concentrations. The effects observed with enhanced activity of *h*TIM, in the presence of greater than 2.0 µM PVP, should be further investigated as well as the differences between the non-PVP kinetics and kinetics of the controls done in the presence of PVP. Other stabilizing and functionalising options, aside from PVP, should also be investigated. These would include the use of 2,2´-dithiodianiline (DTDA), which was shown to selectively inhibit *T. cruzi* TIM (Olivares-Illana *et al.*, 2007). If this was associated with AgNPs as an outer functional layer it could possibly further enhance the selective inhibition of the AgNPs and theoretically reduce nanoparticle toxicity. Further research and comparison testing could be done using iron, platinum, gold and copper nanoparticles. In addition to this, the option of functionalizing the nanoparticles in various ways with multiple layers could be investigated and tested, which would add great value to the research, especially if the ultimate goal – of creating a viable nanodrug – is kept in mind. Functionalisations to allow for red blood cell targeting could be investigated, such as using infected erythrocyte endocytosis of ferritins, apoferritins or transferritins – which have been demonstrated to occur in *P. falciparum*-infected erythrocytes – could be a powerful selective delivery mechanism (Burns and Pollack, 1988). The toxicity of the nanodrugs could also be investigated, by performing tissue-culture experiments with various human cell lines or possibly in mice, as carried out by Lasagna-Reeves *et al.* (2010), using gold nanoparticles.

The lethal nature of any developed nanoparticle system could be tested against live *P. falciparum* parasite cultures. The toxicity of selected nanoparticle-based systems can then be each investigated by testing their interactions with human tissue cultures and on live rats or mice.

From these data and knowledge from literature, a proposed hypothesis for a possible future research project is as follows. “Silver nanoparticles encapsulated in ferritin or apoferritin will become incorporated into *P. falciparum* infected erythrocytes releasing the silver nanoparticles and result in decreased parasite proliferation”.

References

Albertyn, J., Tonder, A. van, Prior, B., 1992. Purification and characterisation of glycerol-3-phosphate dehydrogenase of *Saccharomyces cerevisiae*. The Federation of European Biochemical Societies Journal Letters 3013, 130–131.

Aregawi, M., Cibulskis, R., Otten, M., Williams, R., 2011. The World Malaria Report 2011.

Atteke, C., Ndong, J.M.M., Aubouy, A., Maciejewski, L., Brocard, J., Lébibi, J., Deloron, P., 2003. In vitro susceptibility to a new antimalarial organometallic analogue, ferroquine, of *Plasmodium falciparum* isolates from the Haut-Ogooué region of Gabon. The Journal of Antimicrobial Chemotherapy 51, 1021–1024.

Baca, A.M., Hol, W.G., 2000. Overcoming codon bias: a method for high-level overexpression of *Plasmodium* and other AT-rich parasite genes in *Escherichia coli*. International Journal for Parasitology 30, 113–118.

Banner, D.W., Bloomer, A.C., Petsko, G.A., Phillips, D.C., Pogson, C.I., Wilson, I.A., 1975. Structure of chicken muscle triose phosphate isomerase determined crystallographically at 2.5Å resolution: using amino acid sequence data. Nature 255, 609–614.

Bash, P.A., Field, M.J., Davenport, R.C., Petsko, G. a, Ringe, D., Karplus, M., 1991. Computer simulation and analysis of the reaction pathway of triosephosphate isomerase. Biochemistry 30, 5826–5832.

Beisenherz, G., Bücher, T., and Garbade, K.H. (1955). Methods in Enzymology Vol. 1, pp 387, 195

Bergmeyer, H.U. (1974). Methods of Enzymatic Analysis I, pp 468, 515.

Blacklow, S., Raines, R., Lim, W., Zamore, P., 1988. Triosephosphate isomerase catalysis is diffusion controlled. Biochemistry 27, 1158–1165.

Bradford, M.M., 1976. A rapid and sensitive method for the quantitation of microgram quantities of protein utilizing the principle of protein-dye binding. Analytical Biochemistry 72, 248–254.

Burns, E., Pollack, S., 1988. *P. falciparum* infected erythrocytes are capable of endocytosis. In Vitro Cellular & Developmental Biology 24, 481–486.

Centres for Disease Control, 2010, *About Malaria*, [WWW]: Accessed 11/07/2012, http://www.cdc.gov/malaria/about/biology/index.html

Charoenphol, P., Huang, R.B., Eniola-Adefeso, O., 2010. Potential role of size and hemodynamics in the efficacy of vascular-targeted spherical drug carriers. Biomaterials 31, 1392–1402.

Charoenphol, P., Mocherla, S., Bouis, D., Namdee, K., Pinsky, D.J., Eniola-Adefeso, O., 2011. Targeting therapeutics to the vascular wall in atherosclerosis--carrier size matters. Atherosclerosis 217, 364–370.

Chen, J., Wang, D., Xi, J., Au, L., Siekkinen, A., Warsen, A., Li, Z., Zhang, H., Xia, Y., Li, X., 2007. Immuno gold nanocages with tailored optical properties for targeted photothermal destruction of cancer cells. Nano Letters 7, 1318–1322.

Chen, P.C., Mwakwari, S.C., Oyelere, A.K., 2008. Gold nanoparticles: From nanomedicine to nanosensing. Nanotechnology, Science and Applications 1, 45–66.

Clarke, A., Wigley, D., Chia, W., Barstow, D., Atkinson, T., Holbrook, J.J., 1986. Site-directed mutagenesis reveals role of mobile arginine residue in lactate dehydrogenase catalysis. Nature 324, 699–702.

Connor, E.E., Mwamuka, J., Gole, A., Murphy, C.J., Wyatt, M.D., 2005. Gold nanoparticles are taken up by human cells but do not cause acute cytotoxicity. Small 1, 325–327.

Conte, L.L., Chothia, C., Janin, J., 1999. The atomic structure of protein-protein recognition sites1. Journal of Molecular Biology 285, 2177–2198.

De Jong, W.H., Borm, P.J.A., 2008. Drug delivery and nanoparticles:applications and hazards. International Journal of Nanomedicine 3, 133–149.

De la Roche, M., Tessier, S.N., Storey, K.B., 2012. Structural and functional properties of glycerol-3-phosphate dehydrogenase from a mammalian hibernator. The Protein Journal 31, 109–119.

Dondorp, A., Nosten, F., Yi, P., Das, D., 2009. Artemisinin resistance in *Plasmodium falciparum* malaria. New England Journal of Medicine 361, 455–467.

Eksi, S., Czesny, B., van Gemert, G.-J., Sauerwein, R.W., Eling, W., Williamson, K.C., 2006. Malaria transmission-blocking antigen, Pfs230, mediates human red blood cell binding to exflagellating male parasites and oocyst production. Molecular Microbiology 61, 991–998.

Elechiguerra, J.L., Burt, J.L., Morones, J.R., Camacho-Bragado, A., Gao, X., Lara, H.H., Yacaman, M.J., 2005. Interaction of silver nanoparticles with HIV-1. Journal of Nanobiotechnology 3, 6-16.

Entzeroth, R., Mattig, F.R., Werner-Meier, R., 1998. Structure and function of the parasitophorous vacuole in Eimeria species. International Journal for Parasitology 28, 1015-1018.

Fan, R., Chew, S.W., Cheong, V.V., Orner, B.P., 2010. Fabrication of gold nanoparticles inside unmodified horse spleen apoferritin. Small 6, 1483–1487.

Fairbanks, G., Steck, T., Wallach, D., 1971. Electrophoretic analysis of the major polypeptides of the human erythrocyte membrane. Biochemistry 10, 2606–2617.

Fischer, N.O., McIntosh, C.M., Simard, J.M., Rotello, V.M., 2002. Inhibition of chymotrypsin through surface binding using nanoparticle-based receptors. Proceedings of the National Academy of Sciences of the United States of America 99, 5018–5023.

Frevert, U., Sinnis, P., Cerami, C., Shreffler, W., Takacs, B., Nussenzweig, V., 1993. Malaria Circumsporozoite Protein Binds to Heparan Sulfate Proteoglycans Associated with the Surface Membrane of Hepatocytes. Journal of Experimental Medicine 177, 1287–1298.

Gadek, T.R., Nicholas, J.B., 2003. Small molecule antagonists of proteins. Biochemical Pharmacology 65, 1–8.

Gerdes, S., Overbeek, R., 2012. Embden Meyerhof glycolytic pathway and Gluconeogenesis [WWW]: Accessed 11/08/2012, Fellowship for Interpretation of Genomes. URL http://www.theseed.org/SubsystemStories/Glycolysis/story.pdf

Ginger, M.L., McFadden, G.I., Michels, P. a M., 2010. Rewiring and regulation of cross-compartmentalised metabolism in protists. Philosophical transactions of the Royal Society of London. Series B, Biological sciences 365, 831–845.

Gómez-Puyou, A., Saavedra-Lira, E., Becker, I., Zubillaga, R. A., Rojo-Domínguez, a, Pérez-Montfort, R., 1995. Using evolutionary changes to achieve species-specific inhibition of enzyme action--studies with triosephosphate isomerase. Chemistry and Biology 2, 847–855.

Goodman, C.M., McCusker, C.D., Yilmaz, T., Rotello, V.M., 2004. Toxicity of gold nanoparticles functionalized with cationic and anionic side chains. Bioconjugate Chemistry 15, 897–900.

Gracy, R.W., 1975. Triosephosphate isomerase from human erythrocytes. Methods in Enzymology 41, 442–447.

Greco, W., Hakala, M., 1979. Evaluation of methods for estimating the dissociation constant of tight binding enzyme inhibitors. Journal of Biological Chemistry 254, 12104–12109.

Greenbaum, D.C., Mackey, Z., Hansell, E., Doyle, P., Gut, J., Caffrey, C.R., Lehrman, J., Rosenthal, P.J., McKerrow, J.H., Chibale, K., 2004. Synthesis and structure-activity relationships of parasiticidal thiosemicarbazone cysteine protease inhibitors against *Plasmodium falciparum, Trypanosoma brucei, and Trypanosoma cruzi*. Journal of Medicinal Chemistry 47, 3212–3219.

Guzmán, M., Dille, J., Godet, S., 2008. Synthesis of silver nanoparticles by chemical reduction method and their antibacterial activity. World Academy of Science, Engineering and Technology 43, 357–364.

Hanahan, D., 1983. Studies on transformation of *Escherichia coli* with plasmids. Journal of Molecular Biology 0, 557–580.

Hrkach, J., Von Hoff, D., Mukkaram Ali, M., Andrianova, E., Auer, J., Campbell, T., De Witt, D., Figa, M., Figueiredo, M., Horhota, A., Low, S., McDonnell, K., Peeke, E., Retnarajan, B., Sabnis, A., Schnipper, E., Song, J.J., Song, Y.H., Summa, J., Tompsett, D., Troiano, G., Van Geen Hoven, T., Wright, J., LoRusso, P., Kantoff, P.W., Bander, N.H., Sweeney, C., Farokhzad, O.C., Langer, R., Zale, S., 2012. Preclinical development and clinical translation of a PSMA-targeted docetaxel nanoparticle with a differentiated pharmacological profile. Science Translational Medicine 4, 128-139.

Huang, X., El-Sayed, I.H., Qian, W., El-Sayed, M.A., 2006. Cancer cell imaging and photothermal therapy in the near-infrared region by using gold nanorods. Journal of the American Chemical Society 128, 2115–2120.

Huang, R.B., Mocherla, S., Heslinga, M.J., Charoenphol, P., Eniola-Adefeso, O., 2010. Dynamic and cellular interactions of nanoparticles in vascular-targeted drug delivery (review). Molecular Membrane Biology 27, 190–205.

Inoue, H., Nojima, H., Okayama, H., 1990. High efficiency transformation of *Escherichia coli* with plasmids. Gene 96, 23–28.

Jain, P.K., Qian, W., El-Sayed, M. a, 2006. Ultrafast cooling of photoexcited electrons in gold nanoparticle-thiolated DNA conjugates involves the dissociation of the gold-thiol bond. Journal of the American Chemical Society 128, 2426–2433.

Joseph, D., Petsko, G.A., Karplus, M., 1990. Anatomy of a conformational change: hinged "lid" motion of the triosephosphate isomerase loop. Science 249, 1425–1428.

Kaiser, K., Camargo, N., Kappe, S.H.I., 2003. Transformation of sporozoites into early exoerythrocytic malaria parasites does not require host cells. The Journal of Experimental Medicine 197, 1045-1050.

Karp G. (2005). Chapters: Techniques in cell and molecular biology, *Cell and Molecular Biology Concepts and Experiments*, 4th Edition, (Karp, G., Ed), pp 775-778, John Wiley & Sons, Inc., 111 River Street, Hoboken, NJ 07030-5774, USA.

Kasyutich, O., Ilari, A., Fiorillo, A., Tatchev, D., Hoell, A., Ceci, P., 2010. Silver ion incorporation and nanoparticle formation inside the cavity of *Pyrococcus furiosus* ferritin: structural and size-distribution analyses. Journal of the American Chemical Society 132, 3621–3627.

Kaufman, E.D., Belyea, J., Johnson, M.C., Nicholson, Z.M., Ricks, J.L., Shah, P.K., Bayless, M., Pettersson, T., Feldotö, Z., Blomberg, E., Claesson, P., Franzen, S., 2007. Probing protein adsorption onto mercaptoundecanoic acid stabilized gold nanoparticles and surfaces by quartz crystal microbalance and zeta-potential measurements. Langmuir : the ACS Journal of Surfaces and Colloids 23, 6053–6062.

Kholoud, M.M., El-Nour, A., Eftaiha, A., Al-Warthan, A., Ammar, R. a. a., 2010. Synthesis and applications of silver nanoparticles. Arabian Journal of Chemistry 3, 135–140.

Kim, J.S., Kuk, E., Yu, K.N., Kim, J.-H., Park, S.J., Lee, H.J., Kim, S.H., Park, Y.K., Park, Y.H., Hwang, C.-Y., Kim, Y.-K., Lee, Y.-S., Jeong, D.H., Cho, M.-H., 2007. Antimicrobial effects of silver nanoparticles. Nanomedicine : nanotechnology, biology, and medicine 3, 95–101.

Knowles, J., 1991. Enzyme catalysis: not different, just better. Nature 350, 121–124.

Knowles, J., Albery, W., 1977. Perfection in enzyme catalysis: the energetics of triosephosphate isomerase. Accounts of Chemical Research 10, 105–111.

Knowles, J.R., Leadlay, P.F., Maister, S.G., 1972. Triosephosphate Isomerase: Isotope Studies on the Mechanistic Pathway. Cold Spring Harbor Symposia on Quantitative Biology 36, 157–164.

Lasagna-Reeves, C., Gonzalez-Romero, D., Barria, M. a, Olmedo, I., Clos, a, Sadagopa Ramanujam, V.M., Urayama, a, Vergara, L., Kogan, M.J., Soto, C., 2010. Bioaccumulation and toxicity of gold nanoparticles after repeated administration in mice. Biochemical and Biophysical Research Communications 393, 649–55.

Lévy, R., Shaheen, U., Cesbron, Y., Sée, V., 2010. Gold nanoparticles delivery in mammalian live cells: a critical review. Nano Reviews 1, 1–18.

Lian, L.-Y., Al-Helal, M., Roslaini, A.M., Fisher, N., Bray, P.G., Ward, S. a, Biagini, G. a, 2009. Glycerol: an unexpected major metabolite of energy metabolism by the human malaria parasite. Malaria Journal 8, 38-41.

Link, P., 2008. Biological Buffers [WWW Document]. Applichem. URL www.aplichem.com

Liu, F.-K., Huang, P.-W., Chang, Y.-C., Ko, C.-J., Ko, F.-H., Chu, T.-C., 2005. Formation of silver nanorods by microwave heating in the presence of gold seeds. Journal of Crystal Growth 273, 439–445.

Lolis, E., Petsko, G.A., 1990. Crystallographic analysis of the complex between triosephosphate isomerase and 2-phosphoglycolate at 2.5-Å resolution: implications for catalysis. Biochemistry 29, 6619–6625.

Longnecker, M.P., Rogan, W.J., Lucier, G., 1997. The human health effects of DDT (dichlorodiphenyltrichloroethane) and PCBS (polychlorinated biphenyls) and an overview of organochlorines in public health. Anual Review of Public Health 18, 211–244.

Lynch, I. & Dawson, K.A., 2008. Protein-nanoparticle interactions. Nano Today, 3(1), 40–47.

Madigan, M.T., Martinko J.M. (2006). Chapters: Bacterial Genetics, *Brock Biology of Microorganisms – Principals of Microbiology*, 11th edition, (Carlson, G., Ed), pp 288-289, Pearson Education, INC, Upper Saddle River, NJ USA.

Maithal, K., Ravindra, G., Balaram, H., Balaram, P., 2002. Inhibition of plasmodium falciparum triose-phosphate isomerase by chemical modification of an interface cysteine. Electrospray ionization mass spectrometric analysis of differential cysteine reactivities. The Journal of Biological Chemistry 277, 25106–25114.

Majzik, A., Patakfalvi, R., Hornok, V., Dékány, I., 2009. Growing and stability of gold nanoparticles and their functionalization by cysteine. Gold Bulletin 42, 113–123.

Malabadi, R.B., Meti, N.T., Mulgund, G.S., Nataraja, K., 2012. Synthesis of silver nanoparticles from in vitro derived plants and callus cultures of Costus speciosus (Koen.); Assessment of antibacterial activity. Research in Plant Biology 2, 32–42.

Malaria Research and Reference Reagent Resource Center (MR4), as a part of the American Type Culture Collection, 2011. [WWW]: Accessed 03/03/2011 http://www.mr4.org/

Mande, S.C., Mainfroid, V., Kalk, K.H., Goraj, K., Martial, J. a, Hol, W.G., 1994. Crystal structure of recombinant human triosephosphate isomerase at 2.8 A resolution. Triosephosphate isomerase-related human genetic disorders and comparison with the trypanosomal enzyme. Protein Science : a Publication of the Protein Society 3, 810–821.

Mann, K.G., Nesheim, M.E., Church, W.R., Haley, P., Krishnaswamy, S., 1990. Surface-dependent reactions of the vitamin K-dependent enzyme complexes. Blood 76, 1–16.

Meyerhof, O., 1935. Über umkehrbare Reaktionen im Verlauf der biologischen Zuckersplatung. Naturwissenschaften 23, 490–493.

Michels, P. a, 1988. Compartmentation of glycolysis in trypanosomes: a potential target for new trypanocidal drugs. Biology of the Cell 64, 157–164.

Mier, P., Cotton, D., 1970. Enzymes of the Glycolytic Pathway in Skin. British Journal of Dermatology 598–602.

Miller, L.H., Baruch, D.I., Marsh, K., Doumbo, O.K., 2002. The pathogenic basis of malaria. Nature 415, 673–679.

Mota, M.M., Pradel, G., Vanderberg, J.P., Hafalla, J.C., Frevert, U., Nussenzweig, R.S., Nussenzweig, V., Rodríguez, a, 2001. Migration of *Plasmodium* sporozoites through cells before infection. Science (New York, N.Y.) 291, 141-144.

Nasongkla, N., Bey, E., Ren, J., Ai, H., Khemtong, C., Guthi, J.S., Chin, S., Sherry, A.D., Boothman, D.A., Gao, J., 2006. Multifunctional Polymeric Micelles as Cancer-Targeted, MRI-Ultrasensitive Drug Delivery Systems. Nano Letters 6, 2427–2430.

Nickbarg, E.B., Davenport, R.C., Petsko, G. a, Knowles, J.R., 1988. Triosephosphate isomerase: removal of a putatively electrophilic histidine residue results in a subtle change in catalytic mechanism. Biochemistry 27, 5948–5960.

Olivares-Illana, V., Rodríguez-Romero, A., Becker, I., Berzunza, M., García, J., Pérez-Montfort, R., Cabrera, N., López-Calahorra, F., De Gómez-Puyou, M.T., Gómez-Puyou, A., 2007. Perturbation of the dimer interface of triosephosphate isomerase and its effect on *Trypanosoma cruzi*. PLoS Neglected Tropical Diseases 1, 1-8.

Olszewski, K., Mather, M., Morrisey, J., Garcia, B., Vaidya, B., Rabinowitz, J., Llinás, M., 2010. Branched tricarboxylic acid metabolism in *Plasmodium falciparum*. Nature 466, 774–778.

Olszewski, K.L., Llinás, M., 2010. Central carbon metabolism of *Plasmodium* parasites. Molecular and Biochemical Parasitology 175, 95–103.

Omenn, G.S., 2007. THE HUPO Human Plasma Proteome Project. Proteomics. Clinical Applications 1, 769–779.

Orosz, F., Oláh, J., Ovádi, J., 2006. Triosephosphate isomerase deficiency: facts and doubts. International Union of Biochemistry and Molecular Biology - Life 58, 703–715.

Paciotti, G., Kingston, D., Tamarkin, L., 2006. Colloidal gold nanoparticles: a novel nanoparticle platform for developing multifunctional tumor targeted drug delivery vectors. Drug Development 54, 47–54.

Painter, H.J., Morrisey, J.M., Mather, M.W., Vaidya, A.B., 2007. Specific role of mitochondrial electron transport in blood-stage *Plasmodium falciparum*. Nature 446, 88–91.

Pal, A., Shah, S., Devi, S., 2009. Microwave-assisted synthesis of silver nanoparticles using ethanol as a reducing agent. Materials Chemistry and Physics 114, 530–532.

Parthasarathy, S., Eaazhisai, K., Balaram, H., Balaram, P., Murthy, M.R.N., 2003. Structure of *Plasmodium falciparum* triose-phosphate isomerase-2-phosphoglycerate complex at 1.1-A resolution. The Journal of Biological Chemistry 278, 52461–52470.

Parthasarathy, S., Ravindra, G., Balaram, H., Balaram, P., Murthy, M.R.N., 2002. Structure of the *Plasmodium falciparum* triosephosphate isomerase-phosphoglycolate complex in two crystal forms: characterisation of catalytic loop open and closed conformations in the ligand-bound state. Biochemistry 41, 13178–13188.

Plaut, B., Knowles, J.R., 1972. pH-dependence of the triose phosphate isomerase reaction. The Biochemical Journal 129, 311–320.

Pompliano, D., Peyman, A., Knowles, J.R., 1990. Stabilization of a reaction intermediate as a catalytic device: definition of the functional role of the flexible loop in triosephosphate isomerase. Biochemistry 29, 3186–3194.

Putman, S.J., Coulson, a F., Farley, I.R., Riddleston, B., Knowles, J.R., 1972. Specificity and kinetics of triose phosphate isomerase from chicken muscle. The Biochemical Journal 129, 301–310.

Rafique, S., Idrees, M., Nasim, A., Akbar, H., Amin, A., 2010. Transition metal complexes as potential therapeutic agents. Biotechnology and Molecular Biology Reviews 5, 38–45.

Rai, M., Yadav, A., Gade, A., 2009. Silver nanoparticles as a new generation of antimicrobials. Biotechnology advances 27, 76–83.

Ramachandran, G.K., Hopson, T.J., Rawlett, A.M., Nagahara, L. a, Primak, A., Lindsay, S.M., 2003. A bond-fluctuation mechanism for stochastic switching in wired molecules. Science (New York, N.Y.) 300, 1413–1416.

Rana, S., Yeh, Y., Rotello, V., 2010. Engineering the nanoparticle–protein interface: applications and possibilities. Current Opinion in Chemical Biology 14, 828–834.

Ratledge, C., Kristiansen, B. (2006). Chapters: Genome management and analysis: prokaryotes, *Basic Biotechnology*, 3rd Edition, (Ratledge and Kristiansen., Ed), pp 91-93, Cambridge University Press., The Edinburgh Building, Cambridge CB2 2RU, UK.

Ravindra, G., Balaram, P., 2005. *Plasmodium falciparum* triosephosphate isomerase: New insights into an old enzyme. Pure and Applied Chemistry 77, 281-289.

Ray, S. Balaram, H. Balaram, P., 1999. Unusual stability of a multiply nicked form of *Plasmodium falciparum* triosephosphate isomerase Soumya. Chemistry and Biology 625–637.

Robert, A., Benoit-Vical, F., Dechy-Cabaret, O., Meunier, B., 2001. From classical antimalarial drugs to new compounds based on the mechanism of action of artemisinin. Pure and Applied Chemistry 73, 1173–1188.

Robichon, C., Luo, J., Causey, T.B., Benner, J.S., Samuelson, J.C., 2011. Engineering *Escherichia coli* BL21(DE3) derivative strains to minimize *E. coli* protein contamination after purification by immobilized metal affinity chromatography. Applied and Environmental Microbiology 77, 4634–4646.

Rogan, W.J., Chen, A., 2005. Health risks and benefits of bis(4-chlorophenyl)-1,1,1-trichloroethane (DDT). Lancet 366, 763-773.

Sabatino, P., Casella, L., Granata, A., Iafisco, M., Lesci, I.G., Monzani, E., Roveri, N., 2007. Synthetic chrysotile nanocrystals as a reference standard to investigate surface-induced serum albumin structural modifications. Journal of Colloid and Interface Science 314, 389–397.

Sahoo, S.K., Parveen, S., Panda, J.J., 2007. The present and future of nanotechnology in human health care. Nanomedicine : Nanotechnology, Biology, and Medicine 115, 20–31.

Sellers, H., Ulman, A., Shnidman, Y., Eilers, J.E., 1993. Structure and binding of alkanethiolates on gold and silver surfaces: implications for self-assembled monolayers. Journal of the American Chemical Society 115, 9389–9401.

Shang, L., Wang, Y., Jiang, J., Dong, S., 2007. pH-dependent protein conformational changes in albumin:gold nanoparticle bioconjugates: a spectroscopic study. Langmuir : the ACS journal of surfaces and colloids 23, 2714–2721.

Shekinah, S.P., Rajadurai, M., 2008. A Study of in silico Drug Docking for Triosephosphate Isomerase in *Plasmodium falciparum*. Journal of Biotechnology 7, 10-13.

Sheridan, C., 2012. Proof of concept for next-generation nanoparticle drugs in humans. Nature Biotechnology 30, 471–473.

Sherman, I., 1979. Biochemistry of *Plasmodium* (malarial parasites). Microbiological Reviews 43, 453–495.

Sidhu, A., Verdier-Pinard, D., Fidock, D., 2002. Chloroquine resistance in *Plasmodium falciparum* malaria parasites conferred by pfcrt mutations. Science 298, 210–213.

Sigma-Aldrich, 2012 website, http://www.sigmaaldrich.com, including sub-pages: http://www.sigmaaldrich.com/etc/medialib/docs/Sigma/Bulletin/b6916bul.Par.0001.File.tmp/b6916bul.pdf
http://www.sigmaaldrich.com/etc/medialib/docs/Sigma/Datasheet/2/t2507dat.Par.0001.File.tmp/t2507dat.pdf
http://www.sigmaaldrich.com/etc/medialib/docs/Sigma/Datasheet/2/t6258dat.Par.0001.File.tmp/t6258dat.pdf, [Accessed 2011, 2012, 2013]

Singh, S.K., Maithal, K., Balaram, H., Balaram, P., 2001. Synthetic peptides as inactivators of multimeric enzymes: inhibition of *Plasmodium falciparum* triosephosphate isomerase by interface peptides. The Federation of European Biochemical Societies Journal Letters 501, 19–23.

Sivaraman, S.K., Elango, I., 2009. A green protocol for room temperature synthesis of silver nanoparticles in seconds. Current Science 97, 1055–1059.

Smith, D.J., Miggio, E.T., Kenyon, G.L., 1975. Simple alkanethiol groups for temporary blocking of sulfhydryl groups of enzymes. Biochemistry 14, 766–771.

Snedeker, S., 2001. Pesticides and breast cancer risk: a review of DDT, DDE, and dieldrin. Environmental Health Perspectives 109, 35-47.

Sondi, I., Salopek-Sondi, B., 2004. Silver nanoparticles as antimicrobial agent: a case study on E. coli as a model for Gram-negative bacteria. Journal of colloid and interface science 275, 177–182.

Sørensen, H.P., Mortensen, K.K., 2005. Advanced genetic strategies for recombinant protein expression in *Escherichia coli*. Journal of Biotechnology 115, 113–128.

Sperling, R., Gil, P., Zhang, F., Zanella, M., Parak, W., 2008. Biological applications of gold nanoparticles. Chemical Society Reviews 37, 1896–1908.

Studier, F.W., 2005. Protein production by auto-induction in high-density shaking cultures. Protein Expression and Purification 41, 207–234.

Sturm, A., Amino, R., van de Sand, C., Regen, T., Retzlaff, S., Rennenberg, A., Krueger, A., Pollok, J.-M., Menard, R., Heussler, V.T., 2006. Manipulation of host hepatocytes by the malaria parasite for delivery into liver sinusoids. Science (New York, N.Y.) 313, 1287-1290.

Su, X.Z., Wu, Y., Sifri, C.D., Wellems, T.E., 1996. Reduced extension temperatures required for PCR amplification of extremely A+T-rich DNA. Nucleic Acids Research 24, 1574–1575.

Sweryda-Krawiec, B., Devaraj, H., Jacob, G., Hickman, J.J., 2004. A new interpretation of serum albumin surface passivation. Langmuir : The ACS Journal of Surfaces and Colloids 20, 2054–2056.

Toogood, P., 2002. Inhibition of protein-protein association by small molecules: approaches and progress. Journal of Medicinal Chemistry 45, 1543–1558.

Trager, W., Rudzinska, M. a, Bradbury, P.C., 1966. The fine structure of *Plasmodium falciparum* and its host erythrocytes in natural malarial infections in man. Bulletin of the World Health Organization 35, 883–885.

Trampuz, A., Jereb, M., Muzlovic, I., Prabhu, R.M., 2003. Clinical review: Severe malaria. Critical Care (London, England) 7, 315–323.

Tuteja, R., 2007. Malaria - an overview. The Federation of European Biochemical Societies Journal 274, 4670-4679.

Ugwu, S., Apte, S., 2004. The effect of buffers on protein conformational stability. Pharmaceutical Technology 86–113.

Vaidya, A.B., Mather, M.W., 2009. Mitochondrial evolution and functions in malaria parasites. Annual Review of Microbiology 63, 249–267.

Veech, R.L., Raijman, L., Dalziel, K., Krebs, H. a, 1969. Disequilibrium in the triose phosphate isomerase system in rat liver. The Biochemical Journal 115, 837–842.

Velanker, S.S., Ray, S.S., Gokhale, R.S., Balaram, H., Balaram, P., Murthy, M.R.N., 1997. Triosephosphate isomerase from *Plasmodium falciparum*: the crystal structure provides insights into antimalarial drug design. Structure 5, 751–761.

Voet, D. and Voet, J.G. (2004). Chapters 9: Protein folding dynamics and structural evolution 14: Rates of Enzymatic Reactions, 16: Introduction to Metabolism, 17: Glycolysis, In: Biochemistry, 3rd Edition, (Harris, D. & Fitzgerald, P., Eds), pp 280-283, 549-553 and 581-624, John Wiley & Sons, Inc., 111 River Street, Hoboken, NJ 07030, USA.

Von Kalm, L., Weaver, J., DeMarco, J., MacIntyre, R.J., Sullivan, D.T., 1989. Structural characterisation of the alpha-glycerol-3-phosphate dehydrogenase-encoding gene of *Drosophila melanogaster*. Proceedings of the National Academy of Sciences of the United States of America 86, 5020–5024.

Warkentin, D.L., Fondy, T.P., 1973. Isolation and characterisation of cytoplasmic L-glycerol-3-phosphate dehydrogenase from rabbit-renal-adipose tissue and its comparison with the skeletal-muscle enzyme. European Journal of Biochemistry 36, 97–109.

Wilkesman, J., Kurz, L., 2009. Protease analysis by zymography: a review on techniques and patents. Recent Patents on Biotechnology 3, 175–184.

Willner, I., Basnar, B., Willner, B., 2007. Nanoparticle-enzyme hybrid systems for nanobiotechnology. The Federation of European Biochemical Societies Journal 274, 302–309.

Wilson, K., Walker, J. (2005). Chapters: Molecular biology bioinformatics and basic techniques, *Principals and Techniques of Biochemistry and Molecular Biology*, 6th Edition, (Wilson, K., Ed), pp 207-213, Cambridge University Press, 40 West 20th Street, New York, NY 10011-4211, USA.

Word, J.M., Lovell, S.C., LaBean, T.H., Taylor, H.C., Zalis, M.E., Presley, B.K., Richardson, J.S., Richardson, D.C., 1999. Visualizing and quantifying molecular goodness-of-fit: small-probe contact dots with explicit hydrogen atoms. Journal of Molecular Biology 285, 1711–1733.

Wu, Z., Zhang, B. & Yan, B., 2009. Regulation of enzyme activity through interactions with nanoparticles. International journal of molecular sciences, 10(10), 4198-4209.

You, C.-C., De, M., Rotello, V.M., 2005. Monolayer-protected nanoparticle-protein interactions. Current Opinion in Chemical Biology 9, 639–646.

Appendices

Appendix A

Equipment and Reagents	Suppliers
EcoRI	ThermoFisher Scientific, USA
NdeI	ThermoFisher Scientific, USA
XhoI	ThermoFisher Scientific, USA
E. coli BL21(DE3)	Promega, USA
E. coli JM109	Promega, UK
pMK-T	Life Technologies, USA
pRARE2	Novagen, USA
pET28(b+)	Novagen, USA
Phusion Hot start II *Pfu* DNA Polymerase	ThermoFisher Scientific, USA
T4 DNA Ligase and 10 x buffer	ThermoFisher Scientific, USA
pJET1.2 Kit	ThermoFisher Scientific, USA
QiaPrep Miniprep Kit	Roche Applied Sciences,
Viva-Spin2 columns 10K MWCO	Sartorius Stedim
EDTA free protease inhibitor tablet	Roche, Germany
PageRuler™ protein ladder	Inqaba Biotechnology, RSA
GeneRuler DNA ladder mix	Inqaba Biotechnology, RSA
All primers were synthesised by Integrated DNA Technologies (IDT, USA)	- IDT, USA
SDS-PAGE and agarose gel Equipment	Bio-Rad, USA
2-Methyl-2-butanol	Sigma-Aldrich, USA
B-mercaptoethanol	Merck, South Africa
Acetic Acid	Saarchem, South Africa
Adenosine diphosphate (sodium salt)	Sigma-Aldrich, USA
Adenosine triphosphate (disodium salt)	Sigma-Aldrich, USA
Agar (Bacteriological)	Biolab, South Africa
Agarose	Whitesci, USA
Ammonium per sulphate	Bio-Rad, South Africa
Ampicillin	Roche, Germany
30%/0.8% Acrylamide/Bis-Acrylamide	Bio-Rad, South Africa
Bovine Serum Albumin	Bio-Rad, South Africa
Bradford's Reagent	Sigma-Aldrich, Germany
Calcium chloride	Sigma-Aldrich, Germany
Chloramphenicol	Sigma-Aldrich, USA
Coomassie Brilliant Blue R250	Merck, South Africa
Diethiothreitol	Merck, South Africa
Dimethyl sulfoxide (DMSO)	Sigma-Aldrich, USA
dNTP mix	ThermoFisher Scientific, USA
EDTA, sodium salt	Saarchem, South Africa
Ethanol	Saarchem, South Africa
Ethidium bromide	Merck, South Africa
α-Glycerol-3-phosphate dehydrogenase 100U	Sigma-Aldrich, USA
Glacial acetic acid	Saarchem, South Africa
Glycerol	Saarchem, South Africa
HEPES	Sigma-Aldrich, USA
MES	Sigma-Aldrich, USA
TAPS	Sigma-Aldrich, USA
MOPS	Sigma-Aldrich, USA
Hydrochloric Acid	Saarchem, South Africa
Imidazole	Sigma-Aldrich, USA
Kanamycin sulphate	Sigma-Aldrich, USA
Lysozyme	Sigma-Aldrich, USA

Methanol	Saarchem, South Africa
Magnesium chloride ($MgCl_2$)	Saarchem, South Africa
Magnesium Sulphate ($MgSO_4$)	Saarchem, South Africa
Polyethylene Glycol 3000 (PEG-3000)	Merck, South Africa
Polyvinylpyrrolidone (PVP)	Merck, South Africa
Potassium acetate (KOAc)	Merck, South Africa
Potassium chloride (KCI)	Merck, South Africa
Potassium hydroxide (KOH)	Merck, South Africa
Potassium phosphate (K2HPO4)	Merck, South Africa
Potassium dihydrogen phosphate (KH2PO4)	Merck, South Africa
Sodium carbonate (Na2CO3 / NaHCO3)	Merck, South Africa
Sodium chloride (NaCl)	Merck, South Africa
Sodium dodecyi sulphate (SDS)	Merck, South Africa
Sodium phosphate (NaH2PO4/ Na2HPO4)	Merck, South Africa
Sodium hydroxide (NaOH)	Merck, South Africa
Silver nitrate (AgNO3)	Merck, South Africa
Snake-skin 10 kDa MWCO	Merck, South Africa
TEMED(N,N,N’,N'~tetramethylethylenediamine)	Sigma-Aldrich, Germany
Tris (Tris-2-amino-2-hydroxymethyl-1,3-propanol)	Sigma-Aldrich, Germany -
Triton X-100	Sigma-Aldrich, USA
Tween 20	Merck, South Africa
Yeast extract	Biolab, South Africa
Pancreatic digent of casein (tryptone)	Biolab, South Africa
Biospin gel extraction kit	Bioer, China
Biospin plasmid DNA extraction kit	Bioer, China
DNA Sequencing	Inqaba biotechnology, RSA
*h*TIM gene in pMK-T vector	Life Sciences, USA
FPLC System UPC-900 AKTA	GE Healthcare, USA
Zeiss Libra 120 TEM	Zeiss, Germany
365 nm gel doc #ECX-15-L	Vilber Lourmat
Centrivap Cold trap and DNA concentrator	Vacutec, RSA

Appendix B

List of preparation procedures for buffers, growth media, agar plates, gels and other basic preparations.

Luria Broth (LB-Broth), 1 *l*, pH 7.0 (pH checked but no adjustments ever required)
10 g/l Tryptone (pancreatic digest of casein)
5 g Yeast Extract
5 g NaC*l*
(Autoclave 121°C at 1.21 kg/cm^2 for 20 min)

TB-Buffer, 250 ml
10 mM HEPES
15 mM CaCl_2
250 mM KC*l*
55 mM MnCl_2
(Mix all components except the MnCl_2 then adjust to pH 6.7 with KOH or HC*l* and add the MnCl_2 and filter sterilize with a 0.22 µm filter and store at 4°C)

Super Optimal broth (SOB) Medium, 1 *l*
20 g/l Tryptone (pancreatic digest of casein)
5 g Yeast extract
0.584 g/l NaC*l*
0.186 g/l KC*l*
2.034 g/l MgCl_2-6H_2O
2.464 g/l $MgSO_4$-7H_2O
(Autoclave 121°C at 1.21 kg/cm^2 for 20 min)

Super Optimal broth with Catabolite repression (SOC)-Broth
To 1 *l* of SOB broth after autoclaving add under sterile conditions
20 ml of 1 M glucose (filter sterilized)

LB-Agar plates (With or without antibiotics)
Add 15 g/*l* agar to 1 *l* LB-Broth medium before autoclaving.
After autoclaving allow to cool to approximately 55°C and add any necessary antibiotics, mix by swirling and gently inverting several times and then pour about 20 ml per sterile petri dish plate. Allow to cool to 4°C in fridge and store inverted.

10x TAE Electrophoresis Buffer, 1 *l*
48.4 g of Tris base [tris(hydroxymethyl)aminomethane]
11.4 mL of glacial acetic acid (17.4 M)
3.7 g of EDTA, disodium salt
Deionized water
(Tris, glacial acetic acid and EDTA are dissolved in 800 ml of deionized water and then the buffer is made up to 1 L. This was autoclaved and stored at room temperature. The solution is diluted to 1X from the 10X stock with deionized water prior to use).

Lysis by boiling procedure

The Dirty prep Lysis by boiling procedure started by adding 1.5 ml of broth culture to a 1.5 ml tube and centrifuging at 14000 rpm for 30 sec discarding the supernatant. Pelleted cells are resuspended in 350 µl STET buffer (5% {v/v} Triton X-100, 50 mM Tris-HC*l*, 50 mM EDTA, and 8% {w/v} sucrose at pH 8.0). To this 25 µl lysozyme (10 mg/ml) was added and the sample was vortexed for 3 sec. Tubes were placed in 100°C heat block for 40 sec and then centrifuged at 14000 rpm for 10 min at room temperature in a micro centrifuge. Pellet debris was removed using a toothpick and 40 µl of 2.5 M sodium acetate at pH 5.2 was added along with 420 µl of isopropanol. Sample was vortexed and left to precipitate at RT for 5 min. This was then centrifuged at 14000 rpm for 5 min and the supernatant carefully discarded. To the tube 1 ml of ice cold 70% ethanol was added and it was centrifuged at 14000 rpm for 2 min. Supernatant was discarded and the sample dried by placing it in a 45°C heat block with the lid open for 10 min. Sample was then dissolved in 50 µl 10 mM Tris-HC*l* buffer pH 8.0 using an auto-pipette. This sample was then used in double digest reactions and run on a 0.8% agarose gel for screening.

ZY medium, 1*l*

10 g pancreatic digest of casein (tryptone)
5 g of yeast extract
(Fill to 1 *l* of dddH_2O and autoclaving).

20x NPS solution, 200 ml

0.5 M $(NH_4)_2SO_4$,
1 M of KH_2PO_4
1 M Na_2HPO_4
(Filter sterilized using a 0.22 µm sterile filter into a pre-autoclaved bottle)

50x, (505)/(5052), 100 ml

250 g/*l* glycerol,
25 g/*l* glucose,
100 g/*l* α-lactose
(Filter sterilized using a 0.22 µm sterile filter into a pre-autoclaved bottle)

1 M $MgSO_4$, 10 ml

1.2 g in 10 ml dddH_2O
(Filter sterilized using a 0.22 µm sterile filter into a pre-autoclaved bottle)

ZYP505/5052, 1*l*

50 ml of 20x NPS,
20 ml of 50x 505/5052,
2 ml of 1 M $MgSO_4$ and
1 *l* of ZY media.

$KHPO_4$ Working buffer
1 M K_2HPO_4 (base) 1 *l* prepared and autoclaved
1 M KH_2PO_4 (acid) 500 ml prepared and autoclaved
(The above 2 buffers were mixed approximately 77(base):23(acid) while monitoring pH until pH 7.4 was reached, 100 ml of this was then mixed with 900 ml deionised H_2O to make the 0.1 M Working buffer).

FPLC Running buffer, 1 *l*
20 mM $KHPO_4$ (pH 7.4)
40 mM imidazole
0.5 M NaC*l*

FPLC Elution buffer, 500 ml
20 mM $KHPO_4$ (pH 7.4)
500 mM imidazole
0.5 M NaC*l*

FPLC 4x loading buffer, 100 ml
80 mM $KHPO_4$ (pH 7.4)
160 mM imidazole
2.0 M NaC*l*

FPLC $dddH_2O$, 1 *l*
FPLC 20% Ethanol, 1 *l*
(Note: All FPLC buffers filtered through 0.45 µM filtration membrane and degassed)

FPLC Gel filtration running buffer
50 mM $KHPO_4$
50 mM NaC*l*
(Adjusted to pH 7.4, then degassed and autoclaved)

SDS-PAGE Resolving gels 12.5%
1.518 ml 30%/0.8% Acrylamide/Bis-Acrylamide,
485 µl 3 M Tris-HC*l*, pH 8.8
1.641 ml sterile $dddH_2O$
91 µl 10% SDS
12.5 µl 10% ammonium persulphate (APS)
2.5 µl Tetramethylethylenediamine (TEMED)
(APS and TEMED added just prior to pouring of the gel. Once poured a few drops of H_2O saturated Tert-Amyl alcohol (2-Methyl-2-butanol) were added to prevent oxygen access and ensure it set level. Gels were allowed 1 h to set before pouring the stacking gel).

SDS-PAGE Stacking gels 4%
0.2 ml 30%/0.8% Acrylamide/Bis-Acrylamide
105 µl 0.5 M Tris-HC*l*, pH 6.8
1.185 ml sterile $dddH_2O$
15 µl 10% SDS
15 µl 10% APS
2.5 µl TEMED
(After pouring 10 tooth combs were inserted into the gels and left to set for 1 h).

SDS-PAGE 10x running buffer, 1*l*
30.28 g Tris
144 g Glycine
10 g SDS
(Buffer sterilised and diluted down to 1x using dddH_2O prior to running SDS-PAGE).

SDS-PAGE TD solution
1 ml 10% SDS
50 µl β-mercaptoethanol
(Always prepared fresh)

SDS-PAGE TS solution
13.3 ml 3 M Tris-HC*l*, pH 8.8
2 ml 0.5 M Ethylenediaminetetraacetic acid (EDTA)
40 ml Glycerol
20 mg bromophenol blue.

SDS-PAGE loading solution TD + TS
200 µl TS solution
50 µl of TD solution
(This constituted the loading solution which was mixed 1:1 with protein sample heated on a heat block (100°C, 10 min) and 25 µl loaded per well).

SDS-PAGE Fairbanks destaining solutions
Fairbanks A, 0.05% coomassie blue R-250, 25% isopropanol, and 10% acetic acid
Fairbanks B, 0.005% coomassie blue R-250, 10% isopropanol, and 10% acetic acid
Fairbanks C, 0.002% coomassie blue R-250, and 10% acetic acid
Fairbanks D, 10% acetic acid

Triethanolamine HC*l* (TEA) buffer for α-G3PDH and TIM assays, 500 ml
300 mM Triethanolamine HC*l* (TEA)
(Adjusted to pH 7.4 for α-G3PDH assays and pH 7.6 for TIM assays with KOH or HC*l*)

DHAP substrate for αG3PDH assays
76 mM Dihydroxyacetone phosphate (DHAP)
(Prepared in sterile MilliQ H_2O and frozen in aliquots)

β-Nicotinamide Adenine Dinucleotide in reduced form (β-NADH)
8 mM β-Nicotinamide Adenine Dinucleotide (reduced form)
(Prepared fresh in TEA buffer, pH 7.4 or 7.6, dependant on assay being performed).

DL-GAP Substrate for TIM assays
20 mM of DL-Glyceraldehyde-3-phosphate dilithium salt (DL-GAP)
(Prepared in sterile MilliQ H_2O and frozen in aliquots)

αG3PDH enzyme preparation for αG3PDH and TIM assays
Lyophilised αG3PDH in 100 U vials (Sigma-Aldrich) were re-suspended in TEA buffer (300 mM, pH 7.4, 1 ml, 0.05 µl β-mercaptoethanol, 6-7 drops 50% glycerol) and stored (4°C, up to 2-weeks). This helped maintain the αG3PDH enzyme in reduced form which has been shown to improve stability and freezing this enzyme is known to result in a total loss of activity (Albertyn *et al.,* 1992; De la Roche *et al.,* 2012). The (100 U/ml) stock was diluted down to working concentrations (1 U/ml) for αG3PDH assays, (20 U/ml) for TIM assays and (40 U/ml) for TIM kinetics assays. Dilutions made just prior to performing relevant assay.

pH Buffer cocktail
Four buffers in all were used in the buffer cocktail to achieve the pH range 3.5 to 9.0. These were, sodium acetate for pH (3.5 to 5.5), 2-(*N*-morpholino) ethanesulfonic acid (MES) for pH (5.6 to 6.7), 2-[4-(2-hydroxyethyl)piperazin-1-yl] ethanesulfonic acid (HEPES) for pH (6.8 to 8.2) and finally 3-[[1,3-dihydroxy-2-(hydroxymethyl)propan-2-yl]amino]propane-1-sulfonic acid (TAPS) for pH (7.7 to 9.1).

A 500 ml stock solution (20 mM) of each of these four buffers was prepared. The pH of the stock buffer was adjusted using KOH or HC*l* to create individual buffers (20 ml each) covering pH 5.5 to 9.1. For buffers covering pH 3.5 to 5.0 pH adjustments were done using acetic acid. After preparation, each of the individual buffers was filter sterilised using a syringe and a 0.45 µm filter. Overall 12 pH buffers were prepared in 0.5 pH increments covering values from pH 3.5 to pH 9.0.

Testing for change in pH due to buffer
Both purified enzymes were stored in $KHPO_4$ buffer (100 mM, pH 7.4). To test if this buffer may have altered the pH of the buffer cocktail being used, an identical $KHPO_4$ buffer (100 mM, pH 7.4) was prepared. This was diluted 1/300 (the lowest dilution used in tests) with buffer cocktail samples at pH values 3.5, 7.0 and 9.0. Change in pH level was then measured for each and it was shown that no significant pH change occurred (i.e. +/- <0.05 pH units).

An additional pH evaluation was done to test for pH changes when buffer cocktail mixed with the TIM assay buffer Triethanolamine HC*l* (TEA) (300 mM, pH 7.6). This was performed using (1:20 ratio pH 3.5 buffer cocktail to TEA). The observed pH change recorded was -0.12 which was deemed would not affect the activity assay.

Appendix C

Plasmodium falciparum cDNA sequence, Primer design and analysis.
Forward

5'-atggctagaaaatattttgtcgcagc-3'
Length=26 A=8.0 G=6.0 T=8.0 C=4.0 CG=38.5%
Complexity = 91%
Primer's PCR Efficiency = 72%

Tm = 56.3°C (Allawi's thermodynamics parameters)
Tm = 64.7°C (Sugimoto's thermodynamics parameters)
Tm = 57.1°C (SantaLucia's thermodynamics parameters)
Tm = 55.3°C (Tm = 75.1 + 11.7Log[K+] + 0.41(GC%) - 528/L)
Tm = 54.8°C (Tm = 64.9 + 41(nG + nC - 16.4)/L)

IDT Analysis

LENGTH:	26
GC CONTENT:	38.5 %
MELT TEMP:	56.3 °C
MOLECULAR WEIGHT:	8009.3 g/mole

pDraw Analysis
Tm 59.8

Reverse
5'-ttacatagcacttttttattatatcaacaaaagattc-3'
Length=36 A=14.0 G=2.0 T=14.0 C=6.0 CG=22.2%
Complexity = 70%
Primer's PCR Efficiency = 77%

Tm = 52.8°C (Allawi's thermodynamics parameters)
Tm = 62.3°C (Sugimoto's thermodynamics parameters)
Tm = 51.2°C (SantaLucia's thermodynamics parameters)
Tm = 54.3°C (Tm = 75.1 + 11.7Log[K+] + 0.41(GC%) - 528/L)
Tm = 55.3°C (Tm = 64.9 + 41(nG + nC - 16.4)/L)

IDT Analysis

LENGTH:	36
GC CONTENT:	22.2 %
MELT TEMP:	54.0 °C
MOLECULAR WEIGHT:	10975.2 g/mole

pDraw Analysis
Tm 56.5

FINAL Primers with restriction endonucleases added.
Forward with NdeI
CATATGatggctagaaaatattttgtcgcagc
Final - Forward with removal of 2nd ATG
CATatggctagaaaatattttgtcgcagc
Final - Reverse with EcoRI
GAATTCttacatagcacttttttattatatcaacaaaagattc

BLAST Scores and Top 3 results (Primer BLAST against all known sequences)

Forward
Plasmodium falciparum 3D7 triosephosphate isomerase (PF14_0378) mRNA, complete cds
Score 52.0 Total Score 74.3 Coverage 100% E-Val 9e-08
Plasmodium falciparum 3D7 chromosome 14, complete sequence
Score 52.0 Total Score 2.977e+04 Coverage 100% E-Val 9e-08
Plasmodium falciparum 3D7 chromosome 12, complete sequence
Score 30.2 Total Score 1.703e+04 Coverage 88% E-Val 0.34

Reverse
Plasmodium falciparum 3D7 triosephosphate isomerase (PF14_0378) mRNA, complete cds
Score 71.9 Total Score 163 Coverage 100% E-val 2e-13
Plasmodium falciparum 3D7 chromosome 14, complete sequence
Score 71.9 Total Score 7.418e+04 Coverage100% E-val 2e-13
Plasmodium falciparum 3D7 chromosome 7
Score 36.2 Total Score 3.078e+04 Coverage 100% E-val 0.010

Plasmodium falciparum cDNA sequence from NCBI translated into DNA code from mRNA sequence. The coding sequence from 318 to 1064 starting with ATG and ending in TAA is highlighted.

```
LOCUS     XM_001348516   1486 bp    mRNA
ORIGIN    Plasmodium falciparum 3D7 triosephosphate isomerase (PF14_0378)
        1 taaattataa tttttataat tgaccacttt ttttcttaat aaagtgaaaa taataaaaaa
       61 aatattccgt atataaaaga aaaacatatc aacaaaaata tattataata tttgcttaat
      121 ttttttaata taatatatta tttttattat atcttccctt cattaaagaa attataatat
      181 tttaaaaaac taatattata agtatataat tttattatta ttatttaaa gtgctaaccc
      241 aaaaaaaatt taattactaa gttttttatt tttttatttt tttattttat tatttttaa
      301 ttttttcttt ttacaaaatg gctagaaaat attttgtcgc agcaaactgg aaatgtaatg
      361 gaactttaga aagtattaaa tctttaacaa acagttttaa caatttggat tttgatccaa
      421 gcaaattaga cgttgttgtt tttcctgttt ccgtacatta tgatcataca aggaaattac
      481 ttcagagtaa gttttctact ggtattcaga atgtatcaaa attcggaaat ggatcataca
      541 caggtgaagt aagtgcagaa attgccaagg atttaaatat tgaatatgtt attattggtc
      601 attttgaaag aagaaaatat ttccatgaaa ccgatgaaga tgttcgtgaa aaattacaag
      661 cttcattaaa aaataattta aaagccgttg tatgttttgg tgaatcttta gaacaaagag
      721 aacaaaataa aactatcgaa gttattacaa aacaagttaa agcatttgtt gatttaattg
      781 ataattttga taatgttatt ttggcttatg aacctttatg ggctattggt actggtaaaa
      841 cagctacacc tgaacaagct caattagtac acaaagaaat cagaaaaatt gtaaaagata
      901 catgcggaga aaaacaagct aaccaaataa gaatattata tggaggtagt gttaatactg
      961 aaaactgctc ttcattaatt caacaagaag atattgatgg tttcttagtt ggaaatgctt
     1021 ccttaaaaga atcttttgtt gatataataa aaagtgctat gtaaaatata tatatatata
     1081 ttacaaatga ataatgaata gatatacata tatatatatt tgataacatt tttcttttat
     1141 atatatttta taaatgcatt tacgacttta aaaaaaaatg aggtgaacgt attctatata
     1201 tatatatata tatatatgtt gcattcaaat tttgaaaaac tatttctcat ttttatcata
     1261 tttatttatt ttatcatatt cgtgttttct cattttctta ttttttatt catcgtcatg
     1321 ttccgaactt ttctcgcaaa agtgtattta taatatttat gcctttatga ttttatcact
     1381 taccaacata taataataat aaaaaaaaaa aaaaaaaaaa aaaaaaaaaa tcaaactctc
     1441 aacattttta acacataaat aaaatttgtg ataagggaaa tgtaaa
```

Appendix D

Gels of *Pf*TIM samples

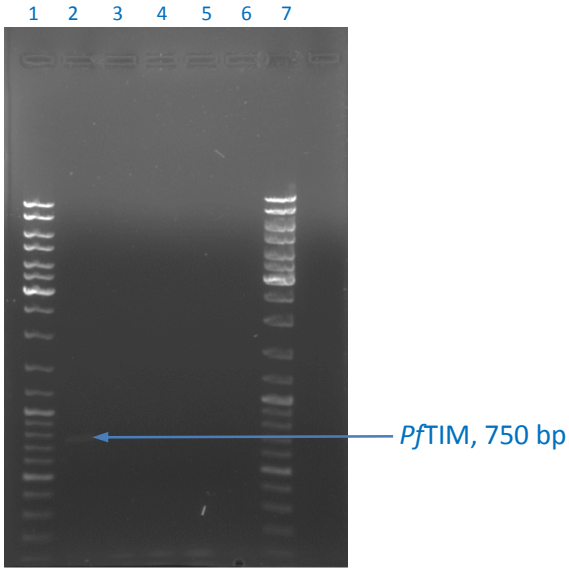

Figure D1: Gradient PCR reactions of *Pf*TIM (lane 1) using cDNA as template

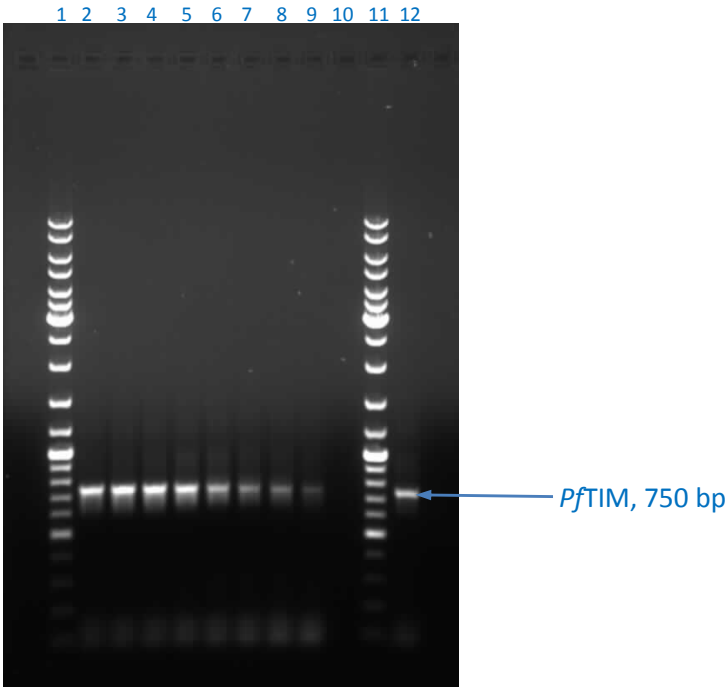

Figure D2: Optimised gradient PCR using cDNA PCR product as template strongest bands seen at 62°C and 57°C double annealing temperature procedure.

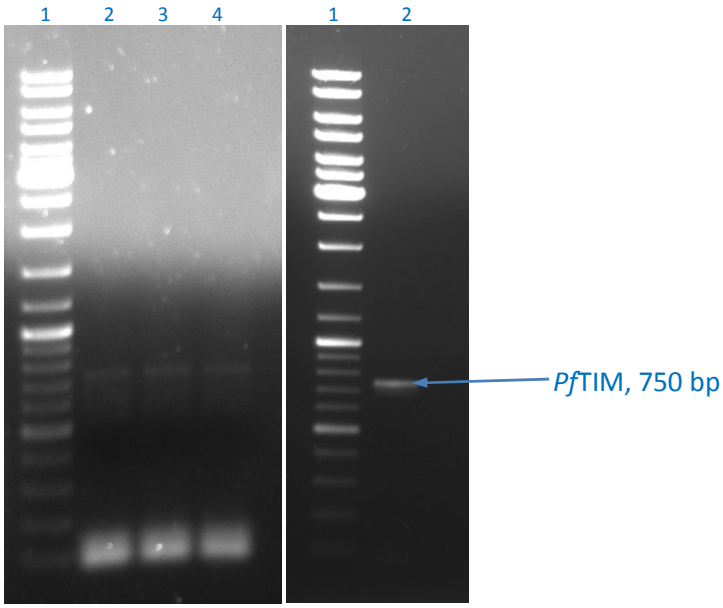

Figure D3: PCR from cDNA using the optimized protocols

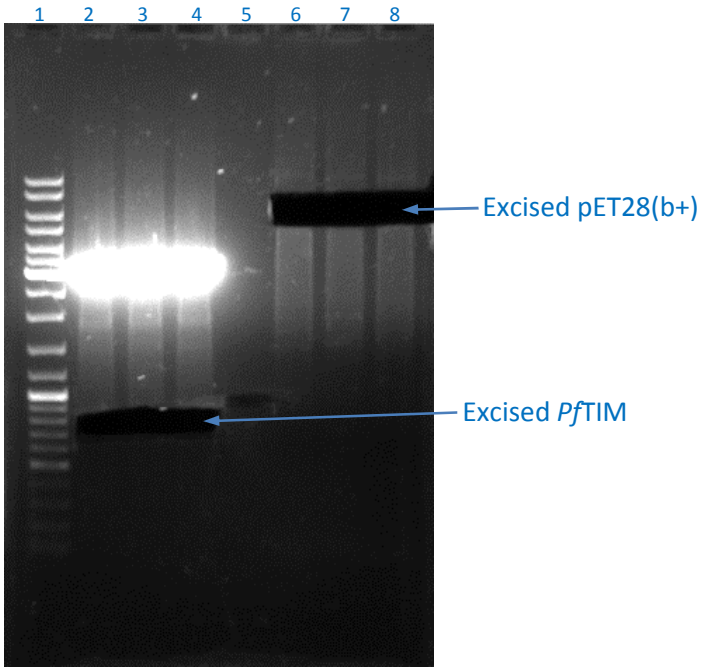

Figure D4: Image of the gel run on the double digest reaction of the pJET1.2 vector (3 Kbp) containing *Pf*TIM (lanes 2 to 4). Note: Image taken after DNA visualization at 365 nm and excision of the *Pf*TIM (cut at 750 bp) sequence for purification using the gel extraction kit. The last 3 lanes (6 to 8) indicate the double digest of the pET28(b+) expression vector (cut at 5.4 Kbp) indicating that it was in linear form. Note this was also extracted and the linearized purified *Pf*TIM and pET28b+ vector were then used for sticky end ligations as they had being digested using the same restriction endonucleased (NdeI and EcoRI).

Appendix E

Plasmid DNA Description:

The synthetic gene TIM_HS was assembled from synthetic oligonucleotides and/or PCR products. The fragment was cloned into pMK-T using SfiI and SfiI cloning sites. The plasmid DNA was purified from transformed bacteria and concentration determined by UV spectroscopy. The final construct was verified by sequencing. The sequence congruence within the used restriction sites was 100%. See the accompanying data sheets for sequences and find the original ABI trace files as well as the assembled sequences electronically on disk.
5 µg of the plasmid preparation were lyophilized for shipping.

Plasmid Map:

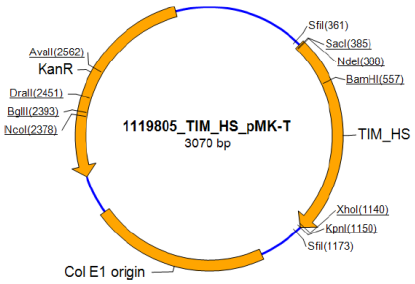

life technologies™

Quality Assurance Documentation: 1119805

Designation:	E.coli K12 (dam+ dcm+)
Gene name:	**TIM_HS**
Gene size:	771 bp
Vector backbone:	pMK-T
Cloning sites:	SfiI / SfiI
Quantity:	~5 µg Plasmid DNA
Note:	Please dissolve lyophilized DNA in 50 µl distilled water or 10 mM Tris-HCl (pH 8.0). We recommend sequence verification after each transformation step.
Date:	2 May 2011

Christian Barth
Quality control

GeneArt AG **www.lifetechnologies.com** **GeneArtSupport@lifetech.com**

Figure E1: Plasmid Map of pMK-T plasmid and essential data about the plasmid provided by life sciences.

Order No: 1119805 Gene Name: TIM_HS
Customer: Rhodes University, Jacqueline van Marwijk

Page: 1

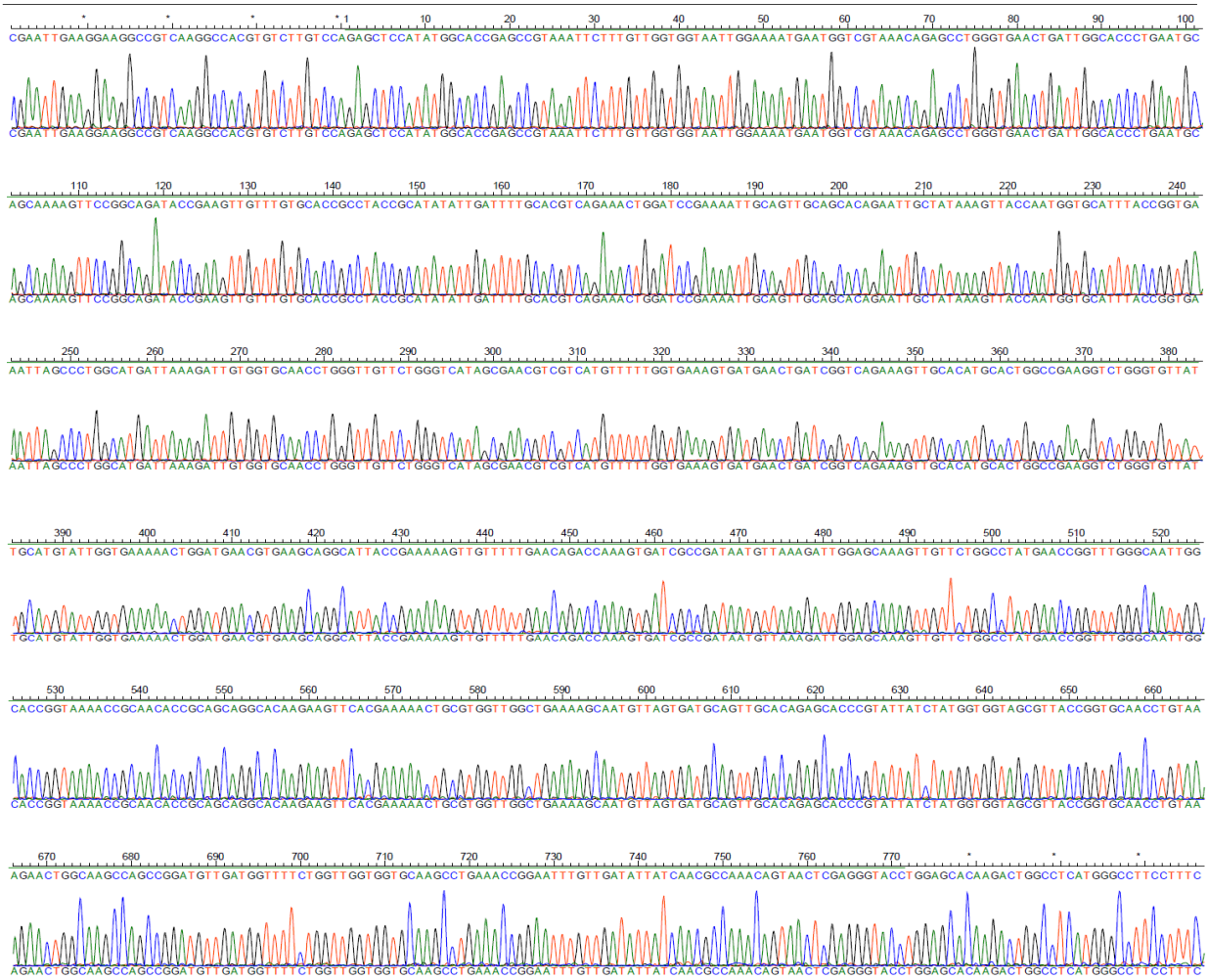

Figure E2: Chromatogram of DNA sequenced data for the purchased *h*TIM sequence.

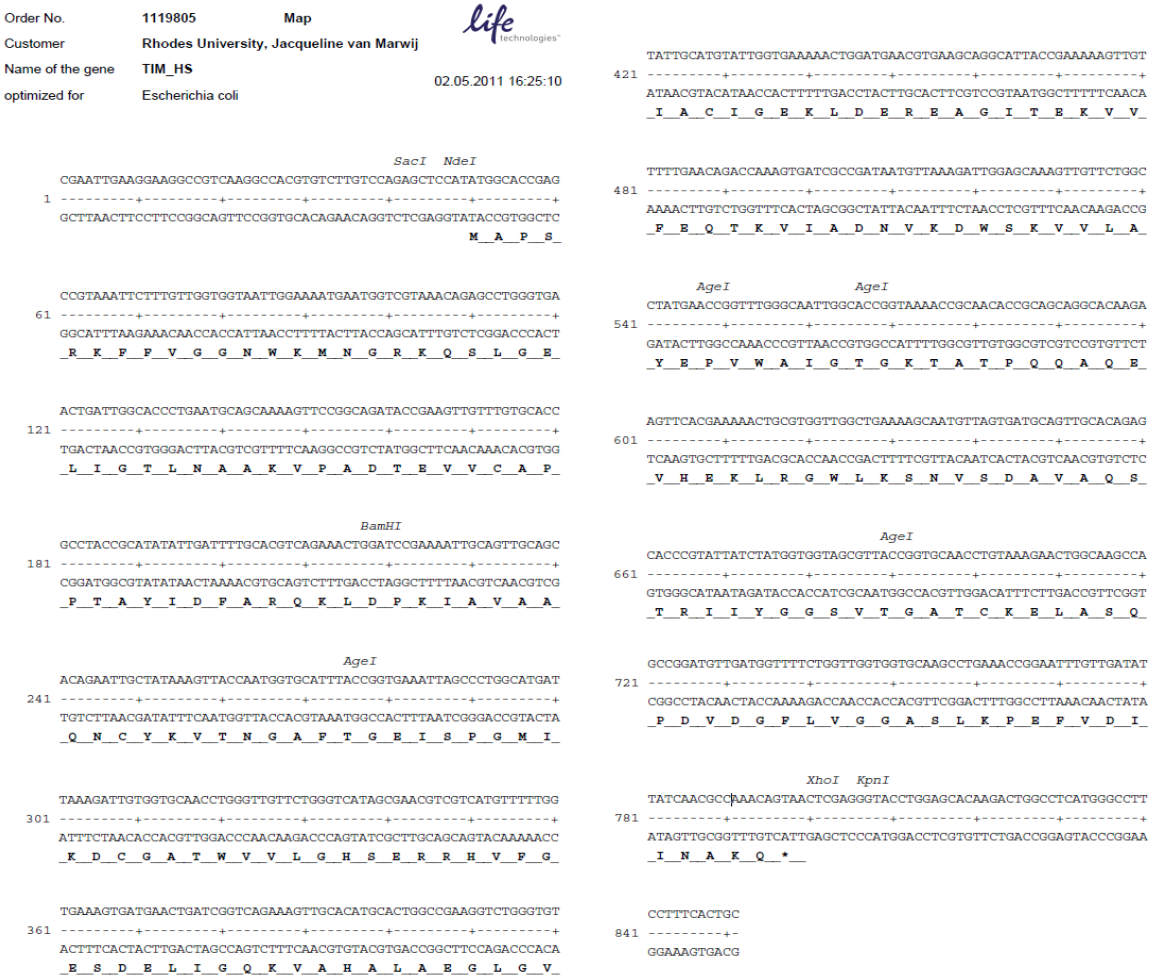

Figure E3: Purchased *h*TIM DNA sequenced translated into an Amino acid sequence.

Below is the BLAST of the translated *h*TIM amino acid sequence alignment obtained versus the known *h*TIM amino acid sequence (from NCBI) this had to be done this way because the purchased DNA sequence was codon optimised for *E. coli* and therefore differed from the human sequence. The DNA sequence arrived in the pMK-T plasmid (Figure E3).

```
Length=250
Score =  511 bits (1317),  Expect = 0.0, Method: Compositional matrix
adjust.
Identities = 250/250 (100%), Positives = 250/250 (100%), Gaps = 0/250 (0%)

Query MAPSRKFFVGGNWKMNGRKQSLGELIGTLNAAKVPADTEVVCAPPTAYIDFARQKLDPKI  60
Sbjct MAPSRKFFVGGNWKMNGRKQSLGELIGTLNAAKVPADTEVVCAPPTAYIDFARQKLDPKI  60
Query AVAAQNCYKVTNGAFTGEISPGMIKDCGATWVVLGHSERRHVFGESDELIGQKVAHALAE  120
Sbjct AVAAQNCYKVTNGAFTGEISPGMIKDCGATWVVLGHSERRHVFGESDELIGQKVAHALAE  120
Query GLGVIACIGEKLDEREAGITEKVVFEQTKVIADNVKDWSKVVLAYEPVWAIGTGKTATPQ  180
Sbjct GLGVIACIGEKLDEREAGITEKVVFEQTKVIADNVKDWSKVVLAYEPVWAIGTGKTATPQ  180
Query QAQEVHEKLRGWLKSNVSDAVAQSTRIIYGGSVTGATCKELASQPDVDGFLVGGASLKPE  240
Sbjct QAQEVHEKLRGWLKSNVSDAVAQSTRIIYGGSVTGATCKELASQPDVDGFLVGGASLKPE  240
Query FVDIINAKQ*  250
Sbjct FVDIINAKQ*  250
```

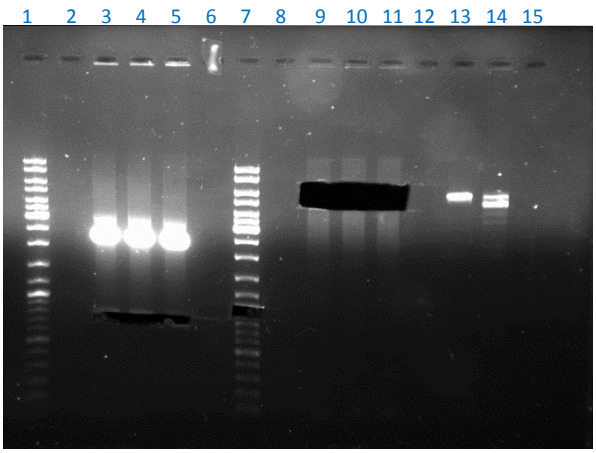

Figure E4: Gel of double digest reactions done on the p-MK-T and pET28(b+) plasmids, which were visualised at 365 nm and the bands corresponding to the *h*TIM gene at 750 bp (lanes 3 to 5) and the linearised pET28(b+) vector at 5.4 Kbp (lanes 9 to 11) were excised from the gel for DNA gel extraction and then ligation of the *h*TIM gene into pET28(b+) vector.

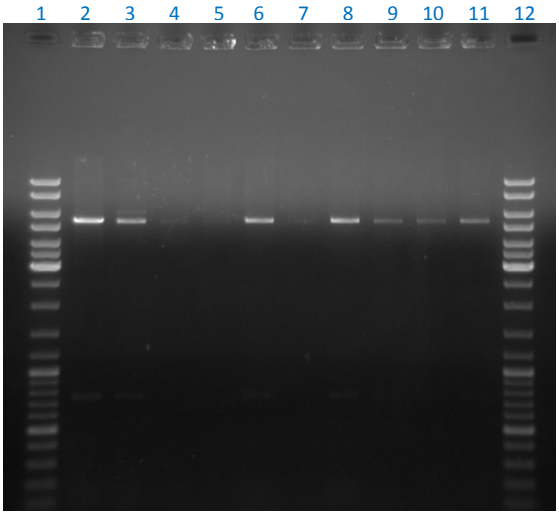

Figure E5: Agarose gel of the 'dirty prep' Lysis by boiling procedure followed by a double digest reaction (Section 2.2.5) used to screen transformed colonies for positive inserts, from this lanes 2 and 8 were selected to undergo a clean preparation procedure using the kit (Section 2.2.4).

Appendix F

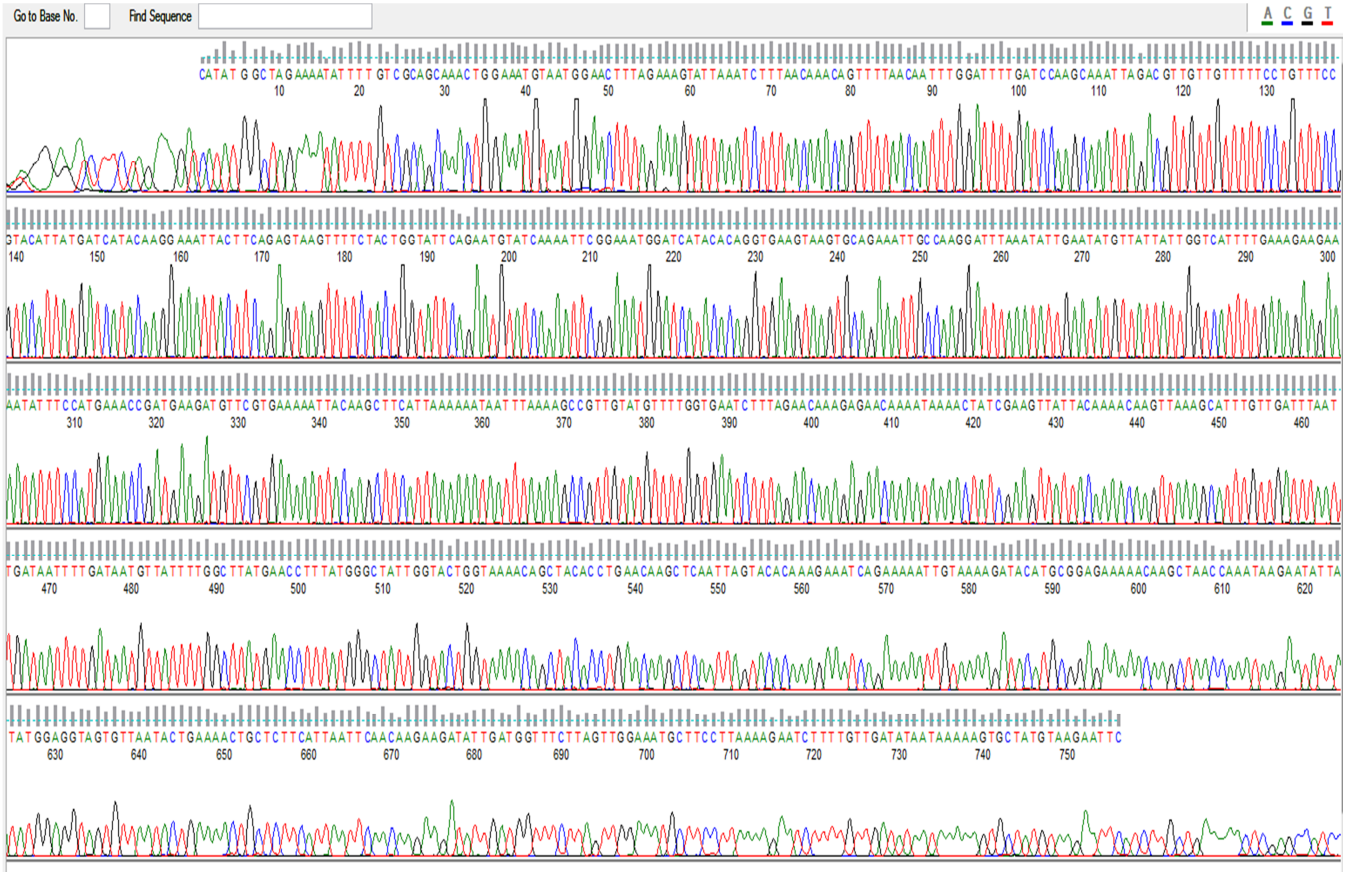

Figure F1: Chromatogram of the DNA sequencing result for the sub-cloned *Pf*TIM DNA sent in for sequencing in the pJet1.2 cloning vector using the pJet1.2 primers that came with the kit. The resulting DNA sequence is shown.

Plasmodium falciparum 3D7 triosephosphate isomerase (PF14_0378) mRNA, complete cds
Sequence ID: ref|XM_001348516.2|Length: 1486Number of Matches: 1
Related Information
Gene-associated gene details
Range 1: 318 to 1064GenBankGraphics Next Match Previous Match First Match

Alignment statistics for match #1

Score	Expect	Identities	Gaps	Strand	Frame
1380 bits(747)	0.0()	747/747(100%)	0/747(0%)	Plus/Plus	

Features:

```
Query  1     ATGGCTAGAAAATATTTTGTCGCAGCAAACTGGAAATGTAATGGAACTTTAGAAAGTATT  60
Sbjct  318   ATGGCTAGAAAATATTTTGTCGCAGCAAACTGGAAATGTAATGGAACTTTAGAAAGTATT  377

Query  61    AAATCTTTAACAAACAGTTTTAACAATTTGGATTTTGATCCAAGCAAATTAGACGTTGTT  120
Sbjct  378   AAATCTTTAACAAACAGTTTTAACAATTTGGATTTTGATCCAAGCAAATTAGACGTTGTT  437

Query  121   GTTTTTCCTGTTTCCGTACATTATGATCATACAAGGAAATTACTTCAGAGTAAGTTTTCT  180
Sbjct  438   GTTTTTCCTGTTTCCGTACATTATGATCATACAAGGAAATTACTTCAGAGTAAGTTTTCT  497

Query  181   ACTGGTATTCAGAATGTATCAAAATTCGGAAATGGATCATACACAGGTGAAGTAAGTGCA  240
Sbjct  498   ACTGGTATTCAGAATGTATCAAAATTCGGAAATGGATCATACACAGGTGAAGTAAGTGCA  557

Query  241   GAAATTGCCAAGGATTTAAATATTGAATATGTTATTATTGGTCATTTTGAAAGAAGAAAA  300
Sbjct  558   GAAATTGCCAAGGATTTAAATATTGAATATGTTATTATTGGTCATTTTGAAAGAAGAAAA  617

Query  301   TATTTCCATGAAACCGATGAAGATGTTCGTGAAAAATTACAAGCTTCATTAAAAAATAAT  360
Sbjct  618   TATTTCCATGAAACCGATGAAGATGTTCGTGAAAAATTACAAGCTTCATTAAAAAATAAT  677

Query  361   TTAAAAGCCGTTGTATGTTTTGGTGAATCTTTAGAACAAAGAGAACAAAATAAAACTATC  420
Sbjct  678   TTAAAAGCCGTTGTATGTTTTGGTGAATCTTTAGAACAAAGAGAACAAAATAAAACTATC  737

Query  421   GAAGTTATTACAAAACAAGTTAAAGCATTTGTTGATTTAATTGATAATTTTGATAATGTT  480
Sbjct  738   GAAGTTATTACAAAACAAGTTAAAGCATTTGTTGATTTAATTGATAATTTTGATAATGTT  797

Query  481   ATTTTGGCTTATGAACCTTTATGGGCTATTGGTACTGGTAAAACAGCTACACCTGAACAA  540
Sbjct  798   ATTTTGGCTTATGAACCTTTATGGGCTATTGGTACTGGTAAAACAGCTACACCTGAACAA  857

Query  541   GCTCAATTAGTACACAAAGAAATCAGAAAAATTGTAAAAGATACATGCGGAGAAAAACAA  600
Sbjct  858   GCTCAATTAGTACACAAAGAAATCAGAAAAATTGTAAAAGATACATGCGGAGAAAAACAA  917

Query  601   GCTAACCAAATAAGAATATTATATGGAGGTAGTGTTAATACTGAAAACTGCTCTTCATTA  660
Sbjct  918   GCTAACCAAATAAGAATATTATATGGAGGTAGTGTTAATACTGAAAACTGCTCTTCATTA  977

Query  661   ATTCAACAAGAAGATATTGATGGTTTCTTAGTTGGAAATGCTTCCTTAAAAGAATCTTTT  720
Sbjct  978   ATTCAACAAGAAGATATTGATGGTTTCTTAGTTGGAAATGCTTCCTTAAAAGAATCTTTT  1037

Query  721   GTTGATATAATAAAAAGTGCTATGTAA  747
Sbjct  1038  GTTGATATAATAAAAAGTGCTATGTAA  1064
```

Appendix G

Bradfords assay standard curve

To determine concentrations of protein from absorbance readings using the Bradfords method (Bradfords, 1976) a standard curve (Figure G1) was constructed using 11 points of known BSA concentrations (0-1.2 mg/ml) and the protocol provided by the Sigma-Aldrich, (2012). All data points were measured in hexlicate (n=6), and the linear equation from Figure G1 reorganised (Equation G1) for the determination of concentration from absorbance readings at 595 nm.

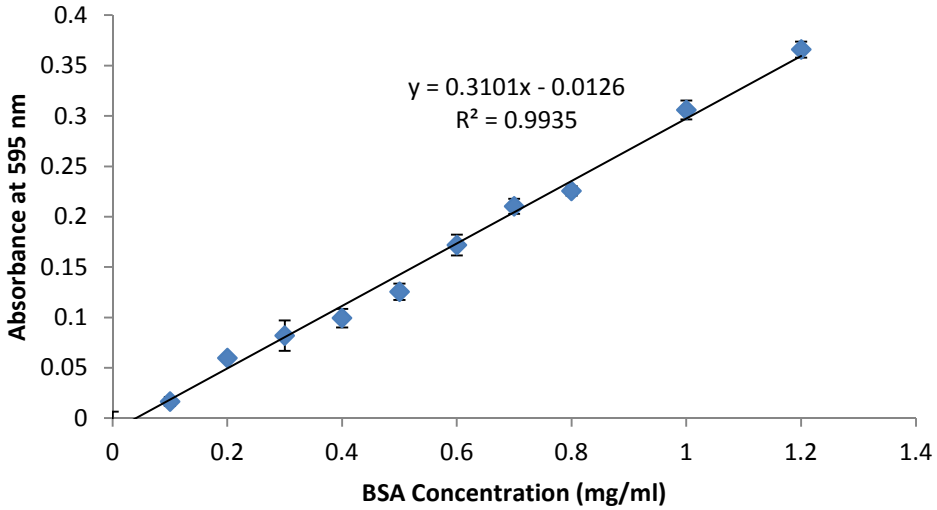

Figure G1: Bradfords assay standard curve made using known concentrations of Bovine Serum Albumin (BSA), error bars (standard deviation), linear equation and R^2 values included.

Equation G1

$$x = (y + 0.0126) / (0.3101)$$

When samples had readings out of range they were diluted 1:1 using distilled H_2O where necessary. If samples required concentration a 10 fold increase was achieved by using 50 µl per well instead of 5 µl (strictly speaking this concentration method is not correct) as it uses less Bradfords reagent per well however due to lower protein concentration (of samples that require concentration) and sufficient Bradfords reagent in the protocol for over 1 mg/ml protein full colour development does in fact occur using this method and an accurate result is produced.

Appendix H

Optimizing assay protocols

To optimize the TIM standard assay different concentrations of αG3PDH were tested. Figure H1 and Table H1 indicate the decrease in absorbance at 340 nm and the activity of *r*TIM when (13 U/ml, 20 U/ml and 40 U/ml) of αG3PDH are used. Standard concentrations for all other relevant reagents were used. These data indicate no significant increase in activity when 13 U/ml, 20 U/ml and 40 U/ml of αG3PDH are used. This was expected as the assay uses a large excess of αG3PDH. From these data it was decided that 20 U/ml of αG3PDH would be used for standard TIM assays and only kinetics assays which use large substrate concentrations would require 40 U/ml αG3PDH.

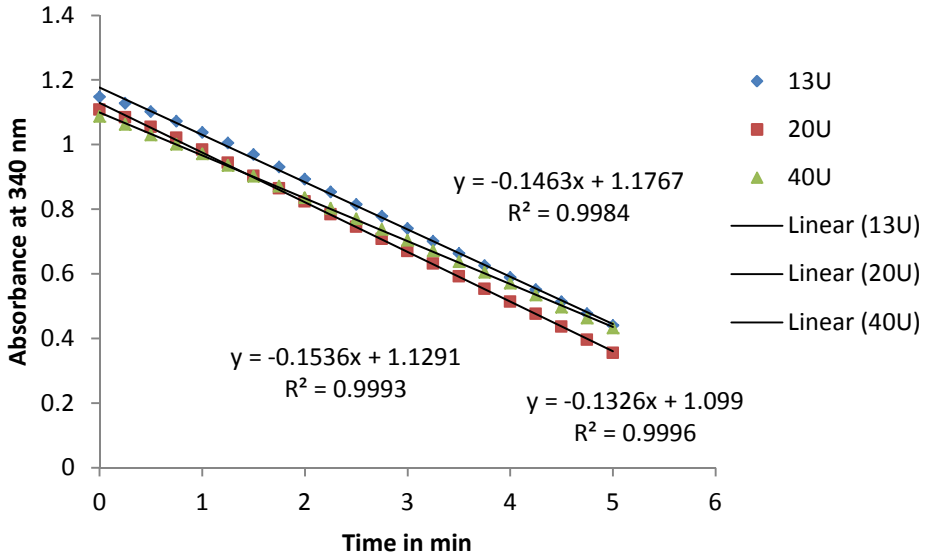

Figure H1: The activity of set *r*TIM concentrations using different concentrations (13 U/ml, 20 U/ml and 40 U/ml) of coupling αG3PDH (n=3).

Table H1: Calculated TIM activity using (13 U/ml, 20 U/ml and 40 U/ml) of αG3PDH

αG3PDH concentration	Calculated activity
13 U	0.704 mM/min
20 U	0.738 mM/min
40 U	0.636 mM/min

Averaged assay data on identical samples revealed the assay has an inherent margin of error of +/- 5-10%. Careful refinement of the operating steps and standardising conditions such as: timing and mixing procedures, brought this margin of error down to approximately +/- 5%. As such results within this margin of error range are considered to be equivalent in assays.

The other important optimization was to find the correct dilutions of the different recombinant TIM enzymes. Each of which showed different protein concentrations and activity levels after purification. Standardised running conditions recommended for this assay (Bergmeyer, 1974; Plaut and Knowles, 1972), require the assay to 'complete' or deplete NADH supply, in 5-8 min. This time range is optimally suited to allow increased or decreased enzymatic activity to be observed satisfactorily during experimentation. Many different dilutions of *h*TIM and *Pf*TIM were attempted until a 1/2000 dilution for *h*TIM and a 1/300 dilution for *Pf*TIM were able to achieve these optimal time constraints. These obviously represented different enzyme concentrations but to optimize the assay this was required. Activity per mg could then easily be calculated using the protein concentration data obtained for each TIM by Bradfords method assays and multiplying out by these set dilution ratios. These dilution ratios were used for all subsequent experiments and done as a two-step serial dilution, to achieve the highest possible level of consistency. Additionally they were always done fresh and comparisons which varied other parameters always used dilutions made from the same stock and prepared on the same day.

Optimizing assays also involved determining a negative control system for each and every individual well sample, to ensure no contamination was present. This was possible due to the coupled nature of the assay in which the monitoring of wells prior to the addition of the reaction initiating enzyme (TIM) could be used as a negative enzyme control for TIM assays. Change in absorbance monitored during pre-incubation steps was analysed over many samples and shown to be zero which was used in the equations to determine activity. This was done for a few key reasons. First: initial inconsistency in the 2 min incubation period resulted in a slight but practically insignificant gradient that could be either positive or negative, before the system equilibrated and levelled off. Second: gradient readings taken were all very low and bordering on insignificant. Third: analysis of this process over an extended period of time (~15 min) using many samples, showed that after an initial gradient change, samples would equilibrate until the gradient would level off forming a straight line of a gradient of zero. Forth: The process could be accelerated in reaching this point by using a pipette to initiate more rapid mixing by pipetting up and down, (replicating the inversion step of the 3 ml assay). Fifth: at the point of starting the enzymatic assay this level off point had being reached. For practical reasons pipette mixing could not be done on all sample wells as this would likely have increased the chance of cross contamination, exposure to other contaminants and altered very carefully measured volumes. The 2 min incubation of the

negative controls for each well also proved effective in monitoring for contamination and in cases where controls showed residual activity during pre-incubation those samples were repeated and/or eliminated from the data set.

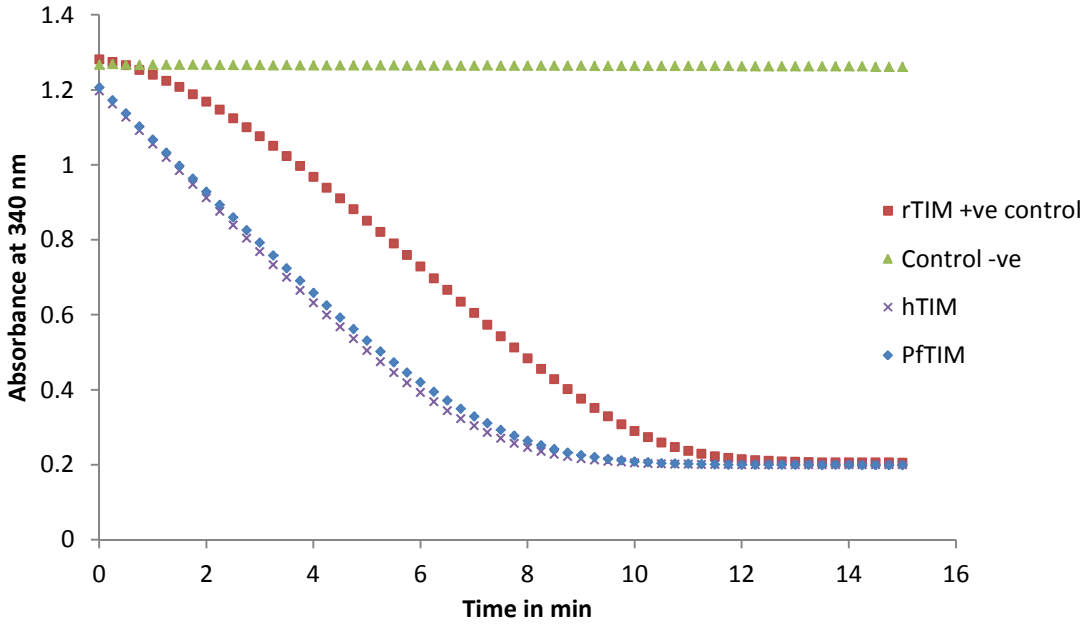

Figure H2: The activity of set *r*TIM versus *h*TIM (1/2000 dilution) and *Pf*TIM (1/300 dilution) (n=3).

Figure H2 indicates that the purified recombinant TIM enzymes are both active. Activity cannot be compared to that of the +ve control *r*TIM as the concentrations were not the same. This assay proved activity was present in both samples and the assay was functional and running to completion within the desired time duration of 5-10 min as it should. The fact that the recommended concentration of *r*TIM ran this assay to completion in approximately 10 min also indicates that all concentrations, dilutions and mixing procedures were effective and functioning.

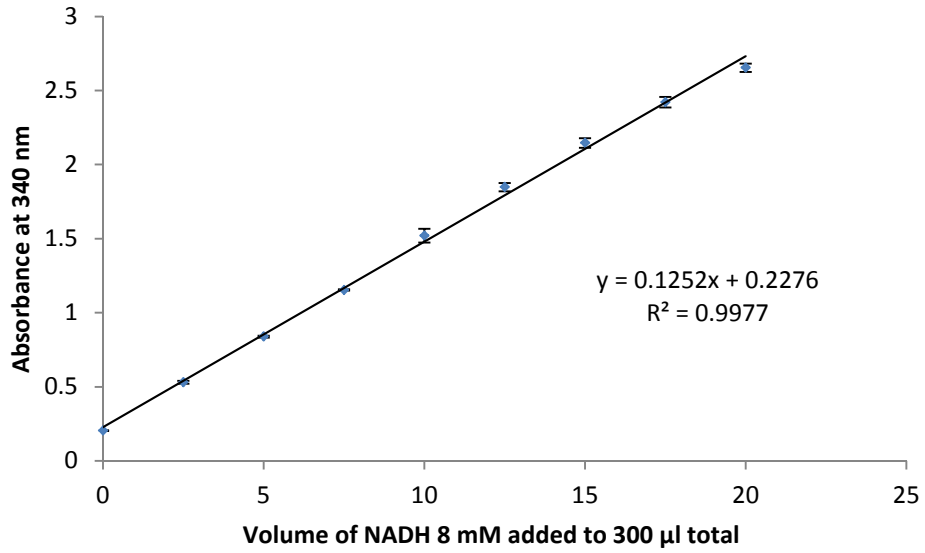

Figure H3: NADH linear response range versus volume of 8 mM NADH added, samples run in triplicate and error bars calculated using standard deviation.

From these data it was assumed that NADH produced a linear response curve in the Synergy MX spectrophotometer used up to and absorbance reading at 340 nm of 2.5. The R^2 value indicated on the graph of 0.9977 confirms the strong linear correlation of the response.

Appendix I

Activity assays to determine the activity at each step during the purification of *h*TIM (Figures I1 and I2) and *Pf*TIM (Figures I3 and I4) samples to draw up the purification tables are indicated. Activity was calculated using Equation 3.1 (chapter 3). The gradient of each curve (Figures I1 and I2) was determined by linear regression in MS Excel, taking only the most linear portion of each curve into consideration and samples were all done in triplicate. Further details such as dilution factors used and calculations for each and every sample are included in the laboratory note books handed in with this thesis.

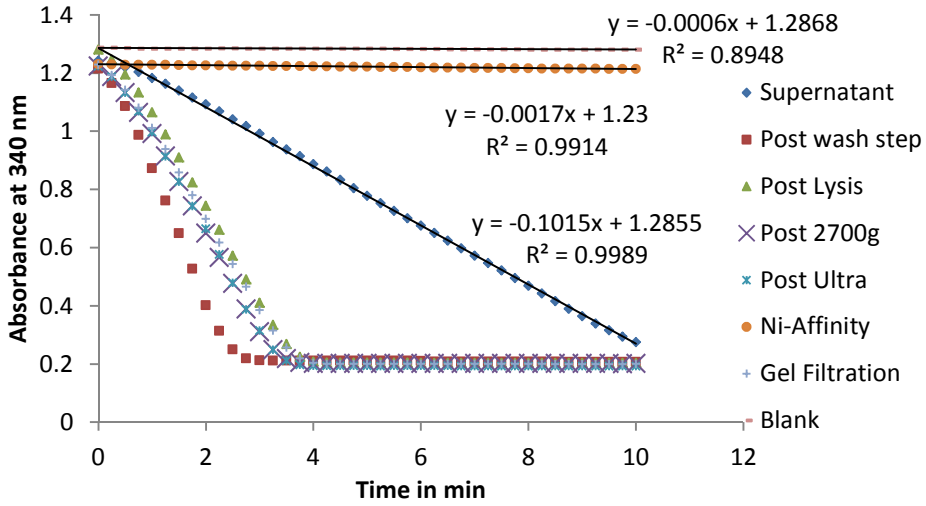

Figure I1: Coupled activity assay for *h*TIM with linear graph equations for the determination of activity. Legend indicates which purification step it was taken from (n=3).

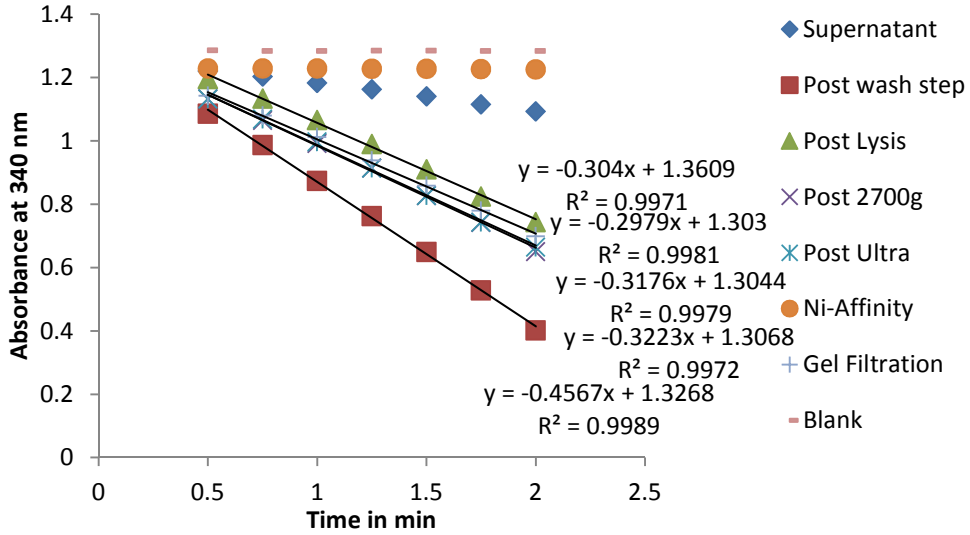

Figure I2: Coupled activity assay for *h*TIM with linear graph equations for the determination of activity. Legend indicates which purification step it was taken from (n=3).

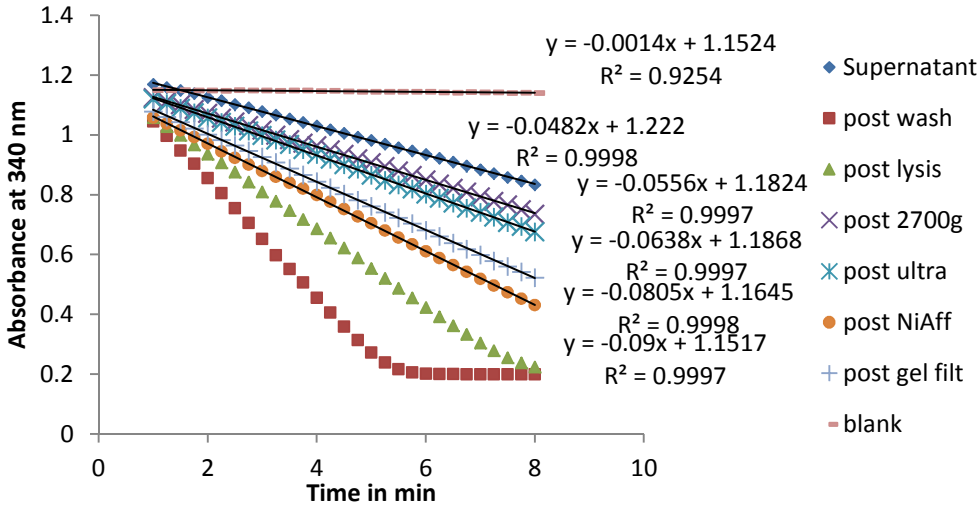

Figure I3: Coupled activity assay for *Pf*TIM with linear graph equations for the determination of activity. Legend indicates which purification step it was taken from (n=3).

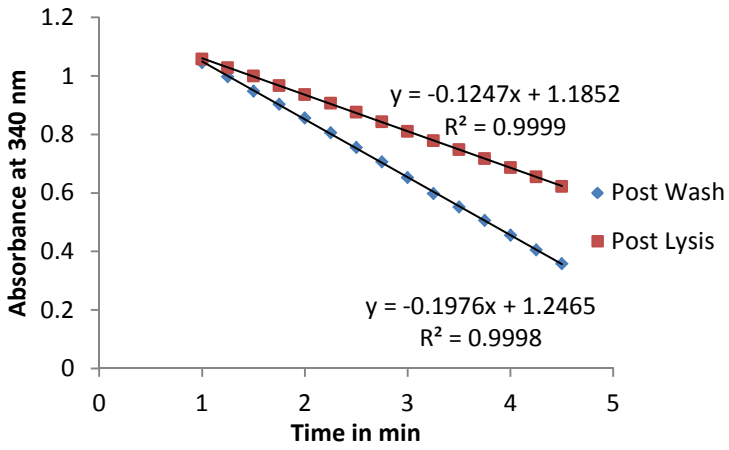

Figure I4: Coupled activity assay for *Pf*TIM with linear graph equations for the determination of activity. Legend indicates which purification step it was taken from (n=3).

For all TIM assays conducted used this method of deriving curve gradients and Equation 3.1 to calculate the activity. An example of Equation 3.1 is indicated below for the *Pf*TIM post 2700 x g centrifugation step (Figure I3, purple x).

Equation 3.1 example:

Activity = (dA/min*0.3 ml)/(6.22 µM*0.01 ml) x df
Activity = (0.0556*0.03)/(6.22*0.01) x 1000
= 0.2681672 mM/min/ml x 1000
= 268.2 µmol^{-1}.ml^{-1}.min^{-1}
Or = 268.2 Units of activity.

Appendix J

pH and temperature tests

A full breakdown of all the experiments conducted in the pH study is shown in Appendix K. All tests were done in triplicate and error bars were calculated with standard deviation. These data were then pooled for select time frames of 15 min and 45 min and there activities converted into a relative activity value based on the highest activity recording level across all tests.

Substrate concentrations in these assays were adjusted accordingly to determined K_m values for each TIM, because these tests are only ever compared with themselves to determine optimum parameters, and this was standardised for all the temperature and pH tests this does not affect the relative percentage activity or the determined pH or temperature optima as it is

always only relevant or compared with identically assayed samples.

The setup was as follows for pH and temp assays was as before, in a first set of wells: 10 µl of NADH (8 mM) and 10 µl of αG3PDH (20 U/ml) and 25 µl of DL-Glyceraldehyde-3-Phosphate (DL-GA3P) (20 mM) for *h*TIM assays and 30 µl of DL-GA3P (20 mM) for *Pf*TIM assays, was added per a well. Lastly 205 µl or 200 µl respectively of TEA buffer at pH 7.6 was added, totalling 300 µl. In a second set of wells 10 µl of the diluted TIM enzyme being tested was added (dilutions, *Pf*TIM 1/300 and *h*TIM 1/2000) prepared as 2 ml volumes and incubated in 2 ml tubes at the tested pH or temperature. Samples were then assayed using the following procedure.

Micro-titre plates were monitored in a Synergy MX spectrophotometer at (340 nm, 25°C). The system shook the micro-titre plates for 30 sec and monitored the first set of wells for change in absorbance (340 nm, 2 min, 15 sec intervals). The tray was then ejected, 290 µl taken from first set of wells and pipetted into the second set of wells containing 10 µl of the TIM enzyme being tested. The tray was immediately sent back into the machine and shaken variably for 3 sec then monitored for changes in absorbance at 340 nm for 10 min taking readings every 15 sec.

Kinetics

A drop in NADH absorbance at 340 nm was observed at highest substrate concentrations which were later eliminated from tests. This was due to small amounts of DHAP within the DL-GA3P solution reacting with the αG3PDH and oxidising NADH. This might be expected however as these two molecules are structural isomers and have identical chemical formulae, $C_3H_7O_6P$ and molecular weight of 170.06 g/mol. Any DHAP impurities in the assay are rapidly reacted away by the high concentrations (40 U/ml) of αG3PDH used for the coupled assay, meaning it wouldn't interfere with the assay, but still oxidises NADH. The concern introduced by this however was whether enough NADH was still left to monitor the coupled assay reaction when run. An additional 2 µl NADH could alleviate this problem however.

Appendix K

Calculated 'in assay' enzyme activity for all pH study tests, for activity of undiluted TIM samples, multiply by the dilution factor, 2000 x (for *h*TIM) and 300 x (for *Pf*TIM).

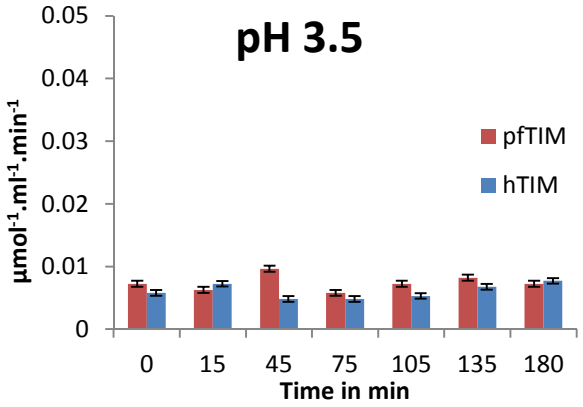

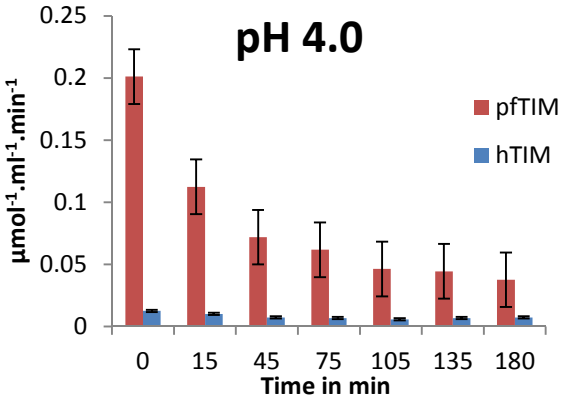

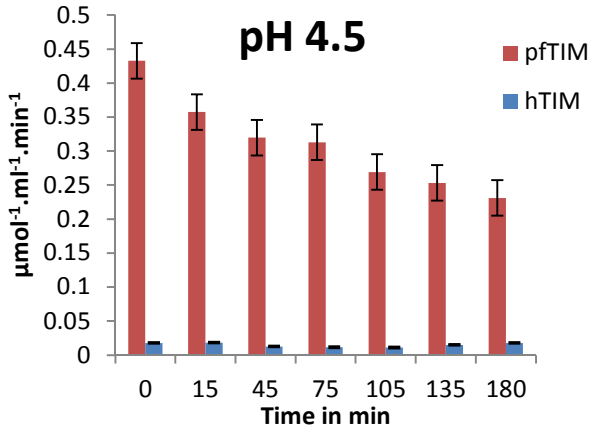

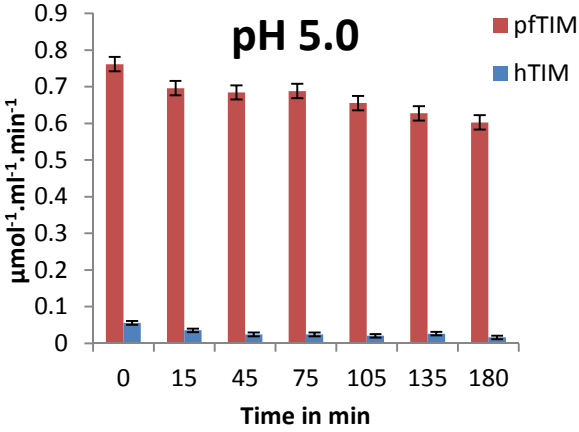

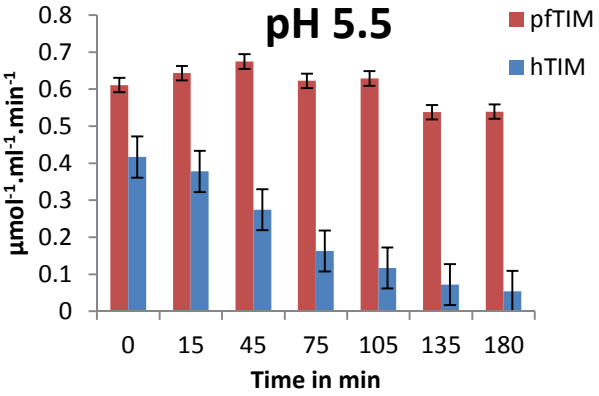

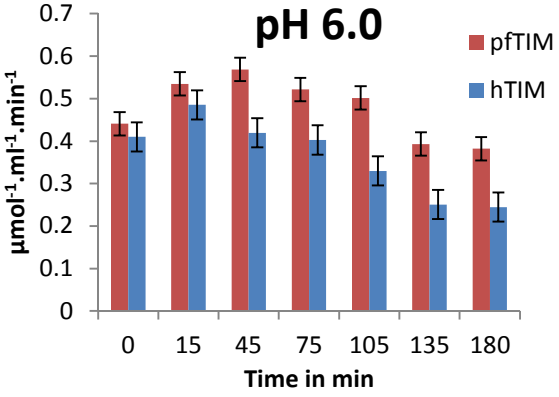

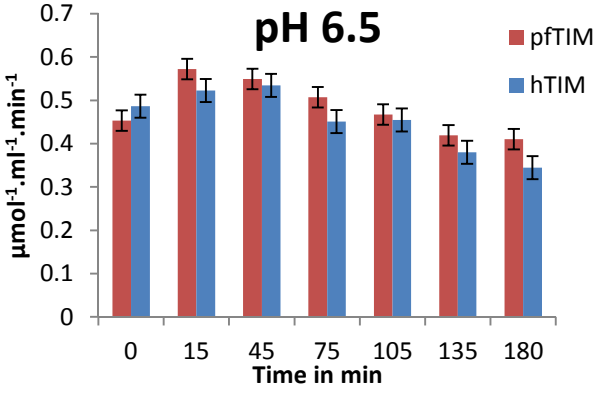

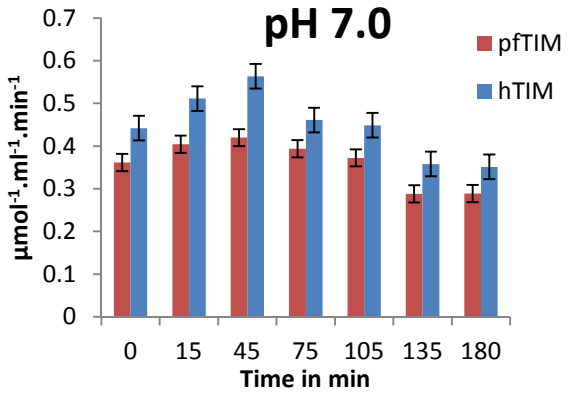

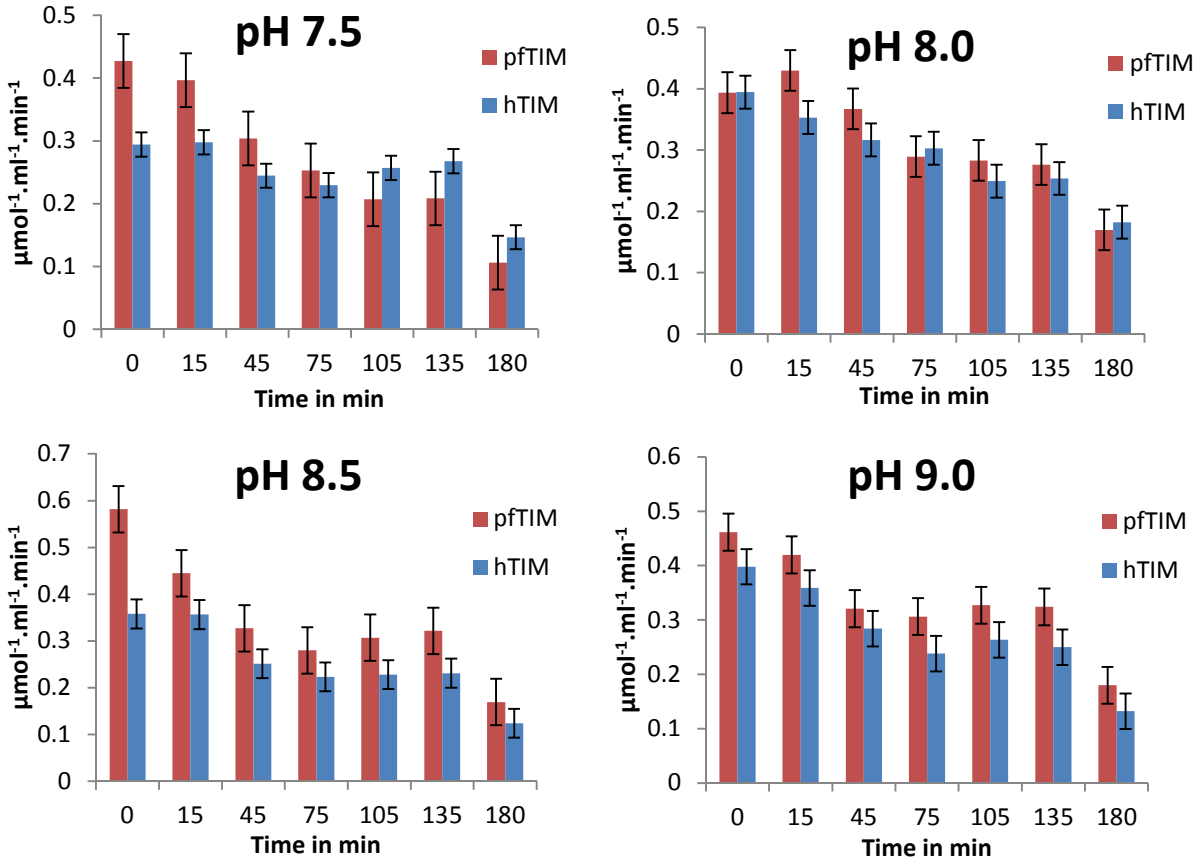

Figure K1: Activity over time for *h*TIM (red) and *Pf*TIM (blue) samples assayed from pH 3.5- pH 9.0 (n=3). Error bars use standard deviation.

Appendix L

Temperature study

Calculated 'in assay' enzyme activity for all temperature study experiments done in triplicate. Again to determine the activity of the undiluted purified TIM, the values in the graphs should be multiplied by the dilution factors used for the different TIMs, 2000 x (for *h*TIM) and 300 x (for *Pf*TIM).

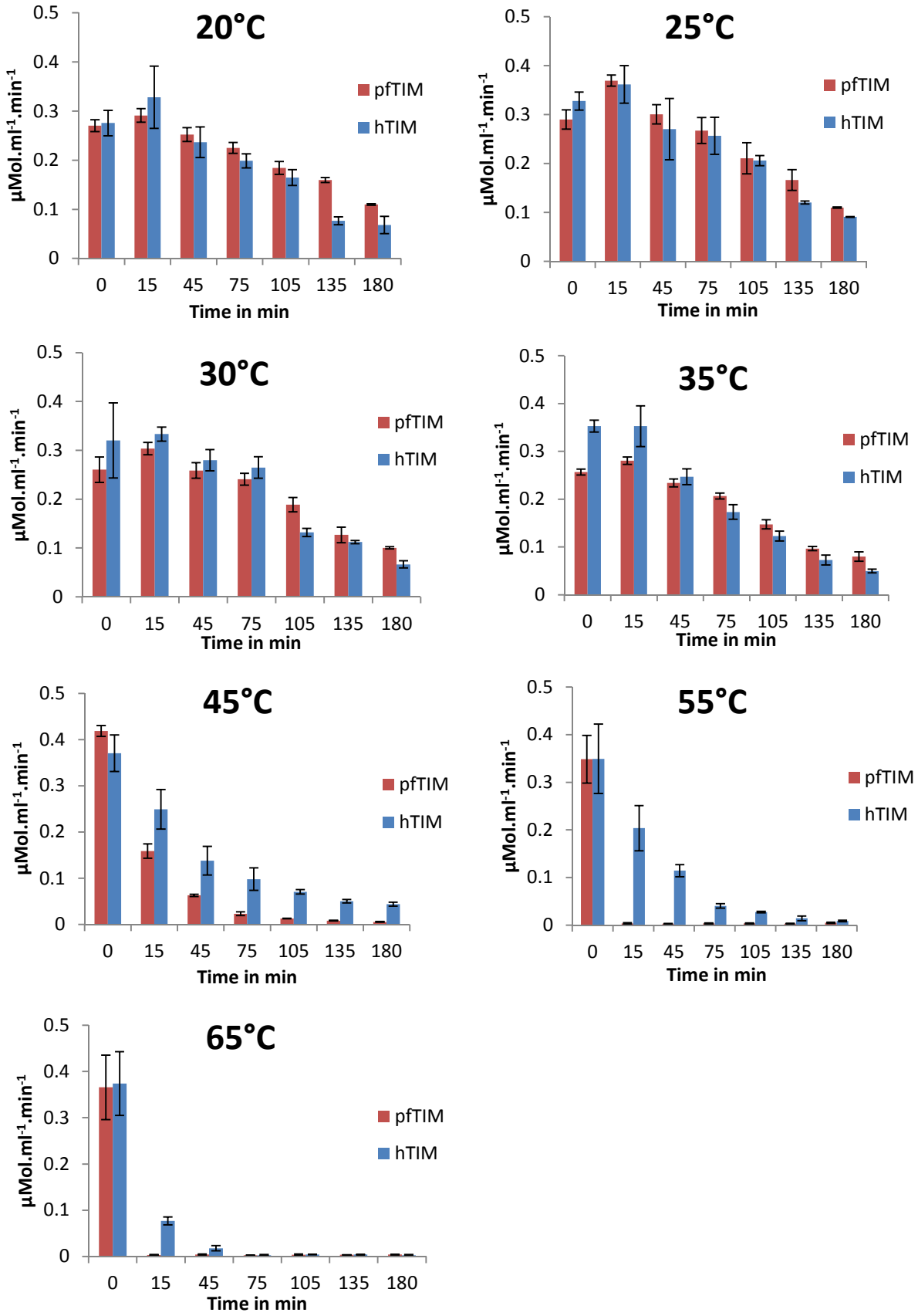

Figure L1: Activity over time for *h*TIM (blue) and *Pf*TIM (red) samples assayed at temperatures ranging from 20°C to 65°C (n=3). Error bars use standard deviation

Appendix M

It is noted that for kinetics experiments the highest substrate concentrations planned (20 mM) were unable to be used due to noticeable NADH depletion observed at the highest concentrations prior to the addition of TIM. This was due to a small amount of DHAP being present in the DL-GA3P purchased from Sigma-Aldrich, note – DHAP and DL-GA3P are structural isomers. That said excellent results up to 10 mM DL-GA3P concentrations were obtained which could then be extrapolated.

From the graphs of Figure 4.5 and using the linear regression equations determined and shown in the Lineweaver-Burk plot Figure 4.5a values for K_m and V_{max} were calculated as indicated in Equations M1 below.

Equation M1: Lineweaver-Burk calculations

K_m/V_{max}=grad	= 3.3788
$-1/K_m$ = x-int	= -1.2884/3.3788
Hence x-int	= -0.38132
K_m	= -1/ x-int
K_m	**= 2.622477 mM**
V_{max}	= 1/y-int
V_{max}	= 1/1.2884
V_{max}	= 0.776156 µMol.ml^{-1}.min^{-1} (conversion to *l* to drop volume)
V_{max}	**= 776.1565 µMol.min^{-1}**

As with the Lineweaver-Burk the Hanes-Woolf plot was also used to derive K_m and V_{max} values for the *h*TIM graph indicated in the right of Figure 4.5. Equation M2 below details the calculations to obtain K_m and V_{max} values from the Hanes-Woolf plot of Figure 4.5b.

Equation M2: Hanes-Woolf calculations

x-int = $-K_m$	= -3.2973/1.3705
Therefore	
K_m	**= 2.405910252 mM**
y-int	= K_m/V_{max}
V_{max}	= K_m/y-int
V_{max}	= 0.729660708 µMol.ml^{-1}.min^{-1} (conversion to *l* to drop volume)
V_{max}	**= 729.6607078 µMol.min^{-1}**

Equation M3: Non-linear regression calculation methodology

First off the difference of squares is calculated as follows using experimental data and an unsolved Michaelis-Menten equation with K_m and V_{max} values of 1.

1. Squared difference $\{V- [V_{max}\,[S]/(K_m+[S])]\}^2$
2. The above is calculated and added for all substrate concentration values.
3. Starting with undetermined K_m and V_{max} values set to 1 in MS-Excel.
4. The squared differences are added to give a single 'test' value.
5. The solver tool in MS-Excel is used to minimise the 'test' result (sum of squared values) by altering the value of K_m and V_{max} cells that were set to 1.
6. The solver algorithm iterates as long as necessary (probably in the millions) repeating the above equation by altering values of K_m and V_{max} and evaluating against its test, (the sum of difference of squares) each time until the lowest possible test value is obtained.
7. The resulting K_m and V_{max} represent the absolute best fit curve to the experimental data which follows the Michaelis-Menten equation and returns the resulting K_m and V_{max} to the cells that were each set to 1 earlier.

Equation M4 $\boldsymbol{K_{cat} = V_{max}/E_T}$ (Concentration of enzyme catalytic sites in µmols)

Example $K_{cat} = V_{max\,(\mu Mol/min)} / E_{T\,(\mu mol)}$ Therefore: (units are in min^{-1})
To calculate E_T = n x (# catalytic sites per enzyme)

Note for *h*TIM (df =2000; Conc = 1.49 $mg^{-1}.ml^{-1}$; M_w = 54 Kda; a 27 Kda dimer with 2 active sites)

*h*TIM = n = M/M_w = (1.49 $g^{-1}. l^{-1}$) / 54000 $g^{-1}.l^{-1}.mol^{-1}$
n = 27.592 x 10^{-6} mols in undiluted *h*TIM
n = 27.592 x 10^{-6} / 2000 (df for *h*TIM assays)
n = 13.796 x 10^{-9} mols

Therefore E_T = n x (#catalytic sites) TIM is 2 x 27 Kda monomers (as a 54 Kda Dimer)
E_T = 13.796 x 10^{-9} mols x 2 catalytic sites/molecule (TIM is a homodimer)
E_T = 27.592 x 10^{-9} mols convert to µmols
E_T = 27.592 x 10^{-3} µmols for *h*TIM

Therefore $K_{cat} = V_{max\,(\mu Mol/min)} / E_{T\,(\mu Mol)}$

E.g. (non-linear reg *h*TIM control from AgNP experiment)
K_{cat} = 1389.4 µmols.min^{-1} / 27.592 x 10^{-3} µmols
K_{cat} = $\underline{5.04 \times 10^{-4}\ .min^{-1}}$

Likewise the K_{cat} for *Pf*TIM samples was also calculated.
Note for *Pf*TIM (df = 300; Conc = 0.38 mg/ml; M_w = 54 Kda; a 27 Kda dimer with 2 active sites)

For easy reference a copy of Equation 4.1: Michaelis-Menten equation is provided below.

Equation 4.1 $V = V_{max}\,[S]/(K_m+[S])$

Appendix N

AgNP, PVP and ethanol concentration calculations for inhibition studies

The AgNPs were made using a 0.1 M solution of $AgNO_3$ and 0.2 ml of this was added to a 10 ml volume. Nanoparticle concentrations are calculated in terms of molar concentrations and also referred to as containing a size distribution of NPs. An actual count of nanoparticles was never attempted as such this would be either extremely inaccurate or impossible.

Thus 0.1 M x 0.2 ml / 10 ml = 0.002 M of $AgNO_3$ and therefore Ag^+ ions present

Concentration = 0.002 M x1000

= 2 mM $AgNO_3$ in the NP solution

From the standard 2 mM stock a 1/100 dilution was prepared by serially performing two 1/10 dilutions using 100 µl AgNPs in 900 µl optimised pH buffer used for either *h*TIM or *Pf*TIM dilutions done separately for each solution. This gave a 0.02 mM or 20 µM stock. This was incorporated into the 2 ml tubes used to dilute the respective TIM enzymes to obtain the working concentrations of NPs used for the AgNP interaction incubations that were performed at 25°C and readings were taken at T0 min and T45 min.

Final concentrations of AgNPs made were 0, 0.015, 0.03, 0.06, 0.12, 0.25, 0.5, 0.75, 1.0, 1.5, 2.0 µM. An example equation, shown below indicated how one of these concentrations was prepared.

Equation

For a final AgNP concentration of 0.12 µM AgNPs the following calculations and dilutions were performed.

To obtain this concentration using the 20 µM/ml stock the 20 µM/ml needs to be diluted by an unknown amount this unknown is calculated below.

20 µM / 0.12 µM = 166.667 (this is how much it must be diluted)

So given the above and a desired final volume of 2000 µl we can calculate how many µl of the 20 µM AgNP stock needs to be added to the 2000 µl tube. This calculation is shown below.

2000 µl / 166.667 (dividing factor) = 12 µl.

The mathematics of this calculation can be easily verified by the standard C1V1 = C2V2 equation as indicated below.

C2 = (12 µl x 20 µM) / 2000 µl

C2 = 0.12 µM (this is what was desired)

Similarly a separate divisor was calculated for each desired final concentration as described above and all the different AgNP incubation concentrations were prepared. EtOH and polyvinylpyrrolidone (PVP) containing controls were made using for equivalent concentration values of 0.12, 0.25, 0.5 and 2.0 µM. The dilutions for these controls were done exactly as described using a PVP and EtOH sample with no Ag in it. The controls were prepared identically to the AgNP containing samples and even included the microwaving step required for AgNP seed creation. This ensured control samples were completely consistent with the AgNP samples.

As the controls with PVP and EtOH were created in the exact same manner as that of the AgNP samples their concentration of relevant materials PVP and ethanol are also calculated in a similar manner to the above calculations.

PVP is a complex branched polymer with a chemical formula of $(C_6H_9NO)n$ as such molar Mr values are estimated averages (i.e. Sigma-Aldrich reports an average mol weight as 360000 g/mol). For this reason I refer to PVP concentration in g/ml. In the 10 ml solution 0.1 g was used this made it 0.01 g/ml.

As before

0.001 x 1/100 = 0.00001 g/ml or 0.01 mg/ml of 10 µg/ml in the stock

For the 0.12 µM AgNP equivalent dilution which used 12 µl in 2000 µl solution the same was done for this control with PVP. (1/166.667 dilution). Thus

10 µg/ml PVP / 166.667 = 0.05999 µg/ml PVP or approximately 60 ng/ml PVP in this dilution.

Thus the 4 controls dilution equivalents contained 60, 125, 250 and 1000 ng/ml PVP in the incubation with nanoparticles. This became 1.94, 4.03, 8.06 and 32.25 ng/ml PVP within the assay volume after dilution with other assay reagents and enzymes.

Likewise the absolute ethanol was 95% vol (190 proof). Thus its concentration in the AgNP TIM incubations was therefore

0.95 /100 / 166.667 = 0.00570 % EtOH in the 0.12 µM/ml AgNP sample

Thus EtOH concentrations were 0.00071, 0.00123, 0.00285, 0.00570, 0.01188, 0.02375, 0.033563, 0.0475, 0.07125 and 0.095 % over the 10 different AgNP dilutions used, namely 0, 0.015, 0.03, 0.06, 0.12, 0.25, 0.5, 0.75, 1.0, 1.5, 2.0 µM and also in the relevant equivalently diluted control samples. The term ‘equivalent dilutions’ was used to simplify the comparisons as it is easier to understand what the equivalent PVP and ethanol control is relevant to that to use the ng/ml concentrations of PVP and obscurely low % ethanol values relevant.

IC_{50} calculations

These are very basically done using a linear regression and the inhibition data from 45 minute incubations with AgNPs, because of the rapid drops in activity seen with increasing concentrations only 4 data points for *h*TIM and 3 data points for *Pf*TIM could be used.

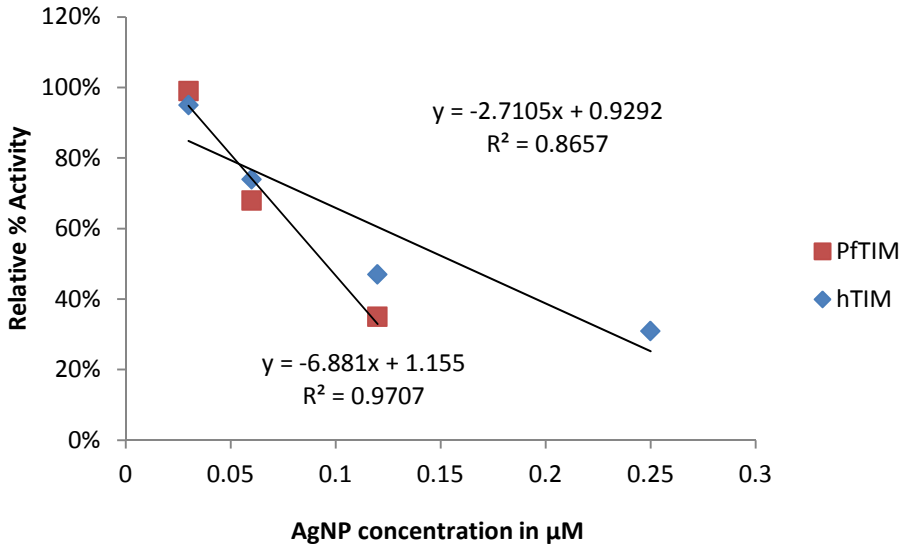

Figure N1: Linear range of decrease in relative percentage activity for *h*TIM (blue) and *Pf*TIM (red), linear regression equations were reorganised to determine IC_{50} levels as Equations N1 and N2 (below).

Equations: N1 and N2

For *h*TIM		For *Pf*TIM	
Equation N1		**Equation N2**	
if	y = 50%	if	y = 50%
then	x = (0.5-0.9292)/-2.7105	then	x = (0.5-1.155)/-6.881
x =	0.158347 µM AgNPs	x =	0.09519 µM AgNPs
IC_{50}	0.158347 µM AgNPs	IC_{50}	0.09519 µM AgNPs

The above calculations are only considered as a rough estimate of IC_{50} AgNP concentration levels.

Appendix O

Spectral scans taken immediately after the microwave process had slight peaks with an absorbance of less than 0.2 prior to any dilution. This is compared to a week old sample with an absorbance peak of 1.6 using a 1:3 dilution (Figure O1).

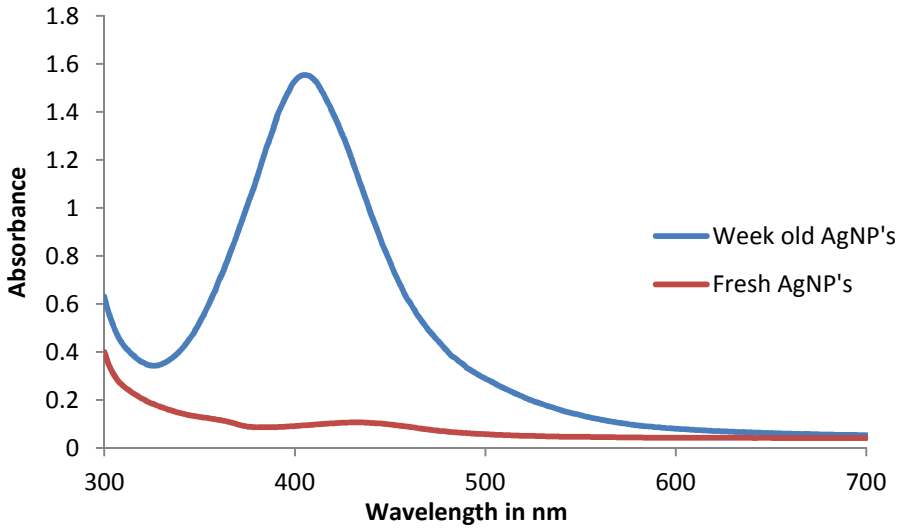

Figure O1: Fresh AgNPs versus one week old AgNPs.

The above figure demonstrates that AgNP seeds need time to mature after removal from the microwave. This confirms that AgNP growth occurs through a seeded growth process, other experiments done over the 1st few hour after removal from the microwave confirmed that this seeded growth period mainly occurs within the 1st 2 hours after removal from the microwave. Further experiments indicated barely any detectable change occurs from 1 day old AgNPs to 3 month old AgNPs, with only a slight level of aggregation occurring during this time. Thus it was concluded that as long as the AgNPs had being allowed to mature overnight the seeded growth phase was assumed to have finished and they were ready for use.

This indicated that the seeded growth period also completed overnight. In addition to this a test was conducted making spectral scans after 30 min 1, 2 and 3 hours. These scans tracked an increasing peak height which increased rapidly over the first 2 hours after microwaving (data not shown). This indicated nanoparticle growth was still occurring for at least a couple of hours after removal from the microwave, but confirmed no further growth of the nanoparticles occurred after day 1. Consequently all nanoparticle samples were allowed a period of at least 1 day for seed growth after microwaving before use. This also helped ensure no free Ag^+ ions remained in AgNP solutions.